Atomistic Simulations of The Structure of Calcium Silicate Hydrates: Interlayer Positions, Water Content And A General Structural Brick Model

THÈSE N^{O} 8840 (2018)

PRÉSENTÉE LE 18 SEPTEMBRE 2018

À LA FACULTÉ DES SCIENCES ET TECHNIQUES DE L'INGÉNIEUR
LABORATOIRE DE TECHNOLOGIE DES POUDRES
PROGRAMME DOCTORAL EN SCIENCE ET GÉNIE DES MATÉRIAUX

ÉCOLE POLYTECHNIQUE FÉDÉRALE DE LAUSANNE

POUR L'OBTENTION DU GRADE DE DOCTEUR ÈS SCIENCES

PAR

Aslam KUNHI MOHAMED

acceptée sur proposition du jury:

Prof. P. Muralt, président du jury
Prof. P. Bowen, Dr S. C. Galmarini, directeurs de thèse
Prof. S. Parker, rapporteur
Prof. C. Greenwell, rapporteur
Dr D. Kulik, rapporteur

ÉCOLE POLYTECHNIQUE
FÉDÉRALE DE LAUSANNE

Suisse
2018

Acknowledgements

First of all, I would like to thank everyone who contributed directly or indirectly to this thesis and make my life as a PhD student memorable. There are four key people I am very grateful to and without whom I would not be able to enjoy my thesis work.

Prof. Paul Bowen (EPFL) is definitely one of the best PhD director you can ever wish for. He has given me the freedom to learn different methods, topics, explore and at the same time making sure I achieve my PhD goals and be pragmatic in designing my scientific projects or goals. I also thank him for making my personal and academic life much easier with his friendly and easy going approach.

Prof. Karen Scrivener (EPFL) has been instrumental in my life for the past seven years and without her guidance, support and caring I would not be able to reach to this day of my life. It was a pleasure working with a world renowned cement scientist and a visionary. It is impossible to express my gratitude to Karen with words, I thank her for everything she has been to me.

Prof. Steve Parker (University of Bath) is probably the nicest person I have ever met. I thank him for welcoming me in his group in Bath several times during the past four years and for being overly kind and patient to all my questions. It was my immense pleasure to work with a brilliant computational chemist and I sincerely thank him for all the help and discussions on computational methods and general chemistry which has been extremely motivating and inspiring.

Dr. Sandra Galmarini (EMPA) is a talented material scientist who is my co-advisor and have always inspired me to learn and improve my understanding. I am really thankful to her for all the guidance, teachings and discussions during the past four years and without her expertise on my side I would not be able to go this far.

I would also like to thank Dr. Ulrich Aschauer for guiding me on several aspects of simulations.

I would like to thank Prof. Heinrich Hofmann for ensuring a pleasant atmosphere at LTP. In addition to these, I would also like to thank Abhishek and Jirawan (the mini C-S-H group) for all the nice discussion on C-S-H, improving my experimental knowledge of C-S-H, sharing food and making the trips to Nanocem meetings always memorable. A special thanks to Azade for being the best and the coolest office mate and a great friend. I am very thankful for the interesting discussions and help on simulations. Thanks to Irena for the frequent coffee breaks with thought-provoking discussions on a variety of topics and creating an energetic atmosphere at LTP. I also would like to thank the rest of

the LTP members David, Weitian, Marijana, Nadia, Debora, Sami, Silvia, Joao, Aurelie, Amar, Bhuvanesh, Abhishek Tewari, Lionel, Marie-Gabrielle, Masood, Milica, Gabie, Carlos, Shawn and anyone whom I have unfortunately missed. I also thank Anne Remillet, ex- LTP secretary who made the administrative works very simple.

One of the best part of my life at EPFL was also the time I spent at LMC and where I have made several friends. A great and special thanks to my ex-office mates and friends Elise and Pawel. They made my life at EPFL and in Switzerland easy and unforgettable with very good memories, I thank them profoundly for being such great friends. A special thanks to Pawel for sharing the love for mountains and food. Thanks to Julien Bizzo for being a very good friend and the trips we went with Pawel. Thanks to all other LMC members : Francois, John, Berta, Mo, Ruben, Hadi , Amelie, Lily, Arnaud, Mathew, Cyrille, Julien, Alexandre, Xeurun, Aurelie, Mink, Anna, Wioletta, Franco, Yosra, Lionel, Emmanuel and others whom I might have forgotten to mention, I sincerely apologize. I would also like thank the LMC secretaries Anne-Sandra, Maude and Marie-Alix for always being there for me and very helpful.

Thanks to all collaborators, especially Brennan, Albert, Ratan, Hegoi and Prof. Lyndon Emsley. I also thank Dr. Barbara Lothenbach and Prof. Robert Flatt for their comments and discussions on C-S-H.

A very special thanks to Dr. Patrick Juilland (Sika Technology AG Zurich) for being the primary inspiration for me to pursue this PhD and being a good friend.

I would also like to thank Swiss National Foundation (SNF 153044) for the funding and the Nanocem consortium for including our project as a partner project.

I would also like to thank my friends Edy, Damien and Alvaro for all the fun. Thanks to Anand for making me less homesick and be there for me always.

Finally, my beautiful family and thank the Almighty for everything.

Aslam,

Lausanne 2018

Abstract

Portland cement (PC) based concrete is the most used material in the world. Portland cement has been in use by human civilization for over a century. Yet, we do not fully understand its hydration reaction mechanisms due to the complexity of the system and its continued reaction over time making it hard to study it experimentally. Additionally, it contributes to about 10 % of the world carbon dioxide emission. In order to make cement more sustainable, supplementary cementitious materials (SCMs) are substituted for PC. There are many undesirable effects of some SCMs on the early age hydration and later age properties limiting a wider application. One of the key factors hindering the educated designing of new sustainable cements is the lack of knowledge of the atomistic structure of the main hydrate phase of PC, Calcium Silicate Hydrate $(C-S-H)$ and its interaction with SCMs.

$C-S-H$ has a variable stoichiometry, nano sized morphology, variable water content and a complex layered structure. Although $C-S-H$ has been studied for decades, the atomic structure of this nano crystalline phase is not clearly known or agreed upon and remains an open question. The proposed structures of $C-S-H$ are mainly based on 14 Å tobermorite, a natural mineral. A defective structure with different Ca/Si ratios is created by depolymerizing silicon chains and/or by addition of Ca in the interlayer space of a tobermorite supercell structure. There are two main models for C-S-H based on atomistic simulations (Qomi et al. Nat Comm. 2014, Kovačević et al. CCR 2015) which have been reported in literature. Both contain defects that have been created in a random fashion in top down approach, from order to disorder. However, this approach has resulted in $C-S-H$ structures which are inconsistent with the available experimental evidence on several key atomic features such as no monomeric silicates, silicate chains as 3n-1 mers (where n is a positive integer) and calcium coordination of six or above.

In this thesis a new bottom up approach has been developed to precisely define and create defects or 'chemical building blocks' in a reduced unit cell of 14 Å tobermorite called the "Brick model". In this model, a string of characters can represent the multitude of structural features in $C-S-H$ with precise control over its arrangement. This is done by assigning a letter of notation for each building block and a string of these letters, written in a fashion coherent to their arrangement in a unit cell, represents a defective reduced unit cell or a "brick" with precise definition of defects in it.

A chemical reaction scheme to assess the relative stability of these defect containing bricks, from the reaction enthalpy calculated using molecular dynamics (MD) simulations, was also developed. The model can efficiently capture the structural features of C-S-H and can propose a probable full scale atomic structure of $C-S-H$ including surfaces. The model can be extended to other tobermorite or jennite based structures and an instance of translating an existing atomistic model in literature to the brick model nomenclature was also shown, thus enabling effective comparisons.

In a collaborative work as an application of the brick model, Dynamic Nuclear Polarization Nuclear Magnetic Resonance (DNP NMR) experiments combined with density functional theory (DFT) calculations on structures generated using the brick model was used to understand the atomic level structure of high Ca/Si ratio synthetic $C-S-H$. In addition to quantifying the silicate speciation and its connectivity and confirming a tobermorite-like underlying structure, the existence of a new calcium position was discovered which bridges the terminal silicates of two silicate chains and induces a strong hydrogen bonding in the interlayer. It was concluded that the calcium at the bridging site is a characteristic feature of $C-S-H$. These insights are used as constraints to generate a series of atomic structures for $C-S-H$ of different Ca/Si ratios wholly consistent with experiment. These are highly defective 14 Å tobermorite-like structures.

To further understand the complex interlayer structure of $C-S-H$ and the interaction between the defects within the bulk material, the brick model was used to generate a variety of distinct defects and calculate their enthalpies. Our results indicate that the presence of silanols in $C-S-H$ are energetically unfavourable and a lower water content results in a more ordered or crystalline interlayer region. We discovered a second new enthalpically stable position for the interlayer calcium and identified two types of water based on their "crystallinity" or how strongly the water molecules are coordinated to calcium ions in the interlayer. The results on the defects' interactions indicate that the structural units of $C-S-H$ with different interlayer volumes, due to the presence of different types of defects interact and create strains in the $C-S-H$ sheet structure. However, the calculated interaction energy is not prohibitive of their existence. With these findings explanations for the lack of long range order or nano-crystallinity of $C-S-H$ have been proposed which give us valuable insights into key aspects of C-S-H such as growth mechanisms and ageing. Thus the current results can be expected to facilitate the engineering of the C-S-H mesostructure and eventually leading to more sustainable and futuristic cements with less carbon footprint and energy demand.

Keywords: $C-S-H$, Cement, Molecular Dynamics, Density Functional Theory

Résumé

Le béton à base de ciment Portland (PC) est le matériau le plus utilisé au monde. Le ciment Portland est utilisé par la civilisation humaine depuis plus d'un siècle. Pourtant, nous ne comprenons pas complètement ses mécanismes de réaction d'hydratation en raison de la complexité du système et de sa réaction continue au fil du temps, ce qui rend difficile l'étude expérimentale. De plus, il contribue à environ 10% des émissions mondiales de dioxyde de carbone. Afin de rendre le ciment plus durable, des matériaux cimentaires supplémentaires (MCS) sont substitués au PC. Cependant, il existe de nombreux effets indésirables de certains MCS sur l'hydratation précoce et les propriétés de l'âge tardif limitant une application plus large. L'un des facteurs clés qui entrave la conception raisonnée de nouveaux ciments durables est le manque de connaissance de la structure atomique de la phase hydrate principale du PC, l'hydrate de silicate de calcium (C-S-H) et son interaction avec les MCS.

C-S-H a une stœchiométrie variable, une morphologie de taille nanométrique, une teneur en eau variable et une structure en couches complexes. Bien que le C-S-H ait été étudié pendant des décennies, la structure atomique de cette phase nanocristalline n'est pas clairement connue ou convenue et reste une question ouverte. Les structures proposées de C-S-H sont principalement basées sur le 14 Å tobermorite, un minéral naturel. Une structure défectueuse avec différents rapports Ca / Si est créée en dépolymérisant les chaînes de silicium et / ou en ajoutant du Ca dans l'espace intercouche d'une structure de supercellule tobermorite. Il existe deux modèles principaux de C-S-H basés sur des simulations atomistiques qui ont été rapportés dans la littérature. Les deux contiennent des défauts qui ont été créés de manière aléatoire dans l'approche descendante, de l'ordre au désordre. Cependant, les approches ont abouti à des structures C-S-H qui sont incompatibles avec les preuves expérimentales disponibles sur plusieurs caractéristiques atomiques clés telles que les silicates monomères, les chaînes silicatées comme 3n-1 mers (où n est un entier positif) et la coordination du calcium de six ou plus. .

Dans cette thèse, une nouvelle approche ascendante a été développée pour définir et créer avec précision des défauts ou des «blocs de construction chimiques» dans une cellule unitaire réduite de 14 Å tobermorite appelée «modèle de brique». Dans ce modèle, une chaîne de caractères peut représenter la multitude de caractéristiques structurelles dans C-S-H avec un contrôle précis sur son agencement. Ceci est fait en assignant une lettre de notation pour chaque bloc de construction. Ainsi, une chaîne de ces lettres, écrite d'une manière cohérente vis-à-vis leur disposition dans une cellule unité, représente une cellule unité réduite défectueuse ou une "brique" avec une définition

précise des défauts. Un schéma de réaction chimique pour évaluer la stabilité relative de ces briques contenant des défauts, à partir de l'enthalpie de réaction calculée en utilisant des simulations de dynamique moléculaire (MD), a également été développé. Le modèle peut saisir efficacement les caractéristiques structurelles de C-S-H et permet de proposer une structure atomique probable à grande échelle de C-S-H, y compris des surfaces. Le modèle peut être étendu à d'autres structures à base de tobermorite ou de jennite. Plus particulièrement, nous avons montré qu'il est possible de transposer un exemple de modèle atomistique existant dans la littérature à la nomenclature du modèle de brique, permettant ainsi des comparaisons efficaces.

Dans un travail collaboratif en application du modèle de brique, des expériences de Dynamic Nuclear Polarization Nuclear Magnetic Resonance (DNP NMR) combinées avec des calculs de Densité Fonctionnelle (DFT) sur des structures générées à l'aide du modèle de brique ont été utilisées pour comprendre la structure atomique de Ca/Si du C-S-H synthétique. En plus de quantifier la spéciation du silicate ainsi que sa connectivité et de confirmer la structure sous-jacente de type tobermorite, on a découvert l'existence d'une nouvelle position de calcium qui lie les silicates terminaux de deux chaînes de silicate et induit une forte liaison hydrogène dans l'intercouche. Il a été conclu que le calcium sur le site de pontage est une caractéristique du C-S-H. Ces données ont été utilisées comme des contraintes pour générer une série de structures atomiques pour C-S-H avec différents rapports Ca / Si entièrement compatibles avec l'expérience. Ce sont des structures de type tobermorite 14 Å hautement défectueuses.

Pour mieux comprendre la structure complexe des couches intermédiaires de C-S-H et l'interaction entre les défauts dans le matériau en vrac, le modèle de brique a été utilisé pour générer une variété de défauts distincts et de calculer leurs enthalpies. Nos résultats indiquent que la présence de silanols dans C-S-H est énergétiquement défavorable et une teneur en eau plus faible aboutit à une région intercalaire plus ordonnée ou cristalline. Nous avons découvert une seconde nouvelle position enthalpiquement stable pour le calcium de l'intercouche et identifié deux types d'eau en fonction de leur «cristallinité» ou de la façon dont les molécules d'eau sont coordonnées aux ions calcium dans l'intercouche. Les résultats sur les interactions des défauts indiquent que les unités structurales de C-S-H avec différents volumes d'intercouches, en raison de la présence de différents types de défauts, interagissent et créent des déformations dans la structure en feuillet du C-S-H. Cependant, l'énergie d'interaction calculée n'est pas prohibitive de leur existence. Fort de ces résultats, des explications sur le manque d'ordre à long terme ou la nano-cristallinité de C-S-H ont été proposées, qui nous donnent des indications précieuses sur des paramètres clés de C-S-H tels que les mécanismes de croissance et le vieillissement. Ainsi, les résultats actuels devraient faciliter

l'ingénierie de la structure et de la mésostructure du C-S-H conduisant éventuellement à des ciments plus durables et futuristes.

Keywords : $C-S-H$, Le béton, MD, DFT

Table of Contents

List of Figures

List of Tables

Chapter I. Introduction

1.1 System

Cement is the most used material in the world and when mixed with water it transforms from a fluid suspension to a solid composite at room temperature. Concrete used in construction is a hardened mixture of cement, aggregates, sand and water. Cement in general refers to any binder, in a powder form, when mixed with water or a gas, it will eventually change into a hard solid substance that can glue to other materials. In the construction industry, cement is generally a mixture of Portland cement (PC), specific additives depending on the application and supplementary cementitious materials (SCMs). Among these, Portland cement is the major constituent and SCMs are currently added to reduce the carbon footprint of cements. The production of Portland cement contributes to about 10 % of the world CO_2 emission[1]. In order to meet the needs of growing population and urbanization in the developing countries, the use of concrete is expected to double in the next 30 years [1] and consequently there is an increased demand for a more sustainable cement. Although Portland cement is in use for over a century, little is known about several aspects of its hydration when mixed with water. The reason for this poor understanding of cement hydration mechanisms is primarily due to the difficulties in understanding the complex atomic structure of the main cement hydration product, calcium silicate hydrate (C-S-H).

Table 1: Phase composition of typical Portland cements [2]

Phase name	Mineral	Typical amount	Impurities (< 5 %)
Alite	Tricalcium silicate (C_3S)	**50-70 %**	Oxides of Al Mg Fe,Na,K, Mn, Ti , S, P..
Belite	Dicalicum silicate (C_2S)	10-20 %	
Aluminate	Tricalcium aluminate (C_3A)	5-10 %	
Ferrite	Tetracalcium aluminoferrite ($C_4(A,F)$)	5-15 %	

Portland Cement is composed of mainly calcium alumino silicates [2]. The four main phases present in Portland cement are alite (impure tricalcium silicate, C_3S), belite (impure dicalcium silicate, C_2S),

aluminates (impure tricalcium aluminate, C_3A) and ferrites (with approximate stoichiometry, $C_4(A,F)$)[1] (for more details on typical cement compositions see Table1). Mixing this complex material with water results in a set of reactions influenced by the presence of surface defects, impurities and the nucleation and growth of different hydrate phases [3–5]. To reduce the carbon footprint a part of the Portland cement is replaced by SCMs, such as the industrial waste products, fly ash, blast furnace slag, silica fume and natural pozzalans such as calcined clays [6]. The SCMs often modify the hydration or setting kinetics and thus can influence early age strength, generally lowering early age strength[4,7]. This is of great practical importance for both construction norms as well as possible effects on durability. How the use of SCMs affects hydration kinetics is poorly understood. Thus understanding the mechanisms of cement hydration is of great significance and will help us towards a sustainable built environment [4,6–8]. Often to reduce the complexity of the system, studies are carried out in a simpler system with one of the principal components of Portland cement. The main phase, impure tricalcium silicate or alite (C_3S), which constitutes about 50-70% of the Portland cement, reacts with water to form the calcium silicate hydrate, C-S-H [2] in cement nomenclature[1]. A general equation for this reaction can be written in cement nomenclature[1] as follows.

$$C_3S + H \rightarrow C - S - H + CH \qquad (1)$$

This reaction indicates that calcium hydroxide (CH) crystals, also called portlandite are also formed along with C-S-H. Portlandite, the second most abundant phase in hydrated cementitious systems is known to affect the nucleation and growth of new C-S-H particles [9]. Recently Galmarini [10–13] has carried out simulations using molecular dynamics to study its morphology and surface interactions with ions giving insights into their influence on portlandite and C-S-H growth.

C-S-H being the most abundant phase imparts mechanical strength to cement [2]. In addition to having a poorly nano crystalline structure, C-S-H is found to have a variable stoichiometry, Ca/Si atomic ratio changing over time, and water content [14–17]. It has very high surface area leading to significant amount of water-solid interfaces with the pore solution. All these features of C-S-H have in turn made it nearly impossible to characterize it fully. Naturally occurring crystalline calcium silicate minerals like tobermorite and jennite are often used as starting points to model the structure of C-S-H [18–23]. It is found to have different morphological growth, for example, foil-like growth and sheaf of wheat/needle-like, depending on the type of ions present [24] in the surrounding solution (called pore solution in cement terminology). Moreover, these C-S-H phases are nearly X-ray

[1] Cement nomenclature: C –CaO, S- SiO_2, A- Al_2O_3, F- Fe_2O_3, H -H_2O, $- SO_3

amorphous or nano-crystalline [18,21,23,25–27]. Hence it is difficult to comprehend the underlying mechanisms of its nucleation and growth leading to the observed morphologies. Understanding the exact atomistic structure of C-S-H is the biggest challenge towards unravelling all the related experimental observations. Atomistic modelling tools are immensely useful in such a case. This thesis is aimed at developing model atomistic structures of C-S-H with the help of molecular dynamics and other atomistic simulation techniques that can help elucidate C-S-H structural features in more detail than previously achieved.

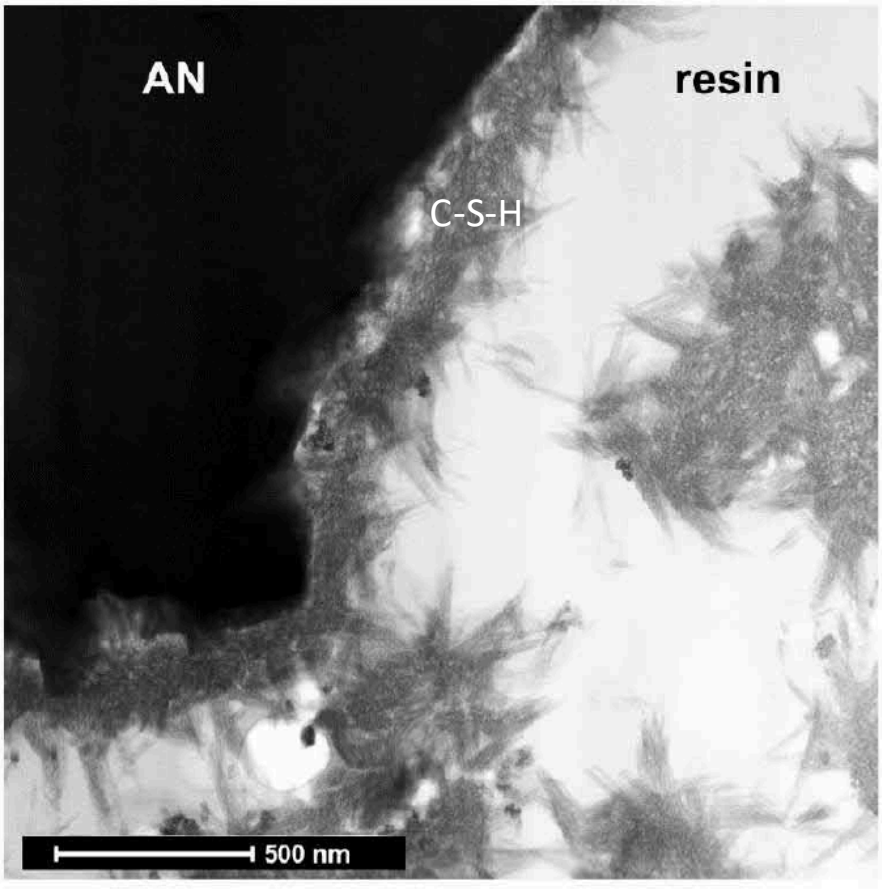

Figure 1: Scanning electron microscope image in secondary electron mode showing surfaces of C3S (AN) hydrating with the light grey oriented foil-like C-S-H growing on its surface.[24]

1.2 Atomistic modelling

Atomistic modelling has gained great importance in the last few decades with the advancement of the computing power and better algorithms implemented in the simulation codes. All matter is made up of some arrangement of atoms. A crystalline material has a well ordered periodic arrangement of atoms such that you can define a representative small box of side length in the

order of 10^{-10}m or a few Angstrom (Å) which is called a unit cell. A unit cell box shape is defined such that it contains specific sites where atomic or molecular species can occupy (lattice points), giving a stoichiometric unit of the material within this unit cell. For instance, the unit cell of common salt, NaCl will have sodium and chlorine in a 1:1 ratio. A three dimensional arrangement of this unit cell will make the solid crystalline structure within the macroscopic single crystal that we see with our naked eyes as particles. These atoms are bound in this solid form through different attractive and repulsive forces to keep them at a specific distance between each other, just like the gravitational forces between the earth and the moon maintaining an optimal distance between them. It will become a liquid phase when the atoms gain sufficient energy (melting) or become unstable (dissolution) to break this ordered arrangement and gain both vibrational and translational motions with less attractive forces between them. These forces between the atoms are mainly electrostatic and van der Waals' interactions. The interactions between any pair of atoms can thus be modelled using empirical sets of equations. In short, we can study the time evolution of the interactions of atoms of interest with the help of atomistic simulations at the nanoscale.

One of the greatest advantages of these simulations is that we can model the interactions at a solid-liquid interface which has potential applications, for example, in biological systems [28,29], cement industry [30–32] and marine environments [33]. The insights gained from these interface simulations can greatly help us understand the underlying atomistic events dictating certain macroscopic observables in materials. Such insights can thus facilitate in designing new processes or advanced materials with tailored properties. Some of the other applications of atomistic modelling is to understand the atomic-level mechanisms of defects in solids [34], complexations of ions or molecules in liquids [12], diffusion of ions or molecules [35], nucleation and growth of solids [36] and drug discovery [37]. The classical atomistic simulation techniques, based on classical mechanics, are energy minimization, molecular dynamics and Monte Carlo methods, these will be described in chapter 3 of the thesis..

However, the greatest drawback of these so called classical atomistic simulations is the inability to model the breaking and making of bonds. For instance, the dissolution of common salt in water cannot be accurately studied. But a calculation of interfacial energies between any crystallographic surfaces of NaCl with water will give an indication that it is highly unstable when the simulation is carried out at relevant temperatures. In order to model this, the atoms need to have a variable charge to go from a solid state with anions and cations surrounding it in a three dimensional crystal lattice to a liquid state where it has a solvation shell with hydronium ions, hydroxyl ions and water molecules. Since an atom is in turn made up of a positively charged nucleus and a cloud of electrons

around it, the variable charge can only be modelled if we explicitly solve the electronic structure of each atom. Thus, a switch from classical mechanics to quantum mechanics is necessary. The quantum state of an electron is obtained from solving Schrodinger's equation, an exact solution of which is not possible for a many body system. A reasonable approximation is done in the framework of density functional theory (DFT) where the ground state density distribution of an electron cloud is solved rather than explicitly treating each electron. Since DFT is also a computationally expensive technique, we are limited in the time scale we can simulate. It is generally used to answer a very specific question, to understand the underlying mechanism, predict or explain spectroscopic and microscopic data and to design and predict new materials of novel properties [38,39]. For instance, with the aid of crystal structure predictive algorithms based on DFT calculations stable sodium chloride compounds with unexpected stoichiometries, namely $Na_3Cl, Na_2Cl, Na_3Cl_2, NaCl_3$ and $NaCl_7$ have been discovered and the authors were able to synthesize some of the compounds [40]. Some of the major limitations of DFT are that it can only simulate a few hundred atoms for a few pico seconds and van der Waals forces are not correctly captured .

In this thesis both classical atomic simulations and DFT will be used. More details of the techniques can be read in Chapter 3.

1.3 Objectives of the thesis

- To understand the atomic structure of calcium silicate hydrates using atomistic simulations
    - To explore how defects in tobermorite can be used to develop a C-S-H model consistent with the available experimental structural knowledge
    - To evaluate the energetics and interactions of defects in a bulk C-S-H structure
    - To understand the intricate interlayer structure of C-S-H

1.4 Organization of the thesis

The thesis is divided into seven chapters. Certain chapters are based on material already published (Chapters 4 and 5), and chapter 6 is written in paper format and is expected to be submitted in the near future.

Chapter 1- Introduction to the thesis and a general overview of cement

Chapter 2- State of the Art: Introduction to C-S-H and a review on the current understanding of C-S-H from both experimental and modelling perspectives

Chapter 3- Methods: A brief description of the theoretical methods used in this work and the improvement of the force field for cementitious materials

Chapter 4- Brick Model: A methodology to precisely define the defective tobermorite that represents the structural features of C-S-H

Chapter 5- Synthetic C-S-H: A collaborative published work applying the brick model to understand the calcium silicate main layer structure of C-S-H

Chapter 6- Interlayer : Brick model has been used to understand from both energetic and structural point of view, the nature of interlayer of C-S-H.

Chapter 7- Summary and Outlook: Summarizes the work and discusses the future work that should lead to further clarification and better understanding of cement hydration in the presence of SCMs, additives towards more sustainable and durable concrete technology.

Bibliography- The references from all the chapters except Chapter 4, where the references are given in section 4.9

Appendix- Contains any supplementary information associated with the publications from this thesis.

Co-authored Publications- Contains any co-authored publications not directly a part of this thesis.

Chapter II. State of the Art

In this chapter, the current understanding of the calcium silicate hydrate is reviewed, from both experimental and modelling perspective.

2.1 Introduction

The main product of the hydration reaction of Portland cement is the poorly crystalline calcium silicate hydrate (C-S-H). In cement chemistry it has been given the abbreviation C-S-H and not CSH due to its variable stoichiometry. Early X-ray diffraction (XRD) results have provided evidence suggesting that C-S-H is made of a layered structure similar to that seen in natural minerals tobermorite and jennite [18,19]. Most of the characterization analysis of C-S-H has then been carried out based on these mineral structures. Hence, it is worthwhile reviewing the structural features of these rare crystalline calcium silicate minerals.

The most noticeable feature of these water containing calcium-silicate minerals is a layered structure with a three-unit repetition silicate tetrahedral chain structure known as the "dreierketten" structure. Both jennite and tobermorite contain infinite linear "dreierketten" silicate chains. In jennite, which has a Ca/Si ratio of 1.5 and a molar water content of 42 %, the calcium silicate layers are separated by an interlayer space containing water and calcium [41]. The main calcium layer in the jennite structure is corrugated, as seen in Figure 2(a). The chemical formula of jennite is $Ca_9Si_6O_{18}(OH)_6 \cdot 8H_2O$ and 33% of the charge of calcium ions is compensated by the OH group. In the case of tobermorite there are three different variants often used to characterize C-S-H. The most widely used one is 14 Å tobermorite with a Ca/Si ratio of 0.83, interlayer distance of 14 Å and molar water content of 42 % [42]. The other variants are normal and anomalous 11 Å tobermorite with Ca/Si ratio of 0.75 and 0.67, an interlayer distance of 11 Å and a molar water content of 34 and 38 % respectively [43]. These tobermorite structures are also characterized by an interlayer space containing water and calcium. Unlike jennite, the main calcium layer in tobermorite is in the form of a planar sheet flanked on both sides by the infinitely long linear silicate chains (Figure 2, (b), (c) and (d)). The crystal chemical formula of 14 Å tobermorite is $Ca_5Si_6O_{16}(OH)_2 \cdot 7H_2O$, $Ca_{4.5}Si_6O_{16}(OH) \cdot 5H_2O$, for normal and $Ca_4Si_6O_{15}(OH)_2 \cdot 5H_2O$ for anomalous 11 Å tobermorite . Tobermorite structures, as opposed to jennite structures, only have Si-OH bonds in the bridging silicate tetrahedra and no $Ca - OH$ bonds. Normal 11 Å tobermorite structure originally proposed by Hamid [44] is often used in characterizing C-S-H [17]. However, experimental observations [43,45] have indicated the presence of cross-linking of the silicate chains between the

layers. The original Hamid structure did not have any cross-linking and thus it has a calcium-silicate layer structure closer to the one found in 14 Å tobermorite. Irrespective of this discrepancy, Hamid 11 Å tobermorite is sometimes used as a model structure for C-S-H which is described in detail later in section 2.3.

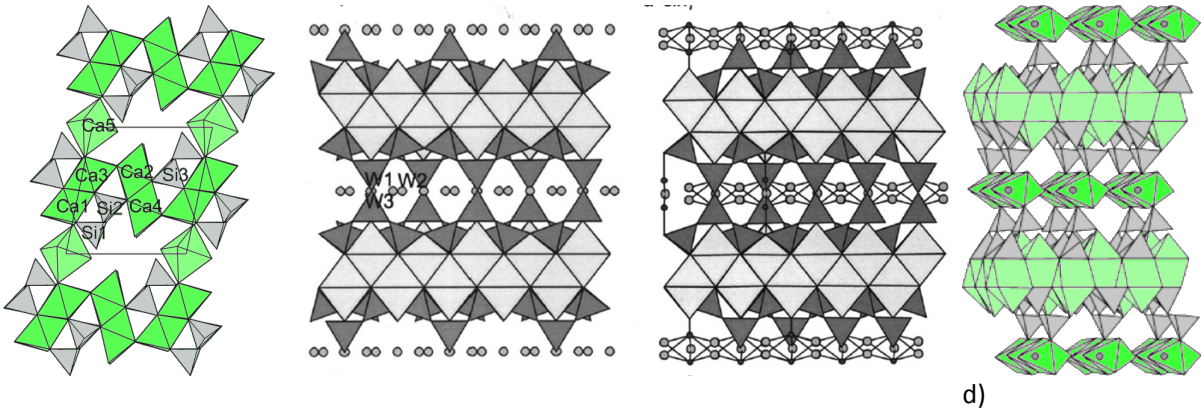

a) b) c) d)

Figure 2: Crystal structure of (a) jennite [41] *as seen along [010], green: Ca polyhedron, grey: Si tetrahedron ; (b) 11 Å anomalous tobermorite* [43] *as seen down [210], grey: Ca polyhedron, dark grey: Si tetrahedron; (c) 11 Å normal tobermorite* [43] *as seen down [210],], grey: Ca polyhedron, dark grey: Si tetrahedron; (d) 14 Å tobermorite* [42] *as seen down [010], green: Ca polyhedron, grey: Si tetrahedron.*

2.2 Experimental work on C-S-H

The structural features of the C-S-H that are experimentally observed using different characterization techniques are discussed in some detail here.

2.2.1 Nearly X-ray amorphous

From Powder X-ray diffraction (XRD) of C-S-H [25], only two weak broad peaks are usually observed for C-S-H with repeat distances of about 1.82 Å and 3.05 Å. These XRD results were later successfully repeated with the help of Selected area electron diffraction studies on C-S-H [21]. Repeat distances of 3 and 1.8 Å corresponding to $Ca - O$ units are also seen in the structures of calcium hydroxide (CH), jennite and tobermorite. Consequently, this has necessitated the use of other advanced techniques for characterization of C-S-H keeping in mind C-S-H that has a variable chemical composition. At a young age (age of hydration less than a year), the composition of C-S-H is claimed to be bimodal in Portland cement and the bimodality decreases with age [2]. This means that C-S-H forming at the early ages with Ca/Si atomic ratios varying between 1.2 and 2.2 will eventually move towards an equilibrium composition of Ca/Si ratio roughly around 1.75 [22,46]. The variation in Ca/Si

ratio is directly linked to the silicate chain length in the calcium silicate compositional units that constitute the C-S-H. Hence, determining the structure of Si groups became critical to unravel the atomistic structure of C-S-H. C-S-H has been observed to have nanosized regions with AFM [23] and TEM [27] for both synthetic C-S-H and that from Portland cement hydration, and has been recently augmented by total x-ray scattering measurements [26,47,48]. Skinner et al. observed crystalline ordering to a distance of 35.5 Å in synthetic C-S-H of Ca/Si ratio 1.0 [26].

2.2.2 Silicate chains exist mainly as dimers, pentamers and octamers

One of the first attempts to characterize Si groups was done via trimethylsilylation (a method of leaching out silicate ions and converting them into stable trimethylsilyl esters which reflects their original chain structure, suitable for quantifying short chain structures) followed by chromatography [49]. In the first few days of hydration the authors observed the formation of dimers from the C_3S in which the silicate ions were monomeric. After a few days and up to about six months, increased formation of dimers and some polymerization of these are observed until the hydration of C_3S is completed. The amount of dimers then diminished to 40 % and the content of polymer increased to a value of 60% of the total silicate species. The authors found reasonable agreement of these values to those observed for the 22-30 year old pastes. ^{29}Si Neutron Magnetic Resonance (NMR) spectroscopy has been widely used to investigate the silicate structural arrangements in C-S-H [14,16,22,50–55]. From Si NMR one can clearly identify the different species of Silicon/silicate tetrahedra in terms of its bonding to one another. Thus we have Si monomers and Si connected to n other Si species denoted by Q^0 and Q^n respectively, as shown in Figure 3. From the amounts of Q^1 and Q^2 species present we can assess the mean silicate chain length and a qualitative idea about the existence of silicate chains as dimers, pentamers or **n-mers**. The mean chain length of silicates is found to increase from 2 (dimers) to a value less than 5 in synthetic C-S-H, consistent with the previous study by Mohan and Taylor [49]. All these NMR studies also conclude that mean silicate chain length decreases with increasing Ca/Si ratio, i.e., appearance of more Q^1 and less Q^2. Another key feature to note is the absence of monomers, Q^0 [16] or in some cases less than ~2% [14] of the total silicate species. At later stages of hydration, silicate chains exist mainly as dimers, pentamers and octamers [56] and no cross-linking or Q^3 species are observed [51]. The silicate chain length is also observed to fit the characteristic formula of "dreierketten" structure, $3 \cdot n - 1$ where n is an integer. Thus with the help of models fitted to the NMR spectra, it was concluded that C-S-H has dimers connected by a bridging Si tetrahedra in a three-unit repetition fashion as seen in jennite and tobermorite. These results indeed indicate that with the age of hydration, it achieves an equilibrium

silicate framework that could be described by a model or a set of model structures for C-S-H based on a 'dreierketten" framework.

Most of these studies were conducted either on synthetic C-S-H [16,51,52,54] or C-S-H gel in cement paste [49,56]. For instance, advanced NMR techniques (^{29}Si MAS NMR, ^{29}Si homonuclear and $^{1}H - {}^{29}Si$ heteronuclear NMR) were used on C-S-H prepared by mixing SiO_2 and CaO in a water suspension at different Ca/Si ratios [51]. The authors observed the increase in Q^1 signals with increasing Ca/Si ratio. These results on synthetic C-S-H were in coherence with the results for C-S-H from cement paste [49,56]. Cross-linking of the silicate chains through observed Q^3-Q^3 correlations disappeared with increasing Ca/Si ratios. In conclusion, the silicates in C-S-H exist as dimers, pentamers and octamers [21,56] with no monomers (Q^0) and cross-linking (Q^3).

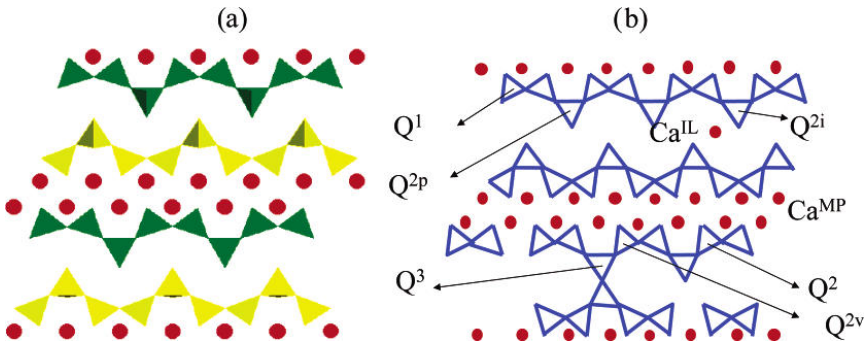

Figure 3: (a) The layered structure of tobermorite is composed of a calcium plane (red dots) bordered by two silicate planes (yellow and green chains) and separated by the interlayer space containing water molecules, hydroxyl groups and some calcium ions. (b) The silicate planes are composed of silicate chains with a specific three-unit repetition ("dreierketten"): two silicate tetrahedra, noted as Q^2, are coordinated by calcium planes (red dots), whereas the third silicate (called the bridging tetrahedron and noted as Q^{2p} or Q^{2i}) is not. The end-chain tetrahedra are noted Q^1. The tetrahedra linking two silicate chains in the interlayer space are noted Q^3 whereas the sites Q^2 next to Q^3 are named Q^{2v}. The calcium ions belonging to the main plane are noted Ca^{MP} whereas those in the interlayer are noted Ca^{IL}. Taken from [51]*. This image is from one of the first thorough NMR characterization of C-S-H and the notations used are from French words. A better notation widely used in the literature is Q^{2p} for the pairing tetrahedra (Q^2 and Q^{2v} in the image) and Q^{2b} for the bridging tetrahedra (Q^{2p} and Q^{2i} in the image).*

2.2.3 Characterization of Calcium ions in C-S-H

Not many studies can be found in the literature on distinguishing the different calcium environments in C-S-H. One of the few shedding light on the calcium environment in synthetic C-S-H was done using Extended X-ray Absorption Fine Structure (EXAFS) [57]. The authors have shown that different

crystallographic sites and the distribution of first and higher coordinate shells make the calcium environment in synthetic C-S-H (Ca/Si ratio from 0.7 to 1.4) complex, found to be more similar to that in 14 Å tobermorite than jennite.

2.2.4 Hydrogen species

In C-S-H, hydrogen exists as part of water and hydroxyl groups as has been first characterized using ^{1}H NMR [58], $^{17}O - {}^{29}Si$ MAS and Cross Polarization Magic Angle Spinning (CPMAS) NMR [59]. The two hydroxyl groups present are $Si - OH$ and $Ca - OH$. Rassem et. al studied the early age (up to 6 hours) hydration of tricalcium silicate using proton NMR [58]. The authors observed decreasing signal for $Si - OH$ bonds with the hydration time, and vice versa for $Ca - OH$ bonds. Cong et al. used ^{17}O and ^{29}Si MAS NMR to study C-S-H from hydration of C_2S and that synthesized directly [59]. The authors studied samples up to 100 days of hydration indicating the presence of $Ca - OH$ and possibly some $Si - OH$. These results were later confirmed by several other authors [16,45,51,53,54,60,61]. The presence of $Si - OH$ in C-S-H of Ca/Si ratios of around 1.75 is still controversial. At low Ca/Si ratio, Brunet et al. observed $Si - OH$ bonds using 2D $^{1}H - {}^{29}Si$ HETCOR (heteronuclear two dimensional) NMR with the signals decreasing with increasing Ca/Si ratio in synthetic C-S-H (0.7-1.5) [51]. These NMR results have also been confirmed by infrared spectroscopy measurements [60], in which synthetic calcium silicates with Ca/Si ratios 1.5 were not available.

Another issue is the location of the $Ca - OH$ groups. It could be in the main Ca layer, interlayer or at the surface owing to the high surface area of C-S-H. At Ca/Si ratio of 0.9, Bruno et al. observed that the protons from $Ca - OH$ groups interact with the bridging tetrahedra only [51]. The authors argued that if C-S-H has a tobermorite-like structure, this would mean that $Ca - OH$ groups are present in the interlayer and not in the Ca layer. But, at Ca/Si ratio of 1.5, all silicate species seem to interact with the $Ca - OH$ groups, indicating that either the interlayer distance has shrunk, or these groups are located in the main Ca layer. From the decalcification of white Portland cement and C3S Chen et al. observed using small-angle neutron scattering (SANS) that the surface area of C-S-H decreases with increasing Ca/Si ratio [55]. This lead the authors to the argument that if all the $Ca - OH$ were on the surface then the surface area should increase to accommodate the increasing $Ca - OH$ groups with the Ca/Si ratio. Hence they concluded that not all the $Ca - OH$ groups can be on the surface and the possibility of it being in the interlayer and main Ca layer is still not clear. Thomas et al., used inelastic neutron scattering (INS) to quantify the amount of $Ca - OH$ bonds in a C-S-H gel of an 8-month hydrated C3S paste [61]. They showed that at a Ca/Si ratio of 1.7, approximately 23 % of the charge of the Ca^{2+}ions in C-S-H are compensated by the hydroxyl groups assuming all the $Ca - OH$ bonds occur in the main $Ca - O$ layer. Decalcification of the C_3S paste

resulted in a decrease in $Ca-OH$ content with negligible values at Ca/Si ratios below 1, as observed from the NMR results mentioned before.

The water content of C-S-H is another very complex issue with the high specific C-S-H/pore solution interfacial area, making it difficult to clearly distinguish the types of water present. Assuming a crystalline silicate mineral like structure, the water can exist in the interlayer space chemically bound [2]. Water adsorbed in pores larger than the interlayer spacing is generally found to be physically bound. Early works of Cong et. al identified the presence of water in the structure [59]. Later, the authors [16] quantified the total amount of water to be 42-53 mol% and it slightly increases with increasing Ca/Si ratio. In a more recent work by Muller et al. using ^{1}H NMR relaxometry, the molar water content was estimated to be 40 % excluding the surface water [62].

2.2.5 Interlayer distance

Cong et al. observed a decrease in interlayer spacing with an increase in Ca/Si ratio [16]. This has also been confirmed using X-ray Rietveld analysis [17] and total x-ray scattering measurements [47]. Renaudin et al. used the Hamid 11 Å tobermorite structure [44] to refine the structure of C-S-H with Ca/Si ratio from 0.8 to ~1.59 with X-ray Rietveld analysis [17]. The authors observed the decrease in interlayer spacing from 14 Å for a Ca/Si ratio of 0.82 to 11 Å for a Ca/Si ratio of 1.1. The authors were able to refine the whole series of structures with the Hamid 11 Å tobermorite but not with jennite [41] or 11 Å normal or anomalous tobermorite [43] or 14 Å tobermorite [42].

2.2.6 Bond distances

The mean $Si-O$ bond lengths around 1.638 Å for the silicate tetrahedra in C_3S and C_2S have been measured using ^{29}Si MAS NMR [63]. In synthetic C-S-H, Meral et al. has measured the $Si-O$, $Ca-O$ mean distances, ~1.64 and ~2.41 Å respectively, using total x-ray scattering measurements [48]. Yu et al observed with IR spectroscopy that the general chain structure of the silicates does not change with Ca/Si ratio in synthetic C-S-H [60]. The radial pair distribution obtained using total x-ray scattering [26,47,48] showed no changes in the nearest neighbor distances with increasing Ca/Si ratios, consistent with the IR spectroscopy results [60]. Yu et al. also observed at higher Ca/Si ratio a broadening of the $Si-O-Si$ bending peak, which is coherent with a decreasing polymerization of the silicate chains. Raman spectroscopic studies on synthetic C-S-H samples by Garbev et al. [64] confirmed a decrease in polymerization by having a narrowing of the $Si-O-Si$ bond angle with increasing Ca/Si ratio. The mean $Si-O-Si$ bond angle in C-S-H was estimated to be around 139.7-140.7˚, which is close to that found in 14 Å tobermorite.

One of the main difficulties in resolving C-S-H atomic structure is the non-availability of efficient experimental techniques to resolve the calcium environment. In the case of $Ca-O$ bond lengths, not much evidence is found in the literature for C-S-H other than the results from the total x-ray scattering as mentioned previously [48]. Recently, ^{43}Ca MAS NMR has been used to distinguish the six-coordinated Ca in jennite and seven-coordinated Ca in 11 Å tobermorite. Although this method looks promising to be useful in resolving the different Ca^{2+} environments in C-S-H, only one such study is carried out on synthetic C-S-H. Moudrakovski et al. studied unhydrated C_3S, C_2S samples, 11 Å tobermorite and synthetic C-S-H samples [65]. But the authors did not produce any significant results other than confirming the existence of two types of Ca environment in C-S-H. Total X-ray scattering measurements indicate that the $Ca-O$ coordination decreases slightly from ~7 to ~6 with the increase in Ca/Si ratio [47,48].

In short we can say that C-S-H has been the subject of extensive research for the past 60 years. It is found to have a nanocrystalline nature. The silicate structure in C-S-H is more or less well studied and is found to have a mean chain length between 2 and 5, with mainly dimers, pentamers, and octamers. Negligible amount of silicate monomers and cross-linking of the silicate layers are found. The average value of Ca/Si atomic ratio for sufficiently aged C-S-H (in plain Portland cement pastes or C_3S) is 1.7. Two types of Ca environment are seen, but still require more work towards understanding it in detail. The presence of Ca-OH bonds is found to increase with Ca/Si ratio with an average of 23 % of Ca charge compensated by OH groups at a Ca/Si ratio of 1.7 and the location of this bond can be on the surface, interlayer or the main Ca layer. The presence of $Si-OH$ bond is found to decrease with Ca/Si ratio and is negligible at high Ca/Si ratio. The mean $Si-O-Si$ bond angle, $Si-O$ and $Ca-O$ distances in C-S-H were estimated to be around 139.7-140.7˚, 1.64 Å and 2.41 Å respectively. The interlayer distance is found to decrease with increasing Ca/Si ratio. The water content is found to vary with mean molar water content of 40 %. C-S-H is found to have an approximate stoichiometry of $Ca_{1.7}SiO_{3.7} \cdot 1.8H_2O$ with a density of 2.65 $\frac{g}{cm^3}$ [62].

2.2.7 Proposed model structures

A large number of different structural models for C-S-H have been proposed in the literature from the available experimental results [16,20,21,23,66]. Richardson [27] has reviewed some of these different models drawing similarities and differences between them, the prominent ones being a tobermorite based model [23] with additional Ca^{2+}in the interlayer space, tobermorite based models with the additional $Ca-OH$ bonds in the main layer [21] and mixed tobermorite/jennite models [18]. Although the Ca/Si ratio (1.5) and the charge compensation of Ca by OH groups (33 %)

in jennite are similar to that observed in C-S-H (Ca/Si = ~1.75, Ca charge compensation by OH groups ~23 %), Cong et al. concluded that the high polymerization and local ordering make it impossible for jennite to be a good structural model for C-S-H [16]. According to the authors, a defective 14 Å tobermorite can better represent the high amount of defects and lower degree of silicon polymerization seen in C-S-H. The calcium environments in C-S-H are also found to be more similar to 14 Å tobermorite structure [57]. Tobermorite presents a significant order disorder character, with different polymorphs and stacking sequences [42] and has an effective calcium to silicon (Ca/Si) ratio of 0.83. This is quite low compared to Ca/Si ratio of C-S-H which varies between 1.2 and 2.1, with an average value of 1.75 [15,22]. In order to achieve higher Ca/Si ratio, the possible ways proposed are by the removal of bridging silicate tetrahedra ($SiOOH$), the deprotonation of silanol groups which can be charge compensated by additional calcium ions, $0.5\ Ca^{2+}$ or a $CaOH$ unit in the interlayer [21,23,67] (for an example see Figure 4). Thus C-S-H can essentially be seen as a defective tobermorite structure with varying composition. By removing some silicate tetrahedra, the infinite silicon chain is broken leading to the increased appearance of Q^1 in NMR spectra [14,16,51,52,54]. Then the question of how these defects can be distributed and consequently if C-S-H is really homogenous at the nm scale is yet to be addressed. Recently, Richardson [20] has reviewed all the possible bond distances and coordination numbers possible for $Ca - O$ in naturally occurring crystalline calcium silicate minerals and proposed possible model structures for C-S-H. Often the bond lengths in crystalline calcium silicate minerals from their natural coordination are used to select model structures [20,21,27]. Permutations and combinations of the three defect-creating methods mentioned above can indeed give us a large number of variations of defects possible and it is quite challenging to quantify experimentally the kind of defects present in C-S-H. This has attracted the application of theoretical approaches to study the variations of possible defects in model C-S-H structure, including the use of atomistic simulations, which will be discussed in the next section

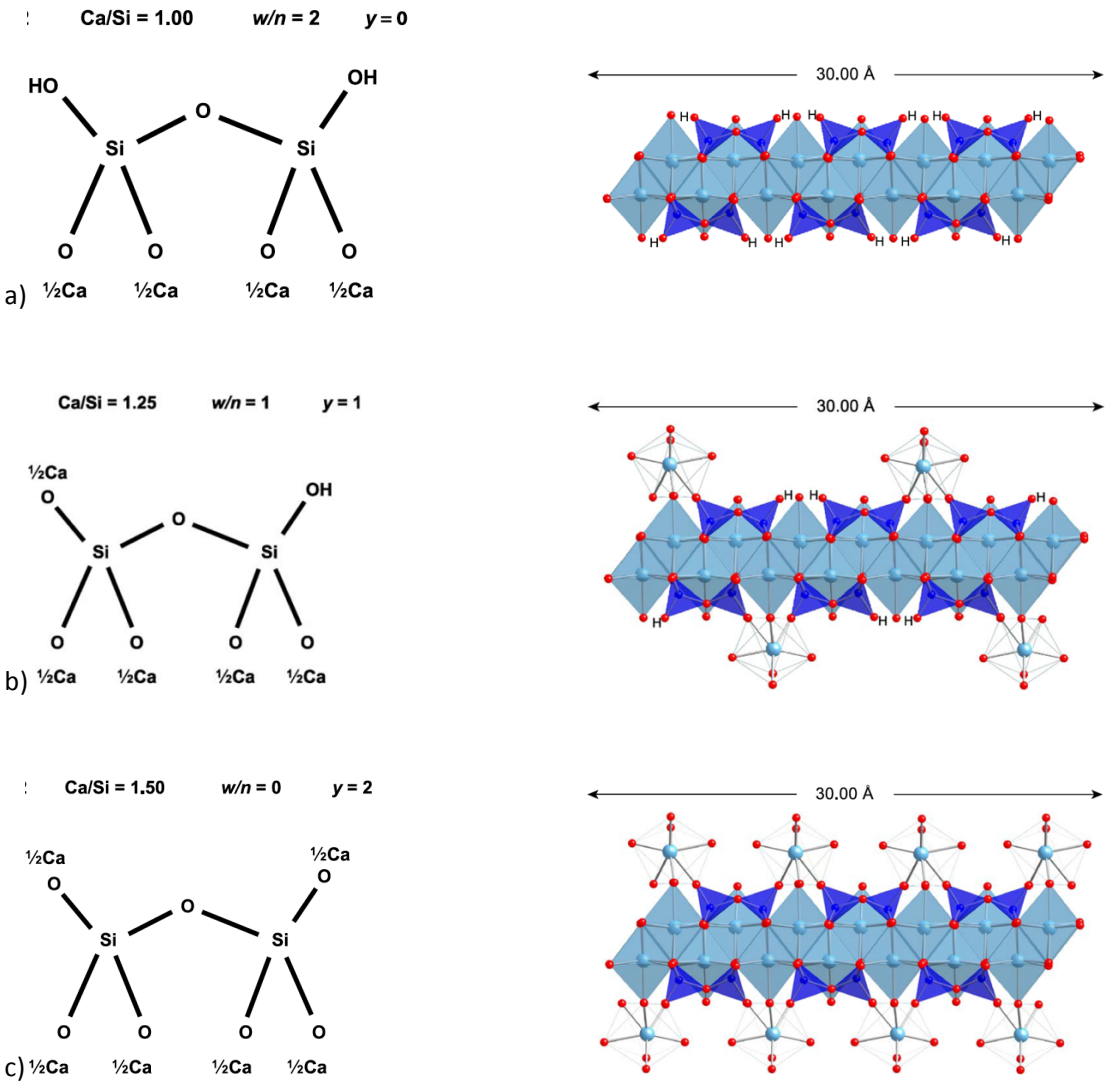

Figure 4: Schematic illustration of tobermorite-based dimers (n=1) that has the minimum, intermediate and maximum degree of de-protonation of the silicate chains. On the right hand side of each schematic, realistic structural representations are shown with silicate chains aligned along the plane of the paper. Taken from [21]*. The color codes used are calcium in light blue, silicon tetrahedra in dark blue and oxygen in red.*

2.3 Atomistic scale modeling on C-S-H

Several attempts at understanding the C-S-H atomistic structure can be found in the literature [30,68,77–81,69–76]. None of these studies have been totally successful in building a really representative C-S-H model structure when confronted with experimental data. The structure and properties of water as well as the chloride binding were studied using classical molecular dynamics simulations with interactions defined using the CLAYFF force field [72–74]. For their MD calculations, the authors used 9 Å tobermorite structure, which is not regarded as a particularly good model for C-S-H. Manzano et al. used *ab-initio* MD to identify the basic building blocks of C-S-H gel and the

growth mechanisms [75]. The authors proposed that a structure composed of two silicate dimers and a single calcium oxide layer consisting of four Ca atoms, could be identified as the basic brick of early C-S-H gels. Under different Ca/Si ratios, these structures form tobermorite-like clusters dominated by bond formation growth mechanism and jennite-like units dominated by dipole-dipole interactions. Rejmak et al. has simulated ^{29}Si NMR of mode C-S-H structures derived from 14 Å tobermorite and jennite using DFT [80]. The authors found good agreement between the calculated NMR results of defective 14 Å tobermorite and that observed experimentally for C-S-H.

Dolado et al. carried out classical MD simulation in NVT ensemble to study the polymerization of silicic acids in the presence of calcium ions that could lead to the formation of calcium silicate hydrates [77]. The authors studied four systems with different Ca/Si ratios by randomly mixing appropriate amounts of $Si(OH)_4$ and $Ca(OH)_4\ 4H_2O$ molecules in a cubic simulation cell at 300 K initially and then increasing the temperature up to 1800 K for accelerating the polymerization reaction. Then the cells were brought down to 300 K by linear decrease in temperature and then the degree of polymerization in terms of Q^n values and bond distances were averaged for 50 ps. The bond distances of $Si - O$ were found to be 2.3 Å, which is quite high compared to the mean value of ~1.64 Å in C-S-H. Another important limitation of this method was the resultant particles had high content of monomers (Q^0 30-70%). The authors have then carried out further MD calculations and simulated SANS and X-ray spectra [78] without correcting the limitations in their previous work.

Work involving classical MD, which is used in this thesis, have been made by Pellenq et al. [79,82] and Kovačević et al. [67]. Both of these authors started with Hamid 11 Å tobermorite as the base structure and then randomly removed SiO_2 groups and, in the case of Kovačević et al., added some Ca ions in different steps. Pellenq et al. started with dry tobermorite with 4× 2×1 crystallographic unit supercell and removed SiO_2 groups guided by NMR results. Water adsorption was done in a Grand Canonical Monte Carlo simulation at 300 K, but in addition to the interlayer the water also went in between the silicate chains, which was not expected. Other main drawbacks of this model are the absence of OH ions and an extremely high percentage of monomers, Q^0. The authors have tried to take account of these shortcomings in more recent work using the ReaxFF potential to split water molecules, making it possible to have hydroxyl groups and thus forming $Ca - OH$. The hydrogen of the split water molecules mainly reacted with non-bonding oxygen of the silicate chains, forming protonated silanol groups. However, experimental results indicate that the amount of protonated silanol groups in C-S-H at the Ca/Si ratios investigated (around 1.7) is negligible [60]. In order to remove the monomers, they allow for (random) polymerization of the silicates, yet this leads to a silicate chain structure that is in violation of the dreierketten pattern that exist in C-S-H,

where we only have dimers, pentamers, octamers and so on. Comparison of the total pair correlation functions from their simulations to that from high energy X-ray diffraction [47] revealed that the $Ca-O$ correlation peak is broader and the mean value does not coincide. Also the correlations of calcium with other species are shifted possibly due to the inaccurate description of calcium atoms in the ReaxFF force field [83]. The mean chain lengths of the silicate were also found to go below 2 with Ca/Si ratio greater than 1.5 (Figure 2.c in [82]), indicating the presence of monomers even though the authors claim to have removed them completely from the structure. Irrespective of all these shortcomings in the description of the structural features of C-S-H, the authors and several others have used this methodology to study mechanical properties, water transport, aluminate incorporation, and adsorption [84–90].

Kovačević et al. have compared three different ways of increasing the Ca/Si ratio of tobermorite in order to approach the C-S-H structure [67] and compared them to the early model by Pellenq et al. [79]. The approach first consisted of removing only bridging tetrahedrons and adding additional $Ca(OH)_2$ units to the structure. The second consisted of removing both dimers and bridging tetrahedra from the silicate chains. The third approach was to randomly remove silicate tetrahedra, similar to the approach taken by Pellenq et al. The authors then relaxed the structures using the ReaxFF force field, similar to the approach in the recent work of Abdolhosseini Qomi et al. [82] All the models have the final Ca/Si ratio of 1.65 and their total energies and the local order of the structures are calculated to conclude what structure is most probable in C-S-H. The authors concluded that the way of constructing the initial structure has a significant influence and the addition of $Ca(OH)_2$ in the interlayer needs to be included when constructing a C-S-H model. One of the main limitations with this work is that the unit cell predicted by the ReaxFF force field MD is 30% bigger than the expected unit cell parameter form experimental work. Errors of around 5% maybe tolerated for atomistic simulations but 30% is far too high. Interesting as the reactive force fields are, they still need to be better parameterized. As mentioned earlier in the recent works of Pellenq et al. [79,82,91,92] Ca (in CaO and $Ca(OH)_2$) has a partial charge of 1.1 or 1.2 where something between 1.5 and 2 is more realistic. Such changes in partial charges can strongly influence bond lengths, strengths and interfacial energies, as seen from their study itself.

Very recent work of Galmarini [93] has used classical molecular dynamics with force field potentials, also adopted in this work, to study the different local structures and defects, including a larger range of possible structures, to determine which would need to be included in a model to construct a realistic C-S-H structure [93] . Combination of these defects in a single bulk structure to get a required Ca/Si ratio was not studied. By systematically studying the possible combinations of defects

in bulk 14 Å tobermorite, it should be possible to build a defective tobermorite structure that could properly represent the available experimental results of C-S-H. This approach is presented and discussed in chapter 4 of this thesis.

In conclusion, many attempts towards getting a representative C-S-H model structure exist in the literature. But none of these have been able to really capture all the structural variations observed in the experimental studies of C-S-H. Some models for instance [79,82] have species in the end structures that are inconsistent with respect to silicate polymerization, Ca bonding, $Si-OH$ bonding and location of water in C-S-H. Kovačević et al showed that the way in which the defects are generated in the initial structure could affect the stability of the structure. Thus, a systematic study on the structural variations possible in a model C-S-H structure with different defects needs to be done for a more accurate description of this complex material from both structural and energetic points of view. In addition to this, the nano crystalline feature of C-S-H leading to high surface interactions need to be accounted for in a realistic C-S-H model. Hence, a thorough study of different crystallographic surfaces and its interaction with ions in solution is quite important in our quest towards a realistic C-S-H model.

Chapter III. Methods

This chapter describes the technical details of the methods employed. There are two sections in this chapter. The first one includes a brief description of the simulation methods employed in the thesis. The second section introduces the force field used and the improvements made in the framework of this thesis.

3.1 Simulation

A simulation done in this thesis consists of the simulation box with atoms and molecules, explicit description of the atomic forces (in some cases) and the simulation techniques applied to it. A brief description of each is given in the following sections.

3.1.1 Simulation box

A simulation box is defined by its edge lengths and angles similar to the Bravais lattices. In most of the simulations, an orthogonal box is chosen for the ease of calculation. However, the current algorithms can nowadays also compute non-orthogonal boxes efficiently. A simulation box can be a single unit cell of a material, a supercell of it (multiple spatially arranged unit cells with their origins translated by non-zero integer multiples of the unit cell vectors) or a box which can contain a slab of a material with vacuum or water or ions or molecules around it and so on (see Figure 5). In this work, a simulation box consists of a single unit cell in energy minimization (EM) or Density Functional Theory (DFT) calculations, and of a supercell in molecular dynamics (MD) simulations.

In order to simulate a bulk-like behaviour, periodic boundary conditions (PBC) are applied to these simulation boxes. The atoms interact with the periodic images of the simulation box in all the three cell or simulation box vector directions. Thus the (periodic) system considered is infinitely large, close to the situation in e.g. in a bulk solid. For example, if we consider a simulation box of a single unit cell of cell vectors $\vec{a}$, $\vec{b}$ and $\vec{c}$ with a single atom A at position $\vec{p}$. Then, the atom A will see the six nearest images of itself at $\vec{p} \pm \vec{a}, \vec{p} \pm \vec{b}$ and $\vec{p} \pm \vec{c}$. However, this means that it is computationally expensive to calculate all the interactions. For this reason, a cut-off radius for the atomic interactions is defined and the long range Coulombic forces are computed with a sum in reciprocal space. More details on these will be discussed in the next section, once the forces between atoms are introduced.

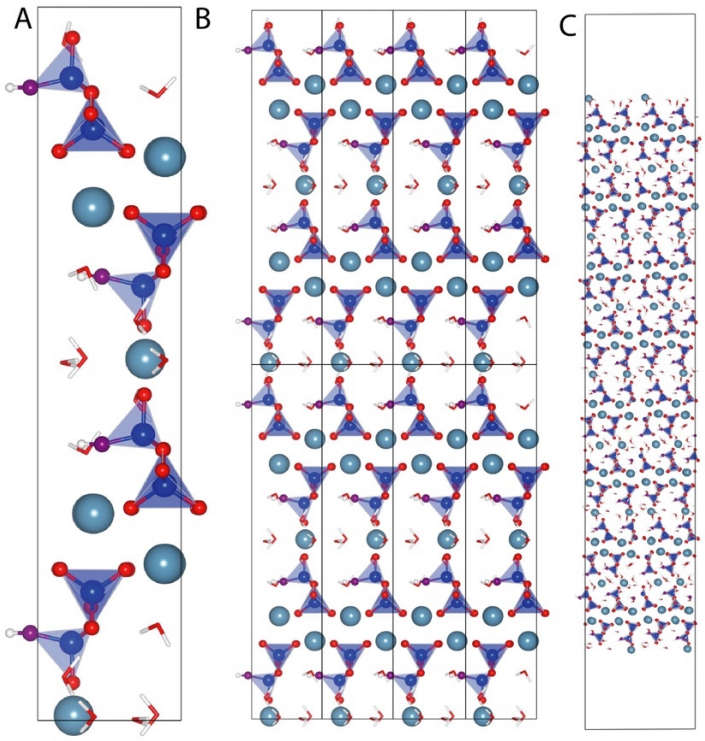

Figure 5: Types of simulation boxes (A) unit cell of 14 Å tobermorite viewed along [010] direction, (B) supercell of 14 Å tobermorite grown 4 times in [100] direction and (C) (001) surface of 14 Å tobermorite viewed along [010] direction where the surfaces are separated by a vacuum region. Atomic color code used are calcium - turquoise, silicon - dark blue, oxygen – red, hydroxyl oxygen – purple, hydrogen - white.

3.1.2 Atomic Forces

Atoms are the basic building blocks of matter. They are composed of a positively charged nucleus and negatively charged electrons orbiting around the nucleus. In the classical description of atoms, when forming ionic bonds with other species, they either gain or lose electrons resulting in an effective charge. Thus, in solid, liquid and gaseous phases, atoms are often charged with the atomic charge defined from the valence electronic configuration. For example, hydrogen is an electron donor and has a formal charge of +1. Oxygen is an electron acceptor and except with fluoride, it has a formal charge of -2. In classical atomistic simulations, this concept of atoms having an effective atomic charge is utilized to describe the forces between them. They are considered as point charges with a mass. The electrostatic interactions are described with the Coulomb's law. However, there are other forces acting between the atoms or molecules, called the van der Waals' forces. An effective potential energy of an atom i interacting with a system of N atoms in a simulation box can thus be described as

$$U_i = \sum_{j \neq i}^{N} U_{i,j}^{coul} + U_{i,j}^{vdW} \quad (2)$$

Where $U_{i,j}^{coul} = \frac{q_i q_j}{4\pi\epsilon_0 \cdot r_{i,j}}$, ϵ_0 is the permittivity of free space, $r_{i,j}$ is the distance between atoms i and j, and $U_{i,j}^{vdW}$ can take many functional forms and is generally described by empirically fitted parameters. Lennard-Jones type functions (equation (2) are commonly used to describe the van der Waals' forces , with the interactions vanishing faster as a function of r^{-6} compared to Coulomb interactions which attenuate over a longer range with the r^{-1} term.

$$U_{i,j}^{LJ} = 4\epsilon \cdot \left[\left(\frac{\sigma}{r_{i,j}} \right)^{12} - \left(\frac{\sigma}{r_{i,j}} \right)^{6} \right] \quad (3)$$

ϵ in equation (3) is the depth of the potential well and σ is the distance of the minimum of the interaction energy where the van der Waals forces on a pair of atoms are zero. Essentially, the van der Waals interactions are short-range and the electrostatic interactions are long-range. In addition to these, there can be additional interactions due to some constraints between some atoms. These constrained interactions could be due to covalent bonds with a dependence on distances, angles or dihedral angles between the concerned atoms. In classical atomistic simulations such as molecular dynamics and energy minimization, the atomic forces are described by empirically fitted force field sets. More details on force fields can be found in the last section of this chapter.

3.1.3 Ewald Summation

As mentioned earlier, with the periodic boundary conditions it is impossible to calculate all the pairwise electrostatic interactions, as an atom has to interact with the atoms in that box and its periodic images, leading to an infinite system with infinite number of atoms. In order to make the calculations possible, a cut off radius, r_{cut} , is defined for the electrostatic interactions of an atom. Thus, the interactions of an atom with other atoms outside this sphere of radius r_{cut} is either neglected or, in the case of electrostatic (Coulomb) interactions, calculated in reciprocal space using the Ewald summation method.

The Ewald summation [94] is a faster method to compute the long range interactions between atoms or molecules. The total electrostatic interaction energy in a periodic simulation box can be written as

$$U = \frac{1}{2 \cdot 4\pi\epsilon} \sum_{i=1}^{N} \sum_{j=1}^{N} \sum_{n \in \mathbb{Z}^3, n=0\ i \neq j} \frac{q_i q_j}{\left(r_{i,j} + \bar{n} \cdot \bar{L}\right)} \tag{4}$$

and

$$\bar{n} = \begin{bmatrix} n_x & 0 & 0 \\ 0 & n_y & 0 \\ 0 & 0 & n_z \end{bmatrix}; \ \bar{L} = [\ \vec{a} \quad \vec{b} \quad \vec{c}\ ] \tag{5}$$

where ϵ is the dielectric constant, q_i is the charge of the atom i , q_j is the charge of the atom j, $r_{i,j}$ is the vector distance between atoms i and j, n_x is an integer , $\vec{a}$ is one of the simulation cell vectors such that $\bar{n} \cdot \bar{L}$ represents the distance of an image from the original box. This equation decays as a function of the inverse of the distance r. Thus, the interaction can be separated into a short range part, computed explicitly in real space $\forall \left| r_{i,j} + \bar{n} \cdot \bar{L} \right| \leq r_{cut}$, and a long range part, computed in the reciprocal space for faster convergence. This is done by adding a Gaussian charge distribution ($\rho_1 = -\frac{q_i \cdot e^{\left(\frac{-r^2}{2\sigma^2}\right)}}{(2\pi\sigma^2)^{\frac{3}{2}}}$, σ is the width of the Gaussian) equivalent to the point charge but with opposite sign to the short range potential, such that these attenuate faster with increasing interatomic distances, and thus, reduce the error due to the cut off. This forms the real part summation U^{real}. However, to correct for the additional term in the short range potential, another Gaussian charge distribution with opposite charge ($\rho_2 = -\rho_1$) has to be added to the long range potential and to make the system charge neutral. The calculation of the long range potential (U^k) is then done in reciprocal space where it converges faster. Unlike a point charge, the Gaussians will interact with itself, which is corrected for in the U^{self} term. Thus, the electrostatic interaction in the equation (4) is written in the Ewald method as

$$U = U^{real} + U^k - U^{self} \tag{6}$$

$$U^{real} = \frac{1}{2 \cdot 4\pi\epsilon} \sum_{i=1}^{N} \sum_{j=1, |r_{i,j}+\bar{n}\cdot\bar{L}| \le r_{cut}}^{N} \frac{q_j \cdot q_i}{\left(r_{i,j} + \bar{n} \cdot \bar{L}\right)} \cdot \left[1 - \mathrm{erf}\left(\frac{|r_{i,j} + \bar{n} \cdot \bar{L}|}{\sqrt{2}\sigma}\right)\right] \quad (7)$$

$$U^{k} = \frac{1}{2\epsilon V} \sum_{i=1}^{N} \sum_{j=1}^{N} \sum_{k \neq 0} \frac{q_j \cdot q_i}{k^2} \cdot \ e^{-(\sigma^2 k^2/2)} \cdot e^{ik\cdot(r_i - r_j)} \quad (8)$$

$$U^{self} = \frac{1}{4\pi\epsilon} \cdot \frac{1}{\sqrt{2\pi}\sigma} \cdot \sum_{i=1}^{N} q_i^2 \quad (9)$$

3.2 Simulation techniques

Three atomistic modelling techniques that are relevant to this thesis are described in this section. In Energy Minimization (EM) and Molecular Dynamics (MD), the electronic states of the atoms are not explicitly solved, but rather an empirical set of potentials is used to simulate the behaviour of the atoms. The Density Functional Theory (DFT), however, solves the electronic structure of the atoms to find the ground state configuration instead of the empirical set of potentials. A brief description of each technique is given in the following subsections.

3.2.1 Energy minimization

Energy minimization (EM) is a minimization technique where the positions of the atoms in a unit cell of the system of interest ae optimized to get a ground state configuration, such that the resulting structure has the lowest energy at 0 K temperature. Essentially, this method minimizes the interaction energy of the system using Newton-Raphson or other root-finding algorithm to find a minimum in the energy landscape. There are no dynamics or atomic vibrations and hence temperature in EM. The METADISE code [95], a popular energy minimization software developed by Parker and co-workers, is used in this thesis. As mentioned earlier, in this technique the interatomic interactions are simulated with force fields. The total energy of the system comes only from the potential energy of the individual atoms, which is calculated as the summation of constrained and non-constrained pairwise and multi-body interactions. The constrained interactions result from confining the distance, angle or dihedral angles between a set of atoms in a molecule which are generally referred to as bonded interactions. The non-constrained or non-bonded interactions are from pairwise Coulombic and van der Waals' forces between the atoms.

$$E_{total} = E_{coulomb} + E_{vdW} + E_{bond} + E_{angle} + E_{dihedrals} \quad (10)$$

The energy expression in equation (10) is iteratively minimized by adjusting the positions of the atoms, either keeping a constant volume or a variable volume to minimize the stresses. A variable cell minimization scheme (CONP in METADISE) is generally preferred for minimizing a bulk structure (unit cell with periodic boundary conditions) such that the resulting structure has no residual stress.

In this thesis, EM is only used in chapters 4 and 5. It is preferable to do EM for a unit cell to ensure the atomic positions are optimized and there is no residual stress before creating supercells and/or performing MD simulations.

3.2.2 Molecular dynamics

Molecular dynamics is a simulation method to evolve a system of interacting atoms or molecules with time by solving Newton's law of motion. The interactions are described by the set of force fields as in the case of EM. The force acting on an atom i with a mass m is the negative distance derivative of the pairwise summation of potentials with the rest of atoms in the box.

$$F_i = m_i a_i = -\nabla U_i \quad (11)$$

$$U_i = \sum_j U_{ij}^{Coul} + U_{ij}^{vdW} + U_{ij}^{bond} + U_{ij}^{angle} + U_{ij}^{dihedrals} \quad (12)$$

The initial velocities of the atoms are generally randomly generated from a Gaussian or Maxwell-Boltzmann distribution at a given temperature. By integrating Newton's Law of motion in equation (11), the position of the atoms after a given timstep δt can be determined, under the assumption that within this, the time step the accelerations remain approximately constant.

$$a_i(t) = \frac{F_i}{m_i} = \frac{dv_i}{dt} \quad (13)$$

$$v_i(t + \delta t) = v_i(t) + a_i(t) \cdot \delta t \quad (14)$$

Integrating it further with time, we get

$$r_i(t+\delta t) = r_i(t) + v_i(t)\cdot\delta t + \frac{1}{2}a_i(t)\cdot\delta t^2 \quad (15)$$

However, the force exerted by the atoms on each other varies with their position and time step. Thus, there are additional terms in a definite integral, and it is more accurate to do a Taylor series expansion of position, velocity and acceleration. For instance, a function f varying with time can be written as

$$f(t+\delta t) = f(t) + \int_t^{t+\delta t} f'(t)\cdot dt \quad (16)$$

This integral can be approximated as a Taylor series of expansion as below

$$f(t+\delta t) = f(t) + f'(t)\cdot\delta t + \frac{1}{2}\cdot f''(t)\cdot\delta t^2 + \frac{1}{6}\cdot f'''(t)\cdot\delta t^3 + \mathcal{O}(\delta t^4) \ldots\ldots \quad (17)$$

where f can be r, v or a. It is computationally impossible to calculate all the terms in this infinite expansion, and we can ignore the cubic and higher terms with an associated error of the order $\mathcal{O}(\delta t^3)$. There are different algorithms which can integrate the position or velocity to give an approximate solution. One of the prominent ones is the Verlet algorithm where the position is expressed as follows

$$r(t+\delta t) = 2\cdot r(t) - r(t-\delta t) + a(t)\cdot\delta t^2 + \mathcal{O}(\delta t^4) \quad (18)$$

This is obtained by finding the difference between the Taylor expansion of $r(t+\delta t)$ and $r(t-\delta t)$. The other widely used approaches are the Leap-Frog and Velocity Verlet algorithms. In the Leap-Frog algorithm, the velocities are calculated first at $t+\frac{\delta t}{2}$ and then these are used to calculate the position at $t+\delta t$.

$$r(t+\delta t) = r(t) + v\left(t+\frac{\delta t}{2}\right)\cdot\delta t \quad (19)$$

$$v\left(t+\frac{\delta t}{2}\right)=v\left(t-\frac{\delta t}{2}\right)+a(t)\cdot\ \delta t \tag{20}$$

and

$$v(t)=\frac{1}{2}\cdot\left[v\left(t-\frac{\delta t}{2}\right)+v\left(t+\frac{\delta t}{2}\right)\right] \tag{21}$$

The precision of these algorithms is similar to that of Verlet algorithm. In the velocity Verlet algorithm, the position at $t+\delta t$ is calculated with the velocity at t. The velocity at $t+\delta t$ is calculated from the acceleration calculated with the positions at t and $t+\delta t$, as shown below

$$r(t+\delta t)=r(t)+v(t)\cdot\delta t+\frac{1}{2}a(t)\cdot\delta t^2 \tag{22}$$

$$v(t+\delta t)=v(t)+\frac{1}{2}[a(t)+a(t+\delta t)]\cdot\delta t \tag{23}$$

Usually, the velocity Verlet or the Leap-Frog algorithms are default algorithms implemented in general molecular dynamics software packages. In this thesis, the DLPOLY classic [96] package is used for all the molecular dynamics simulations and the Leap-Frog algorithm is used. Additionally, the magnitude of the time step should be such that the displacement of the atom at each step is less than its vibrational amplitude (typically of the order of 10^{-11} m).

Once the position, velocity and hence, the energy of the system at each time step can be evaluated, we can look at how, we can obtain ensemble averages of macroscopic observables. In statistical mechanics, an ensemble is a collection of states that a system in a certain thermodynamic state can adopt with a certain probability. An average over a certain physical property of the ensemble thus corresponds to the expected time-averaged or macroscopic property of the system in the specified thermodynamic state. An ensemble average is calculated as follows:

$$\langle A\rangle=\iint\frac{A(p^N,r^N)\cdot e^{-\left[\frac{H(p^N,r^N)}{k_BT}\right]}dp^Ndr^N}{\iint e^{-\left[\frac{H(p^N,r^N)}{k_BT}\right]}dp^Ndr^N} \tag{24}$$

where A is an observable which is a function of atomic positions r and momenta p, H is the Hamiltonian, k_B is the Boltzmann's constant, T is the temperature, and N is all possible states of the system. However, in MD we evolve the system with time and not with the different microstates. According to the ergodic hypothesis, a time average can be equivalent to the ensemble average if we give sufficient time for the system, such that most of the microstates are probable, and hence we can simplify the above equation

$$\langle A \rangle_{ensemble} \approx \langle A \rangle_{time} = \lim_{\tau \to \infty} \frac{1}{\tau} \int_0^{\tau} A\,[p(t), r(t)]dt \tag{25}$$

Here, A is the instantaneous value of the observable as a function of the atomic positions and momenta at time t. The above integral can be solved in a discretized time space as follows

$$\langle A \rangle_{time} \approx \sum_{t=1}^{\varphi} A[p(t), r(t)] \tag{26}$$

where φ is the number of time steps in the simulation. There are different types of ensemble and the ones we are primarily using in our simulations are NVE, NVT, NPT and NST ensembles. The NVE is an ensemble with a constant number of atoms, constant volume and a conserved energy. In the NVT ensemble, the temperature is kept constant with the help of a thermostat. In NPT and NST ensembles, there are barostat algorithms to regulate the pressure (principal stresses) and stress of the system respectively.

(i) Thermostat and Barostat

The thermostat is applied on the instantaneous velocities of atoms by the following expression, with a time dependent frictional coefficient, derived from the Nosé-Hoover [97] Hamiltonian

$$\frac{dp_i(t)}{dt} = -\frac{\partial U_i(t)}{\partial r_i} - \chi(t) \cdot p_i(t) \tag{27}$$

$$\frac{d\chi(t)}{dt} = \left[\sum_{i=1}^{N} \frac{p_i(t)^2}{2m_i} - g k_B \cdot T\right] \cdot \frac{2}{Q} \tag{28}$$

Here T is the set or desired temperature, g is a constant, Q is the imaginary mass of the heat bath, and $\chi(t)$ is the instantaneous frictional coefficient, which is regulated by how the instantaneous temperature from the momenta differs from the set temperature T.

Similarly, there are barostats to control the pressure through fluctuations of the volume of the system, which will also affect the temperature. There are many methods and the Melchionna [98] modification of the Hoover NPT algorithm implementation in DLPOLY is used. Similar to the thermostat, there is an additional damping coefficient, η applied to atomic positions, momenta and the simulation volume:

$$\frac{dp_i(t)}{dt} = -\frac{\partial U_i(t)}{\partial r_i} - [\,\chi(t) + \eta(t)] \cdot p_i(t) \tag{29}$$

$$\frac{dr_i(t)}{dt} = \frac{p_i(t)}{m_i} + \eta(t) \cdot [r_i(t) - R_0(t)] \tag{30}$$

$$\frac{dV(t)}{dt} = 3 \cdot \eta(t) \cdot V(t) \tag{31}$$

where R_0 is the center of mass of the system, and $V(t)$ is the instantaneous volume of the simulation cell. To get a constant stress ensemble (NST), η is replaced by a tensor, and the volume is replaced by the simulation cell vectors.

The details of the molecular dynamics simulation setup will be found in each chapter for the specific simulations done in that chapter.

3.2.3 Density Functional Theory

In the two techniques described above, the smallest particle was the atom, and the role of electrons are simulated through empirical force field equations. To include electrons explicitly, the wave nature of the electrons has to be taken into account, which is not possible with classical mechanics. In quantum mechanics, the Schrödinger equation is analogous to the Newton's law of motion in classical mechanics. The ground state electronic structure is obtained by solving the time-independent Schrödinger equation:

$$\hat{H}\Psi = E\Psi \tag{32}$$

where $\hat{H}$ is the Hamiltonian, Ψ is the wave function of the electron cloud of the system, E is the total energy. In a many electron system, the Hohenberg-Kohn Theorem [99] states that the ground state properties are determined by the ground state electronic density. This means that for an N electron system, the scale of calculation has reduced from $3N$ spatial coordinates to just three spatial coordinates. Thus, the energy functional can be written as

$$E[\rho] = T[\rho] + V_{ext}[\rho] + V_{ee}[\rho] \tag{33}$$

where ρ is the electron density function, T is the kinetic energy (within the Born-Oppenheimer approximation [100] of stationary heavy nuclei), V_{ext} is the interaction of the electrons and the external potential (ions in crystals) which is the classical Coulomb equation, and V_{ee} is the electron-electron interaction potential. Kohn and Sham [101] proposed an approximation for the kinetic energy and the electron-electron functionals by introducing a fictitious system of N non-interacting electrons whose exact kinetic energy T_s and electron density are known. Thus, the energy functional can be rewritten as

$$E[\rho] = T_s[\rho] + V_{ext}[\rho] + V_H[\rho] + E_{xc}[\rho] \tag{34}$$

where V_H is the Hartree energy which can be seen as a classic coulomb-like electron-electron interaction, and E_{xc} is the exchange-correlation functional. Several approximations exist for the exchange-correlational functional. In our work, we use the generalised gradient approximation (GGA) [102]. To reduce the computational cost, an effective potential called pseudopotential [103] is employed to mimic the effect of the core electrons on the core and the valence electrons. The expectation values of the wave functions are calculated in the reciprocal space at certain k-points. The method of k-point sampling used in our calculations is from Monkhorst and Pack [104]. Quantum Espresso [105] package is the default code used, if not specified otherwise.

3.3 Force Field

A force field is a set of empirically fitted parameters to simulate the atomic interactions through a set of potential energy equations. In the first part of the thesis, CementFFv1 [11,32,106] force field was used for describing the interatomic interactions. The short range van der Waals interactions

were defined using Lennard-Jones and Buckingham potentials for different species. For the bonded interactions in the hydroxyl molecules and silicate chains, Morse potential and Harmonic angle potentials are used. Detailed description of the different species and their interaction potentials can be found in Appendix section 8.1. For the water molecule, the TIP4P/2005 rigid model was adopted [107]. This set of potentials has been validated on various cementitious materials [10–12,93]. This potential set is used for the chapters 4 and 5. In chapter 6, an improved version of this force field has been used, as described in the following section.

3.3.1 CementFF- Improvement

A significant drawback of the CementFFv1 was its inability to get the correct coordination numbers for calcium in 14 Å tobermorite. The average coordination number (CN) of calcium from MD calculations was always less than 6. The ideal CN of calcium should be 6.8 with eight main layer calcium in seven-fold coordination and two interlayer-calcium in six-fold coordination from the XRD-resolved structure [108]. In order to correct for this, the shell description of oxygen atoms of the silicates, as in the original force field from which it was adopted, was reinstated. In the core-shell description of an atom, the shell which carries the charge with zero or very small mass are bound to the core which has the atomic mass with a slight counter charge in some cases by a spring. This introduces polarizability to the simulation by allowing the charge to be slightly displaced from the core of the atom. The calcium oxygen shell interaction term used in simulating modified silicate glasses is adopted here. In 14 Å tobermorite it gave a better coordination number of 6.7 for calcium-oxygen cut off distance of 3 Å. It also gave better unit cell parameters for the different cementitious minerals considered (see Table 2).

The other drawback was that the cross-interaction terms with water in CementFFv1 used was adopted from potential sets [109,110] which were not fitted for the TIP4P/2005 water model[107]. However, the charges on the atoms of the different models are different [111], and hence their interactions with other ions should be dealt with differently. Some of these cross-term interactions with water, namely $Ca - O_{H_2O}$, $O_{silicate} - H_{H_2O}$, and $H_{OH} - O_{H_2O}$, were altered to make improvements in the reaction energies calculated as shown in Table 3. The reactions shown in Table 3 are those relevant to cementitious systems. The detail of the parameters in the CementFFv2 can be found in the Appendix section 8.2. However, similar to the CementFFv1 the current version also has limitations in capturing the dissolution reaction of portlandite in water. I observed that this error is from the free hydroxyl group in the water. Hence, care has to be taken when simulating a system with free hydroxyl ions in bulk water. Since no proton exchange or sharing is allowed in the force

field, a reactive term would have to be included into the force field. DFT calculations on selected structures showed that this effect is not overly important for the water in C-S-H.

Table 2: Comparison of the unit cell parameters of the minerals studied with MD simulations using CementFFv2 force field with the experimental values

Mineral	Method	a [Å]	b [Å]	c [Å]	α [°]	β [°]	γ [°]	Volume [Å^3]	Volume deviation [%]
CaO [112]	Exp	4.82	4.82	4.82	90	90	90	111	
	v1	4.82	4.82	4.82	90	90	90	111	
	v2	4.82	4.81	4.81	90	90	90	111	0.2
$Ca(OH)_2$ [113]	Exp	3.59	3.59	4.90	90	90	120	54.5	
	v1	3.67	3.67	4.81	90	90	120		
	v2	3.67	3.69	4.81	90	90	120	56.2	3.2
SiO_2 [114]	Exp	4.92	4.92	5.40	90	90	120	113.3	
	v1	4.99	4.99	5.5	90	90	120		
	v2	4.88	4.89	5.40	90	90	120	111.6	1.4
C_3S [115]	Exp	12.24	7.07	9.30	90	116	90	721.3	
	v1	12.43	7.19	9.57	90	116	90	771	6.9
	v2	12.37	7.14	9.42	90	116	90	748.6	3.8
14 Å Tobermorite [42]	Exp	6.74	7.43	15.33	111	87	123	1170.5	
	v1	6.85	7.26	14.95	112	84	122		
	v2	6.73	7.40	15.33	114	86	123	1146.5	2.1

Table 3: Reaction energies calculated with CementFFv1 ($\Delta \boldsymbol{H_{v1}}$) , CementFFv2 ($\Delta \boldsymbol{H_{v2}}$) and the experimental values. For reactions involving dissociation or formation of water a correction factor of 3.38 eV per $\boldsymbol{H_2O}$ is added. This is because of the different description of hydroxyl groups and water molecules. The error estimation , $\in_{est_{v2}}^{FF}$, is calculated using equation (37). $\in_{est_{v1}}^{FF}$ is the error estimation for the same reactions using CementFFv1

Reactions	ΔH_{v1} [eV]	ΔH_{v2} [eV]	ΔH_{exp} [eV]	$\in_{est_{v1}}^{FF}$ [eV]	$\in_{est_{v2}}^{FF}$ [eV]
$3 \cdot CaO + SiO_2 \rightarrow C_3S$	-1.28	-1.56	-1.2	0.19	0.40
$Ca(OH)_2 \rightarrow [Ca^{2+} + 2 \cdot OH^-]_{aq}$	0.23	0.48	-0.19	0.42	0.10
$Ca(OH)_2 + SiO_2 \rightarrow [CaSiO_4H_2]_{aq}$	2.31	2.44	2.46	0.61	0.37
$2 \cdot Ca(OH)_2 + SiO_2 \rightarrow [Si(OH)_4]^-{}_{aq} + 2 \cdot CaO$	8.55	7.19	7.60	1.03	0.73
$CaO + H_2O \rightarrow Ca(OH)_2$	-1.08	-0.56	-0.66	0.53	0.10
$2 \cdot H_2O + SiO_2 \rightarrow [Si(OH)_4]^-{}_{aq}$	6.4	6.07	6.27	0.91	0.56
$[Ca^{2+} + 2 \cdot OH^-]_{aq} + [Si(OH)_4]^-{}_{aq} \rightarrow [CaSiO_4H_2]_{aq} + 2 \cdot H_2O$	-4.32	-4.1	-3.62	1.44	0.48

3.3.2 Error estimation

The maximum deviation of the relaxed cell parameters from MD calculations was about 1.5 %, for tricalcium silicate. In the case of cell angles, the maximum deviation was about 3 degrees for 14 Å tobermorite, as shown in Table 2. With this information, we can safely say that the distances and angles calculated using CementFFv2 will be within ± 3% and ± 5 degrees, respectively. This is a considerable improvement compared to the older version, but at a cost of the simulation time with the incorporation of shells . An error estimation methodology for the reaction energies was developed for CementFFv1 [11,93]. Here, we adopt the same methodology, and the revised equation for the error estimation is given in equation (37). For a chemical reaction with reactants R and products P,

$$c_1^r \cdot R_1 + c_2^r \cdot R_2 + \ \ldots \rightarrow c_1^p \cdot P_1 + c_2^p \cdot P_2 + \ \ldots \tag{35}$$

where c_1^r and c_1^p are the stoichiometric coefficients, then the enthalpy of this reaction is

$$\Delta H = \sum_i c_i^r \cdot H_i^r - \sum_j c_j^p \cdot H_j^p \tag{36}$$

where H_i^r and H_i^p are the enthalpy calculated from the MD simulation of individual systems of reactants and products, and the error estimate from the force field in calculating the enthalpy of reaction ΔH is

$$\in_{est}^{FF} = 0.065 \cdot \Delta H + 0.000635 \cdot \left(\sum_i c_i^r \cdot |H_i^r| + \sum_j c_j^p \cdot \left| H_j^p \right| \right) \tag{37}$$

More details on the error estimation can be found in the thesis of Galmarini [93].This error estimation is only used for the simulations in Chapter 6 employing the CementFFv2 force field, as the error estimation for force field CementFFv1 has been done previously [11,93].

Chapter IV. Brick Model

In this chapter I will be introducing a new methodology to precisely define the defects in C-S-H. The chemical units in tobermorite and possible defects at different sites of tobermorite are represented by characters such that a collection of characters can represent a defective tobermorite. A method to compare the relative stabilities of these defects in C-S-H is also introduced. This work has been recently published in the Cement and Concrete Research (2018) journal. In the first section of this chapter an overview of the paper is given, followed by the full paper for further reading. All the computational work and development of the structural models was carried out by the candidate. The published manuscript was corrected and modified by the 3 senior co-authors.

4.1 Overview

A defective tobermorite is believed to be the underlying atomic structure of C-S-H. However, there has been no agreement on the exact features of the structural environments in C-S-H. In addition, there are several types of tobermorite which have similar features to C-S-H. In this paper, we have developed a methodology, hereby referred to as “Brick model” in this thesis, which can be applied to any tobermorite-like structure to precisely define the defects in the building blocks of C-S-H.

In this model, a reduced unit cell is defined for 14 Å tobermorite which we call a “brick”. Now we divide this brick into small chemical units denoted by special characters such that a string of characters, <S’<C7>S’> , represents a reduced unit cell of 14 Å tobermorite as shown in Figure 7. Additional chemical species are defined, which can replace the original tobermorite species and either occupy those crystallographic sites or occupy the free space in the tobermorite unit cell as shown in Fig 3. Thus, <C<oC7>S’> is a defective tobermorite brick with the bridging silicate tetrahedra having a hydroxyl group in it, S’, being replaced by a calcium and a hydroxyl molecule in the interlayer. More details on the different types of defects considered can be read in the paper. In order to compare the stabilities of each bricks, a reaction enthalpy has been defined. The enthalpy of a brick is compared to a stoichiometric equivalent of lime, quartz and water as shown in equation (46 that enabled the relative stabilities of these defects to be assessed. Finally, a full atomistic model using the brick model description of C-S-H is proposed. In short, the brick model is a bottom up approach method developed in this paper to facilitate a better understanding and modelling of C-S-H atomic structures.

Supplementary information of this paper is in Appendix section 8.3

4.2 Paper Abstract

Cement and Concrete Research 107 (2018) 221–235

Contents lists available at ScienceDirect

Cement and Concrete Research

journal homepage: www.elsevier.com/locate/cemconres

An atomistic building block description of C-S-H - Towards a realistic C-S-H model

Aslam Kunhi Mohamed[a,*], Stephen C. Parker[b], Paul Bowen[a], Sandra Galmarini[c]

[a] Laboratoire de Technologie des Poudres, Ecole Polytechnique Fédérale de Lausanne, Switzerland
[b] Computational Solid State Chemistry Group, Department of Chemistry, University of Bath, UK
[c] Building Energy Materials and Components, Empa, Switzerland

ARTICLE INFO

Keywords:
Crystal structure
Cementitious systems
Molecular dynamics
Density functional theory
C-S-H

ABSTRACT

Understanding the atomistic structure of Calcium silicate hydrate (C-S-H), the main product of cement hydration, is of paramount importance to better formulate sustainable cement. The existing atomistic models are not in total agreement with experimental results and fail to explain the nanosized nature of C-S-H. Here, we present a new approach for describing the complexity of these structures at the molecular level, enabling a detailed comparison of C-S-H models. The new methodology encodes a full, large scale atomistic C-S-H structure by a simple, readable string of characters, similar to the way the base sequence in DNA encodes a vast range of different proteins. We then use the methodology to assess 14 Å tobermorite-defect structures and their stabilities using DFT and classical molecular dynamics. Finally we highlight how the model may be extended to develop reliable atomistic C-S-H models for a range of Ca/Si ratios and conditions.

4.3 Introduction

Hydrated cement is the binder or glue that holds together the sand and aggregates that all together make up concrete- the most used material in the world. Although per kg cement is inherently a low carbon material [1, 2], the vast quantities used mean that cement is responsible for about 5-8% of global CO_2 emissions. The optimization of the mechanical properties and durability of concrete can therefore aid in the reduction of CO_2 emissions. This would be greatly aided by a better fundamental knowledge of the material at the atomistic structure level.

A better understanding of cementitous systems is complicated by the fact that the exact atomistic and nanoscale structure of the main hydration product (C-S-H) is poorly known. One reason for this is that both X-ray diffraction (XRD) and selected area diffraction show only two weak signals, indicating repeat distances of about ~ 1.82 – 1.83 Å and ~ 2.7 – 3.2 Å [3, 4]. This implies that C-S-H does not have any 3D long range order. It also means that the exact atomistic structure of C-S-H cannot be resolved by conventional XRD techniques.

A further complication is the varying chemical composition of C-S-H. The composition varies significantly not only between different samples but also within one and the same sample. In neat

tricalcium silicate (C_3S) pastes, local energy dispersive X-ray analysis (EDS) has shown that on a scale of 100 nm $\frac{Ca}{Si}$ varies between 1.2 and 2.1, with an average calcium to silica ratio $\frac{Ca}{Si}$ of 1.75 [5].

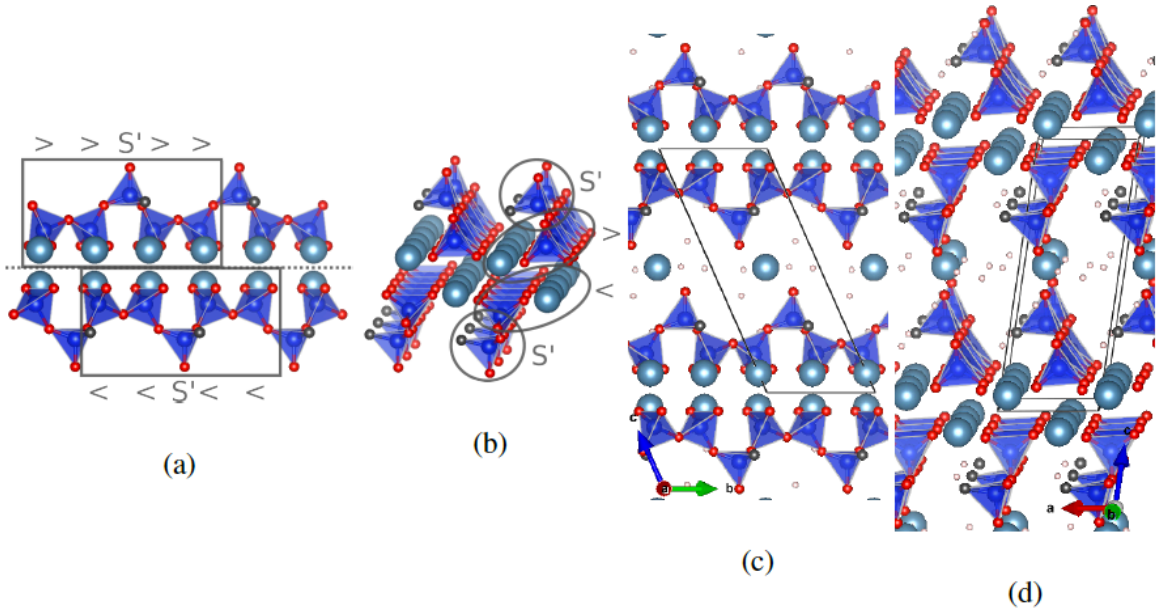

Figure 6 : Ca-Si layer of 14 Å tobermorite with characteristic linear dreierketten structure of silicate chains ((a) and (b)) as well as their stacking in 14 Å tobermorite ((c) and (d)). Si: blue, Ca: turquoise, O: red, OH: black. Also shown is the structural abbreviation introduced in section 4.5.1(i)

The type of silicate species present in C-S-H was first studied by Mohan et al. with trimethylsilylation followed by chromatography [6]. This technique revealed that only silica chains with a length of 3n-1 (i.e. dimers, pentamers, octamers and some longer chains) are present in C-S-H. This indicates a so called dreierketten structure with silicate dimers that can be linked by bridging silicate tetrahedra (see Figure 6).Subsequent NMR studies revealed, that no connectivity larger than 2 exists between the different silicate chains [7, 8, 9, 10, 11, 12, 13]. In other words, the silicate species in C-S-H are composed of linear chains without cross-linking. Also NMR distinguishes between different species within the linear chains: so called non bridging chain tetrahedra Q^2 and the bridging tetrahedra Q^2 [8, 13]. The ratio between the two in C-S-H being 2:1. This confirms the dreierketten structure where only chains of length 3n-1 can exist.

Additionally, transmission electron microscopy (TEM) images of carefully dried samples show different morphologies of C-S-H, often with a pronounced texture [4]. The smallest characteristic dimension of C-S-H, corresponding to both the size of the solid regions [4, 14, 15] and of the crystallites [16, 17] is in the order of 3-6 nm. The largest characteristic dimension is less clear. For

the crystalline domains in OPC the largest characteristic dimension is typically in the order of 6-15 nm [16, 17], however some order can persist over much longer length scales of >100 nm [4, 18], which could be either due to a partially continuous structure [19] or to a colloidal material [20] with long length scale ordering similar to that observed in e.g. liquid crystals. TEM images with an even higher resolution have revealed layering of the material with an approximate interlayer distance of ~ 12-14 Å [21].

Different water containing, layered calcium-silicate crystal structures containing linear silicate-"dreierketten" have been reported in the literature. The ones most commonly compared to C-S-H are the different tobermorites (e.g. 14 Å tobermorite: $\frac{Ca}{Si}$ = 0.83, interlayer distance 14 Å, molar water content: 42 %) and jennite ($\frac{Ca}{Si}$ = 1.5, molar water content: 42 %). Both 14 Å tobermorite and jennite consist of calcium-silicate layers separated by an interlayer space containing both water and calcium. The main layer calcium ions in 14 Å tobermorite form a planar sheet, the calcium layer in the jennite structure is corrugated.

However the calcium to silicon ratio $\frac{Ca}{Si}$ of all these minerals is significantly smaller than that observed for C-S-H. An indication as to what structural trends lead to an increase of the $\frac{Ca}{Si}$ ratio in C-S-H can be gleaned from experimental observations. In C-S-H produced from tricalcium silicate (C_3S) pastes cured for 12 months, about 60 % of the silicate species are present as dimers and 40 % as longer chains [6] with a mean chain length (MCL) of 3.3.

Similar results are found for ordinary Portland cement paste (OPC)[4]. The chain length continues to increase over the next couple of decades but even for ~ 20 year old pastes there are still a lot of dimers (~ 40 %[6]) and the MCL is still less than 5 [4]. This means that, compared to the model structures with infinite silicate chains, a significant part of the bridging silicate tetrahedra are missing in C-S-H, which will increase the $\frac{Ca}{Si}$.

Additionally both $^{1}H - ^{29}Si$ NMR measurements [8] and infrared spectroscopy [22] indicate the existence of Ca-OH groups in C-S-H. Thomas et al. used inelastic neutron scattering to quantify the amount of Ca-OH bonds in C-S-H [23]. They found that at a calcium to silicon ratio of 1.7 about 23 % of the charge of the Ca^{2+} ions in C-S-H are compensated by hydroxyl groups. This value is in between that of tobermorite (no $Ca - OH$ groups) and that of jennite (33 %). Thus these results indicate either a mix between jennite and tobermorite or additional $Ca - OH$ groups incorporated in a tobermorite like structure would be needed to give the appropriate $\frac{Ca}{Si}$ ratio. Additionally the

number of $Si-OH$ groups decreases with increasing $\frac{Ca}{Si}$. In contrast to a non-defective 14 Å tobermorite, the number of silanol groups in a C-S-H with a $\frac{Ca}{Si}$ ratio of 1.7 is below the detection limit of different experimental techniques [22, 11].

While these results would indicate a closer resemblance of C-S-H with a typical $\frac{Ca}{Si}$ ratio of 1.7 to jennite than to tobermorite, structural measurements such as XRD and Raman spectroscopy [24, 16, 25] as well as theoretical work [26] indicate a closer resemblance of the C-S-H structure to tobermorite rather than to jennite.

In summary, from these results we infer that C-S-H is composed of defective, nanocrystalline tobermorite with missing bridging silicate tetrahedra, leading to a decreased silicate chain length, and deprotonated silanol groups, the charge of which is compensated by additional calcium ions in the water-interlayer and with additional $Ca-OH$ groups. Furthermore, experimental measurements revealed that the Ca-O and Si-O nearest neighbour distances in C-S-H with $\frac{Ca}{Si}$ up to 1.75 are similar to the ones in tobermorite while the Ca-O coordination number decreases almost linearly with increasing $\frac{Ca}{Si}$ (6.0 ± 0.2 at $\frac{Ca}{Si}$ = 1.75, as compared to 7.1 ± 0.2 for $\frac{Ca}{Si}$ =0.6 and 7.0 ± 0.2 at $\frac{Ca}{Si}$ = 0.8) [27, 28]. The approximate stoichiometry is estimated to be $Ca_{1.7}SiO_{3.7} \cdot 1.8\, H_2O$ with a density of about 2.6 $\frac{g}{cm^3}$, excluding the water at the surface [29, 15]. XRD measurements indicate that the interlayer distance may be smaller than 14 Å in C-S-H with $\frac{Ca}{Si}$ = 1.7 (around 11 or 12 Å [16, 11, 27]).

An atomistic model should take into account all the experimental evidence presented above. Additionally it should give some indications as to why C-S-H displays the rather unique properties it does: How can we explain the consistently nanoparticulate nature of C-S-H? And why does the stoichiometry vary extensively within one and the same C-S-H sample (no homogeneity at the nanoscale)? In recent years, several atomistic models for C-S-H have been proposed [30, 21, 31, 32, 33]. Despite capturing some of the salient features of C-S-H, none of the models are entirely satisfactory, when confronted with the experimental evidence available and they leave several questions regarding the properties and behavior of C-S-H unresolved.

Recently, Pellenq et al. [21, 31] and Kovačević et al.[32, 34] used the Hamid [35] and the Merlino [36] 11 Å tobermorite respectively as the base structure to model C-S-H using classical molecular dynamics simulations. In order to arrive at the required $\frac{Ca}{Si}$ ratio, Pellenq et al. randomly removed SiO_2 groups and started with dry tobermorite structure with subsequent water adsorption using

Grand Canonical Monte Carlo. This resulted in a very high percentage of monomers and the presence of water within the Ca-Si layers, both inconsistent with the experimental results available. Other limitations of their model were the absence of hydroxyl groups as well as bond lengths and coordination numbers that are inconsistent with natural calcium-silicate mineral structures [33]. The authors have tried to address some of these shortcomings in a recent work using the ReaxFF potential to split water molecules, making it possible to have hydroxyl groups and thus forming Ca-OH [31]. However, the hydrogen of the split water molecules mainly reacted with non-bonding oxygen of the silicate chains, forming protonated silanol groups which, according to experimental results, is found in very small or negligible amounts at high $\frac{Ca}{Si}$ ratios [11, 22]. Also, in order to eliminate the unexpectedly high concentration of silicate monomers as observed by Pellenq et al. they allowed for (random) polymerization of the silicates in their revised model structures. However, this leads to a silicate chain structure that is in violation of the dreierketten pattern that has been shown to exist in C-S-H, with only chain lengths of $3n-1$ being observed [6, 7, 8, 9, 10, 11].

Kovačević et al.[32, 34] explored three different ways to arrive at a $\frac{Ca}{Si}$ ratio of 1.65 from the Merlino 11 Å tobermorite starting structure [36]. Namely (1) removal of only the bridging silicate tetrahedra and addition of $Ca(OH)_2$, (2) removal of bridging silicate as well as dimers and (3) random removal of all the silicate species as done by Pellenq et al. [31]. This enabled them to compare the energies, calculated via energy minimization [32] and molecular dynamics [34], of many different C-S-H structures with respect to the way the $\frac{Ca}{Si}$ ratio was increased. The authors concluded that the structures generated using the first method, removing only the bridging tetrahedra and adding $Ca(OH)_2$ in the interlayer space are the most stable. The authors conclude that the way of constructing the initial structure has a significant effect on the energy and final properties of the C-S-H model structures. This means that an in-depth discussion about the different ways to construct C-S-H models is needed in order to be able to construct better models leading to a better understanding of C-S-H.

Finally, Richardson [33] derived a fully crystalline model for C-S-H based solely on measured XRD structures of different calcium-silicate structures. The model consists of different perfectly ordered layers with different $\frac{Ca}{Si}$ ratios. General guidelines for the type of defects present as well as geometrical reasoning was used to construct these. While the guidelines developed are very valuable for future work, a perfectly ordered bulk structure seems to be unlikely and makes it difficult to understand the nanoparticulate nature of C-S-H.

The aim of the current paper is to thus develop an atomistic structure for C-S-H that can describe the nanostructuring, facilitate the comparison of models and provide some new insights into C-S-H using atomistic modelling. Hence, in section 4.5.1 a building block description of C-S-H is developed, which is able to describe both different base structures and different $\frac{Ca}{Si}$ increasing defects. This method of describing C-S-H facilitates the development and construction of new model structures and the comparison of existing models. It allows the fast calculation of a range of characteristics (charge distribution, mean chain length, percentage of dimers, ratio of protonation of silanol groups, OH/Ca ratio). The method will be used to revisit different models reported in the literature. In the second section, the building block description together with both classical molecular dynamics (CMD) and density functional theory (DFT) is used to discuss 14 Å tobermorite as another possible basis for C-S-H models by looking at different possible $\frac{Ca}{Si}$ increasing defects, extending the range of the defects considered in the work reported in the literature to date.

It is our view that this novel building block description will significantly help in identifying a more precise atomistic structure of C-S-H and understanding its characteristics, allowing researchers to go one step further from proposing single models which are difficult to compare between each other. However before discussing the model in depth, we briefly describe the simulation methods.

4.4 Methods

4.4.1 Density Functional Theory Calculations

DFT calculations were performed using the VASP code [37, 38], in which a plane wave basis set describes the valence electronic states and the projector augmented wave (PAW) approach [39, 40] models the core-valence interaction. The exchange and correlation is treated with the generalized gradient approximation (GGA) via the Perdew- Burke-Ernzerhof (PBE) functional [41]. The inability of standard DFT to account for van der Waals interactions is well-known [42, 43]. In this work, we applied the DFT-D3 method of Grimme [44] which applies dispersion corrections in a pairwise manner. The Monkhorst-Pack k-points mesh 4 x 4 x 2 and a plane wave cut-off of 500 eV were used to ensure convergence. All DFT calculations used a primitive unit cell with half the volume of the original unit cell reported by Bonaccorsi et al. [45]. The cell parameters of 14 Å tobermorite, relaxed with DFT, can be found in Table 4 and the simulated XRD patterns in the supplementary materials. Both are compared to the experimentally determined structure [45]. The XRD patterns were generated by the software Mercury [46] using a wavelength of 1.54 Å (Cu-Kα) varying from 5 to 50 degrees at an interval of 0.02 °. The DFT calculations with dispersion correction describe the 14 Å

tobermorite structure with good accuracy, the maximum deviation on lattice cell parameters compared to experimental values being 2 % and 1 ° on the angles (see Table 4 and Figure S35 in the supplementary materials).

4.4.2 Classical Atomistic Simulations

Molecular dynamics calculations using classical force fields to describe the atom interactions used DL POLY 2.20 [47] and Metadise for energy minimisation [48]. The formal charge force field used for the description of the ions in solution and for the solid is based on an adaptation of Freeman et al. [49] for the use of the force field originally developed by Lewis and Catlow [50] and further developments by various authors [51, 52, 53, 54, 55, 56] for the use with the TIP family of force fields. For water, the TIP4P/2005 rigid model [57] is adopted. The full force field used here has been previously tested for a wide range of calcium-silicate-hydrate structures and an empirical estimation of the error on structural properties and energies has been developed [56]. The error estimations are used here to give an estimation on the accuracy of the results. The full list of parameters used can be found in [56]. Ewald summation [58] was used to estimate the long range electrostatic forces, with a cutoff radius between the long range and the short range domain of 8.5 Å. Energy minimization calculations have been done under constant pressure (CONP). The time step for the molecular dynamics simulations was 0.7 fs.

A simulation cell of 4x3x1 full 14 Å unit cells (4x3x2 primitive unit cells as considered with DFT) has been used for molecular dynamics calculations. Due to the difference in size of the simulation cells, comparison between DFT and MD is not always possible. The system has been relaxed for > 210 ps before data was collected over 700 ps. After introduction of isolated defects, the system has been first relaxed at zero temperature, followed by equilibration for 35 ps and data collection over a simulation period of 105 ps. The anisotropic NPT ensemble with flexible angles was used. To ensure that the equilibration and simulation period was enough, the simulation was extended to 1 ns for two defects where large relaxations were observed (second structure with $\frac{Ca}{Si}$ ratio of 1.20 and structure with $\frac{Ca}{Si}$ ratio 1.25 in Table 5). No further structural relaxation was observed for either defect.

For additional validation, XRD patterns for 14 Å tobermorite were compared for the DFT relaxed structure and after molecular dynamics simulation using the force field potentials (see supplementary material section 8.3.5 for more details). The general structure is well captured and the interatomic distances remain within an acceptable mean deviation of ± 0.13 Å (or 6.4%) which is comparable with the estimated force field error (5% on interatomic distances [56]). Similarly the

higher $\frac{Ca}{Si}$ structures considered with DFT (see section 4.7.1) were subsequently energy minimized with the classical force field the resulting simulated XRD spectra compared to the one of the DFT structure, the spectra showed good consistency as shown in the supplementary materials.

Table 4: Unit cell parameters of 14 Å tobermorite calculated with different techniques (molecular dynamics (MD) and density functional theory (DFT)) compared to the experimental values. Errors on MD from [56].

	a [Å]	b [Å]	c [Å]	α [°]	β [°]	γ [°]
MD [56]	6.85 ± 0.34	7.26 ± 0.36	27.95 ± 1.40	90 ± 10	93 ± 10	123 ± 10
DFT_{vdW}	6.63	7.37	28.52	89	91	122
Exp. [45]	6.74	7.43	27.99	90	90	123.25

4.5 Results and Discussion

The results and discussion part is divided into three sections. In the first section, a building block description facilitating the comparison and construction of models is developed. In the second section, the formalism is used to examine atomistic structures previously published in the literature. In the final part, the building block description is then used to look at different possible 14 Å tobermorite defects. The different types of defects likely to be present are discussed based on structural and energetic considerations. From the insights gained on different defects, a first step is made towards possible full scale models by presenting model structures. The aim here is not to present a final full scale model, but rather to present a method on how future models can be constructed, tested and compared to previous models (e.g. those by Kovačević et al. [32] and Richardson [33]).

4.5.1 Model for Atomistic Structure Description of tobermorite based C-S-H

What is clear from the different atomistic simulation efforts of C-S-H is that it is unlikely that we can define the exact atomistic structure in the same way a crystalline structure is defined. Rather there will be a large number of possible local arrangements, which will give rise to the overall C-S-H properties observed experimentally. This means that entropic effects are likely to be important. However, the first step to be able to include configurational entropy is an efficient way to correctly describe the full phase space of possible arrangements. Within the current paper we will limit

ourselves to the description of tobermorite-like structures, although the model may be easily adapted to other structures.

(i) Building Block description of 14 Å tobermorite

Our aim is to be able to describe a larger scale C-S-H structure, comprising of over a thousand atoms, in a simple, readable way. In crystals this is done by defining a unit cell. This unit cell, containing only a few atoms, if repeated in space, is able to represent a larger crystal. For C-S-H, assuming a certain underlying crystal structure, we can define a unit cell as for crystals. However, the atoms in each unit cell will vary, meaning that we additionally need a method to specify the atomic arrangement in each consecutive unit cell. For this, we will introduce a short-hand notation for the different groups of atoms. Each atom group or chemical unit has a defined stoichiometry and charge represented by a unique symbol containing information about the relative arrangement of the atoms. The symbols for the atom groups are then used to develop short strings which represent the different "defective" unit cells of tobermorite. The atomic structure within the unit cell will be given both by the symbols used and their position within the string. Finally, a sequence of such strings, each representing a unit cell, will be indicative of stacking units with different compositions and will thus describe a larger scale C-S-H structure. In other words, these short strings form the building blocks with which to build different C-S-H models. We will first develop the method for 14 Å tobermorite based models, before discussing the extension to other possible base crystals.

We want to represent each unit cell with as small a repeat unit as possible, similar to that chosen for crystals. However, it is important that the limits of the unit cell are well defined and that chemical units are grouped together. Consequently, we choose a primitive crystallographic unit cell with a reduced volume and the following dimensions: a_{red}: 6.735(2) Å, b_{red}: 7.425(2) Å, c_{red}: 15.325(7) Å, α: 111.34(7) °, β: 87.36(8) °, γ: 123.25(1) ° (see Figure 6 and Figure 7) The position of the cell within the 14 Å tobermorite structure is chosen such that; the $a_{red} \times b_{red}$ surface of the unit cell lies in the middle of the the calcium-silicate layers, the $a_{red} \times b_{red}$ is such that the silicate chains are cut in the middle of the silicate dimers and the $b_{red} \times c_{red}$ is between two adjacent linear silicate chains. Stacking of these primitive unit cells or building blocks will lead to the 14 Å tobermorite structure as described by [45] (see e.g. Figure S31 of the supplementary materials). An atomistic configuration file for such a unit cell can be found in the supplementary materials.

Now the chemical units and the symbols representing them have to be defined (Figure 7). Let us first consider the calcium-silicate layers of the tobermorite structure as shown in Figure 6 These layers contain two Ca-Si sheets of equal composition but different orientation, loosely related by a

glide plane symmetry. The sheets themselves are composed of linear silicate chains and a range of calcium ions. The silicate chains consist of dimers which are linked by a bridging silicate. Each silicate tetrahedra of the silicate dimer is associated with a calcium ion of the sheet. Let us define such an atom group, composed of a dimer silicate with its associated calcium and which has a stoichiometry of $CaSiO_{3.5}$ as one chemical unit. We will choose two different symbols for this unit depending on the relative position of the calcium with respect to the silica chain (above or below) and consequently on whether the unit belongs to the upper sheet of the calcium-silicate layer: < will represent a dimer silicate and the associated calcium above that silicate and > the equivalent unit with the calcium below the silicate (Figure 7). We next represent the bridging silicate with a stoichiometry of SiO_2 and zero charge by an *S*, independent of which sheet it belongs to. Additionally we have to take into account the possible protonation of the silanol groups. Let us note a protonated silanol group by an apostrophe (’), stoichiometrically representing an *H* and a charge of +1.

To be able to describe defective structures as well, a few additional units have to be defined. Firstly, in some tobermorite structures the linear silicate chains are cross-linked via the bridging silica tetrahedra. A cross-linked silica tetrahedra is indicated by a vertical line to indicate the shared oxygen: $|S$. Such a cross-linked bridging silica has a stoichiometry of $SiO_{1.5}$ and a charge of +1. Finally it is possible to replace a dimer silicate $<$ or $>$ by a calcium hydroxide unit with stoichiometry $Ca(OH)_2$ and zero charge. For this replacing unit we will again distinguish the orientation and represent it by a / if the calcium is above the hydroxyls and \ if the calcium is below. If only one of two paired $<$ is replaced, the second will no longer be part of a dimer but will be a monomer (or end-member of a chain). Such a monomer, with a stoichiometry of $CaSiO_4$ and a charge of -2, will be represented by (if the calcium is above and by) if the calcium is below the silicate.

In addition, we have to define three interlayer species: calcium ions (stoichiometry *Ca*, charge +2) are represented by *C* and hydroxyl ions (stoichiometry *OH*, charge −1) by °. Finally water molecules are represented by a number, indicating the total number of water molecules in the interlayer. The full overview of the symbols can be found in Figure 7.

Now that we have defined the symbols for each chemical group, we need to define the string of symbols defining the arrangement of these groups within the unit cell. To do so, we will specify the groups within the unit cell layer by layer first in b_{red} direction (left to right in Figure 7) then in $-c_{red}$ direction (top to bottom in Figure 7) Thus, we will start with the calcium-silicate sheet above the interlayer. For a non-defective 14 Å tobermorite we have

Code	Unit	Stoichiometry	Charge	Code	Unit	Stoichiometry	Charge
Ca-Si sheet above interlayer				Ca-Si sheet below interlayer			
<		$CaSiO_{3,5}$	-1	>		$CaSiO_{3,5}$	-1
S		SiO_2	0	S		SiO_2	0
[S]'		[SiO]H	+1	[S]'		[SiO]H	+1
/		$Ca(OH)_2$	0	\		$Ca(OH)_2$	0
(		$CaSiO_4$	-2	)		$CaSiO_4$	-2
S|		$SiO_{1,5}$	+1	|S		$SiO_{1,5}$	+1
[		$Ca(OH)_{1,5}$	+0.5	]		$Ca(OH)_{1,5}$	+0.5
interlayer							
C		Ca	+2	°		OH	-1
1		H_2O	0				

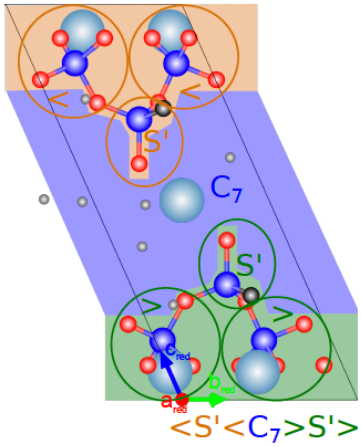

Figure 7: Definition and notation of different atom groups used for the description of different structures derived from 14 Å tobermorite (left) as well as a primitive unit cell $< S' < C_7 > S' >$ of 14 Å tobermorite with the following dimensions: a_{red}: 6.735(2) Å, b_{red}: 7.425(2) Å, b_{red}: 15.325(7) Å, α: 111.34(7) °, β: 87.36(8) °, γ: 123.25(1) °. Si: blue. Ca: turquoise, O: red, H_2O: white, OH: black.

a dimeric calcium silicate, a bridging silicate and a second dimeric calcium silicate in this sheet, where the calcium is above the silicate. Thus, we can represent it by $< S <$. There are two silanol groups on the bridging silicate *S*. The one to the right is protonated in 14 Å tobermorite, therefore, we will add a ' to the right of the *S*: $< S' <$. This part of the string fully describes the Ca-Si sheet above the interlayer. Now we add the interlayer. Here, we have one calcium ion (*C*) and 7 water molecules (7). Thus, the string for the top Ca-Si sheet and the interlayer becomes: $< S' < C_7$. Finally, the Ca-Si sheet below the interlayer is equivalent to the top sheet, except for the orientation of the dimeric species: $> S' >$. This means that for a full unit cell of pristine 14 Å tobermorite our building block string is: $< S' < C_7 > S' >$.

We can now consider different possible defects within 14 Å tobermorite. A simple defect would be to deprotonate two silanol groups and compensate the charge by an additional calcium ion in the interlayer: $< S' < C_7 > S' > \rightarrow < S < CC_7 > S >$ (Figure 8). Similarly, the inverse is also possible, leading to a structure with no calcium in the interlayer:

$< S' < C_7 > S' > \rightarrow < 'S' <\ _7 > 'S' >$. Additionally, we can cross-link the silicate chains via the silanol group to the left of the bridging *S*, again leading to Ca-Si layers without a charge and thus, no calcium in the interlayer: $< S' < C_7 > S' > \rightarrow < |S' <\ _7 > |S' >$.. However, the latter is only

possible if we change the geometry of the unit cell, such that the cross-linking is geometrically possible (see section 4.5.1).

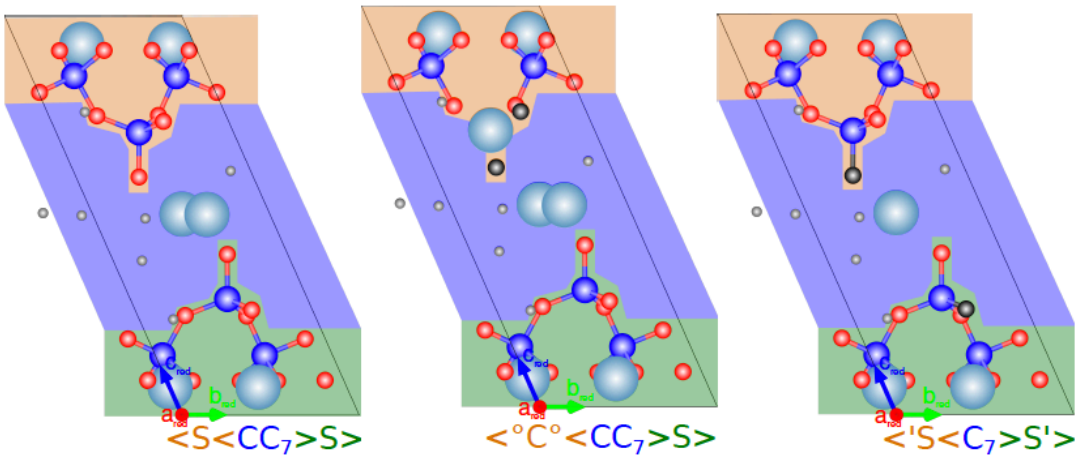

Figure 8: Different possible defective building blocks of 14 Å tobermorite (dimensions: a_{red}: 6.735(2) Å, b_{red}: 7.425(2) Å, c_{red}: 15.325(7) Å, α: 111.34(7) °, β: 87.36(8) °, γ: 123.25(1) °): from left to right: deprotonation, charge compensated by calcium: $< S < CC > S >$, depolymerisation of the silicate and additional $Ca(OH)_2$: $< {}^{o}C^{o} < CC > S >$ and exchange of proton between silanol groups: $< {}'S < C > S' >$. Si: blue. Ca: turquoise, O: red, H_2O: white, OH: black

Another reported defect [4] is a missing bridging silicate: $< S' < C_7 > S' > \rightarrow < {}' < C_9 > S' >$. If a silicate unit is missing, the silanol groups are transferred to the neighbouring silicate groups (one per neighbour). This means that the same sequence of protonation as for the non-defective chains are possible: $<' {}' < {}_9 > 'S' > \rightarrow < {}' < C_9 > S' > \rightarrow < < CC_9 > S >$. A missing *S* can also be replaced by a calcium (*C*). Such a calcium or any calcium in the interlayer may be partially charge compensated by a hydroxyl group. For example, a bridging silicate in a fully deprotonated silicate chain being replaced by a calcium and two hydroxyls can be denoted as: $< S' < CC_7 > S > \rightarrow < {}^{o}C^{o} < CC_7 > S >$ (Figure 8). Also, additional calcium hydroxide units can be added to the interlayer, maybe at the same time reducing the number of water molecules: $< \mathrm{S}' < \mathrm{C}_7 > \mathrm{S}' > \rightarrow < \mathrm{S}' < {}^{\mathrm{o}}\mathrm{C}^{\mathrm{o}}\mathrm{C}_5 > \mathrm{S}' >$

Finally, where the *S* have already been removed, there is also the possibility of defect clusters involving the silicate dimers of two consecutive building blocks in b_{red} direction. For example, one possibility would be the substitution of a silicate dimer (<<) by two $Ca(OH)_2$ units (/ /), maybe increasing the number of water molecules at the same time to fill up the interlayer:

$< \ ' < C_7 > S' > < \ ' < C_7 > S' > \rightarrow < \ /C_{11} > S' > / < C_{10} > S' >$. In theory it would also be possible to remove a single silicate of the dimer, and thus creating an end-chain silicate: $< \ ' < C_7 > S' > < \ ' < C_7 > S' > \rightarrow < \ /C_{10} > S' > \ (' ' < C_7 > S' >$. The extra ' is necessary to preserve charge neutrality as can be seen from Figure 7. A number of possible defects are schematically illustrated in Figure 9.

Finally, to give the stacking of these building blocks we again first give the sequence in b_{red} direction:

$$\ldots < S < CC_7 > S > \ < S' < CC_{11} > \backslash \ < S' < C_{10} \backslash > \ldots$$

This means that we keep together the building blocks forming the same linear silicate chains. In this way, the geometry of one silicate chain can easily be found by looking at only one of the Ca-Si sheets in the building blocks: ...< S < < S' < < S' <… or ... > S > >\\>… Next, we will indicate stacking in a_{red}direction (back to front in Figure 7) by consecutive lines of building block sequences. This will keep the units from the same Ca-Si sheets together. Finally stacking in $-c_{red}$ direction is shown by consecutive paragraphs. For example, a structure comprising 3 x 3 x 2 units we have:

<S<CC7>S> <S'<C11> \ <S'<C10\ >
<S<CC7>S> <S'<C7>S'> < '<C8>S'>
<S'<C7>S'> <S'<C7>S'> <°C°<CC7>S >

<S'<C7>S'> <S'<C7>S'> <°C°<CC7>S >
<S<CC7>S> <S<°C°CC5>S> <S'<C7>S'>
<S'<C11> \ <S'<C10\ > <S<CC7>S>

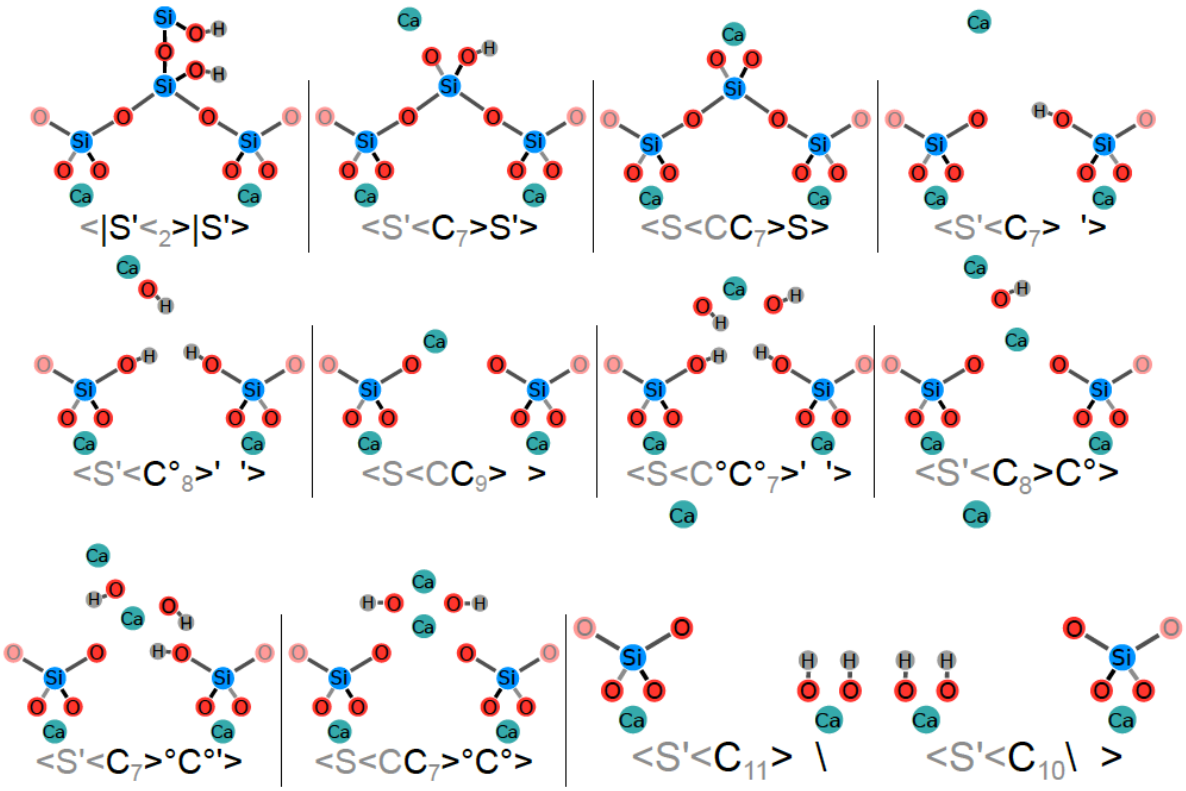

Figure 9: Schematic view of different 14 Å tobermorite structural defects considered leading to changing $\frac{Ca}{Si}$ *ratio. The (mostly) unchanging upper part of the unit cell and the water molecules are not shown on the schematics. Si: blue. Ca: turquoise, O: red,* H_2O*: white, OH: black, Semi-transparent oxygen atoms (O): shared oxygen atoms between the silicate dimers forming the Si-O-Si bond as seen in Figure 6.*

(ii) Disorder and Stacking Faults

The unit cell defined here is closely related to the MDO2 C centered *a', b', c'* unit cell defined by Bonaccorsi et al. [45], with $a_{red} = a'$, $b_{red} = b'$ and the origin situated at the center of the unit cell. Only the c_{red} parameter defined here differs. It is almost equal to the stacking vector t_1 defined by Bonaccorsi et al., but with b_{red} added ($c_{red} = 0.5 \cdot (c' - a') - b'$), to be able to take into account the ions shared between the two adjacent calcium-silicate layers. However, this definition corresponds to one of two possible positions of the calcium ion in the interlayer region. The other one gives rise to a unit cell with $c_{red,2} = 0.5 \cdot (c' - a') + b'$ (see Figure 10). According to Bonaccorsi et al., these two calcium positions in the interlayer are present each at about 50 %. Since we are noting the species within the unit cell layer by layer in b_{red} direction, in this second unit the Ca-Si sheet below the interlayer will be first, followed by the interlayer and the Ca-Si sheet above the interlayer. This leads to building bricks of the form: $> S' > C < S' <$ (Figure 10). In order to preserve the same calcium-silicate layer structure, the two possible unit cells have to be shifted by

$b'/2$. This could, for example, correspond to alternating layers with different calcium positions (Figure 10). It is also possible to shift from one type of unit cell to another within one and the same layer (see Figure S32 of the supplementary material). Due to the shift in origin between the two types of unit cells, a transition building block with only a part of the upper chain, e.g. $< \mathrm{S} < \mathrm{C}_3$, is needed between a $< \mathrm{S}' < \mathrm{C}_7 > S' >$ and a $> \mathrm{S}' > \mathrm{C}_7 < \mathrm{S} <$, to complete the upper calcium-silicate layer.

Similarly, if the two types of unit cells are inverted, a $> \mathrm{S} > \mathrm{C}_3$ transition unit cell is needed in-between to complete the lower calcium-silicate layer. The origin of these transition unit cells is displaced by $0.75 \cdot b_{red}$ compared to the full unit cells.

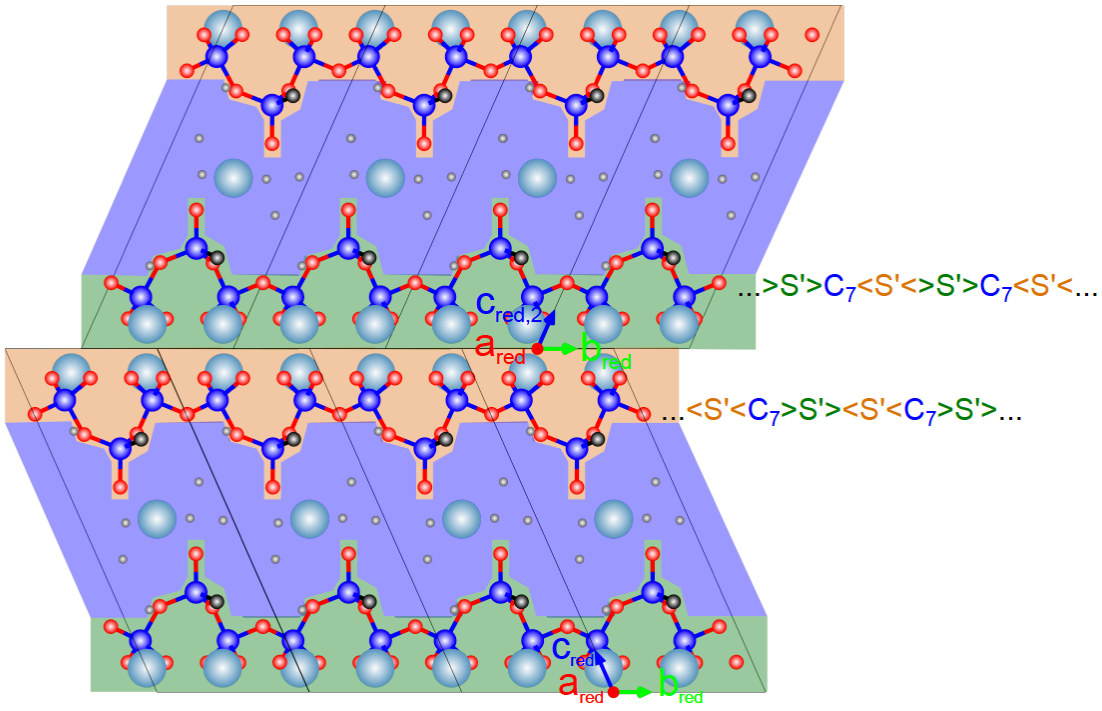

Figure 10: Alternate layers with $a_{red} = a'$, $b_{red} = b'$, $c_{red} = 0.5 \cdot (c' - a') - b'$ *and* $a_{red,2} = a'$, $b_{red,2} = b'$, $c_{red,2} = 0.5 \cdot (c' - a') + b'$ *unit cells respectively..*

Apart from the disorder coming from the position of the calcium in the interlayer, in their original description of the 14 Å tobermorite structure Bonaccorsi et al. [45] also discuss the extensive presence of stacking faults in the structure. The authors mention that there are two possible ways of stacking which lead to a slightly different symmetry of the calcium silicate layers: in addition to the stacking described above, where layers with the same orientation are stacked without any shift of the origin (t_1), there is also a stacking sequence (t_2), where the origin is shifted by $b_{red}/2$. This leads

to calcium silicate layers where bridging silicate tetrahedra on either side of the calcium silicate layer are only displaced by $a_{red}/2$ but not in the b_{red} direction (see Figure S33 of the supplementary material), in contrast to the t_1 stacking where the bridging silicate on either side of the calcium silicate layer are also shifted by $b_{red}/2$ (see Figure 10). We propose to indicate a t_2 stacking sequence by a *T* at the beginning of the layer. Bonaccorsi et al. report that random sequences of t_1 and t_2 stacking were observed experimentally with no marked preference or long scale order. However, the refinement of the structure presented by Bonaccorsi et al. could only be done for the t_1t_1 stacking sequence.

The defects described above can exist in all the different types of unit cells. All the cells described above, including the transitional units, can be found in the supplementary material. With these units it should be easy to construct a wide range of different possible larger scale structures with different amount of order and defects.

(iii) Surfaces

Due to the nanosized nature of C-S-H, surfaces are likely to be very important. There are two directions in which surfaces can be constructed with the units already defined. The first one is the (100) and the (-100) surface (1-10) according to the unit cell defined by Bonaccorsi et al. [45]) . In this direction the silicate chains run parallel to the surface and consequently do not have to be cut (see Figure S34 of the supplementary information). In fact we can use the $<\mathrm{S}'<\mathrm{C}_7>S'>$ or the $>\mathrm{S}'>\mathrm{C}_7<\mathrm{S}<$ (or any defective version of it) directly for the construction of these surfaces. Depending on the direction ($\vec{b}\times\vec{c}\ or\ -\vec{b}\times\vec{c}$) of the surface normal, either a (100) or a (-100) surface is created. The fact that the two surfaces differ is easiest to see when considering the orientation of the hydrogen in the *S'* group (figure 4 of the SI). In the case of the (100) surface, the hydrogens at the surface point in the direction of the surface normal whereas for the (-100) they point towards the bulk of tobermorite.

Another surface which is easy to construct is the surface perpendicular to the calcium-silicate layers i.e. the (001) surface (same miller index for Bonaccorsi et al. notation [45]). This surface is in all probability cut at the interlayer, consequently it can be constructed using the $<\mathrm{S}<\mathrm{C}_3$ or the $>\mathrm{S}'>\mathrm{C}_3$ units, depending on the orientation of the surface (see SI Figure S34). For a (010) surface, the (012) according to Bonaccorsi et al. [45], the silicate chains will be cut. To remain consistent with the silicate speciation reported in literature, this could be done using $<'\ >'$ units to complete the dimers on either side of the interlayer. For surfaces other that the ones described above, the definition of additional surface units would be necessary.

(iv) Extension to other calcium-silicate structures

In the section above we have focused on 14 Å tobermorite. However the notation can easily be extended to other layered calcium-silicate structures. Since the other tobermorite structures (9 Å and 11 Å normal and anomalous tobermorite as well as clinotobermorite [59, 36], see Figure S31 of the supplementary material) contain essentially the same calcium-silicate layers, they can be described with the same notation as introduced above. Only the unit cell needs to be redefined for each structure. As an example, anomalous 11 Å tobermorite is represented by $< |\mathrm{S}' <_{5} > |S' >$ and clinotobermorite by $< |\mathrm{S} < \mathrm{C}_5 > |S >$. The unit cells for 11 Å normal tobermorite, the Hamid 11 Å tobermorite as well as clinotobermorite, which can be used to construct C-S-H structures according to the notation above, can be found in the supplementary materials (Figure S31).

For jennite there are additional $Ca(OH)_{1.5}$ groups in the calcium-silicate layer. We propose to designate them by *[* or *]*, depending on the orientation of the calcium-silicate chains. Such a group has a charge of +0.5. In other words jennite can be represented by $[< \mathrm{S}[< \mathrm{C}_8 >]S >]$ and the corresponding unit cell.

4.6 Characterisation of Previous C-S-H Models

Our approach can also be used to re-examine different C-S-H models previously described in the literature. However, comparison requires a reasonable description of the underlying structure. For the first full scale model reported in literature [21], the authors did not take into account the known silicate speciation to obtain their high calcium to silicon ratio. This lead to very high strains in the structure upon relaxation and to the adsorption of water in the intralayer space. The resulting structure has little resemblance to tobermorite which does not allow us to fully characterize their model. Also in their further work [31], no atomistic configurations were published, so we cannot reconstruct the C-S-H "DNA" used based on the published data. Fortunately, Kovačević et al. [32] provides all relevant data and consequently we can use one of their sample structures to further illustrate our building-block description of C-S-H. However, discussion is limited to the original paper as no atomistic configurations are available for the revised structures reported later [34].

Kovačević et al. used the 11 Å normal tobermorite reported by Merlino et al [36] as a model structure, this means their model can be described using the corresponding primitive crystallographic unit cell (reported in the supplementary materials: 11_a_norm_tobermorite.config) as the basis for building blocks. Their Sample 1 structure, corresponding to one of the lowest energy family of structures, has been divided into 4x4x2 building blocks with dimension a: 7.28 Å, b: 7.68 Å, c:

12.42 Å, α: 81°, β: 107°, γ: 122°. Some of the interlayer water molecules, hydroxyl or calcium ions could be assigned to either of two neighbouring cells. However, this assignment is not so important as it does not significantly change the overall properties of the structure. The final description of their structure can be seen in Figure 11.

Based on our proposed building-block description, we can now calculate different properties of their model. The stoichiometry of the sample structure can be calculated using equation (38) (where n_X is the number of the units of type *X* (see Figure 7 for the list of symbols), different symbols for different orientations are taken together, i.e. $n_<$ is the total number of $<$ and $>$: the resulting stoichiometry is $\mathrm{Ca}_{1.68}\mathrm{Si\ O}_{3.7} \cdot 2.2\ \mathrm{H_2O}$.

$$\mathrm{Ca}_{\kappa_1}\mathrm{Si\ O}_{\kappa_2} \cdot \kappa_3\ \mathrm{H_2O} \tag{38}$$

Where,

$$\kappa_1 = \frac{n_< + n_C + n_/ + n_(}{n_< + n_S + n_(} \tag{39}$$

$$\kappa_2 = \frac{3.5 \cdot n_< + 2 \cdot n_S + 4 \cdot n_(- 0.5 \cdot n' + 0.5 \cdot n_o + n_/}{n_< + n_S + n_(} \tag{40}$$

$$\kappa_3 = \frac{0.5 \cdot (n' + n_o) + n_/ + n_{H_2O}}{n_< + n_S + n_(} \tag{41}$$

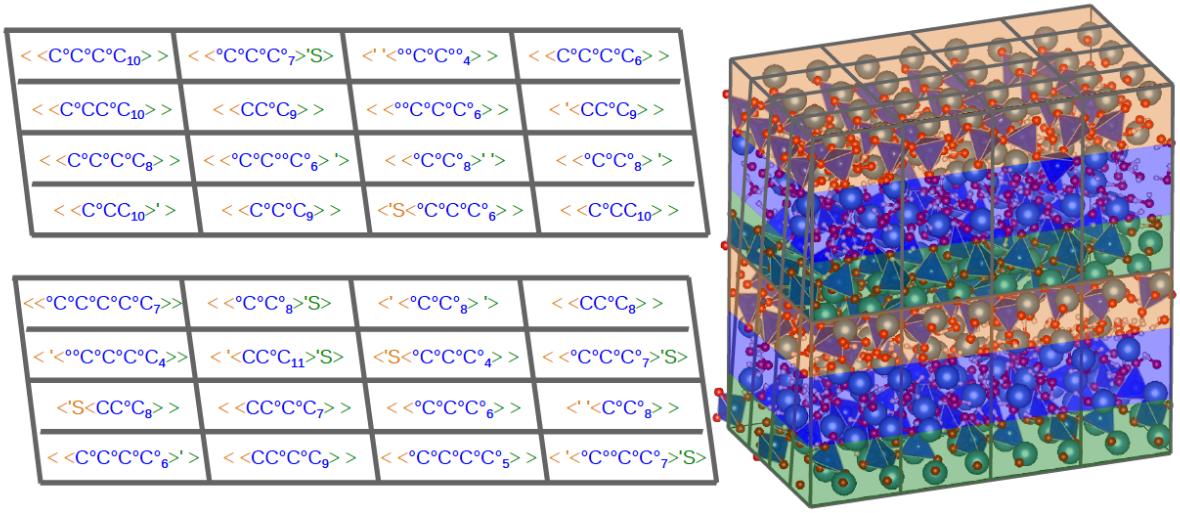

Figure 11: Sample structure (Sample 1) of Kovačević et al as reported in [32] described with the newly proposed notation (left) and representation of the full atomic structure (right). For a larger image of the atomic structure see the supplementary materials or the original paper for the full atomic configuration.

Another quantity that can be easily calculated is the mean chain length *MCL*. The number of silicate chains corresponds to half the number of silicate chain ends (where a monomer counts double) as every silicate chain has two end units. This leads to equation (42) which for the Kovačevič model 1 structure gives a mean chain length of 2.4.

$$MCL = \frac{n_{<} + n_S + n_(}{0.5 \cdot n_{<} - n_S + n_(} \tag{42}$$

There are no silicate monomers in the Kovačevič structure (Figure 11); the structure consists entirely of dimers and longer chains. The ratio between dimers and longer chains depends on the spacial arrangement of the different units and hence cannot be calculated via a generally applicable formula. Rather the number of dimers and longer chains in the structure have to be counted explicitly. If we look for instance on the front most silicate chain of the upper chain of layer 1 of the sample structure we get the following: $< << <<'S << <$. This means that, if we suppose the structure to be periodic and hence repeating, there are two dimers per pentamer in this chain. In this way we can identify the total number of dimers (48) and longer chains (8) in the structure. The percentage of dimers (86 % of all chains) is higher than that measured for OPC systems (60 % [6]) and the mean chain length is shorter than that indicated from experimental data (around 3 for fresh

cement [4]). However, in the revised model Kovačević et al. report a slightly lower percentage of dimers of 72 % [34].

We can also calculate the extent of silanol protonation Q_{prot} (equation (43) 18 % of the silanol groups in the structure are protonated. This is very high compared to the very small or negligible amount of protonated silanol groups reported in the literature for the high $\frac{Ca}{Si}$ ratio of 1.68 [11, 22]. Similarly, the percentage of the charges of the calcium ions that is compensated by hydroxyl groups Q_{comp}^{OH} (equation (44) is calculated to be: 21 % of the charge of the calcium ions which is compensated by hydroxyl groups in the interlayer. This is consistent with experimental measurements [23]. Some of these hydroxyl groups are likely to be formed upon the splitting of water where a hydrogen is donated to a silanol group. This indicates that, in order to reach both the correct hydroxyl and protonated silanol groups concentration, more hydroxyl has to be introduced implicitly in the interlayer.

$$Q_{prot} = \frac{n'}{n_{<} + 2 \cdot n_{(}} \tag{43}$$

$$Q_{comp}^{OH} = \frac{n_o + 2 \cdot n_{/}}{2 \cdot (n_{<} + n_C + n_{/} + n_{(})} \tag{44}$$

Another interesting property to consider is the distribution of charges within the model. The total charge of each unit cell has been calculated based on the building block description equation (45), where Z_X is the charge of unit *X*). Although the overall structure is charge neutral, we can observe significant charge fluctuations for this Sample 1 structure reported by Kovačević et al. For example in the third column from the left (Figure 11) we calculate that a total of -8 e is building up in the upper and -5 e in the lower layer (see supplementary material). We can consider this as a plane with a charge of 1.75 e/nm^2 which is gradually compensated over a distance of 24 Å on either side (i.e. the distance between subsequent charged layers). While charge fluctuations are likely to occur, their magnitude and length scale are likely to be restricted due to the associated Coulombic energy penalty. As no information on the charge fluctuations in C-S-H is currently available, this warrants further study. It would be interesting to see whether these charge fluctuations remained even after the more stringent relaxation procedure used for the revised model of Kovačević et al. [34].

$$Z_{tot}^{bblock} = \sum_{X\epsilon\{<,S,C,H_2O,',o,/,(,\dots\}} n_X \cdot Z_X \quad (45)$$

4.7 Development and Discussion of 14 Å Tobermorite Based C-S-H-Model

4.7.1 Structural Properties

The development of atomistic models for C-S-H has so far mostly been focused on 11 Å tobermorite structures [21, 31, 32]. As noted above, the reasoning for this was mostly the interlayer distance is closer to the one measured for real cements (11-12 Å), and indeed the model structure reported by Kovačević et al. and discussed above [32] has an interlayer distance of 11.87 which is consistent with values reported in the literature, although some scatter and controversy about the influence of sample preparation exists [16, 33, 11, 27]. From a compiled dataset of interlayer distance measurements via XRD, Richardson [33] observed that the interlayer distance of C-S-H decreases from ~13- 14 Å at $\frac{Ca}{Si}$ = 0.8 to ~10 Å at $\frac{Ca}{Si}$= 1.5. Recently, Roosz et al. [60] has shown that severe drying conditions during sample preparations can underestimate the interlayer distance measurement using XRD by about 2.8 Å for a C-S-H of $\frac{Ca}{Si}$= 1.2 having an interlayer distance of 12.5 Å in the fully hydrated state. It seems difficult to reconcile an underlying 11 Å tobermorite structure with the decrease of the interlayer distance observed for C-S-H with increasing $\frac{Ca}{Si}$ ratio. Also the interlayer distance is likely to relax more readily than the calcium-silicate layers. All in all it seems therefore a reasonable assumption that, at least for lower $\frac{Ca}{Si}$ ratios 14 Å might be an equally valid or better base structure than the 11 Å tobermorites. Therefore we consider possible 14 Å tobermorite based C-S-H models and compare them to the pre-existing models using the formalism described above.

Richardson recently published some guidelines for the construction of new models, based on summarized properties of different experimentally determined tobermorite structures [33]. Based on the geometry of possible oxygen environments in the crystals and the change of the interlayer distance he concluded that the best model structure for C-S-H is clinotobermorite. However no further relaxation of the structure other than a change of the interlayer distance was considered. Also part of the measurements found in literature was excluded based on the hypothesis that the larger interlayer distances found were due to an intermixture with calcium hydroxide like phases leading to a higher $\frac{Ca}{Si}$ ratio than is actually observed for the C-S-H phase. However this hypothesis does not seem to be entirely validated and other hypotheses can be put forward to explain different

interlayer distances, such as different underlying tobermorite model structures depending on the exact conditions under which the C-S-H was formed.

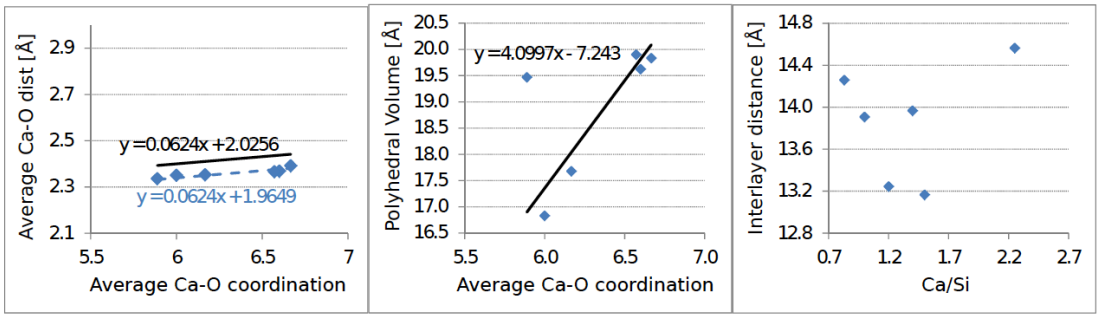

Figure 12: Structural properties of different (defective) tobermorite structures derived from 14 Å tobermorite as calculated by DFT: $< S' < C_7 > S' >$, $< S < CC_7 > S >$, $< S < {}^{o}C^{o}C_7 >'' >$, $< S < CC_7 > {}^{o}C^{o} >$, $< {}^{o}C^{o} < C_9 >'' >$, $< {}^{o}C^{o} < C\,{}^{o}C^{o}C_7 > {}^{o}C^{o} >$, $\frac{Ca}{Si}$ *0.83, 1.0, 1.2, 1.6 1.5 and 2.25 respectively. Trends reported by Ian Richardson shown in black [33]*

To confirm the hypothesis, that other tobermorite model phases cannot *a priori* be excluded, DFT minimizations of a periodically repeated single, defective building block of 14 Å tobermorite [45] structures with varying $\frac{Ca}{Si}$ ($< \mathrm{S}' < \mathrm{C}_7 > S' >$, $< \mathrm{S} < \mathrm{CC}_7 > S >$, $< \mathrm{S} < {}^{o}\mathrm{C}^{o}\mathrm{C}_7 >'' >$, $< \mathrm{S} < \mathrm{CC}_7 > {}^{o}C^{o} >$, $< {}^{o}C^{o} < \mathrm{C}_9 >'' >$, $< {}^{o}C^{o} < \mathrm{C}\,{}^{o}C^{o}C_7 > {}^{o}C^{o} >$) were relaxed and characterized structurally according to the characteristics defined by Richardson [33]. As one can see from the building block description, the number of oxygen atoms in the structure was kept constant, removal of, for example, a silicon tetrahedron being compensated by the addition of either water or hydroxyl molecules.

For the non-defective 14 Å tobermorite ($< \mathrm{S}' < \mathrm{C}_7 > S' >$), the interlayer distance is only overestimated by about 0.3 Å compared to the experimental structure (see Table 4) and the average Ca-O distance is underestimated by 0.06 Å (see Figure 12), giving us confidence in the DFT calculated structures. The Average Ca-O coordination and distances as well as the polyhedral volume is entirely consistent with the structural integrity checks suggested by Richardson [33], except for the highest $\frac{Ca}{Si}$ ratio studied here ($< {}^{o}C^{o} < \mathrm{C}\,{}^{o}C^{o}C_7 > {}^{o}C^{o} >$). If we accept the result of the integrity check, this indicates either that the DFT calculations found an unfavorable local minimum or that this defect structure is not present in this form or only in low concentrations. In addition, up to a $\frac{Ca}{Si}$ of 1.2 the coordination number decreases from 6.6 to 6. This is consistent with

the reported decrease of the coordination number reported by Soyer-Uzun et al. [27]. However, for $< {}^{o}C^{o} < \mathrm{C_9} >'' >$ ($\frac{Ca}{Si}$: 1.5) the coordination number is again 6.7.

Both the deprotonation ($< S' < \rightarrow < S < 0.5C$) and the removal of a silica tetrahedron ($< S' < \rightarrow <'' <$) results in a decrease in the interlayer distance. In contrast, the replacement of a silica tetrahedron with a calcium group ($< S' < \rightarrow < C^{o} <$) does not seem to have an influence on the interlayer distance, while the addition of calcium hydroxyl groups to the interlayer ($ {}^{o}C^{o}$) leads to an increase in the interlayer distance. Taking into account the accuracy of the method, as well as the limited number of structures considered (e.g. the water content has not been varied at all) the results, at least up to a $\frac{Ca}{Si}$ of 1.2 are entirely consistent with the trends reported by Richardson et al. [33] (see Figure 12). The interlayer distance, although at the upper range of the measured experimental data reported [33] decreases linearly for the structures $\frac{Ca}{Si}$ < 1.2 and even the $< {}^{o}C^{o} < \mathrm{C_9} >'' >$ structure with a $\frac{Ca}{Si}$ of 1.5 has a reasonable, although slightly higher than expected interlayer distance of 13.2 Å. Additionally, the interlayer distance might be further decreased by decreasing the number of water molecules in the unit cell.

This is the first time a decrease in the interlayer distance with increasing $\frac{Ca}{Si}$ from 0.83 to 1.2-1.5 as observed experimentally was predicted by atomistic simulations. In addition, the structures conform with the structural guidelines proposed by Richardson [33]. Even though the decrease in interlayer distance is somewhat less than expected, we conclude that 14 Å tobermorite should be further considered as a model structure for C-S-H at the very least for low $\frac{Ca}{Si}$. However to further explore this route, larger scale defects and larger scale structures should be considered. Consequently in the next section, $\frac{Ca}{Si}$ increasing defects in larger scale structures are studied with molecular dynamics and compared to the results in this section.

4.7.2 Structure and Energies of Defective Building Blocks

In the preceding section, a single building block ($< S' < \mathrm{C_7} > S' >$) is used for DFT calculations. This means that the defect concentrations are very high and will be strongly interacting, which will reflect in the DFT results. Consequently, to assess the energy and properties of non-interacting defects an isolated defective building block in a supercell of 4x3x2 14 Å tobermorite building blocks ($< S' < \mathrm{C_7} > S' >$) is considered, resulting in a simulation cell of 27x21x28 Å. Classical MD was used to take advantage of dynamics and its rapid calculation of interatomic forces to efficiently probe the energy landscape, and thus, evaluate the relaxation of larger scale structures compared to DFT.

Additionally, to start addressing the large structural disorder seen in tobermorite structures - leading to positional disorder, stacking faults and polymorphism - a second structure was investigated in addition to the $< \mathrm{S}' < \mathrm{C}_7 > S' >$ 14 Å tobermorite reported by Bonaccorsi et al. [45]. For the second 14 Å polymorph ($< \mathrm{S}' < \mathrm{C}_7 > S' >$ the orientation of the protonated silanol group is different on either side of the interlayer, leading to a different orientation of the silicate tetrahedron, similar to that observed for clinotobermorite (see Figure S31 of the supplementary materials).

Structural Relaxation within the Building Blocks:. A substantial amount of relaxation was observed in the interlayer. Both the positions of the ions and the water molecules in the interlayer as well as the orientation of the silicate tetrahedron changed significantly during relaxation [61]. Consequently, choosing the exact starting position of the species in the interlayer does not appear to be critical that, e.g., a $< {}^{o}C^{o} < \mathrm{CC}_7 > S >$ unit will be equivalent to a $< \mathrm{C} < {}^{o}C^{o}\mathrm{C}_7 > S >$ unit. However, if more complicated structures are studied, this point needs to be verified, and a more detailed search of configurational space is required to identify the relevant local and global minima.

The structure of the silicate layers, on the other hand, does not relax as readily. In particular, due to the low symmetry of the system, the positioning of the hydroxyl groups on the two available sites is not equivalent. This means that a $< {}'\mathrm{S} < \mathrm{C}_7 > S' >$ unit is not equivalent geometrically to a $< \mathrm{S}' < \mathrm{C}_7 > S' >$ unit. In fact, the first corresponds to the polymorph used for some of the calculations as described above. Similarly a $< {}' < \mathrm{C}_7 > S' >$ unit is not equivalent to a $<' < \mathrm{C}_7 > S' >$ unit, even after extensive relaxation. Also the relaxation of the whole structure can be very important. Depending on the energy minimization and relaxation path, the structure can relax to a different minimum with a different hydrogen bonding network and will no longer relax to the more pronounced minimum even after more than 1 ns of molecular dynamics. In Table 5 the different energies of two differently relaxed $< \mathrm{S}' < \mathrm{C}_7 > S' >$ structures can be seen. This underlines the importance of testing a number of different structures and extensive structure relaxation to get a realistic estimation of the structure and energies. In this context, the current results, especially for the classical atomistic calculations, are meant as an initial point. A more in-depth study of these effects is currently under way and results will be presented in a separate article.

Defect Energies:. The enthalpy of the different defects are difficult to compare, not least due to their different stoichiometries. Consequently, the raw energies are converted to reaction enthalpies, by calculating the enthalpy of formation from quartz (SiO_2), lime (CaO) and water (H_2O) (9).

$$n_1 \cdot CaO + n_2 \cdot SiO_2 + n_3 \cdot H_2O \rightarrow [(CaO)_{n_1}(SiO_2)_{n_2}(H_2O)_{n_3}]_{tob} \quad (46)$$

For the atomistic MD calculations, a correction had to be used for any $H_2O + O \rightarrow 2 \cdot OH$ occurrences [56]. Generally, reaction enthalpies are given per unit or mole of product. However, as there is no clear structural unit of C-S-H and its stoichiometry is variable, the notion of a mole or unit of C-S-H is not well defined. Therefore, in the literature energies are generally normalized per silicon [32]. The disadvantage of such a normalization is that this makes the reaction enthalpy undefined for silica free phases such as portlandite, the comparison of which with C-S-H is however often interesting. Therefore, we chose another way to normalize the energy by fixing $n_1 + n_2 + n_3 = 1$. While it is not possible to directly compare energies of C-S-H structures with different stoichiometries, it makes it easy to estimate relative stabilities using possible reactions between different structures.

Table 5 shows the defect energies for a series of more than 10 different defects with different $\frac{Ca}{Si}$ ratios. All the defects shown are energetically stable (negative enthalpies) compared to pure CaO, SiO_2 and water for the configurations studied (i.e. an isolated defect in a block of 24 unit cells for MD calculations). The enthalpies have been calculated for both polymorphs considered here: ($< {}'\mathrm{S} < \mathrm{C}_7 > S' >$ and $< \mathrm{S}' < \mathrm{C}_7 > S' >$). The enthalpies for the same defect are very similar in both structures (see Table 5). The differences between the structures are smaller than the expected errors for all defect energies. This again confirms the hypothesis that there will be some structural variety for C-S-H, similar to the polymorphism and order-disorder character observed for tobermorites [36, 45, 59].

Where possible, the defect energies calculated with classical molecular dynamics have been compared to the DFT calculations described in Section 4.7 (Table 5). As mentioned before, a single building block with half the volume of the original tobermorite unit cell is used to do all the DFT calculations. This means that the defects are strongly interacting and consequently the DFT results are not necessarily expected to be equivalent to the classical molecular dynamics results, where defects are considered to be non-interacting as isolated defects in an non-defective 14 Å tobermorite matrix. However, the results are generally in relatively good agreement. The biggest difference is observed for the ${}^{o}C^{o}{}_{3.5} >' ' >$ defect. For this defect, large structural relaxations were observed leading to a decrease of the interlayer distance to 13.24 Å (see Figure 12). For an isolated defect on the other hand, the interlayer distance is fixed by the surrounding non-defective

structure. Consequently, the energy of the isolated defect is expected to be less favorable, which is what is observed (Table 5).

As mentioned above, the energies themselves can only be directly compared between defects with the same stoichiometry. What is observed when comparing defects with equivalent stoichiometry (i.e. $< \mathrm{S}' < \mathrm{C}_9 > \ ' >$ with $< \mathrm{S}' < \mathrm{C}^{o}{}_8 > \ ' \ ' >$ as well as the series $< \mathrm{S} < \mathrm{CC}_9 >> \ , < \mathrm{S} < C^{o}\mathrm{C}^{o}{}_7 >' \ ' >, < \mathrm{S}' < \mathrm{C}_8 > C^{o} >$ and $< \mathrm{S}' < \mathrm{C}_7 > \ ^{o}C^{o} \ ' >$) is that defective structures with deprotonated silanol groups are preferred. This is consistent with experimental observations, where a decrease of the concentration of protonated silanol groups is observed with increasing $\frac{Ca}{Si}$ ratio [22, 11]. Also at a $\frac{Ca}{Si}$ ratio of 1.2, an additional calcium ion in the interlayer ($< \mathrm{S} < C^{o}\mathrm{C}^{o}{}_7 >' \ ' >$) seems to have a very similar energy to a calcium ion substituting a bridging silica ($< \mathrm{S}' < \mathrm{C}_7 > \ ^{o}C^{o} \ ' >$), although the two defects are structurally distinct. This second defect has often been omitted from previous modelling of C-S-H [21, 31, 32] yet has been shown to be important by Kumar et al [13].

Another property we can look at is the local charge neutrality of the structure. All, except one of the building blocks discussed above, (6.7 x 6.2 x 14.0 Å before relaxation) are charge neutral. Consequently, any larger structure constructed from those units will also be charge neutral. However, in reality, charged building blocks may also exist, compensated by a space charge region. Consequently, we have looked at charged units in one instance: in addition to the charge neutral defect $< \mathrm{S} < \mathrm{CC}_7 > S >< \mathrm{S}' < \mathrm{C}_7 > S' >$, we have also looked at an equivalent defect, where the calcium ion is shared between two units: $< \mathrm{S}' < \mathrm{CC}_7 > S >< \mathrm{S} < \mathrm{C}_7 > S' >$. These charged building blocks have very similar energies (see Table 5). Thus, the building blocks do not need to be charge neutral even if the total structure is. This means the magnitude and the length scale of realistic charge fluctuations also remain to be studied.

*Table 5: Table of calculated enthalpies for different defects in 14 Å tobermorite in eV. An eV corresponds to 96.49 kJ/mol. The corresponding table in kJ/mol can be found in the supplementary materials. All the defects shown here are energetically favourable compared to pure CaO, SiO_2 and water. Although some of these defects were previously proposed to model C-S-H, this is the first time the energetic stabilities of these defect structures have been calculated. ‡ Different structure obtained from different relaxation process will not relax to the lower energy structure even after > 1 ns of molecular dynamics. $\Delta H_{reac}^{<'S<C_7>S'>}$ is for the polymorph of 14 Å tobermorite. †Note: shows large interlayer contraction. * calculated from an equivalent unit where a calcium is shared between two neighbouring building blocks: <S<CC7>S'><S'<C7>S>*

$\frac{Ca}{Si}$	Formula	n_{CaO}	n_{SiO_2}	n_{H_2O}	$\Delta H_{reac}^{<S'<C_7>S'>}$ [eV]	$\Delta H_{reac}^{<'S<C_7>S'>}$ [eV]	ΔH_{reac}^{DFT} [eV]
0.83	<S'<C_7>S'>	0.26	0.32	0.42	-0.37±0.06		-0.27
0.83	<S'<C_7>S'>‡	0.26	0.32	0.42	-0.16±0.04	-0.16±0.04	
1.00	<S<CC_7>S>	0.32	0.32	0.37	-0.30±0.04	-0.28±0.03	-0.25
1.00	<S<CC_7>S>*	0.32	0.32	0.37	-0.30±0.04	-0.34±0.03	
1.00	<S'<C_9> '>	0.25	0.25	0.50	-0.15±0.04	-0.14±0.03	
1.00	<S'<C°$_8$>' '>	0.25	0.25	0.50	-0.02±0.04		
1.20	<S<CC_9> >	0.30	0.25	0.45	-0.25±0.03		
1.20	<S<C°C°$_7$>' '>	0.30	0.25	0.45	-0.15±0.05	-0.17±0.04	-0.28†
1.20	<S'<C_8>C°>	0.30	0.25	0.45	-0.21±0.04		
1.20	<S'<C_7>°C°'>	0.30	0.25	0.45	-0.14±0.05		
1.25	<S'<CC_{10}>\<S'<$C_{10.5}$ \>	0.24	0.20	0.56	-0.26±0.04		
1.40	<S<CC_7>°C°>	0.35	0.25	0.40	-0.36±0.05	-0.31±0.04	-0.29
1.50	<°C °<C_9>' '>	0.29	0.19	0.43			-0.26†
2.25	<°C°<C°C°C_7>°C°>	0.39	0.17	0.43			-0.24
1.67	full model see Figure 14	0.39	0.23	0.38	-0.29±>0.08		

To compare the defect energies between different stoichiometries, reaction enthalpies between the different defects, and where appropriate related phases such as SiO_2 , CaO, $Ca(OH)_2$ and H_2O, should be calculated. As an example, to compare the enthalpy of $< \mathrm{S} < \mathrm{CC}_7 > S >$ and $< \mathrm{S}' < \mathrm{C}_9 > ' >$ we can look at the reaction $0.79 \cdot [(CaO)_{0.316}(SiO_2)_{0.316}(H_2O)_{0.368}]_{tob} + 0.2 \cdot H_2O \rightarrow [(CaO)_{0.25}(SiO_2)_{0.25}(H_2O)_{0.5}]_{tob}$. As the reaction enthalpy for pure water is defined here as zero, the enthalpy for this reaction is equal to $\Delta H_{reac}^{<S'<C_9>'>} - (-0.79) \cdot \Delta H_{reac}^{<S<CC_7>S>} = 0.09 \pm 0.7\ eV\ \left(8.7 \frac{kJ}{mol}\right)$, indicating that, neglecting any entropic effects, the $< \mathrm{S} < \mathrm{CC}_7 > S >$ defect appears to be slightly more favorable. However, these reaction enthalpies can be more readily estimated and trends seen if the reaction enthalpies are plotted on a ternary diagram (Figure 13). For the atomistic MD calculations, only the lowest energy for a specific stoichiometry is reported. From the ternary diagram, points lying on the straight line formed by three points or a point inside a triangle formed by three other points can be readily compared, as reactions between them can be defined. A thorough knowledge of the energy landscape within this ternary diagram would not only help immensely to understand the thermodynamic behavior of C-S-H, but would also serve as a quick check whether new theoretical atomistic models are reasonable. However, plotting the previously reported experimentally based thermodynamic models from literature (the tobermorite/jennite solid solution model from the CEMDATA thermodynamic database [62] as well as the CSH3T and CSHQ models from [63]) illustrates that more work is still needed to reach this goal. Due to the uncertainties of the atomistic structure of C-S-H, the resulting energies from the different thermodynamic models will largely depend on the underlying model assumptions. But globally, the results from the experimental models indicate that the enthalpy likely lies between -0.33 to -0.25 eV (-31.8 to -24.1 kJ/mol) with less negative energies being expected for structures containing more water.

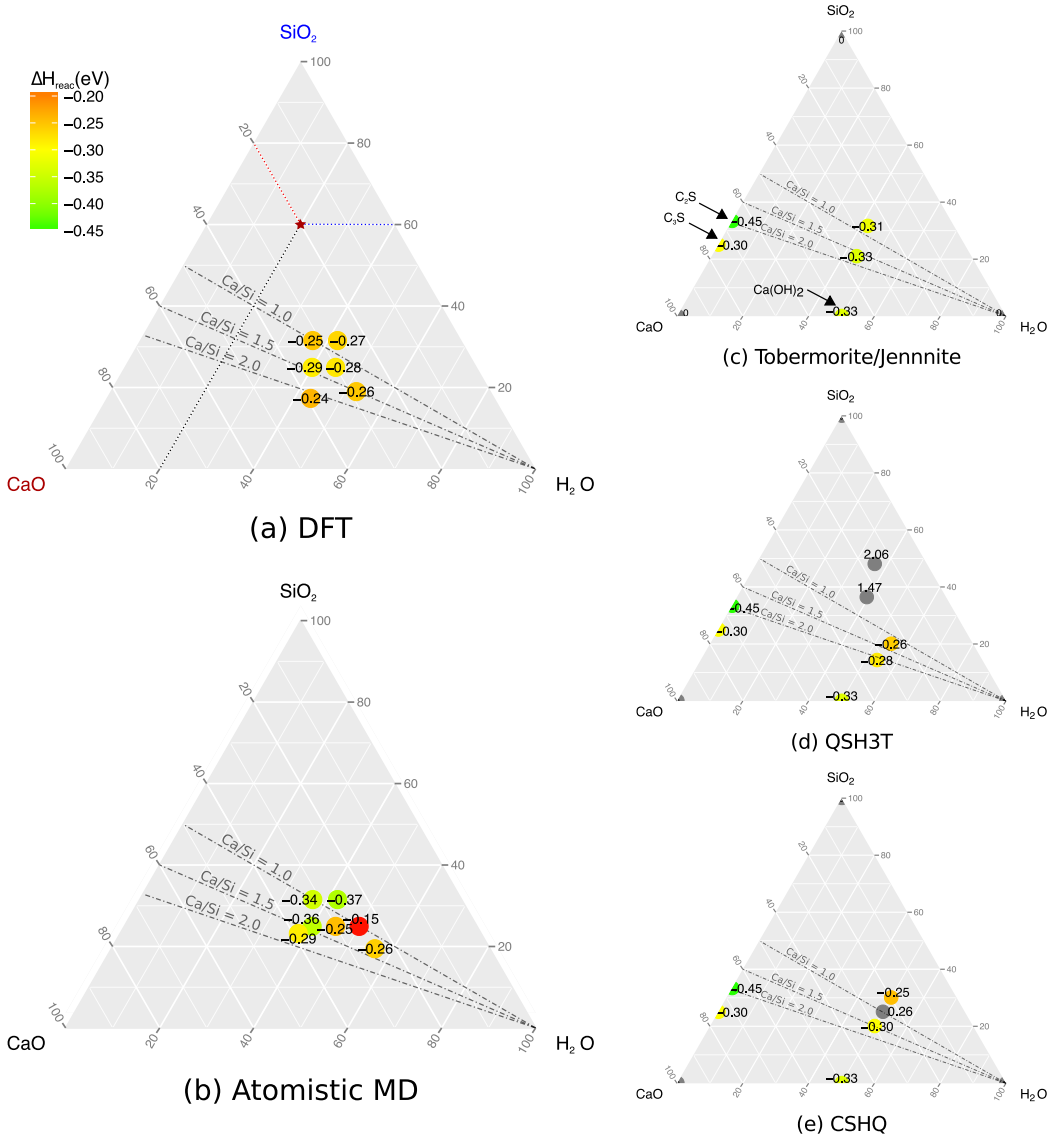

Figure 13: Variation of the calculated reaction enthalpy in eV for the building blocks considered from (a) DFT and (b) classical MD calculations compared with different thermodynamic models of C-S-H; (c) the Tobermorite/jennite solid solution model from the CEMDATA thermodynamic database [62] and (d,e) the CSH3T and CSHQ models from [63]. An eV corresponds to 96.49 kJ/mol. Important cement phases C_3S, C_2S and $Ca(OH)_2$ are also shown on (c, d and e) diagrams. The bottom edge of the ternary diagram shows increasing water content from left to right, the edge on the right hand side shows increasing silica content from bottom to top and the edge on the left hand side shows increasing lime content from top to bottom. For illustration, an example composition with stoichiometry $(CaO)_{0.2}(SiO_2)_{0.6}(H_2O)_{0.2}$ is shown in (a) (red star) together with a guide as to how to read compositions. The reaction enthalpies calculated for 14 Å tobermorite (26 % CaO, 32 % SiO_2, 42 % H_2O) from DFT, MD and the Tobermorite/Jennite model are -0.27, -0.37 and -0.31 eV respectively. Thus allowing a reliable comparison between the different techniques. Same colour scale

for the reaction enthalpy (see legend) is used for all plots, positive reaction enthalpies are shown in gray.

For both the DFT and the molecular dynamics results, the calculated energies largely follow these trends. Even for the defect comprising a missing dimer ($< \mathrm{S}' < \mathrm{CC}_{10} > \backslash < \mathrm{S}' < \mathrm{C}_{10.5} \backslash >$) the energy does not seem to be outside the expected range. At the same time, the defect is unlikely to be stable at large concentrations, as this would significantly change the nature of the calcium-silicate sheets, which is not observed experimentally [24, 16]. This makes this defect difficult to investigate with DFT. However, based on the defect energy calculated here, it seems likely that missing dimers occur to some extent at higher $\frac{Ca}{Si}$ ratios. The biggest difference between the thermodynamically expected and calculated enthalpies are observed for the defective structure involving the removal of a silicate tetrahedron without replacement and a protonated silanol group on a silicate dimer ($< \mathrm{S}' < \mathrm{C}_9 > \ ' >$). Based on the comparison with DFT, large structural relaxation of the interlayer distance is expected when removing a silicate dimer without replacement, making an isolated defect much less energetically favorable than a fully defective structure. Also, as discussed above, protonated silanol groups for higher $\frac{Ca}{Si}$ ratio structures do not seem to be energetically favorable. Even though the removal of a silicate dimer is a relatively large scale defect, the structural relaxation of the position of the calcium within the calcium-silicate layer is small [61].

Finally, it has to be mentioned that, while the range of expected enthalpies seem to make it possible to exclude some unrealistic energies, for a complete estimation of the relative stability of structures the Gibbs free energy and not the enthalpy should be used. Especially the configurational entropy, favoring more disordered structures, is likely to significantly influence results. The study of these effects is currently ongoing and will be the subject of a follow-up article.

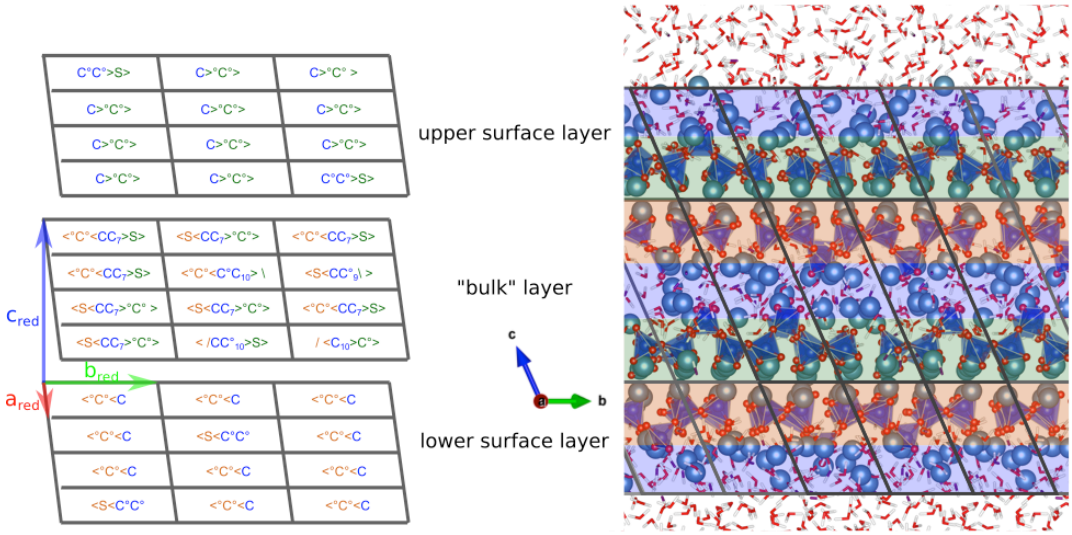

Figure 14: Example of a new proposed structure based on the newly developed notation (left) and full atomic structure after relaxation (right, Si: blue, Ca: turquoise, O: red, H: white). For a larger image of the atomic structure, see the supplementary materials for the full atomic configuration. The dimensions of the structure before relaxation is 22.5 x 22.3 x 28.0 Å.

4.7.3 Full Atomistic Model

We can use the building block description to predict and build a larger scale model, inspired by the defect energies calculated above and experimental observation by different authors. Let us consider a C-S-H like slab 4x3 units in $a_{red}$and b_{red} direction respectively and 2 units in c_{red} direction. In order to take into account the nanosized character of C-S-H, let us assume that the slab is terminated on both sides by a surface in c_{red} direction. We can now describe each consecutive layer in the above described notation (see Figure 14).

This structure was generated ad hoc using the building block description such that its $\frac{Ca}{Si}$ ratio, stoichiometry and the chemical features are comparable to that of an industrially relevant C-S-H or high $\frac{Ca}{Si}$ ratio synthetic C-S-H that has recently been produced for the first time [13]. The exact stoichiometry of the structure can be calculated according to equation (38). For the complete sample structure, we get a stoichiometry of $Ca_{1.7}SiO_{3.7} \cdot 1.3\ H_2O$ with a calcium to silicon ratio $\frac{Ca}{Si}$ of 1.67. This is consistent with measurements by different authors of the calcium to silicon ratio of C-S-H in Portland cement [4, 29, 15]. The 1.3 formula units of water in the average stoichiometry is partly present as both molecular water and OH^- ions. In fact 22 % of the charge of the calcium ions is compensated by hydroxyl groups (see equation 7). The amount of hydroxyl groups is

consistent with measurements by Thomas et al. [23], who reported that around 23 % of the charge of the calcium ions is compensated by hydroxyl groups. However, the overall water content is somewhat lower than what has been reported in literature [29, 15]. Following experimental results in the literature for high $\frac{Ca}{Si}$ ratio C-S-H [22, 11] , which are confirmed by our enthalpy calculations, defects with protonated silanol groups are not included in the full model. Based on our results, two defects are included which have not been considered in (most) previously reported atomistic models in the literature [21, 31, 32]: the replacement of a bridging silica tetrahedra ($< S < or > S >$) by a calcium ion ($< C < or > C >$) as well as the replacement of a silicate dimer by hydroxyls ($< \mathrm{S}' < \mathrm{CC}_{10} > \backslash < \mathrm{S}' < \mathrm{C}_{10.5} \backslash >$). The inclusion of the former is in accordance with recent work by Kumar et al.[13], where they found calcium at the bridging site as a defining feature of C-S-H. All building blocks are charge neutral.

The mean chain length of the model is 3.3 (eq 5). This is consistent with reported values for fresh cement [7, 4, 8, 9, 10, 11]. There are 23 dimers and 12 longer chains in the structure, which corresponds to 63 % dimers. Again, this is more or less consistent with results reported for fresh cement in literature [6], where 60 % dimers were reported.

Molecular dynamics calculations of the structure lead to an interlayer distance of 13.76 Å, which is larger than generally expected. However, as discussed above, there is still some debate about the interlayer distance of C-S-H [16, 33, 11, 27]. The Ca-O environment with a coordination number of 5.8 and an average Ca-O distance of 2.3 Å (nearest neighbour cut-off of 3.0 Å) is both consistent with the trends reported in Figure 12 (a) and with the coordination number of around 6 reported by Soyer-Uzun [27]. The definition of the density is complicated by the corrugated surface. However, we can give the density of the central units, which is 2.35 g/cm^3. If on the other hand we assume that the building blocks at the surface only occupy about one third of the volume of a full building block and that all water at the surface is part of the pore water and not of the C-S-H structure[29], we can calculate a density of 2.70 g/cm^3 for the whole structure, which should give an upper limit. Given the uncertainties, the results seem reasonable compared to experimental results [29, 15].

Compared to previous models in the literature (see section 4.6), our model includes surfaces, an extended range of different defects (replacement of bridging silicate tetrahedron with calcium and of a silicate dimer with hydroxyl groups), is entirely composed of neutral building blocks and is based on the 14 Å tobermorite reported by Merlino et al. [45]. This leads to a model structure where the concentration of protonated silanol groups as well as the silicate chain speciation and

the mean chain length is more consistent with experimental measurements than previous models (see Section 4.6).

However the water content of the model is lower and the interlayer distance larger than expected, areas where previous models were performing better (see Section 4.6). As for the magnitude and length scale of charge fluctuations, these still have to be further looked at.

Finally, we have estimated the reaction enthalpy for this structure and compared it to the DFT and MD results of single defects discussed above (Table 5 and Figure 13). The reaction enthalpy has been calculated excluding all water at the surface. Although the error on this energy is likely to be quite large (> 0.08 eV or 8 kJ/mol, the estimated force field error), both to the thermodynamic ensemble used for the calculations (NVT) and due to the uncertainties concerning the inclusion or not of the surface water, the reaction enthalpy of -0.29 eV (-28 kJ/mol) is well within the expected values (see Table 5). The full atomistic model reported here serves as an example to illustrate the feasibility and ease of the bottom up building block approach introduced in this paper. A more thorough study on different combinations of defective building blocks to better understand the disordered, stochastic nature of C-S-H structures is currently underway and will be the subject of a future publication. (Chapter 6 in this thesis)

4.8 Conclusions

The complexity of C-S-H structures has meant that the generation of reliable atom-level structural models has been elusive. One of the major difficulties in C-S-H model construction is the generation of the correct silicate-chain speciation with a low concentration of protonated silanol groups and an appropriate $\frac{Ca}{Si}$ ratio. Additionally, full atomistic models are often developed for a single stoichiometry or $\frac{Ca}{Si}$ ratio and results are difficult to extrapolate to other C-S-H stoichiometries [32, 21]. In the first part of this paper, we described a novel way for generating and describing C-S-H structures using a building block approach. The building block description encodes all important features of a full atomic C-S-H model in a simple, readable string of characters. The most relevant properties of a C-S-H model structure, such as calcium silicate ratio, silica chain length distribution, number of interlayer hydroxyl groups and degree of protonation of the silanol groups can be directly calculated from the building block description. In addition, the building block description can be used for C-S-H models based on different model crystal structures (14 Å tobermorite, 11 Å tobermorite, jennite etc.) and can deal with larger scale defects such as stacking faults and surfaces. This makes it

easier to construct and compare structures without having to analyse and manipulate the full atomic structure. This was illustrated for a model structure taken from the literature.

We then investigated different defective 14 Å tobermorite based building blocks. We applied both DFT and classical MD simulations to calculate structural relaxations and energies. DFT calculations on high defect concentrations show structural evolutions consistent with previously reported experiments, at least for $\frac{Ca}{Si} \leq 1.5$. Normalising reaction energies and plotting them on a ternary diagram additionally allows the comparison of a range of C-S-H building blocks and structures. Based on these results, we propose that two new variations should be included for the construction of future models, namely the replacement of bridging silicate tetrahedra with calcium and of silicate dimers with hydroxyl groups. Also, we find that deprotonated silanol groups are more stable than protonated ones at high $\frac{Ca}{Si}$ ratio, which is consistent with experimental results [22, 11]. Many of the defective building blocks studied here have similar energies, emphasizing the disordered character of C-S-H, where many different local defects are likely to be distributed randomly within the overall structure.

Finally to emphasize the capabilities of the building block description and based on the insights of the calculations on single defective building blocks, an "ad-hoc"-constructed, larger-scale C-S-H example structure is presented and discussed. The model has a reasonable energy and both the concentration of protonated silanol groups and the silicate chain length distribution is more consistent with experimental measurements compared to the previous models. The model includes surfaces and other defects (replacement of bridging silicate tetrahedron with calcium and of a silicate dimer with hydroxyl groups) that have not been considered so far in full scale atomistic models. However, further work is clearly needed to address the discrepancies on water content and the interlayer distance.

In summary, the development of the building block description of C-S-H now makes it easier to propose new models with relative ease and to compare existing models in much more detail than previously possible. In addition, the normalization of the defect energies proposed here and the ternary energy diagrams should make it easier to compare the energies of different structures. This will significantly facilitate the choice, construction and improvement of C-S-H models for a range of $\frac{Ca}{Si}$ ratios in the near future. We further suggest that this will facilitate discussions of what are the characteristics that make C-S-H the material with the very distinctive properties observed experimentally and provide a better fundamental understanding in growth mechanisms, mechanical properties and ageing of cementitious systems.

Acknowledgement

The authors would like to thank Ellis Gartner from Lafarge, Prof. Karen Scrivener from EPFL, Patrick Juilland from SIKA and Uli Aschauer from ETH Zurich for their input and helpful discussions. Additionally the authors would like to thank the industrial-academic research network Nanocem for the funding of the work of Sandra Galmarini. The authors would like to thank Swiss National Foundation for financing the contribution of Aslam Kunhi Mohamed (Grant No. 153044). University of Bath acknowledges the Engineering and Physical Sciences Research Council (EPSRC) for financial support through project EP/K025597/1. Access to HPC computing resources on ARCHER for DFT calculations was provided via the membership of the Materials Chemistry Consortium, which is funded by EPSRC (EP/L000202) and on HPC Belena through the University of Bath.

4.9 References

[1] E. Benhelal, G. Zahedi, E. Shamsaei, A. Bahadori, Global strategies and potentials to curb CO2 emissions in cement industry, Journal of Cleaner Production 51 (2013) 142–161.

[2] K. L. Scrivener, V. M. John, E. M. Gartner, Eco-efficient cements: Potential, economically viable solutions for a low-CO2, cement-based materials industry, Technical Report, UNEP, Paris, 2016.

[3] A. Grudemo, Variation with solid-phase concentration of composition, structure and strength of cement pastes at high age, Cement and Concrete Research 14 (1984) 123–132.

[4] I. G. Richardson, Tobermorite/jennite- and tobermorite/calcium hydroxide-based models for the structure of c- s-h: applicability to hardened pastes of tricalcium silicate, [beta]-dicalcium silicate, portland cement, and blends of portland cement with blast-furnace slag, metakaolin, or silica fume, Cement and Concrete Research 34 (2004) 1733–1777.

[5] I. G. Richardson, G. W. Groves, Microstructure and microanalysis of hardened ordinary portland cement pastes, Journal of Materials Science 28 (1993) 265–277.

[6] K. Mohan, H. Taylor, A trimethylsilylation study of tricalcium silicate pastes, Cement and Concrete Research 12 (1982) 25–31.

[7] J. Skibsted, C. Hall, Characterization of cement minerals, cements and their reaction products at the atomic and nano scale, Cement and Concrete Research 38 (2008) 205–225.

[8] F. Brunet, P. Bertani, T. Charpentier, A. Nonat, J. Virlet, Application of 29Si homonuclear and 1H-29Si heteronu- clear NMR correlation to structural studies of calcium silicate hydrates, The Journal of Physical Chemistry B 108 (2004) 15494–15502.

[9] I. Klur, J.-F. Jacquinot, F. Brunet, T. Charpentier, J. Virlet, C. Schneider, P. Tekely, NMR cross-polarization when TIS>T1rho; examples from silica gel and calcium silicate hydrates, The Journal of Physical Chemistry B 104 (2000) 10162–10167.

[10] A. R. Brough, C. M. Dobson, I. G. Richardson, G. W. Groves, In situ solid-state NMR studies of Ca3SiO5: hydration at room temperature and at elevated temperatures using 29Si enrichment, Journal of Materials Science 29 (1994) 3926–3940.

[11] X. Cong, R. J. Kirkpatrick, 29Si MAS NMR study of the structure of calcium silicate hydrate, Advanced Cement Based Materials 3 (1996) 144–156.

[12] E. Pustovgar, R. P. Sangodkar, A. S. Andreev, M. Palacios, B. F. Chmelka, R. J. Flatt, J.-B. d'Espinose de Lacaillerie, Understanding silicate hydration from quantitative analyses of hydrating tricalcium silicates, Nature Communications 7 (2016) 10952.

[13] A. Kumar, B. J. Walder, A. Kunhi Mohamed, A. Hofstetter, B. Srinivasan, A. J. Rossini, K. Scrivener, L. Emsley, P. Bowen, The atomic-level structure of cementitious calcium silicate hydrate, The Journal of Physical Chemistry C 121 (2017) 17188–17196.

[14] A. J. Allen, Time-resolved phenomena in cements, clays and porous rocks, Journal of Applied Crystallography 24 (1991) 624–634.

[15] A. J. Allen, J. J. Thomas, H. M. Jennings, Composition and density of nanoscale calcium-silicate-hydrate in cement, Nature Materials 6 (2007) 311–316.

[16] G. Renaudin, J. Russias, F. Leroux, F. Frizon, C. Cau-dit Coumes, Structural characterization of CSH and CASH samples–Part i: Long-range order investigated by rietveld analyses, Journal of Solid State Chemistry 182 (2009) 3312–3319.

[17] L. B. Skinner, S. R. Chae, C. J. Benmore, H. R. Wenk, P. J. M. Monteiro, Nanostructure of calcium silicate hydrates in cements, Physical Review Letters 104 (2010) 195502.

[18] A. Bazzoni, S. Ma, Q. Wang, X. Shen, M. Cantoni, K. L. Scrivener, The Effect of Magnesium and Zinc Ions on the Hydration Kinetics of C3s, Journal of the American Ceramic Society 97 (2014) 3684–3693.

[19] E. M. Gartner, A proposed mechanism for the growth of c—s—h during the hydration of tricalcium silicate, Cement and Concrete Research 27 (1997) 665–672.

[20] H. M. Jennings, Refinements to colloid model of c-s-h in cement: CM-II, Cement and Concrete Research 38 (2008) 275–289.

[21] R. J. Pellenq, A. Kushima, R. Shahsavari, K. J. Van Vliet, M. J. Buehler, S. Yip, F. J. Ulm, A realistic molecular model of cement hydrates, Proceedings of the National Academy of Sciences (2009).

[22] P. Yu, R. J. Kirkpatrick, B. Poe, P. F. McMillan, X. Cong, Structure of calcium silicate hydrate (CSH): near-, mid-, and far-infrared spectroscopy, J. Am. Ceram. Soc. 82 (1999) 742–748.

[23] J. J. Thomas, J. J. Chen, H. M. Jennings, D. A. Neumann, Ca-OH bonding in the c-s-h gel phase of tricalcium silicate and white portland cement pastes measured by inelastic neutron scattering, Chemistry of Materials 15 (2003) 3813–3817.

[24] A. Nonat, The structure and stoichiometry of CSH, Cement and Concrete Research 34 (2004) 1521–1528.

[25] R. J. Kirkpatrick, J. Yarger, P. F. McMillan, Y. Ping, X. Cong, Raman spectroscopy of c-s-h, tobermorite, and jennite, Advanced Cement Based Materials 5 (1997) 93–99.

[26] P. Rejmak, J. S. Dolado, M. J. Stott, A. Ayuela, 29Si NMR in cement: A theoretical study on calcium silicate hydrates, The Journal of Physical Chemistry C 116 (2012) 9755–9761.

[27] S. Soyer-Uzun, S. R. Chae, C. J. Benmore, H.-R. Wenk, P. J. M. Monteiro, Compositional evolution of calcium silicate hydrate (C–S–H) structures by total x-ray scattering, Journal of the American Ceramic Society 95 (2012) 793–798.

[28] C. Meral, C. Benmore, P. J. Monteiro, The study of disorder and nanocrystallinity in C–S–H, supplementary cementitious materials and geopolymers using pair distribution function analysis, Cement and Concrete Research 41 (2011) 696–710.

[29] A. C. A. Muller, K. L. Scrivener, A. M. Gajewicz, P. J. McDonald, Densification of C–S–H measured by 1H NMR relaxometry, The Journal of Physical Chemistry C 117 (2013) 403–412.

[30] J. S. Dolado, M. Griebel, J. Hamaekers, A molecular dynamic study of cementitious calcium silicate hydrate (C–S–H) gels, Journal of the American Ceramic Society 90 (2007) 3938–3942.

[31] M. J. Abdolhosseini Qomi, K. J. Krakowiak, M. Bauchy, K. L. Stewart, R. Shahsavari, D. Jagannathan, D. B. Brommer, a. Baronnet, M. J. Buehler, S. Yip, F.-J. Ulm, K. J. Van Vliet, R. J.-M. Pellenq, Combinatorial molec- ular optimization of cement hydrates., Nature communications 5 (2014) 4960.

[32] G. Kovačević, B. Persson, L. Nicoleau, A. Nonat, V. Veryazov, Atomistic modeling of crystal structure of Ca1.67SiHx, Cement and Concrete Research 67 (2015) 197–203.

[33] I. G. Richardson, Model structures for C-(A)-S-H(I), Acta Crystallographica Section B Structural Science, Crystal Engineering and Materials 70 (2014) 903–923.

[34] G. Kovačević, L. Nicoleau, A. Nonat, V. Veryazov, Revised Atomistic Models of the Crystal Structure of C–S–H with high C/S Ratio, Zeitschrift für Physikalische Chemie 230 (2016).

[35] S. A. Hamid, The crystal structure of the 11 a natural tobermorite, Zeitschrift für Kristallographie 154 (1981) 189–198.

[36] S. Merlino, E. Bonaccorsi, T. Armbruster, The real structure of tobermorite 11A: normal and anomalous forms, OD character and polytypic modifications, European Journal of Mineralogy 13 (2001) 577.

[37] G. Kresse, J. Hafner, Ab initio molecular-dynamics simulation of the liquid-metal-amorphous-semiconductor transition in germanium, Physical Review B 49 (1994) 14251–14269.

[38] G. Kresse, J. Furthmüller, Efficient iterative schemes for ab initio total-energy calculations using a plane-wave basis set, Physical review B 54 (1996) 11169.

[39] P. E. Blöchl, Projector augmented-wave method, Physical Review B 50 (1994) 17953.

[40] G. Kresse, D. Joubert, From ultrasoft pseudopotentials to the projector augmented-wave method, Physical Review B 59 (1999) 1758.

[41] J. P. Perdew, K. Burke, M. Ernzerhof, D. of Physics, N. O. L. . J. Quantum Theory Group Tulane University, Generalized Gradient Approximation Made Simple, Physical Review Letters 77 (1996) 3865–3868.

[42] J. F. Dobson, K. McLennan, A. Rubio, J. Wang, T. Gould, H. M. Le, B. P. Dinte, Prediction of dispersion forces: is there a problem?, Australian Journal of Chemistry 54 (2002) 513–527.

[43] Q. Wu, W. Yang, Empirical correction to density functional theory for van der Waals interactions, The Journal of chemical physics 116 (2002) 515–524.

[44] S. Grimme, J. Antony, S. Ehrlich, H. Krieg, A consistent and accurate ab initio parametrization of density functional dispersion correction (DFT-D) for the 94 elements H-Pu, The Journal of Chemical Physics 132 (2010) 154104.

[45] E. Bonaccorsi, S. Merlino, A. R. Kampf, The crystal structure of tobermorite 14 a; (plombierite), a c-s-h phase, Journal of the American Ceramic Society 88 (2005) 505–512.

[46] C. F. Macrae, I. J. Bruno, J. A. Chisholm, P. R. Edgington, P. McCabe, E. Pidcock, L. Rodriguez-Monge, R. Tay- lor, J. van de Streek, P. A. Wood, Mercury CSD 2.0 – new features for the visualization and investigation of crystal structures, Journal of Applied Crystallography 41 (2008) 466–470.

[47] W. Smith, T. R. Forester, DL_POLY_2.0: a general-purpose parallel molecular dynamics simulation package, Journal of Molecular Graphics 14 (1996) 136–141.

[48] G. W. Watson, E. T. Kelsey, N. H. de Leeuw, D. J. Harris, S. C. Parker, Atomistic simulation of dislocations, surfaces and interfaces in MgO, Journal of the Chemical Society, Faraday Transactions 92 (1996) 433.

[49] C. L. Freeman, J. H. Harding, D. J. Cooke, J. A. Elliott, J. S. Lardge, D. M. Duffy, New forcefields for modeling biomineralization processes, Journal of Physical Chemistry C 111 (2007) 11943–11951.

[50] G. V. Lewis, C. R. A. Catlow, Potential models for ionic oxides, Journal of Physics C: Solid State Physics 18 (1985) 1149–1161.

[51] S. Kerisit, S. C. Parker, J. H. Harding, Atomistic simulation of the dissociative adsorption of water on calcite surfaces, The Journal of Physical Chemistry B 107 (2003) 7676–7682.

[52] N. H. De Leeuw, S. C. Parker, Molecular-dynamics simulation of MgO surfaces in liquid water using a shell- model potential for water, Physical Review B 58 (1998) 13901–13908.

[53] K.-P. Schröder, J. Sauer, M. Leslie, C. R. A. Catlow, J. M. Thomas, Bridging hydroxyl groups in zeolitic catalysts: a computer simulation of their structure, vibrational properties and acidity in protonated faujasites (h-y zeolites), Chemical Physics Letters 188 (1992) 320–325.

[54] N. H. de Leeuw, G. W. Watson, S. C. Parker, Atomistic simulation of the effect of dissociative adsorption of water on the surface structure and stability of calcium and magnesium oxide, The Journal of Physical Chemistry 99 (1995) 17219–17225.

[55] N. H. de Leeuw, S. C. Parker, C. R. A. Catlow, G. D. Price, Modelling the effect of water on the surface structure and stability of forsterite, Physics and Chemistry of Minerals 27 (2000) 332–341.

[56] S. Galmarini, P. Bowen, Atomistic simulation of the adsorption of calcium and hydroxyl ions onto portlandite surfaces - towards crystal growth mechanisms, Cement and Concrete Research 81 (2016) 16–23.

[57] J. L. F. Abascal, C. Vega, A general purpose model for the condensed phases of water: TIP4P/2005, The Journal of Chemical Physics 123 (2005) 234505–12.

[58] P. P. Ewald, Die berechnung optischer und elektrostatischer gitterpotentiale, Annalen der Physik 369 (1921) 253–287.

[59] S. Merlino, E. Bonaccorsi, T. Armbruster, Tobermorites: Their real structure and order-disorder (OD) character, American Mineralogist 84 (1999) 1613–1621.

[60] C. Roosz, S. Gaboreau, S. Grangeon, D. Prêt, V. Montouillout, N. Maubec, S. Ory, P. Blanc, P. Vieillard, P. Henocq, Distribution of Water in Synthetic Calcium Silicate Hydrates, Langmuir 32 (2016) 6794–6805.

[61] S. Galmarini, A. M. Kunhi, P. Bowen, K. L. Scrivener, Atomistic structure of C-S-H from defective tobermorite structures: variations of defects and features, Proceedings of the 14th International Congress on the Chemistry of Cement (2015).

[62] B. Lothenbach, T. Matschei, G. Möschner, F. P. Glasser, Thermodynamic modelling of the effect of temperature on the hydration and porosity of portland cement, Cement and Concrete Research 38 (2008) 1–18.

[63] D. A. Kulik, Improving the structural consistency of C-S-H solid solution thermodynamic models, Cement and Concrete Research 41 (2011) 477–495.

Chapter V. Synthetic C-S-H

In this chapter, the Brick model developed in Chapter 4 is applied to decipher the structure of synthetic C-S-H synthesized in the experimental part of this SNF project. This work, featured on the cover page of The Journal of Physical Chemistry C (2017), involved synthesis of C-S-H, characterization of these samples using the Dynamic Nuclear Polarization Nuclear Magnetic Resonance(DNP NMR) technique, theoretical NMR chemical shifts calculations from first principles calculations on atomic structures of defective tobermorite generated using the brick model. In this chapter, a brief summary of the work done in this paper is given followed by the full paper for further reading. The work was a collaborative effort with the first 4 authors contributing equally to the final manuscript guided by the 3 final senior authors.

My contributions are the following

- Interpreting the structural features from the NMR results:
    - To make sense of the quantification of the silicate species confirming the dreierketten structure for the silicates (from the 1D NMR data obtained by the second author)
    - Helped in interpreting correctly the 2D NMR results with respect to the general silicate connectivity in C-S-H
    - From the quantification of the connectivity of silicate species in C-S-H, a distribution of the different types of silicate chains was calculated from a stochastic approach and selected the most probable distribution of the chains fitting the NMR criteria.
- Generated a variety of structural units using Brick model with the focus on capturing the environment close to the terminal silicate species.
- Executed the DFT calculations on these structures
    - These relaxed structures were then used to calculate the chemical shifts by the fourth author

The candidate carried out all the atomistic simulations including the figure designs and the cover feature artwork. The atomistic simulations included, molecular dynamics, use of the brick model of chapter IV to produce the atomistic structures and the DFT calculations used for the NMR spectra simulations as described above.

5.1 Overview

Synthesizing pure C-S-H with an industrial relevant chemical composition has been a great interest for decades. It is the first time a pure and single phase of C-S-H of Ca/Si ratio greater than 1.6 has been achieved. Usually any attempt to synthesize high Ca/Si ratio C-S-H resulted in two phases with C-S-H of Ca/Si ~1.5 and the remaining calcium precipitated as portlandite (CH). This problem was circumvented by a novel design of a micro reactor which allows precise control of the thermodynamics and kinetics of the system [116].Thus, a pure phase of C-S-H was achieved by engineering the chemical conditions ensuring that CH remains undersaturated with respect to CH, thus avoiding CH formation. A variety of characterization techniques were carried out on these synthesized C-S-H confirming the absence of any secondary phases (more details can be found in the thesis of Kumar [117]). In this paper, we have tried to characterize the silicate framework of four C-S-H samples synthesized with different Ca/Si ratios using Nuclear Magnetic Resonance (NMR).

NMR is a powerful technique that can elucidate the local environment around a nucleus of interest. Here, we have used a new NMR technique, Dynamic Nuclear Polarization NMR, which significantly enhances the sensitivity of the signals compared to the conventional NMR techniques. The three types of DNP NMR done in this work are (i) One dimensional ^{29}Si DNP NMR (ii) Two dimensional ^{29}Si - ^{29}Si DNP INADEQUATE NMR and (iii) Two dimensional ^{1}H - ^{29}Si DNP HETCOR NMR. The 1-D NMR gave the relative proportions of the different types of silicate species in our sample, namely the terminal (Q^1), the bridging (Q^{2b}) and the pairing silicates (Q^{2p}). It also confirmed a dreierketten pattern (3n-1 units) of silicates in our C-S-H samples. The NMR signals from the 2-D INADEQUATE experiments showed how these different silicate species were connected. Combining the 1-D and 2-D results we could calculate the relative proportions of the different types of silicate chains in each composition of C-S-H considered. Our results show that the majority of the silicates exist as dimers (> 75 %), pentamers (< 25%), octamers (< 10%) and a few longer chains (< 5 %). Thus, we were able to unravel the silicate structure in our C-S-H.

In the 2-D ^{1}H - ^{29}Si HETCOR experiments, we came across a very interesting observation. A cross section of the ^{1}H signal at the Q^1 silicate signal of all the samples showed a significant proportion of protons with chemical shift greater than 10 ppm, indicative of strong hydrogen bonded proton species. That is, the protons which lie very close to the terminal silicate tetrahedra (within a radius of 5 Å from the Q^1 site) are in a very strong hydrogen bonding environment. In order to understand the origin of this strong hydrogen bonding next to Q^1, we resorted to the brick model. A variety of defective tobermorite structures were generated with a focus on capturing the different types of

species next to the terminal silicate tetrahedra. The following procedure was used for relaxing the structures"

1. Selective relaxation of the interlayer atoms with an energy minimization software, METADISE. The reason for not relaxing all the atoms is due to the fact that at that time the force fields (CementFF v1) was not improved to capture the seven-fold coordination of calcium in tobermorite.
2. The positions of the atoms and the cell vectors were then optimized using the Quantum Espresso code employing ultra-soft pseudo potentials.
3. The optimized structures were then screened for any local charge imbalance. That is, it was observed that since the initial positions of the interlayer Ca^{2+} OH^- and H_2O are arbitrarily set, the DFT optimized structures could result in a case where the hydroxyl groups are not in the first coordination shell of Ca^{2+}, resulting in a charge separation over a 3-5 Å distance. Although such a situation might be interesting to study, we observed that the energy of systems with no charge separation is lower. Hence, we only considered the most stable systems to avoid any artifacts of the initial atom positions.
4. These optimized structures were then accepted to be fit for the chemical shift calculations

The chemical shifts were calculated using the GIPAW method within the Quantum Espresso code by Albert Hofstetter. The results indicated that only those structures which has a calcium at the bridging site replacing the bridging silicate tetrahedra and connecting two terminal silicate tetrahedra were found to have a chemical shift greater than 10 ppm. That is, the presence of this bridging calcium with its associated water molecules induces a strong hydrogen bonding close to the terminal silicate tetrahedra. The majority of the hydrogen species comes from a water molecule either in the first coordination shell of the bridging calcium or that not directly bonded to any calcium. These hydrogen atoms are hydrogen-bonded to the oxygen atom of the terminal silicate tetrahedra that is in turn bonded to the bridging calcium. From this, we concluded that this bridging calcium atom that holds the silicate chains together and induces a strong hydrogen bonding around it, is a defining characteristic feature of C-S-H.

Supplementary information of this paper is provided in Appendix section 8.4

5.2 Paper Abstract

The Atomic-Level Structure of Cementitious Calcium Silicate Hydrate

Abhishek Kumar,[1] Brennan J. Walder,[2] Aslam Kunhi Mohamed,[1] Albert Hofstetter,[2] Bhuvanesh Srinivasan,[1,3] Aaron J. Rossini,[4] Karen Scrivener,[5] Lyndon Emsley[*2] and Paul Bowen[*1]

[1]Powder Technology Laboratory, Institut des Matériaux, Ecole Polytechnique Fédérale de Lausanne (EPFL), CH-1015 Lausanne, Switzerland

[2]Institut des Sciences et Ingénierie Chimiques, Ecole Polytechnique Fédérale de Lausanne (EPFL), CH-1015 Lausanne, Switzerland

[3]Department of Earth & Environmental Sciences, Ludwig-Maximilian University, D-80333, Munich, Germany

[4]Department of Chemistry, Iowa State University, Ames, IA 50011-3020, USA

[5]Construction Material Laboratory, Institut des Matériaux, Ecole Polytechnique Fédérale de Lausanne (EPFL), CH-1015 Lausanne, Switzerland

ABSTRACT: Efforts to tune the bulk physical properties of concrete are hindered by a lack of knowledge related to the atomic-level structure and growth of calcium silicate hydrate phases, which form about 50-60% by volume of cement paste. Here we describe the first synthesis of compositionally uniform calcium silicate hydrate phases with Ca:Si ratios tunable between 1.0 and 2.0. The calcium silicate hydrate synthesized here does not contain a secondary $Ca(OH)_2$ phase, even in samples with Ca:Si ratios above 1.6, which is unprecedented for synthetic calcium silicate hydrate systems. We then solve the atomic-level three-dimensional structure of these materials using dynamic nuclear polarization enhanced ^{1}H and ^{29}Si nuclear magnetic resonance experiments in combination with atomistic simulations and density functional theory chemical shift calculations. We discover that bridging interlayer calcium ions are the defining structural characteristic of single-phase cementitious calcium silicate hydrate, inducing the strong hydrogen bonding that is responsible for stabilizing the structure at high Ca:Si ratios.

5.3 Introduction

Calcium silicate hydrate (C-S-H) is the primary binding component of concrete, forming about 50-60% by volume of hardened cement paste and making it one of the most common substances of the modern world. Because of its ubiquity, it is surprising that a complete description of its atomic-level structure remains the subject of debate [20,118], and consequently its structure-property relationships are not well known. This makes it difficult to engineer C-S-H not only for its primary uses in construction, in which high reactivity and strength at low carbon footprints are desirable, but also for emerging applications such as dental filling and bone repair [119,120], which require biocompatibility; waste water treatment [121,122], which requires high specific surface areas; and encasement of nuclear waste [123], which requires high structural integrity in the presence of significant radionuclide concentrations.

For Portland cements the precipitation of C-S-H occurs in conjunction with the precipitation of other material phases such as crystalline $Ca(OH)_2$, ettringite, and $CaCO_3$. [4,124] The C-S-H phases are known to be rich in calcium, with Ca:Si ratios exceeding 1.75 at early stages of hardening [46]. In contrast, synthetic C-S-H with Ca:Si ratios above ~1.5 are often observed in coexistence with a $Ca(OH)_2$ phase. Because of an inability to synthesize pure C-S-H with Ca:Si ratios above 1.5, many researchers believe that Ca-rich C-S-H systems are intrinsically a binary mixture of a chemically disordered single phase C-S-H material. In such a case, one phase consists of a “proper” C-S-H phase, with a layered silicate chain structure related to that of the naturally occurring calcium silicate hydrate mineral tobermorite and limited to Ca:Si ratios around 1.6. The other phase consists of nanocrystalline $Ca(OH)_2$, which is thought to occur in bulk form occupying pores in the proper C-S-H phase or as chemically distinct ribbons or sheets interwoven within the C-S-H structure itself [20,125–128]. This interpretation has the support of thermodynamic and solubility data analyzing a multitude of C-S-H systems [129]. Furthermore, in spite of a vast amount of experimental data yielding partial characterization, the positions of the calcium atoms in the interlayer, which are the essential aspects of high Ca:Si ratios in C-S-H, remain undefined. Thermodynamic modeling and crystal chemical reasoning have been applied to propose complete C-S-H structural models at Ca:Si ratios greater than 1.5 [20], but for these compositions the focus has been on the binary C-S-H/$Ca(OH)_2$ representation, for which experimental validation is ongoing [130].

Here we introduce a method which achieves the synthesis of C-S-H possessing Ca:Si ratios between 1.0 and 2.0, maintaining a single phase composition even for C-S-H whose Ca:Si ratio exceeds 1.6. Aqueous calcium nitrate and sodium silicate solutions are reacted under conditions of high supersaturation and constant pH, the latter of which is set by the addition of a predetermined

amount of alkali hydroxide. The production of a single phase composition at such Ca:Si ratios has not been achieved using conventional methods for C-S-H synthesis [131–135] relying on combinations of dissolution and direct precipitation [55,118,136] reactions that operate at either lower supersaturation or uncontrolled pH conditions. We also use $\{^{1}H\}^{29}Si$ cross-polarization (CP) MAS NMR to measure populations of Q species, the connectivity between those species, and correlations between ^{29}Si and ^{1}H chemical shifts of the single-phase C-S-H produced using our rapid precipitation method. The greatest drawback of ^{29}Si solid-state NMR is its low sensitivity, which we circumvent by using modern dynamic nuclear polarization (DNP) strategies [137–139] that have been recently used to study the hydration of cementitious systems with tremendous success [140]. The Q species information allows us to quantify the extent of silicate polymerization in the structure. Finally, we use atomistic modeling to establish a connection between the measured ^{1}H chemical shifts and the atomic-level position of calcium atoms in the interlayer, allowing us to solve the three-dimensional atomic-level structure of synthetic cementitious C-S-H.

5.4 Methods

Synthesis: pH governs the type of silicates species available for precipitation of C-S-H. The Ca:Si ratio attained in the solid phase was found to depend on the pH of the solution. Thermodynamic modeling [141,142] also predicts that Ca:Si ratios above 1.5 can only be produced under high pH conditions, as occurs in the hydration of real Portland cement systems, in order to ensure that the electrostatically stable monomeric $SiO_2(OH)_2^{2-}$ species remains in abundance at high supersaturation and rapid precipitation conditions.

To maintain the desired supersaturation, pH, and mixing conditions, and to avoid carbonation, we developed a synthetic apparatus for controlling the reaction conditions to the degree of precision required, aided by real-time acquisition of kinetic data such as Ca^{2+} ion concentration, pH and conductivity. Details regarding its construction are given in the Supporting Information Section II.

All reaction solutions were prepared in decarbonized, demineralized ultrapure water. The reaction chamber was kept under an inert nitrogen atmosphere in order to prevent carbonation. C-S-H precipitates were collected after a duration of 3 hours and again after 24 hours. The products were separated from mother liquor using vacuum filtration over a 20 nm organic filter and later washed with ethanol and water to remove salts and unwanted ions from the surfaces of C-S-H. We produced five different C-S-H powders with nominal Ca:Si ratios of 1.0, 1.25, 1.5, 1.75 and 2.0. The precise experimental conditions for the precipitation of the different stoichiometry of the C-S-H were determined using thermodynamic modelling [141,143], with the exclusion of calcium hydroxide, as

there was no experimental evidence for its formation. Additional details are given in Section IV of the Supplementary Information available online.

Dynamic nuclear polarization: DNP solid-state NMR experiments were carried out on the aqueous suspensions of freshly prepared C-S-H nanoparticles with added impregnation agent and were not dried. The impregnation agent used was 22 mM AMUPol in 65:35 v:v d_8-glycerol:D_2O, which was purged of dissolved oxygen by bubbling with N_2 gas for roughly five minutes. The addition of the radical polarizing agent further dilutes the samples by about 20%, but simple drying steps to increase the concentration of C-S-H led to sample deterioration (Figure S6 section VI in the online Supplementary). About 25 mg of the impregnated gels were worked into a 3.2 mm OD sapphire rotor and plugged with a PTFE insert. The drive caps were zirconia. The DNP enhanced NMR experiments were carried out at a nominal field strength of 9.4 T using a commercial Bruker AV I 400 MHz/263 GHz DNP NMR spectrometer [144]. The samples were rapidly transferred into the stator of the NMR probe which was pre-cooled to 100 K to promote glass formation. Proton DNP enhancements were found to exceed 35 for all samples.

High resolution electron microscopy: HRTEM micrographs were obtained by coating the samples with 6 nm of osmium (gas phase coating). The metallization reduces charging and provides enhanced image contrast. High resolution TEM analysis was performed on a Zeiss Merlin, equipped with the GEMINI II column which combines ultra-fast analytics with high resolution imaging using advanced detection modes. Osmium coated samples were analyzed with acceleration voltage of 1 kV with probing current of 300 nA. On-axis in-lens secondary electron detection mode was employed for imaging. The instrument provides up to 0.6 nm resolution in STEM mode. In TEM mode, the samples were imaged at room temperature using a Tecnai F20 (FEI, The Netherlands) operating at an acceleration voltage of 100kV LaB_6 gun with a line resolution of 0.34 nm, with images being recorded on a high sensitivity 4k x 4k pixel CCD camera. For SEM and TEM analysis, 50 mg of sample was dispersed in 40 mL of isopropanol. A drop of the suspended liquid was allowed to dry on a copper grid (200 mesh grids). The copper grids were glow discharged prior to sample disposition.

FTIR: Freshly prepared samples were analyzed with a PerkinElmer FT-IR spectrometer, with a resolution of 0.5 cm^{-1} to 64 cm^{-1}. Wavelength accuracy was about 0.1 cm^{-1} at 1600 cm^{-1}. FTIR measurements were performed with an attenuated total reflectance (ATR) unit and data was recoded and processed using Spectrum One software. The ATR unit included a diamond crystal and a clamp for pressing solid materials onto the crystal with constant pressure. The transmittance results

of 256 scans were recorded between 4000 and 450 cm^{-1}, with individual measurements taken every 2 cm^{-1}. For the solid gels, air was used as the background.

Raman: Non-invasive Raman microscopy was carried out using a Renishaw inVia Reflex spectrometer equipped with a 785 nm diode laser. The power delivered to the sample was 164 mW at a full power specification. The grating size was 1200 lines/mm with an edge filter for Rayleigh rejection. $Ca(OH)_2$ and $CaCO_3$ standards were measured at 5% power with a single 10 s accumulation period. Freshly prepared C-S-H was measured with multiple accumulation periods, each of 13 s exposure.

MD: Classical molecular dynamics simulation with force field potentials were used to test the structural stability of the proposed structures. The force field parameters used are known to describe well cementitious material systems [12]. Simulations were done in a constant pressure ensemble at 300 K and a time step of 0.7 fs using Velocity Verlet integration algorithms implemented in DLPOLY [145]. Ewald summation was used to take into account the long range forces above a cutoff distance of 8.5 Å.

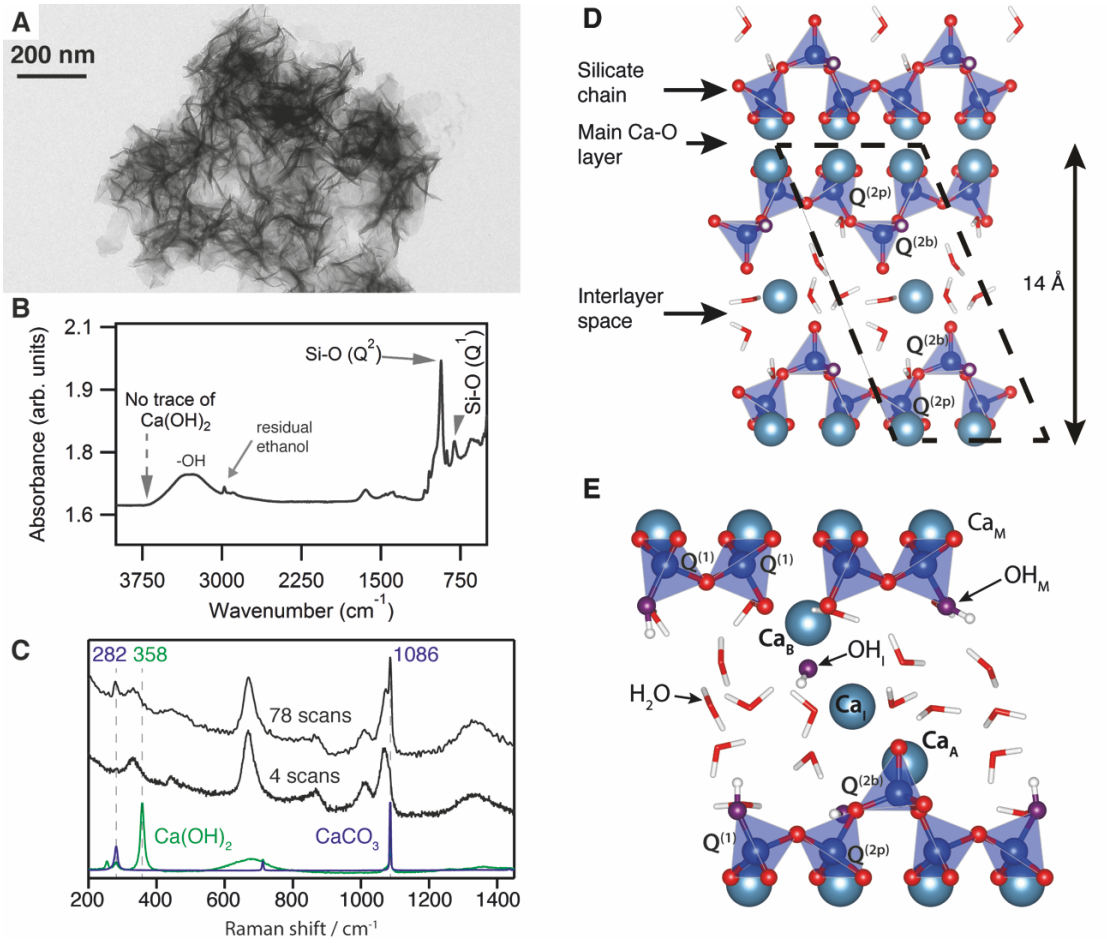

Figure 15: Structural elements of C-S-H. (A) High-resolution TEM image of pure C-S-H with Ca:Si ratio of 2.00, showing its "nanofoil" morphology. (B) Fourier transform IR spectroscopy showed no evidence of phases other than the C-S-H, including $Ca(OH)_2$. (C) Comparison of Raman spectra of $Ca(OH)_2$ (green), $CaCO_3$ (blue), a sample of C-S-H with Ca:Si = 2.0 after 4 scans (lower black), and a sample of C-S-H with Ca:Si = 2.0 after 78 scans (upper black). (D) Chain topology in the layered 14 Å tobermorite (Ca:Si = 0.83). (E) Defective and short dreierketten chains in C-S-H, showing two dimers (n = 0) and one pentamer (n = 1).

NMR shift calculations: Atomic positions and unit cell parameters were optimized as described in the SI section XII. The chemical shielding σ_{calc} was calculated using the generalized gradient approximation (GGA) functional PBE[146] within the Quantum Espresso code [105] and the GIPAW method [147]. In every calculation a plane-wave maximum cutoff energy of 80 Ry, and a Monkhorst-Pack grid of *k*-points [104] corresponding to 0.03 $Å^{-1}$ - 0.04 $Å^{-1}$ in reciprocal space was employed. The chemical shielding was converted into calculated chemical shifts δ_{calc} by the relation $\delta_{calc} = \sigma_{ref} - \sigma_{calc}$, with the value of σ_{ref} determined by a linear regression between the calculated and experimental values for the calcium hydroxide structure (^{1}H chemical shifts) and the unperturbed tobermorite structure [80] (^{29}Si chemical shifts).

5.5 Results and Discussion

5.5.1 Morphology

Two typical morphologies were seen by electron microscopy: “nanoglobules”, for the Ca:Si ratio of 1.00; and “nanofoils”, for Ca:Si ratios ≥ 1.25, which is the morphology shown in Figure 15A. The foil morphology is very similar to morphologies for C-S-H seen in Portland cement systems with high alkaline contents [143,148]. Thicknesses of the foil-like structures are generally between 6 nm and 10 nm. The pure phase C-S-H systems were all shown by high-resolution analytical transmission electron microscopy (TEM) to be uniform for Ca:Si ratios between 1.0 and 2.0 at less than a 9 nm^2 pixel size. This is also supported by X-ray diffraction (XRD) and scanning TEM with energy dispersive X-ray analysis (STEM-EDX), as described in the SI section V. No secondary phases such as $Ca(OH)_2$ were detected by IR or thermogravimetric analysis (TGA), as shown in Figure 15B; however, long exposure of C-S-H sample to open air (for example in TGA or XRD analysis) does eventually lead to the formation of $CaCO_3$. This phenomenon manifests well in the Raman spectra of Figure 15C, showing that $CaCO_3$ forms during prolonged measurements in air, whereas the signature of $Ca(OH)_2$ is never observed regardless of measurement duration. ζ-potential measurements on the samples show negative potential surfaces indicating that calcium does not reside at the surface but is incorporated into the particles.

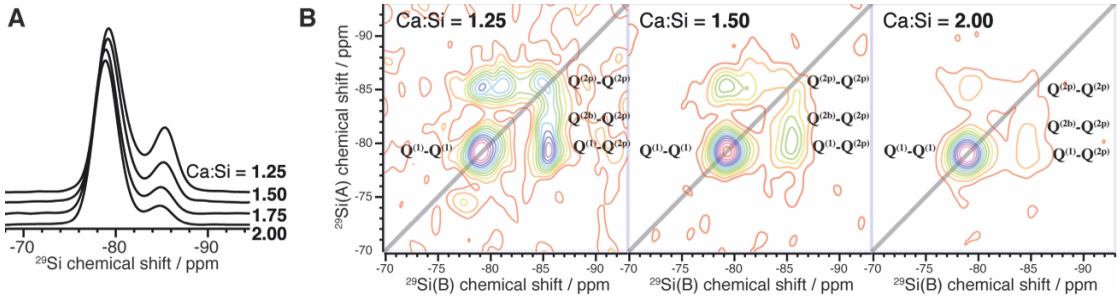

Figure 16: One- and two- dimensional DNP enhanced ^{29}Si CP MAS spectra of C-S-H samples for quantification of silicate chain distributions. (A) 1D spectra across the compositional series. (B) Experimental 2D refocused INADEQUATE spectra for three of the C-S-H compositions studied (the spectra have been sheared to produce a COSY-like representation). Contours are drawn in 10% intervals beginning at 5% of the maximum signal intensity.

5.5.2 Characterization by DNP NMR

C-S-H is a poorly ordered material, making atomic level structural determination using conventional X-ray and neutron diffraction methods challenging, especially for non-dried samples. Solid-state magic-angle spinning (MAS) NMR is a powerful method for studying disordered systems, and has

been extensively used to study the molecular structure of C-S-H and related mineral phases [149]. Previous ^{29}Si MAS NMR [14,16,50,80,150,151] and diffraction studies, often on dried materials, have established that the silicate chains in C-S-H are arranged according to the "dreierketten" model [16,150,152,153], which specifies a repeating unit for the chains comprised of a bridging-type $Q^{(2b)}$ silicate tetrahedron flanked by pairing-type $Q^{(2p)}$ silicate tetrahedrons, highlighted in the tobermorite structure shown in Figure 15D. The silicate chains are flanked by a calcium oxide layer and a hydrous interlayer. Each silicate tetrahedron shares two O atoms with other silicate tetrahedrons and, on this basis, are both classified as $Q^{(2)}$ species. The pairing-type $Q^{(2p)}$ species direct the other two O atoms toward the main calcium layer whereas the bridging-type $Q^{(2b)}$ species direct them toward the hydrous interlayer. Defects occur through the removal of a $Q^{(2b)}$ SiO_2 unit, breaking up the idealized infinite silicate chains of tobermorite into finite segments consisting of (3*n*+2) silicate tetrahedrons, as illustrated in Figure 15E. The segments are terminated by $Q^{(1)}$ silicate species. The interlayer calcium and water present in the original 14 Å tobermorite are Ca_I and H_2O respectively whereas the Ca_B, Ca_A and OH_I are only present in the defective structures. Ca_B sites replace bridging silicate tetrahedrons, Ca_A sites are additional calcium atoms in the interlayer, and OH_I are additional hydroxyl groups in the interlayer to charge compensate the additional Ca ions needed to reach high Ca:Si ratios. Silicate dimers (*n* = 0) have been observed by $\{^{29}Si\}^{29}Si$ correlation NMR experiments to be the dominant species for systems with Ca:Si ~ 1.5, both for synthetic C-S-H systems and during the initial formation of C-S-H in hydrating tricalcium silicate [150,154].

To overcome the low sensitivity of ^{29}Si MAS NMR at natural isotopic abundance we use modern DNP strategies [137–139]. DNP is based on the transfer of large unpaired electron spin polarization to nearby protons by saturation of the electron spin transitions with microwaves, followed by CP transfer of the enhanced polarization to the ^{29}Si nuclei. The electron polarization is provided here by the organic biradical AMUPol [155] that is added to the wet C-S-H as a minimal amount of d_8-glycerol/D_2O solution before the NMR sample is rapidly cooled to 100 K for the experiments [139,156–158]. The cryogenic temperatures are required to maximize the sensitivity enhancements by DNP, but are also important here to quench proton exchange and prevent the C-S-H from degrading during the experiments. Efficient DNP occurs only for those parts of the sample that have successfully passed through the glass transition. We also note that pore water is susceptible to glass formation when rapidly inserted into the pre-cooled NMR probe even without the addition of a glassing agent such as glycerol [159]. We therefore do not expect the C-S-H structure to be disrupted by our experimental conditions; furthermore, even if pore water does crystallize in parts of the sample, inefficient DNP will suppress the NMR signal from these regions.

The polarizing agent contains labile deuterons, which can lead to the formation of calcium silicate deuterate through isotope exchange. At most, 40 mol% of labile hydrogen in the impregnated C-S-H gels (C-S-H hydrogen, D_2O, and the -OD groups of the d_8-glycerol) are deuterons given our DNP sample formulation and estimated C-S-H composition. If a reasonable allowance for excess pore and adsorbed water is made, this falls to about 25%. In fact, this upper limit is almost certainly never reached. Small-angle neutron scattering studies have shown that deuteron exchange into the gel is a diffusion driven process providing full isotope exchange on the time scale of tens of hours [160]. Since the impregnated sample never spent more than 1.25 h, and usually just 0.25 h, at room temperature prior to experiments, we expect the highest degree of partial deuteration to be surface based and the NMR signal should be representative of fully protonated bulk C-S-H. Moreover, there is little in the way of evidence in the small-angle neutron scattering literature to suggest that isotope exchange modifies C-S-H in any structurally significant way.

One-dimensional $\{^1H\}^{29}Si$ DNP CP echo spectra for the five compositions are shown in Figure 16A. With the exception of the Ca:Si = 1.00 composition, good fits to the line shapes are obtained by modeling each of the constituent Q sites as a Gaussian function, whose amplitudes are used to determine the relative populations of the Q species. Relative signal intensities in DNP enhanced CP MAS experiments are not usually in proportion to the relative populations of the nuclei generating the signal as they often are in experiments using direct excitation without hyperpolarization unless we assume that 1) the length scale of hyperpolarization non-uniformity is larger than the unit cell of the particle, and 2) cross-polarization kinetics can be measured and used to adjust the signal intensities appropriately.

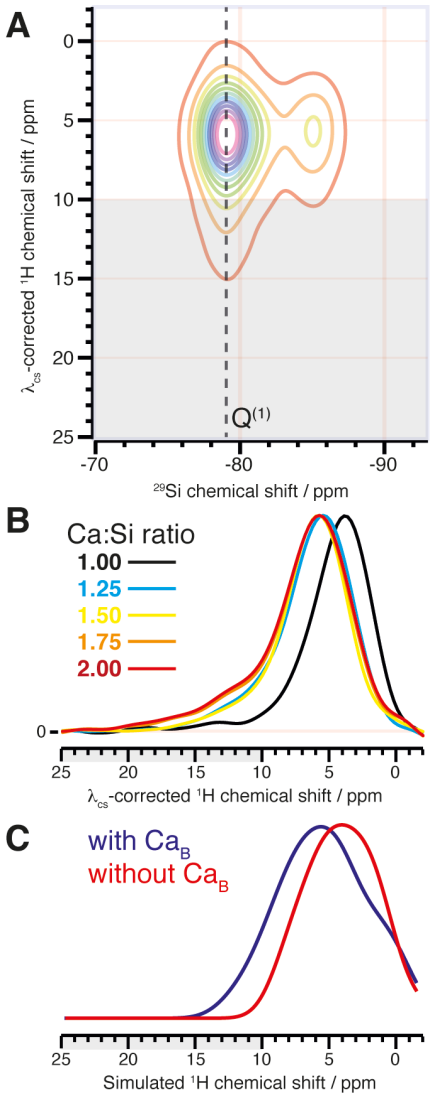

Figure 17: DNP enhanced 2D {^{1}H}^{29}Si HETCOR correlating ^{1}H spectra to specific Si sites. (A) The 2D correlation spectrum for the Ca:Si = 1.50 composition acquired with a 7 ms CP contact time. (B) 1D cross sections parallel to the ^{1}H dimension extracted at the position of the dashed line in the 2D spectrum, representing ^{1}H spectra correlated to $Q^{(1)}$. (C) Simulated ^{1}H chemical shift spectra aggregated over C-S-H substructures that either possess (blue) or lack (red) the bridging calcium site Ca_B. The intensity of these spectra are normalized with respect to the maximum of the $Q^{(1)}$ peak. The region downfield of 10 ppm is shaded to indicate the domain of strongly hydrogen bonded species.

The sizes of the C-S-H particles are sufficiently small and have a proton density sufficient for nearly uniform polarization of the particles over the recycle period. To the second point, we performed cross-polarization measurements for different values of the cross-polarization contact time. This data was fit to a simple *IS* model of CP kinetics for each site [161]. A detailed description of the fitting procedure and the Q populations determined by this method are given in the SI section VIII.

We note here that the failure of the Ca:Si = 1.00 composition to fit well to the three-Gaussian model suggests a different molecular structure.

The $\{^{29}Si\}^{29}Si$ connectivity is measured using 2D refocused INADEQUATE experiments [162], whose application to cementitious systems has hitherto not been feasible without isotopic enrichment [150,154]. In the $\{^{29}Si\}^{29}Si$ INADEQUATE spectrum only signals from covalently bonded $^{29}Si - O - ^{29}Si$ pairs are retained. For linear silicate chains at natural isotopic abundance, these constitute at most 0.5% of all Si – O – Si pairs. The improvement in NMR sensitivity provided by DNP makes it possible to obtain such spectra [163], as shown in Figure 16B. Autocorrelation peaks corresponding to $Q^{(1)}$-$Q^{(1)}$ dimer and $Q^{(2p)}$-$Q^{(2p)}$ extender units are observed, but peaks corresponding to $Q^{(2b)}$-$Q^{(2b)}$ are always absent, consistent with the dreierketten model. Remarkably, the usually dominant $Q^{(1)}$-$Q^{(1)}$ autocorrelation peak is entirely absent for the Ca:Si = 1.00 composition (SI section IX), suggesting that this composition does not contain silicate dimers. Cross peaks from all three Q sites to $Q^{(2p)}$ are also observed. Using the chemical shift constraints from the deconvolution of the 1D CP echo spectra, the INADEQUATE spectra are decomposed using 2D Gaussian line shapes to model each of the six possible correlation peaks. This line shape generates reasonably good fits (SI section IX), suggesting that the chemical disorder is very local. The 2D peak intensities are fit simultaneously across the four compositions for a conditional probability $P(A|B)$ that Q site A is connected to Q site B.

2D $\{^{1}H\}^{29}Si$ HETCOR experiments were used to correlate ^{1}H chemical shifts with the ^{29}Si chemical shifts. Measurements were made using CP contact times of 0.7 ms and 7 ms for each sample. The use of a short contact time biases the contribution to the NMR signal from those protons that are close to the correlating ^{29}Si nuclei, as compared to longer range correlations observed in the long contact time experiment, which samples proton environments out to ~1 nm.

The line shape in the 2D $^{1}H\{^{29}Si\}$ HETCOR spectrum shown in Figure 17A is dominated by inhomogeneous broadening resulting from chemical disorder, which prevents an accurate line shape deconvolution on the basis of proton site. Cross sections of these spectra yield ^{1}H chemical shift spectra correlated to specific Q sites, as shown in Figure 17B for the $Q^{(1)}$ correlation and in the SI section X for the others. We find that the intensity of the of the $Q^{(1)}$ site relative to the $Q^{(2)}$ sites is greater at shorter contact time, implying that $Q^{(1)}$ species are located in a relatively hydrogen rich environment. We also see that the ^{1}H chemical shift profiles for the Ca:Si ≥ 1.25 ratios possess a significant contribution above 10 ppm, indicative of strong hydrogen bonding [164]. A comparison to HETCOR spectra taken at short contact time (SI section X) reveals that the prominence of the downfield region for the $Q^{(1)}$ correlated cross sections increases significantly at short contact time, a

feature which is not shared by the $Q^{(2b)}$ and $Q^{(2p)}$ cross sections. This suggests that the strong hydrogen bonding occurs primarily in association with $Q^{(1)}$ sites. We note that the signature of strong hydrogen bonding is almost entirely absent from the HETCOR spectrum of the Ca:Si = 1.00 composition, once again producing a spectrum deviating substantially from its relatively calcium rich counterparts.

Table 6: Dimer mole fraction x_0 and mean repeat index for the four compositions analyzed.

Sample	x_0	$\sum_{n=0} x_n n$
Ca:Si = 1.25	0.751	0.450
Ca:Si = 1.50	0.816	0.285
Ca:Si = 1.75	0.873	0.185
Ca:Si = 2.00	0.900	0.136

The line shapes lack any significant features near 2 ppm, where basic hydroxide protons would be prominent, suggesting any secondary amorphous or crystalline $Ca(OH)_2$ phase, if present, is not intimately mixed with the C-S-H structure. Such a signal was previously reported for C-S-H compositions with Ca:Si ratios up to 1.5 [150,154]. It may be that the C-S-H/$Ca(OH)_2$ nanocomposite results from excessive drying and aging of the sample. Indeed, a recent high energy X-ray study lending support for a secondary phase of $Ca(OH)_2$ nanosheets interwoven into the C-S-H interlayer suggests that the $Ca(OH)_2$ phase grows as C-S-H ages [130].

5.5.3 Structural determination

It is known that C-S-H resembles a defective tobermorite [16,165]. In contrast to previous structural modeling studies for C-S-H, which consider random defects in tobermorite systems containing hundreds of atoms [16,42], we adopt a methodology that focuses on the systematic creation of structurally well-defined defects. The defective substructures are then used as building blocks to represent C-S-H at higher Ca:Si ratios.

A suitable base structure is required to begin. Tobermorite structures are generally named after their characteristic interlayer distances; namely, 9 Å, 11 Å, or 14 Å tobermorite [42,43,166]. The choice of base structure for modeling depends the Ca:Si ratio [17] and drying conditions [20,128]. A dataset compiled by Richardson [20] has shown that the interlayer distance in C-S-H decreases from ~13-14 Å at Ca:Si = 0.8 to ~10 Å at Ca:Si = 1.5. Recently, Roosz *et. al.* [167] have shown that sample

preparation and relative humidity significantly affect the interlayer distance measurement. The interlayer distance measured for a C-S-H of Ca:Si = 1.2 using XRD in dry and fully hydrated states were 9.5 and 12.3 Å, respectively. Since our samples are hydrated, we choose 14 Å tobermorite (Figure 15D) as the base motif for constructing our atomic-level model of C-S-H.

A defect is introduced by the removal of an SiO_2 unit from a $Q^{(2b)}$ unit. The extent to which we need to create defects is determined by the distribution of silicate chain lengths. With the Q species populations and connectivities we can determine the distribution of chain lengths for each composition, as described in the SI section IX and given in Table 6, to find

$$\sum_{n=0} x_n n = \frac{P(Q^{(2p)})}{P(Q^{(1)})} \tag{47}$$

where x_n is the mole fraction of dreierketten chain species with repeat index n, and

$$x_0 = P\left(Q^{(1)} \middle| Q^{(1)}\right), \tag{48}$$

as the mole fraction of dimers. The quantitative NMR results thereby provide three independent constraints for calculating the distribution of silicate chains for each C-S-H composition. Using these constraints, we adopt a Monte Carlo method to predict the mole fraction distribution for chains up to n = 10, which we report in the SI Section XI (8.4.1) for each composition.

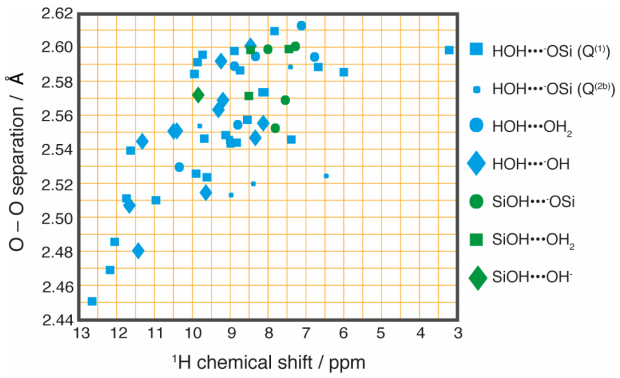

Figure 18: Scatter plot showing the correlation between the O–O distances and the chemical shifts of protons participating in the different types of hydroxyl-oxygen interactions occurring in the C-S-H substructures.

Defect creation transforms the silicate tetrahedrons adjacent to the removed $Q^{(2b)}$ site into $Q^{(1)}$ sites, requiring the addition of H^+ and $CaOH^+$ to satisfy requirements of local charge balance. Additional

molecular units of H_2O and $Ca(OH)_2$ can also be incorporated into the structure. The defective motif is deemed acceptable if correct atomic bond distances, coordination numbers, and local charge balance remain satisfied after structural relaxation using density functional theory (DFT), leading to a series of substructures which are classified on the basis of defect geometry. Reduced unit cells are constructed by connecting the defect units through an aqueous interlayer or an aqueous interlayer with a Ca_I and additional OH^- for charge balance. In order to study medium range effects, we also consider different ways to combine the reduced unit cells, resulting in chain, dimer, and pentamer motifs.

We study the effect of these different defect structures on the ^1H chemical shifts. A set of reduced unit cells are chosen to ensure a wide variety of different local defect environments as represented by the defect classification scheme described in the SI section XI (8.4.1). In Figure 17 C, we show two calculated ^1H chemical shift spectra composed by summing over substructures that either possess or lack Ca_B. In comparison with the experimental ^1H spectra in Figure 17 B, these calculated spectra suggest that *Ca_B is responsible for generating ^1H NMR signals downfield of 10 ppm*. Furthermore, the association between downfield shifted protons and hydrogen bonding leads us to infer that bridging calcium holds terminating chains together by coordinating to the defect site and promoting the formation of strong hydrogen bonds. On this basis we might also conjecture that bridging calcium is preferentially associated with silicate dimers, as suggested by the fact that both strong hydrogen bonds and dimers are lost when crossing under to the Ca:Si = 1.00 composition, though without further evidence this remains speculative.

The proton chemical shift calculations provide additional structural insight regarding the nature of the hydrogen bonding interactions. As Figure 18 shows, there is a linear correlation between the calculated ^1H chemical shift and the O – O separation of the species engaged in electrostatic hydrogen-oxygen interactions, a well-established trend for inorganic oxide systems [164]. In particular, we observe that interlayer water protons that interact with interlayer hydroxide ions and the oxygen atoms of $Q^{(1)}$ sites dominate in their contribution to the ^1H chemical shift signal above 10 ppm. The key observation here is that each of these types of protons are located within 3 to 4 Å of Ca_B. Furthermore, we may consider that the protons involved in hydrogen bonding between interlayer water and a $Q^{(1)}$ oxygen atom are less than a 3 Å from the $Q^{(1)}$ silicon atom and are therefore favored in the HETCOR experiments at short contact time. For only two of the substructures analyzed, one of which lacks Ca_B entirely, the proton from the strongest OH_2–OH^- group is located greater than 5 Å away from a $Q^{(1)}$. We infer that it is these types of protons which explains the prominence of the region downfield of 10 ppm in the $Q^{(1)}$ correlated proton spectrum,

and that their association with bridging calcium in the structures that we have analyzed strengthens the confidence of our association.

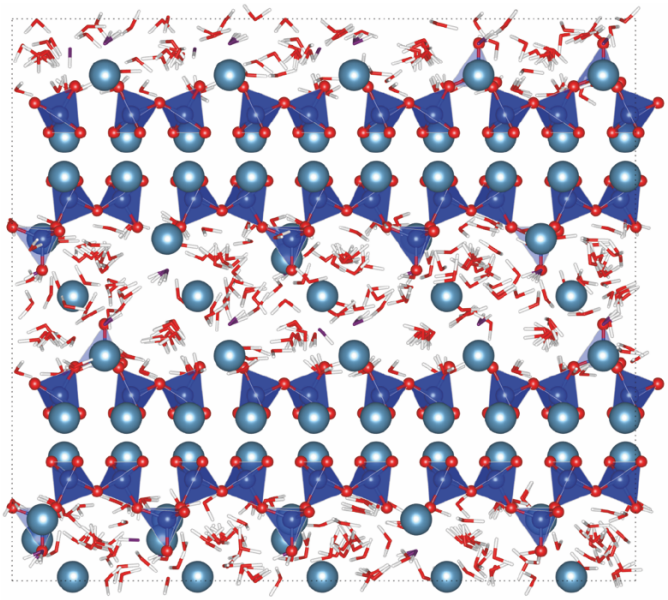

Figure 19: The structure determined here of C-S-H for a Ca:Si ratio of 1.5, viewed along the [A] axis. The relative proportions of dimers, pentamers, octamers, undecamers, and tetradecamers are 81%, 14%, 3% 1%, and 1%, respectively. The chemical composition of this structure is $Ca_{1.5}SiO_{3.35}(OH)_{0.3}\bullet 2H_2O$*. The relative positions of hydroxyls and water molecules have been relaxed keeping all other atoms frozen for ease of visualization.*

Construction of structures that are representative of C-S-H proceeds by drawing from these defective substructures and the defect-free motif and tessellating them in a way that satisfies both the constraints of stoichiometry and the chain distribution determined by the ^{29}Si NMR results. High Ca:Si ratios are obtained by deprotonation of a $Q^{(2b)}$ silanol and adding $CaOH^+$ and $Ca(OH)_2$ in the form of Ca_A to the interlayer (Figure 15E). Our representative C-S-H unit cell is a tessellation of sixty such substructures coming to roughly 3 nm on each side, consistent with the degree of uniformity found by high-resolution analytical TEM. One such bulk C-S-H structure permitted by the ensemble of experimental NMR constraints determined for the Ca:Si ratio of 1.50 is shown in Figure 19. A 2 ns MD simulation at constant pressure and temperature (300 K) shows that the resulting structures are stable, with realistic bond lengths and coordination geometries predicted. The C-S-H structures we propose for each the four compositions are given in the SI section XII (8.4.2). Unlike previously proposed structures based upon defective tobermorite [16,20,21,168], our computational methodology specifies unambiguously the positions and coordination of calcium in the interlayer, rather than leaving them undefined or relegating its existence to a second phase, as in the tobermorite/$Ca(OH)_2$ model. We do not claim that these structures represent the most energetically stable configurations; rather, we locate a viable, locally minimized configuration satisfying the NMR

constraints. The proposed bulk structures are representative of a series of similar structures with similar defect concentrations and slightly different atomic arrangements. This should not change the average properties, but does explain why there is very little structural order seen in X-ray powder diffraction of non-dried C-S-H.

5.6 Conclusions

We introduce a new synthetic method for C-S-H which controls pH throughout the process, and we produced uniform C-S-H with controlled Ca:Si ratios up to 2.0 for the first time. High sensitivity DNP solid-state NMR techniques have been used to characterize unique highly uniform synthetic C-S-H particles with high Ca:Si ratios. In conjunction with atomistic scale modeling, atomic-level structures of defective tobermorite coherent over Ca:Si ratios from 1.25 to 2.00 have been determined without invoking secondary phases or glassy structures as confirmed by the clear absence of a signal from basic Ca-OH units in the 2D $\{^{1}H\}^{29}Si$ HETCOR experiments. To interpret this data, we developed a computational approach which explores defective tobermorite substructural candidates, combining them in a manner satisfying our experimental constraints in order to build a full 3D structure which provides an accurate representation of structural and chemical environments in C-S-H for Ca:Si ratios up to 2.0. An essential aspect of these structures is the inclusion of a calcium site in the interlayer which bridges chain terminating silicate $Q^{(1)}$ sites. This site is associated with an environment of strong hydrogen bonding which stabilizes the structure and, consequently, promotes high Ca:Si ratios in C-S-H. This thus establishes a clear relation between the atomic-level defect structure and the high Ca:Si ratio in C-S-H. This knowledge of the defect structure is a prerequisite for overcoming the self-limiting growth of C-S-H and to better understand growth mechanisms and kinetics. Such knowledge can further help formulate new classes of sustainable cements capable of exhibiting strong chain-bridging hydrogen bonding features while ensuring the early age strength development of the material.

ASSOCIATED CONTENT

Supporting Information

Supplementary text and figures (.pdf)

Coordinate files for substructures and bulk representations

The Supporting Information is available free of charge on the ACS Publications website.

AUTHOR INFORMATION

Corresponding Authors

* Email: lyndon.emsley@epfl.ch, paul.bowen@epfl.ch

Author Contributions

All authors have given approval to the final version of the manuscript.

ACKNOWLEDGMENT

The authors would like to acknowledge funding from the Swiss National Foundation (Grants No. 153044 and 200021_160112) and ERC Advanced Grant No. 320860. We would also like to thank Dr. Sandra Galmarini, Dr. V.K. Parashar, Dr. B. Lothenbach, Dr. T. La Grange, and Dr. D. Demurtas for fruitful discussions. Dr. D. Lambert and Prof. G. Massonnet are thanked for their assistance with collecting the Raman data. The authors declare no competing financial interests.

Chapter VI. Interlayer structure

Title : Interlayer nanostructuring of calcium silicate hydrates

Authors

Aslam Kunhi Mohamed, Sandra Galmarini, Steve Parker, Karen Scrivener, Paul Bowen

Abstract

The layered and porous calcium silicate hydrate (C-S-H) is the glue that holds together cement structures. C-S-H is composed of calcium silicate chains, which are well characterized, separated by an interlayer space consisting of calcium ions with associated hydroxyl ions and water molecules. The interlayer structure of this hydrate material is ill defined and its composition and structure are key for the production of knowledge based cements with lower carbon footprints and our advancement of futuristic cements. Here, we apply a bottom up approach in precisely defining the chemical constituents of C-S-H and unravel the intricate structure of the C-S-H interlayer using atomistic simulations. We discover two main types of water molecule depending on its connectivity and its stochastic relation with calcium leading to a degree of non-crystallinity. A new thermodynamically stable site for interlayer calcium, named “pairing calcium”, is also discovered. A higher water content restricts the interlayer calcium ions capacity to occupy this pairing site. This creates a local ordering and/or disordering of the interlayer depending on the local water content of C-S-H making it a nano -crystalline material and inhibiting ordering at a larger length scale.

In one sentence this paper:

The key to a sustainable and futuristic cement lies in unravelling the intricate structure of the C-S-H interlayer.

Keywords: Nano structure, Calcium silicate hydrate, molecular dynamics, layered materials

6.1 Introduction

Cement is a magical material, when mixed with water it solidifies to form a strong structural material, that last for 50-100 years and is of a relatively low cost made from abundant elements in the earths' crust. Calcium silicate hydrate (C-S-H) is the main product of the Portland cement hydration reaction. Although Portland cement has been known for more than a century, fundamental understanding of its main hydrate C-S-H has greatly limited the advancement to meet the futuristic/technological and sustainability requirements of this century[1,2] . C-S-H is a defective nano crystalline phase with variable stoichiometry[18,23,27,55,169]. This makes it extremely difficult to characterize experimentally. Many studies on C-S-H have been carried out to understand its nano structure over the past two decades[49,51,53,154,170]. Among many factors, the prominent ones that make this material difficult to characterise are (a) the inability to synthesize C-S-H of a similar stoichiometry to cementitious C-S-H, (b) no long-range three-dimensional ordering, (c) delicate layered structure with a varying water content, which can be altered by the procedure involved during characterization (such as drying, relative humidity, temperature, treatment with any solvent/solution).

Some of the prominent techniques employed for characterization include XRD, NMR, SEM, TEM, SAXS, SANS and IR [17,51,60,62,78,169,170]. From the X-ray diffraction patterns, only two broad peaks are observed, indicating a repeat distance characteristic of the calcium-oxygen structure in the so-called calcium plane[25]. From ^{29}Si NMR, the silicate speciation in C-S-H has been thoroughly studied to confirm the presence of a 'dreierketten' structure similar to that found in Tobermorite minerals [42,43]. From the extensive work done on C-S-H, it has been generally agreed that the structure of C-S-H has a close resemblance to tobermorite minerals [14,51,128,171]. There exist a certain number of different tobermorite polymorphs, while at low Ca/Si ratios (~ 0.83) C-S-H seems akin to a nanocrystalline 14 Å tobermorite. The evidence pointing to a certain polymorph is less clear at higher Ca/Si ratio[16,57,170]. The approximate stoichiometry of C-S-H is obtained by incorporating point defects in the perfectly ordered tobermorite structure, and using interlayer calcium and hydroxyl ions to maintain overall charge neutrality, as illustrated in Figure *20*A [27,170,172].

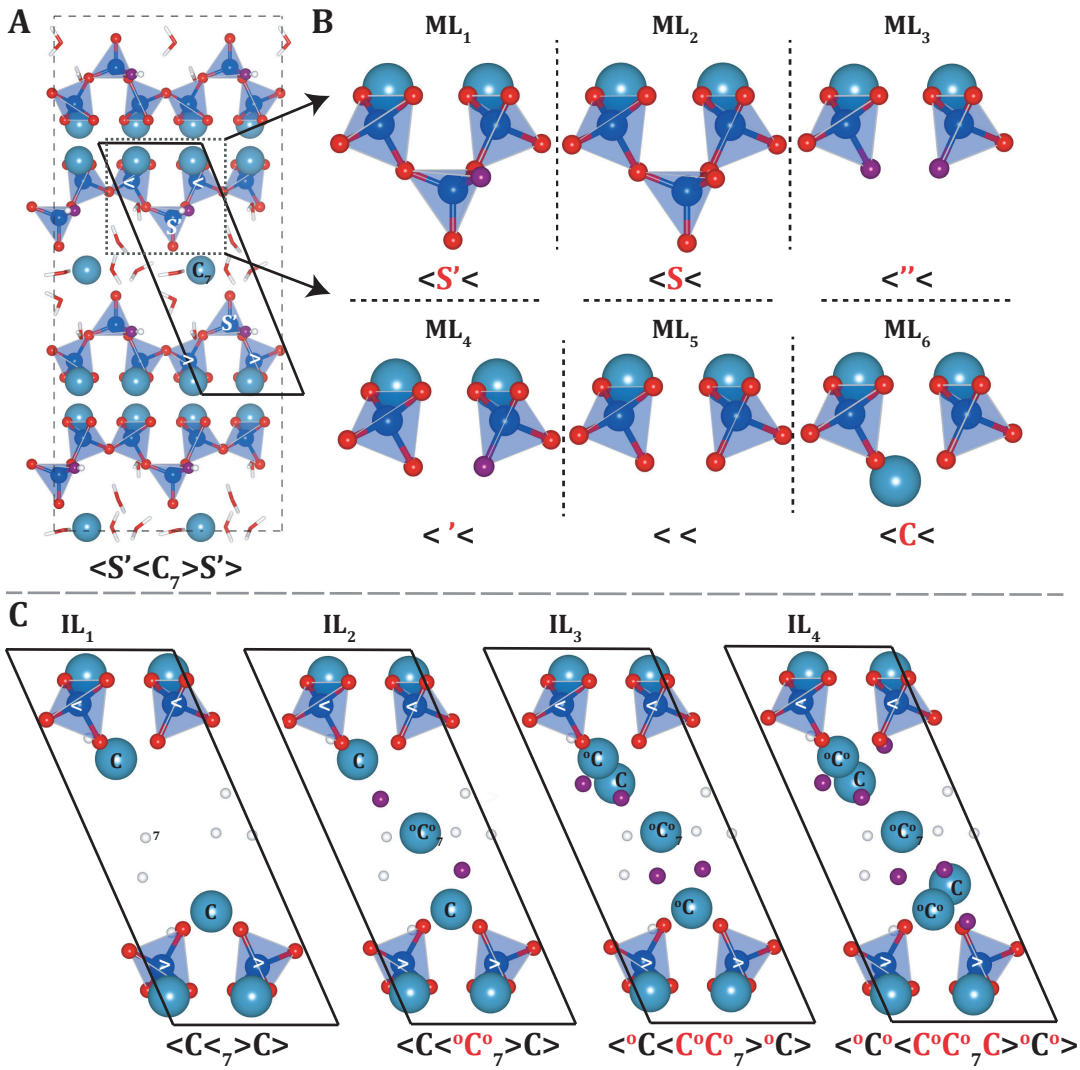

Figure 20*: Bulk structure of a non-defective 14 Å tobermorite with the primitive unit cell indicated as solid black lines (A). The square box with the dotted line shows the "dreierketten" (three-unit repeating) structure of the silicate chain with the notation developed by Kunhi Mohamed et al.*[172]*. The various possible defects considered in this paper are shown in (B) and (C) with its chemical "building block" notation*[172] *written below it. A simpler notation for each type of defects is also shown on top of each images in (B) and (C). There are six main layer (ML) defects on the dreierketten chain shown in (B). The chemical building blocks shown in (B) are not necessarily charge neutral. In (C), the different number of interlayer calcium atoms that can be incorporated in the interlayer are shown for a neutral brick (IL) with the* ML_6 *type main layer chain and seven water molecules. The charge neutrality is maintained by additional hydroxyl groups in the interlayer, added close to the calcium atoms as shown in (C). In addition to these, the water content of these bricks can also be varied from 3 to 11 water molecules per brick, which is not shown in the images here. Detailed description of the chemical "building block" notation can be found in* [172]*. Atomic color code used are calcium - turquoise, silicon -dark blue, oxygen – red, hydroxyl oxygen – purple, hydrogen-white. In (B), hydrogen atoms are not*

shown, and the white spheres shown correspond to water molecules.

A few atomistic models of C-S-H have been proposed in the literature based on either 11 Å tobermorite [67,79,82] or 14 Å tobermorite[170,172]. The first full atomistic model was proposed by Pellenq et al.[79] which had under-coordinated calcium atoms and a significant percentage of silicate monomers. In C-S-H, silicate species are known to exist in chains of 3n-1 in length (n≥1), i.e., mainly as dimers, pentamers, octamers and so on [49,56,154,170]. These shortcomings were later improved by Abdolhosseini Qomi et al.[82] However, the presence of monomers was corrected by random polymerization of silicates, something that resulted in silicate species in violation of the 3n-1 rule. Another prominent model is from Kovacevic et al.[67] where the authors tested three different ways to construct a bulk C-S-H structure, and concluded that the method for making the initial structure determines the energy of the final structure. The authors defined several rules for random removal of silicates and the addition of calcium or $CaOH^+$ ions to the interlayer giving them many energetically equivalent structures. However, these random removal methods in both models from Kovačević et al.[67] and Abdolhosseini Qomi et al.[82] failed to completely define the atomic structure of C-S-H that is in concurrence with experiments. Richardson[20] proposed a hypothetical perfectly ordered crystalline C-S-H based on general guidelines for the type of defects and geometrical reasoning. Although the guidelines written by Richardson look promising, it is unlikely that such an approach will be able to define the defective nano crystalline structure with significant disorder expected for C-S-H.

Recently, based on ^{29}Si and ^{1}H DNP NMR coupled with DFT calculations, Kumar et al.[170] proposed atomic structures of synthetic C-S-H with Ca/Si ratio ranging from 1.25 to 2.0. The authors were able to generate the structures taking into account the silicate connectivity and speciation calculated from the NMR constraints. They also concluded that a calcium ion replacing the bridging silicate of a 14 Å tobermorite is a defining feature of C-S-H. Thus the authors were able to define the calcium-silicate main layer of C-S-H correctly in accordance with the experiments. There are two limitations of this model. In their model, the positions of the interlayer species were randomly defined or derived from 14 Å tobermorite due to the lack of experimental or theoretical evidence. The interlayer consisted of water, additional calcium and hydroxyl ions to meet the required Ca/Si ratio of the structure. The authors neither studied the interactions of the defects used to build the bulk structures nor the different permutations and combinations of arranging them in the bulk structure to yield the most stable configurations . In this paper, we are focussing on addressing the nature of

the C-S-H interlayer environment and thereby building an energetically stable atomic structure of C-S-H.

One of the key reasons for not being able to resolve the atomic structure of C-S-H is the difficulty in characterizing the interlayer. As mentioned earlier, the interlayer is composed of water molecules, calcium ions and hydroxyl ions. In the case of calcium, as of yet, there has been no successful ^{43}Ca NMR done on C-S-H that could resolve the nature of interlayer calcium ions other than identifying two types of calcium: main layer and interlayer. From the results of Kumar et al., with the calcium at the bridging site replacing a silicate tetrahedra and without any interlayer calcium atoms or removing silicate dimers, the highest Ca/Si ratio that can be achieved is 1.5. There are no experimental studies that gives the exact positions of additional calcium in the interlayer. Hence, the exact position of additional calcium ions in the interlayer of C-S-H is *a priori* unknown. From the modeling point of view, in order to have a C-S-H structure of higher Ca/Si ratio, a calcium ion with two hydroxyl groups are arbitrarily added to the interlayer [67,82,170], assuming that the interlayer species are flexible enough to relax to the minimum energy position.

Another aspect is the interlayer water content, which is an integral part of C-S-H. Proton NMR [51,58],relaxometry [62,173,174] measurements and inelastic neutron scattering[61] done on C-S-H have shown the existence of protons in both Si-OH (seemingly negligibly small for higher Ca/Si ratios), Ca-OH and H_2O. However, none of these studies have been able to get any insights on the exact positions and quantities of these different types of protons.

Here, we try to quantify the interactions of defects and understand the complex interlayer structure in C-S-H using classical molecular dynamics simulations and DFT calculations. A bottom up methodology developed in a recent paper by Kunhi Mohamed et al.[172], where a string of characters representative of predefined C-S-H building blocks was used to encode the structure of C-S-H from defective 14 Å tobermorite, is adopted. With the help of this methodology, a set of unique *C-S-H structural units* which we will refer to as “bricks” are created.

6.2 Methods

6.2.1 Simulation details

All molecular dynamics (MD) simulations were done using DLPOLY[96] with an improved set of potentials from that used by Galmarini et al. in the Cement FF force field.[11] The shell model was used for non-hydroxyl and water oxygen atoms[109]. The interaction of calcium and water

(TIP4P/2005 [107]) has been fitted to get a calcium coordination of seven for the main layer calcium atom and six for the interlayer calcium atom of 14 Å tobermorite. The improved force field will be available at the cemff database [32] as CementFFV2. All the calculations are done with a time step of 0.2 fs with a cut off radius of 8.5 Å using Nose-Hoover thermostat. Two types of minimization schemes were employed before the production run for 1.4 ns.

- Soft minimization: Involved a three step pre-production minimization procedure.
    - Zero temperature molecular dynamics (or damped molecular dynamics implemented within the DLPOLY framework) for all atoms
    - Relaxing the water molecules and hydroxyl ions keeping the others frozen in an NVT ensemble at 300 K
    - All the atoms relaxed in a NST ensemble (similar to a NPT ensemble but the in-plane stresses are relaxed: ideal for non-orthogonal simulation box) for 300 ps at 300 K
    - Production run for 1.4 ns in a NST ensemble at 300 K
- Hard minimization: In addition to the steps mentioned above, the structure is subjected to a cyclic heating to 1000 K in NVT ensemble followed by relaxation at 300 K in a NST ensemble, each for 300 ps. This cyclic heating and cooling is done twice making sure the structure has enough energy to relax to a more stable minimum before the production run. We have seen that two cycles are sufficient for most of the bricks to become well ordered.

For selected structures, density functional theory (DFT) calculations were done using the Quantum Espresso[105] package to cross-check the MD results. We used ultrasoft pseudo-potentials with a van der Waals correction (DFT-D2 method)[175], the Monkhorst-Pack k-points mesh of 2 x 2 x 1, and a plane wave cut-off of 80 Rydberg for the structural optimization. A dense mesh was sometimes employed to cross-check the convergence of certain structures.

6.2.2 Types of bricks

The structural units or bricks of C-S-H are enclosed by a primitive cell shown as a solid line in Figure 20A. The detailed information on the notations of the chemical building blocks can be found in the original paper[172] (Figure 7 in chapter 4). As shown in Figure 20B, the dreierketten structure involves two pairing tetrahedra (< or >) and a bridging one (S). The main defects that can be created in the main layer (ML) dreierketten structure to get modified Ca/Si ratios are (as shown in Figure *20*B) remembering that these defective building blocks are not necessarily charge neutral :

1. ML_1: The original dreierketten structure in 14 Å tobermorite.

2. ML_2: From ML_1, the hydrogen atom of the silanol group in the bridging tetrahedra is removed i.e. the silanol group is deprotonated
3. ML_3: From ML_2, the bridging tetrahedra is removed (SiO_2) and two hydrogen atoms are added to the dangling oxygen atoms of the pairing silicates
4. ML_4: Similar to ML_3, but only one hydrogen atom is added
5. ML_5: Similar to ML_3, but no hydrogen atoms are added.
6. ML_6: To ML_5 a calcium ion is added at the bridging site in accordance with the results of Kumar et al.[170]

There can be also a missing dimer defect, absence of two pairing tetrahedra [172], which is not shown in Figure *20*.In the interlayer space, there can be up to three calcium ions which can make a brick with a Ca/Si ratio of maximum 2.25 (IL_4 in Figure *20*C), which is sufficient to describe C-S-H with a Ca/Si ratio always less than 2.1 [2]. As shown in Figure *20*C, a brick is made up of two ML defects parallel to each other separated by the interlayer space on one side. The ML defects and the calcium ions in the interlayer combined with additional hydroxyl ions added close to it, can make the entire brick charge neutral. The initial positions of these interlayer calcium and hydroxyl ions are arbitrarily set. In addition, the number of water molecules in a brick can also be varied from 3 to 9 and occasionally above 10 molecules (in the case of the missing dimer compensating for the large reduction in volume/or to keep the number of oxygen atoms constant). All these can be combined in numerous permutations to get several distinct types of bricks.

A supercell of all the individual bricks (in a 4 x 4 x 2 layout in each direction) are subjected to the hard minimization scheme if not stated otherwise. The stability of these bricks is compared to a stoichiometric equivalent of the well-defined phases of lime, quartz and water as shown in the following reaction.

$$n_1 \cdot CaO + n_2 \cdot SiO_2 + n_3 \cdot H_2O \rightarrow \left[(CaO)_{n_1}(SiO_2)_{n_2}(H_2O)_{n_3}\right]_b , \ \Delta H \quad (49)$$

where ΔH is the enthalpy effect for the brick with the composition $(CaO)_{n_1}(SiO_2)_{n_2}(H_2O)_{n_3}$. where n_1, n_2 and n_3 are fractions with $n_1 + n_2 + n_3 = 1.0$

For the defects interaction calculations, the bottom silicate chain structure of the two bricks considered are kept the same. The interactions in all the three directions are studied by stacking the two bricks adjacent to each other in the cell vector $\vec{a}$, $\vec{b}$ and $\vec{c}$ directions and then making a supercell of 32 bricks (also in 4 x 4 x 2 layout, see Figure S27). That is, the two bricks are arranged such that the origin of the second brick is shifted by the cell vector $\vec{a}$, $\vec{b}$ and $\vec{c}$ respectively for $\vec{a}$, $\vec{b}$ and $\vec{c}$

direction calculations. The soft minimization scheme is used for interaction calculations. In all these cases, the individual bricks are not minimized prior to the interaction calculations. These calculations were also done for pre-minimized individual bricks and the obtained energies were within the error of the computation. The interaction enthalpy is calculated in each direction i using the following equation.

$$\Delta H_i^{b1b2} = H_i^{b1b2} - 0.5\times(H^{b1} + H^{b2}) \qquad (50)$$

where b1 and b2 refer to the individual bricks considered (see Figure S27), H_i^{b1b2} is the enthalpy from MD simulations of bricks b1 and b2 arranged in i direction and H^{b1} is the enthalpy calculated for a supercell of a single brick b1 and similarly for H^{b2}.

6.3 Results and discussion

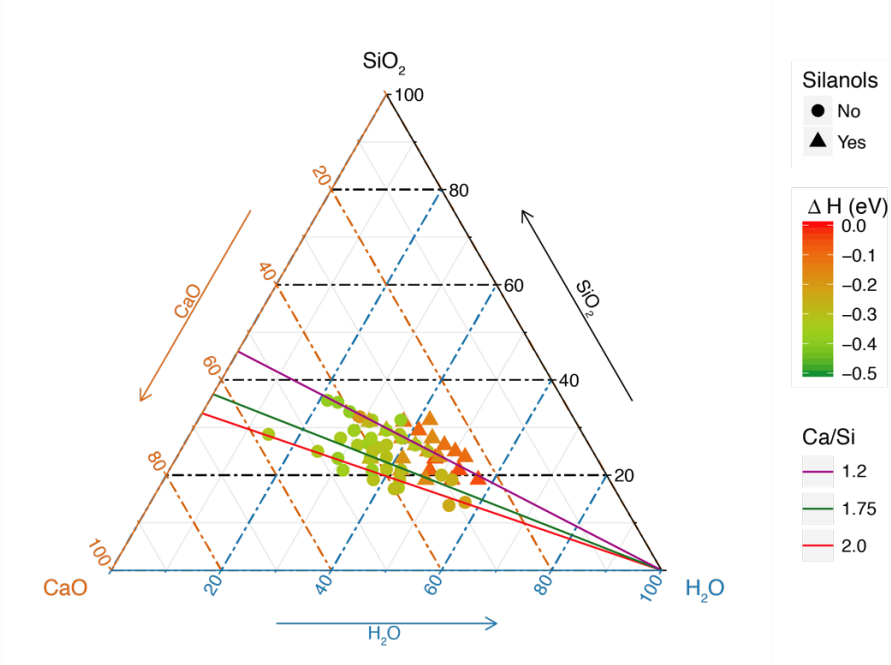

Figure 21: Ternary diagram showing the enthalpies of the bricks calculated using MD showing clearly that those without silanol groups (●) are energetically preferred over those with silanol groups (triangle). We can also see that the greener on the left hand side of the diagram correspond to structures with lower a water content.

The enthalpies of the bricks calculated are plotted in a ternary diagram shown in Figure 21. In this Figure, only the bricks with the lowest enthalpy calculated with a given chemical composition are

shown. There are some chemical compositions with silanols (triangles) and without silanols (circles) that are very similar and hence can overlap but with different energies (colour scale). It can be clearly seen that the structures with silanol groups are found to be less energetically stable. This is consistent with that observed by ^{29}Si NMR [51] measurements on synthetic C-S-H where negligible amounts of silanols are found in synthetic C-S-H .

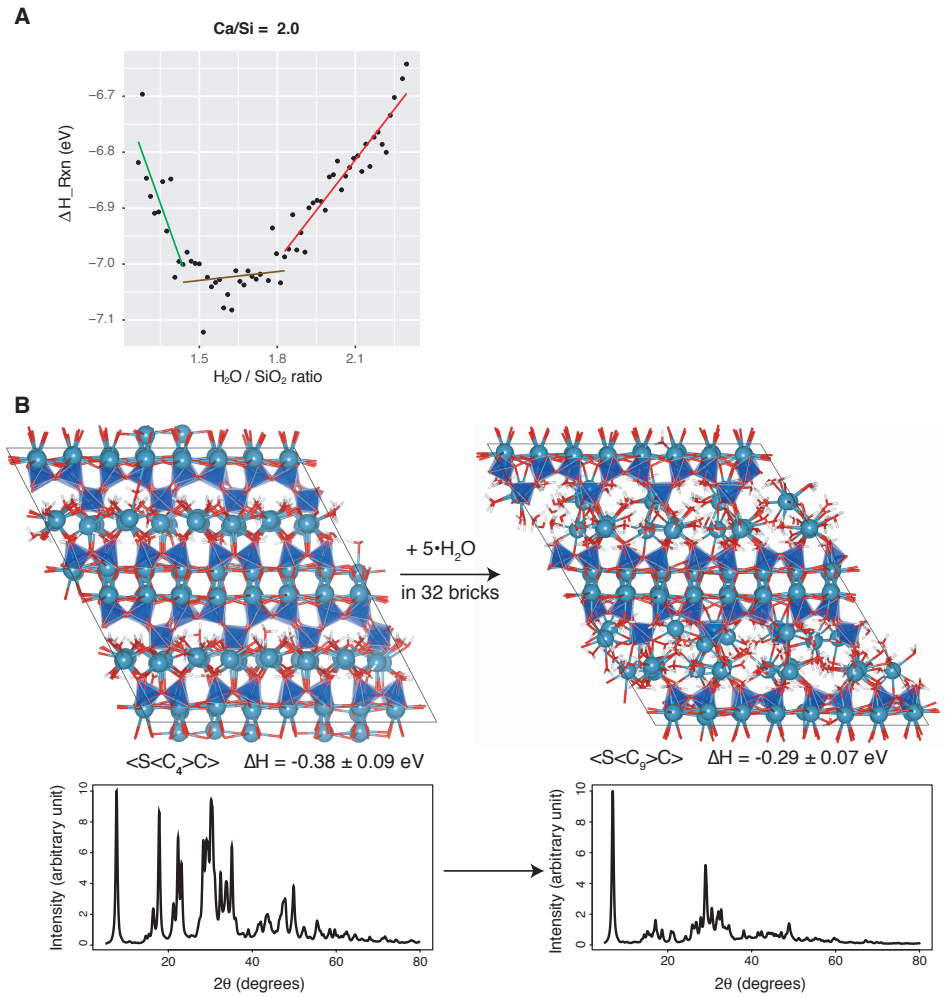

Figure 22: In (A) the enthalpy of $oC < oCXoC > oC >$ bricks without the normalization (ΔH_Rxn) is plotted against the number of water molecules per brick with a fixed Ca/Si ratio and a variable water content $(CaO)_2(SiO_2)_1(H_2O)_x$, with x varying from 1.3 to ~ 2.3 or X from 3 to 7. In (B), supercell structures of two bricks, $b1 = < S < C4 > C >$ and $b2 = < S < C9 > C >$, with the same CaO/SiO_2 ratio of 1.2 but with different H_2O/SiO_2 ratio of 0.8 and 1.8 respectively are compared. A more crystalline structure is obtained with the lower water content structure. The simulated XRD patterns of each structure is shown below its atomic structure image in (B). Atomic colour code used are calcium - turquoise, silicon -dark blue, oxygen – red, hydroxyl oxygen – purple, hydrogen-white.

To understand the permissible amount of water in a brick, a supercell (4×4×2) of a brick , $\mathrm{b} = <$ $\mathrm{oC} < \mathrm{oC_3oC} > \mathrm{oC} >$ is constructed. By adding two water molecules to each of the bricks of this supercell, a series of supercell structures with its overall water content varying from H/Si = 1.3 to 2.3 is achieved. The enthalpy calculated from MD without the normalization in (49), i.e. $n_1 = 8, n_2 = 4$ and $n_3 \in (3, 7)$ are integers with $n_1 + n_2 + n_3 > 1$, averaged over the 32 bricks of the supercell is

plotted in Figure 22A. The slope of this plot is the chemical potential of adding water assuming a negligible entropic contribution at room temperature. We observe three distinct slopes for adding water to this supercell of bricks of Ca/Si = 2 or a stoichiometry of $(CaO)_2(SiO_2)_1(H_2O)_x$, $1.3 \leq x < 2.3$. The H/Si ratio between 1.8 and about 2.2 is found to have a constant chemical potential explaining the possibility of a variable water content in C-S-H (red line in Figure 22A). However, lowering the H/Si to less than 1.8, we find two different regimes, i) for H/Si 1.5 to 1.8 with an almost constant enthalpy (i.e. next to zero slope) and ii) for H/Si < 1.5 with a negative slope and correspondingly a different chemical potential (green line in Figure 22A), indicating that for lower water concentrations, especially H/Si < 1.5, the water molecules are more strongly bound and more difficult to remove from the bricks. These calculations have to be repeated for other bricks to understand how the water content varies with the Ca/Si ratio of the brick. It is also interesting to note that a lower water content leads to a more crystalline interlayer structure (Figure 22B). Here a more crystalline structure is created with a lower water content (H/Si = 0.8) which allows the calcium atoms to move into a preferred site in the interlayer region. This is observed even without resorting to the hard minimization (only the soft minimization was used, see methods section) indicating low energy barriers.

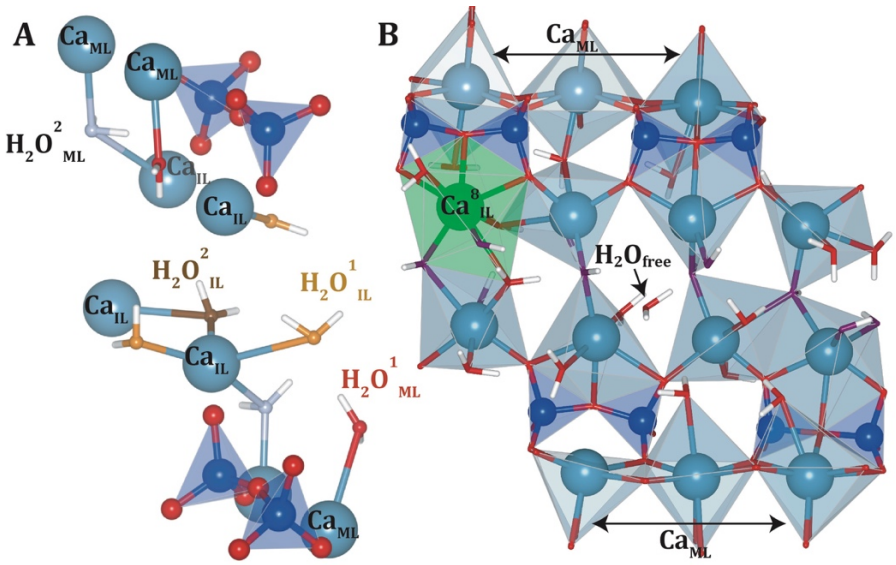

Figure 23: Different types of water in C-S-H bricks are shown. The water molecules which are strongly coordinated or more crystalline are shown in (A), denoted as $H_2O_y^x$ *where* x *indicates the number of calcium ions it is bonded to and* y *indicates whether the water is bonded to only interlayer calcium ions (IL) or to one of the main layer calcium ions (ML). The less crystalline water molecules are shown in (B). The green coloured calcium polyhedra shown in (B) is an eight-fold coordinated calcium with one or two water molecules at a distance of ~ 2.8 Å. The* H_2O_{free} *molecule is at a distance greater than 3 Å from any calcium ion. Atomic color code used are calcium – turquoise or green, silicon -dark blue, oxygen – red, hydroxyl oxygen – purple, hydrogen-white.*

Types of water molecules

By exploring the domain of interlayer species in these different bricks, we have observed that there are mainly two types of interlayer water species in C-S-H as shown in Figure 23. The first category (in Figure 23 A) corresponds to strongly coordinated or *more crystalline* water molecules ($d_{Ca-O_{water}} < \sim 2.5$ Å). Four different subtypes can be distinguished in this category:

(a) water molecules ($\mathrm{H_2O_{IL}^1}$) directly coordinated to one interlayer calcium ion

(b) water molecules ($\mathrm{H_2O_{IL}^2}$) coordinated to two interlayer calcium ions

(c) water molecules ($\mathrm{H_2O_{ML}^1}$) coordinated to one main layer calcium only

(d) water molecules ($\mathrm{H_2O_{ML}^2}$) coordinated to one main layer and one interlayer calcium

All these water molecules are strongly hydrogen bonded with neighbouring hydroxyl groups or any oxygen atoms of the silicate species[170]. In non-defective 14 Å tobermorite[42] the main layer calcium is in seven-fold coordination, 6 with water and one hydroxyl. In order to test if this calcium is always seven-fold coordinated, we made several structures without putting a water molecule close to the main layer calcium atoms. With minimization, the interlayer water adjusts itself such that the main layer calcium atom is in seven-fold coordination and the interlayer calcium ions are in a coordination equal to or greater than six. Thus, the overall coordination of calcium decreases with increasing amount of interlayer calcium in high Ca/Si ratio C-S-H which is in accordance with the total X-ray scattering results on C-S-H [47]. We expect these water molecules to constantly exchange protons with hydroxyl groups in C-S-H.

There are 6 strongly coordinated water molecules in one brick, leading to a water to silica ratio of strongly bound water of 1.5, which corresponds to the limit of the first chemical potential regime found in bricks with a Ca/Si ratio of 2 (see Figure 22A).

The second category (in Figure 23B) consists of water molecules that are:

(a) *coordinated to a calcium which is in eight-fold coordination* ($d_{Ca-O_{water}} \sim 2.8$ Å). From the energetic point of view, structures containing this "bound" or "semi crystalline" water are found to be less ordered than those containing only strongly bound water ($< \mathrm{S} < \mathrm{C9} > \mathrm{C} >$ in Figure 22B). The brick with the lower amount water in Figure 22B does not contain any of the weakly bound water. The presence of these two types of water can determine the degree of crystallinity of the brick as shown in Figure 22B.

(b) *not directly coordinated to any calcium and with the nearest calcium in* $d_{Ca-O_{water}} > \sim 3$ Å

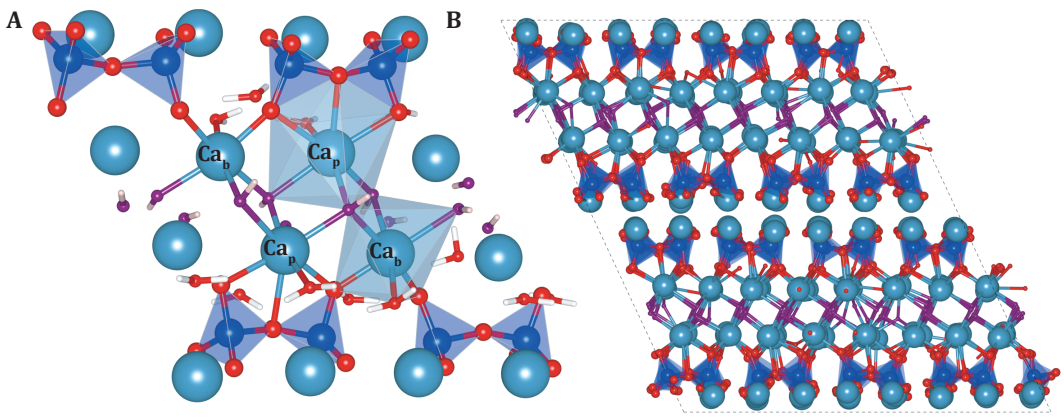

Figure 24: New stable site of interlayer calcium discovered: pairing site. The bridging site calcium (Ca_b) and the pairing site calcium (Ca_p) are shown with their characteristic two and three bonds respectively to the silicate structure in (A) and the interlayer ordering with the calcium at the pairing site for a nano unit of C-S-H is shown in (B). Atomic color codes used are calcium - turquoise, silicon -dark blue, oxygen – red, hydroxyl oxygen – purple, hydrogen-white.

Calcium position in the interlayer

As discussed above, the different types of water are intimately linked with the interlayer calcium ions. Understanding this complex calcium-water relationship is further complicated by the lack of knowledge on the exact positions of interlayer calcium ions in C-S-H as mentioned earlier. In this study, we have discovered a new position of interlayer calcium, which seems to be energetically the most stable calcium position that could exist in the C-S-H interlayer. Any interlayer calcium (excluding the bridging calcium) with an arbitrary initial position is always found to relax to the pairing site after hard minimization schemes and the resulting brick is always the lowest energy configuration achieved. This calcium is coordinated to three oxygens of a pairing silicate tetrahedra , two hydroxyl groups and some water molecules as shown in Figure 24, we call this calcium the "pairing calcium" as it is coordinated to the dimer or pairing silicate tetrahedra. It is observed that the bridging calcium is bonded strongly to the two oxygen atoms of the silicates ($2.2 \leq d_{Ca_b - O_{silicate}} \leq 2.35$ Å) while the pairing calcium is bonded rather weakly to three oxygen of the silicates ($2.4 \leq d_{Ca_b - O_{silicate}} \leq 3$ Å) From our simulations, we have clearly observed that when the interlayer calcium occupies this pairing position then the ordering of the interlayer space in C-S-H is increased (see Figure 24 B).

From the heavy annealing schemes implemented in our molecular dynamics simulations, we expect that in the C-S-H precipitation process at room temperature there will be a significant energy barrier for a calcium aqua complex to reach this site and increase local crystallinity ideally leading to a more ordered C-S-H interlayer. For this to happen, the calcium ion has to lose its solvation shell and then get coordinated to the oxygen atoms of the silicate tetrahedra. Consequently, one could imagine a process in which, when the solid C-S-H starts to form, calcium aqua ions with two hydroxyl groups, $Ca(OH)_2(H_2O)_y$ ($4 \leq y \leq 6$ assuming a maximum coordination of 8 in the interlayer space) become stable (since solvent exchange is more difficult in a solid structure). This stable calcium aqua complex has to lose about three of its water molecules to get to this stable pairing site described above. Additionally, when some of the interlayer calcium ions of a brick are not in the pairing site, its energy is only about 0.03-0.07 eV higher compared to a brick with all the interlayer calcium ions in the pairing site. Due to these similar energies, the interlayer calcium could be distributed in these different metastable sites giving the C-S-H interlayer a certain degree of disorder. Over time, we could expect some equilibration of these positions as C-S-H matures in cement structures, possibly resulting in a better ordering or packing of the interlayer. In order to gain more insights into the local arrangement when the interlayer calcium is not in this pairing position, it would be interesting to do some DFT calculations. Additionally, the activation barrier needed as well as the free energy difference for an interlayer calcium to move to this position could also be calculated with nudged elastic band calculations using DFT in the future.

Double defect interaction

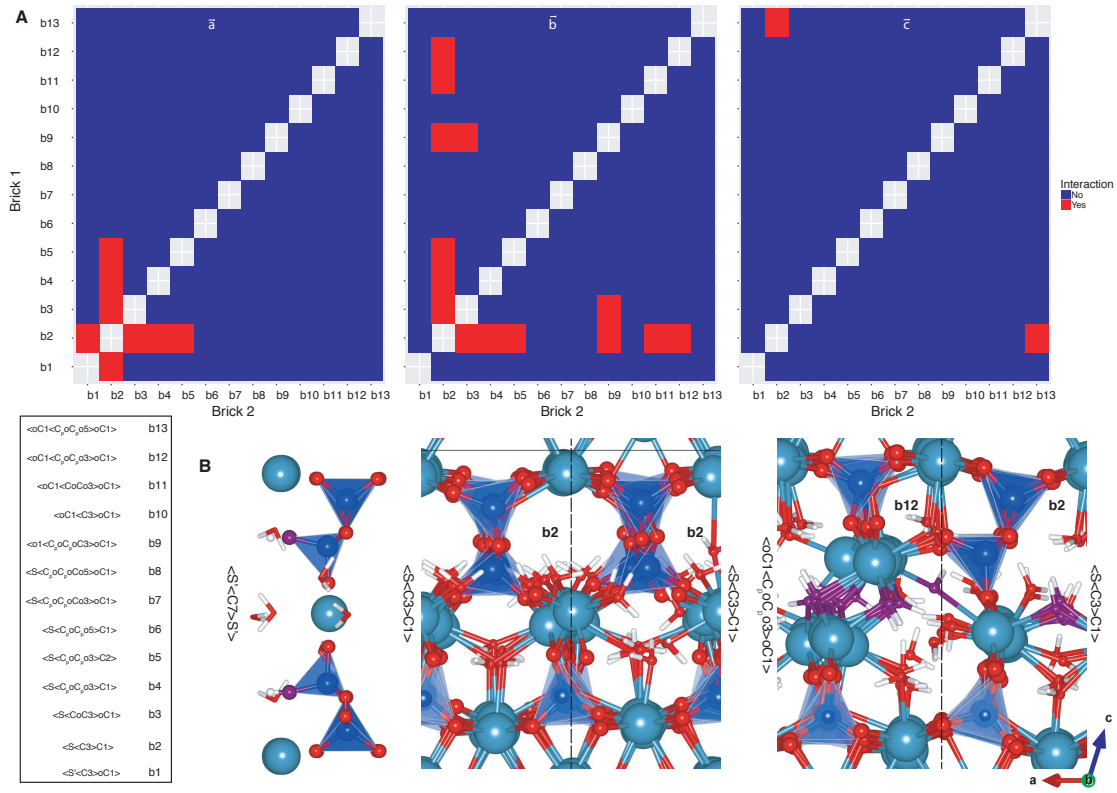

Figure 25: Double brick interaction when arranged roughly in $\vec{a}$, $\vec{b}$ and $\vec{c}$ directions of the reduced unit cell vector [172] *(A). The vertical and horizontal axes show the system studied with brick 1 (b1) and brick 2 (b2) which are adjacent to each other. A Boolean variable "interaction" is plotted in this matrix map with the condition* $\Delta H_{x/y/z}^{b1b2} > \Delta H_{error}^{MD}$*, then "Interaction" = yes = red cell and vice versa. The different types of bricks (b1 to b13) are shown in Figure S28. In (B), the orientation of silicate tetrahedra in a relaxed structure of the original 14 Å tobermorite* $< S' < C7 > S' >$ *viewed along b direction (left image) is compared with that in relaxed structures of a* $< S < C3 > C1 >$ *or b2 brick interacting with itself (middle image) in a single brick calculation and with another brick* $< oC1 < C_p oC_p o3 > oC1 >$ *or b12 when arranged in* $\vec{a}$*-vector direction . The chemical notations of the bricks are written vertically on the sides of the images. In the single brick relaxed structure, the bridging silicate tetrahedra is rotated compared to the original silicate structure and that seen in the double brick relaxed structure. Atomic color codes used are calcium - turquoise, silicon -dark blue, oxygen – red, hydroxyl oxygen – purple, hydrogen-white.*

The defects interaction results are plotted in Figure 25. The bricks (b1 to b13) are selected such that the interactions between all the different distinct type of defects are captured. Hence, even though not the whole ensemble of bricks is shown here, any trend observed is confirmed or checked with similar bricks which are not shown in Figure 25. We have observed that when the building blocks are stacked one over the other in $\vec{c}$ direction, then they are found to be non-interacting since the main calcium silicate layer prevents the defect interaction. The only exception was found for one

combination where it seems like the initial positions of the two bricks were far from equilibrium and lead to a deformation in the chain structure due to the significant volume change for both bricks. This could be avoided probably with smoother equilibration steps. All other significant interactions are only seen in $\vec{a}$ or $\vec{b}$ directions.

Additionally the interaction energy is not significant ($\Delta H_{\vec{a}/\vec{b}}^{b1b2} < \Delta H_{error}^{MD}$) between a bridging silicate, $< S <$, of one brick with an adjacent bridging calcium ion $< C <$, provided the interlayer species and the lower silicate chain are the same. For instance, for the bricks $b1 =< \boldsymbol{S} < CoC3 > oC1 > \ and\ b2 =< \boldsymbol{oC1} < \boldsymbol{C}oCo3 > oC1 >$ with $\Delta H_{\vec{a}}^{b1b2} = 0.015\ eV$ and $\Delta H_{\vec{b}}^{b1b2} = 0.037\ eV$ ($\Delta H_{error}^{MD} = 0.084\ eV$). This is true in all cases when the interlayer species remain the same.

In general, most of the interactions are very small and even if any interaction is observed, the interaction enthalpy is less than 0.08 eV or ~1.8 kcal/mol. Thus we can propose that all these bricks can coexist in C-S-H. More accurate calculations might be needed to observe more precise trends.

Another key aspect learnt from these calculations is that if the individual brick has considerable relaxation by itself, then it is hindered from fully relaxing to its lower energy state when adjacent to a different block in $\vec{a}$ or $\vec{b}$ direction. This is seen in the brick $< S < C3 > C1 >$ where the fully relaxed configuration is achieved by the rotation of bridging silicate by an angle of θ ($45 < \theta < 90°$) as shown in Figure 25B. However, this rotation of the tetrahedra is not always achievable when it is adjacent to a different type of brick leading to an unfavourable interaction in some cases. The reason for such a rotation is because the interlayer calcium goes to the bottom pairing position and forms a calcium plane with the bridging calcium. This necessitates the bridging silicate of the upper layer to rotate such that the local charge neutrality is maintained by bonding both the oxygen atoms of the silicate tetrahedra to calcium ions. This was also seen in other bricks (for instance: <S<C5>C1>) where the interaction energy is below the estimated error in Figure 25A.

In order to test if this always happens, the initial position of the interlayer calcium which was originally at the interlayer calcium site of a non-defective 14 Å tobermorite, was then fixed to the upper pairing site. Upon soft minimization, the interlayer calcium again moved to the bottom pairing site which is quite an interesting observation as the calcium would like to form a plane (with the bridging and pairing calcium sites) whenever it can. The lower water content of the brick facilitated this relaxation of the calcium ion without any annealing. One of the ways to prevent the silicate from rotating is by having two interlayer calcium ions of which one goes to the bottom pairing site and

the second one to the top pairing site with the sequence $< S < CoCo3 > C1 >$. Hence, it is advisable to use $< S < CoCo3 > C1 >$ when there is a bridging silicate tetrahedra in C-S-H building blocks. Another way is to have a calcium rich brick in the $\vec{a}$ direction as shown in Figure 25B. This rotation is also seen when both upper and bottom bridging positions are occupied by silicate tetrahedra as in $< S < CC7 > S >$ or similar bricks. In other words, despite the small interaction energies, the sequence of defects present in C-S-H can probably create some strains in the calcium-silicate sheet structure.

In atomistic simulations of C-S-H structures, one has to consider whether to avoid these kind of interactions and get an atomic bulk structure which is energetically in its most stable state. This allows unwanted error accumulation for a modeller when trying to study the interaction of, for instance, a calcium ion on the surface of a C-S-H sheet. However in C-S-H in cement or even synthetic C-S-H, due to the small differences in enthalpy and entropic considerations, also unfavourable combinations are likely to exist. This in turn might help explaining the nano-sized growth of C-S-H. If we consider two adjacent bricks with significant difference in their interlayer volume, then this might create an unfavourable strain to the growing C-S-H sheet probably resulting in bending and misorientation of the sheets as shown in Figure 26. When more and more dissimilar units come in contact then the C-S-H sheet is too strained to grow any further and exists as nano sized foils as observed in TEM [21,24,170]. Additionally, the types of defects present and their stacking can be expected to have a significant influence on C-S-H morphology and might explain the different morphologies observed under different experimental conditions (needles or foils).

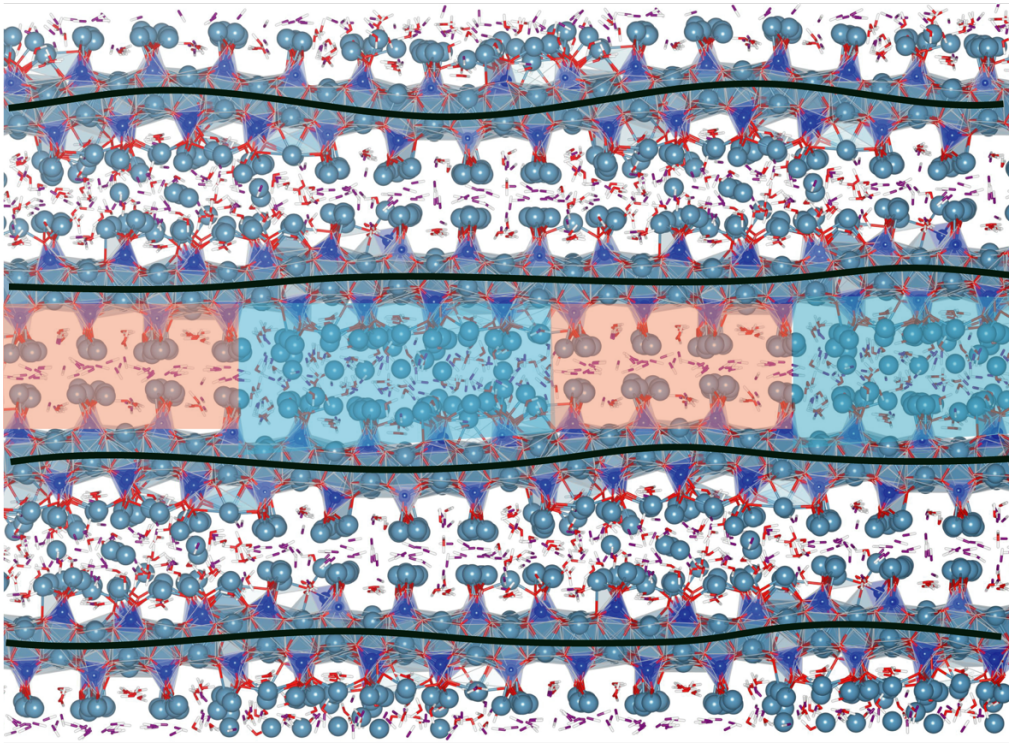

Figure 26: A schematic of the bulk sheet structure of C-S-H with an ordered crystalline interlayer with less interlayer atoms shown in orange shade (corresponding to bricks $< oC < CoCo5 > oC >$ *) and a less ordered interlayer space with more interlayer species in blue shade (corresponding to bricks* $< oCo < CoCo9C > oCo >$*). The horizontal black lines show the misorientation and bending of the calcium silicate main sheet layer after the hard minimization scheme. Atomic color codes used are calcium - turquoise, silicon -dark blue, oxygen – red, hydroxyl oxygen – purple, hydrogen-white.*

We have also observed that some of these unfavourable interactions can be eliminated if a hard minimization is done. This means that in an experimental system, some of the strain accumulated during growth might be relaxed after some time. We propose that the densification of C-S-H as popularly observed in cement hydration[62], in addition to a continuous reaction and the formation of C-S-H, might be the result of slow equilibration of metastable calcium positions in the interlayer, diffusion of water to pores, rotation of bridging or pairing silicate tetrahedra to better packing and bonding in the interlayer as shown in Figure 22B and Figure 25B.

From this study, we can propose that the nano-crystallinity or the lack of long range order of C-S-H are primarily due to the following reasons

- Due to kinetic hindrance, many calcium atoms are not in the energetically favoured pairing position if the precipitation of C-S-H is done at ambient conditions. (Activation energy barrier for the diffusion of calcium to the pairing position from NEB calculations needed to fully support this)
- Stochastic distribution of the calcium in the metastable positions of equivalent energies in the interlayer.
- Less crystalline or loosely coordinated water molecules possibly contribute to inhibiting the formation of a well ordered interlayer structure by preventing calcium from finding the minimum enthalpy position.
- The strain created and accumulated by the adjacent arrangement of different types of bricks.

A bulk C-S-H structure of Ca/Si = 1.75 which is realistic in terms of its consistency with available experimental results and the new findings discussed here, is shown in Figure S30.

Although C-S-H has been studied for several decades, such key insights into its nature were never obtained. This is mainly due to the fact that the metastable and stochastic nature of the water-calcium interaction in the interlayer, the sample preparation, nature of the environment used for the experimental technique greatly affected the results, often resulting in the destruction of the original C-S-H structure. We hope that in future some FTIR or RAMAN, EXAFS, neutron scattering, high resolution synchrotron XRD, or ^{43}Ca NMR techniques , in situ if possible, could be used to confirm our theoretical findings of different types of water molecules and the new interlayer calcium site.

6.4 Conclusion

We have been able to unravel several new aspects of the complex nature of the interlayer in C-S-H. Our key findings on the atomistic scale features of the cementitious calcium silicate hydrate, C-S-H are:

- silanols $(Si - OH)$ in C-S-H are energetically unfavourable , therefore it does not have any or has only very low quantities of silanols.
- C-S-H structure with a lower water content results in a more ordered or crystalline structure.
- Different types of environments for water molecules have been identified depending on how strongly they are coordinated to the calcium.

- A newly discovered Ca position in the interlayer, the pairing site, is enthalpically the preferred site for the interlayer calcium, however there seems to be a strong energy barrier for the calcium ions to move to this site, indicating the possibility of metastable sites being occupied.
- The strain accumulated within the C-S-H structure by the stacking of different defects within the sheets is expected to have a large influence on the poor or nano crystallinity, maturing and final morphology of C-S-H.

It is the first time such key features of the intricacies of C-S-H interlayer have been methodically investigated and deciphered, where even the most sophisticated techniques like SANS, SAXS, NMR have failed. With these new findings, we have been able to better understand the complex interlayer structure of C-S-H, get insights into the densification of C-S-H and give a plausible explanation for the origin of its lack of long range order

6.5 Supplementary images

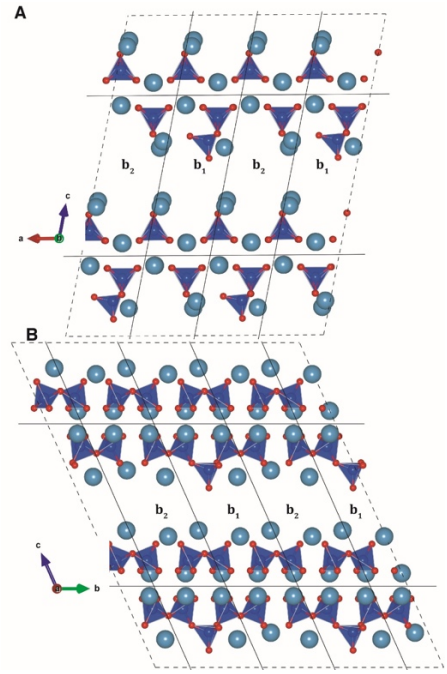

Figure S27: Schematic showing the MD simulation setup of defects interaction calculations. Two types of bricks b1 and b2 are arranged in the cell vector $\vec{a}$ direction in (A) and in the cell vector $\vec{b}$ direction in figure (B).

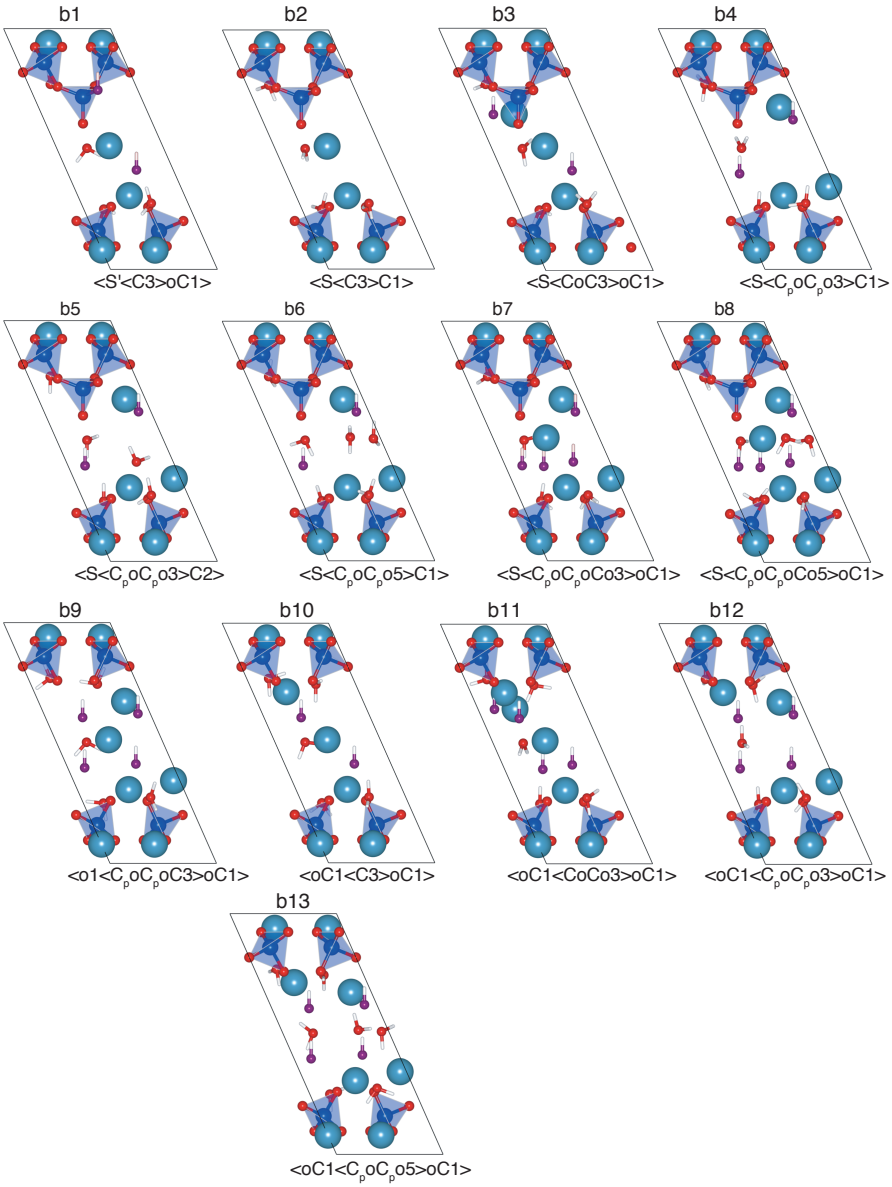

Figure S28: The different bricks in the bricks interaction calculations with the chemical building block notation below each brick and the abbreviation used in Figure 25 is shown on the top of each brick. The interlayer calcium with the initial position at the pairing site is referred to as C_p

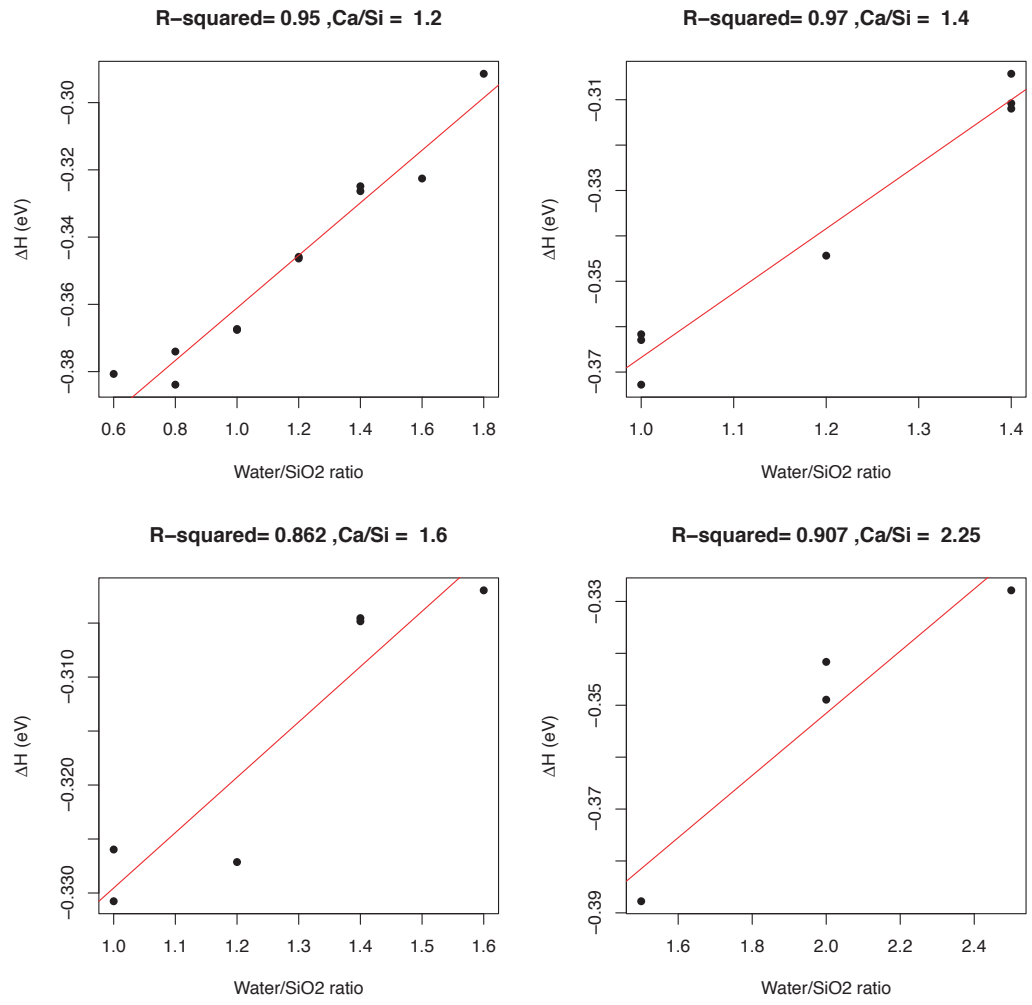

Figure S29: Regression analysis on water content of bricks of different Ca/Si ratio

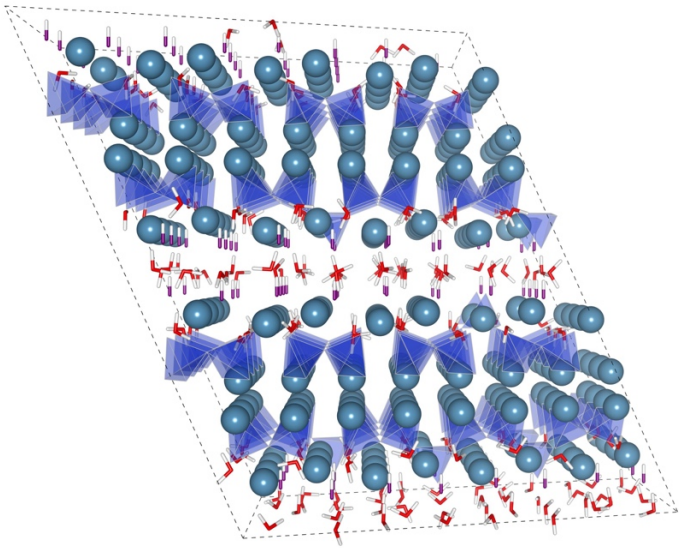

Figure S30: A proposed atomic structure of C-S-H with a stoichiometry $(CaO)_{1.75}(SiO_2)_{1.0}(H_2O)_{1.86}$ *, percentages of* Q^1*= 78.3 % ,* Q^{2b} *= 7.25 % and* Q^{2p}*=14.5 % in accordance with* [170]*. The image shown is the initial structure before relaxation.*

Chapter VII. Summary and Outlook

A summary of the work completed in this thesis towards understanding the atomic structure of Calcium Silicate Hydrate and some of the future work that could be done is discussed. In the first section concluding remarks on the structure of C-S-H in view of the discoveries and new understandings from Chapters 4 to 6 is given. The second section mainly addresses how the current understanding of C-S-H from this work can be utilized to gain better insights needed for the development of more sustainable and durable cementitious materials;

i) the incorporation of ions in C-S-H

ii) construction of C-S-H surfaces

iii) interaction of ions or molecules on such surfaces and

iv) experiments that could be done to further validate or gain more insights

7.1 The atomic structure of C-S-H

C-S-H is the main phase in cement hydration reaction giving the cement its versatile properties such as binding and compressive strength . This nanocrystalline phase has been the subject of research for several decades [18,19,118,170,176]. A better understanding of this complex phase is one of the major roadblocks in cement chemistry. Its atomic structure is generally accepted to be based on a defective tobermorite structure. In this thesis, we have attempted to better understand the defects present, their distribution and generally the detailed structural features of C-S-H.

In Chapter 4, a bottom up approach which can precisely define the structural units in C-S-H has been developed. With this methodology, named the 'Brick model', a variety of chemical units in a 14 Å tobermorite unit cell have been defined, and a method to compare their energetics has been devised. Thus, the Brick model enabled us to develop different types of defective nano-units (bricks) that could make-up a bulk structure of C-S-H. In order to efficiently capture the features of C-S-H, a collaborative work with experimentalists on synthetic C-S-H (Chapter 5) helped us to define the constraints for making a C-S-H model structure.

In the synthetic C-S-H work, an experimental team at EPFL synthesized C-S-H with a range of Ca/Si ratios and characterized the silicate framework using advanced ^{29}Si dynamic polarization nuclear magnetic resonance (DNP-NMR). The main results of this work are the following:

i. From the 1D ^{29}Si DNP NMR, relative amounts of terminal, bridging and pairing silicate tetrahedra are quantified.

ii. From the 2D $^{29}Si - {}^{29}Si$ DNP NMR the connectivity of these silicate tetrahedras are calculated confirming a 3n-1 silicate chain structure.

iii. From the 2D $^{1}H - {}^{29}Si$ CP DNP NMR, a strong hydrogen bonding environment in proximity to a terminal silicate tetrahedra was observed.

iv. From the proton chemical shifts calculated from DFT calculations on defective structures created using the brick model, it was concluded that the presence of a calcium ion bridging the terminal silicate tetrahedra with its coordinated water molecules in the interlayer, induces strong hydrogen bonding.

Thus, we were able to characterize the silicate structure of synthetic C-S-H with industrially relevant Ca/Si ratios for the first time. The discovered new calcium position, the *bridging calcium*, is the first original evidence on the exact location of an interlayer calcium ever reported. In addition to solving the atomic level structure of calcium-silicate sheet of C-S-H, our results revealed how it is intricately linked to the interlayer calcium and water molecules. However, the results from the NMR did not give any indication on the locations of the additional calcium ions, hydroxyl ions and water molecules in the interlayer space which is the most difficult and unexplored part of C-S-H.

Since the main constituent of the interlayer space is water, any experiment carried out on C-S-H which involves drying possibly disrupts the structure. Here, we studied the interlayer structure and composition of C-S-H from atomistic simulations which is the first time a rigorous investigation of the C-S-H interlayer is reported. The brick model was used to make a series of possible defect structures in 14 Å tobermorite. Classical MD was used to relax the structure and their energies were calculated with a reaction scheme proposed in the Brick model. The following are the key results :

1. A new stable calcium position in the interlayer, the *pairing calcium*, was discovered, it is coordinated to the oxygen atoms of the pairing silicate tetrahedra as shown in Figure 24 in Chapter 6.

2. A more crystalline or well-ordered interlayer structure is obtained with lower interlayer water content.

3. Nano-units with similar interlayer volumes are favored to be adjacent to each other, however, the interaction energy is small and thus unfavorable combinations are likely to exist as well, that can lead to strain within the calcium silicate sheets.

4. Structures with silanols are less stable, confirming some of the earliest NMR work on synthetic C-S-H, where the silanol content decreases with increasing Ca/Si ratio.

The new calcium position discovered gives us a hint as to why C-S-H is not able to grow as a fully crystalline phase (one possible contribution to nanocrystallinity). In the simulations, depending on the initial position of the interlayer calcium atoms, sufficient energy had to be given to move the calcium atoms to the pairing position suggesting an activation barrier associated to the move. This might indicate that during the precipitation of C-S-H, the interlayer calcium ions do not always occupy the stable pairing position and are possibly distributed in metastable positions of equivalent energies in the interlayer creating a degree of disorder in C-S-H. In order to confirm this, nudged elastic band (NEB) calculations will be attempted in the near future to find the activation barrier required for a randomly placed interlayer calcium to migrate to the pairing site. Additionally, loosely coordinated water contribute to inhibiting the formation of a well-ordered interlayer structure. It was also observed that the proximity of bricks with dissimilar interlayer volumes is energetically unfavorable, probably causing strain in the calcium-silicate sheet structure resulting in slight bending or misorientation of it. Thus any accumulation of these strains, by the unfavorable proximity of certain C-S-H structures, will hinder the C-S-H sheets to grow any further and thus explain the nano sized foil or needle morphology of C-S-H. With all these findings, Chapter 6 concludes that a possible accumulation of these strains and the different metastable calcium positions in the interlayer might be the reason that C-S-H exists as a nano-crystalline phase without any long-range order.

From the C-S-H atomic structure modeling perspective, we were able to get constraints for the main *calcium-silicate sheet structure* from Chapter 5 and the *interlayer structuring* from Chapter 6. Thus any modeling work in future on C-S-H should make sure these constraints and insights are incorporated to get tangible results. The previous atomistic modeling on atomistic structure of C-S-H [67,82] attempted only to capture the silicate structure of C-S-H according to NMR results. The details of the interlayer were completely ignored and the interlayer species were randomly added to a structural framework of 11 Å tobermorite, thus creating a disordered structure revealing no useful

insights into possible sub-structures in the interlayer. However, with the Brick model combined with the experimental work mentioned in the thesis, we have discovered two stable interlayer calcium positions, unraveled the nature of interlayer water molecules, proposed the role of interlayer, through the defect interactions and metastable calcium positions, in restraining the long range order of C-S-H. In general, this work sheds light on the much debated atomic structure of C-S-H and will help in the fundamental understanding of cement hydration.

With this fundamental knowledge on the features of C-S-H at the atomic scale, we have made significant advances that can, in the future, facilitate the understanding of how the different ions in Portland cement or blended cement systems with SCMs affect the nucleation and growth of C-S-H through altering the hydration kinetics. That is, from this thesis work, we know the structure of C-S-H and the role of interlayer species in determining the crystallinity of C-S-H. With the addition of other species like aluminum, sulphate or alkali in the blended system, one can now look at how these intricate interlayer features and sheet structure are affected and how these will determine the nature of the surfaces and edges of the C-S-H. This thesis has thus opened doors for several scientific avenues yet to be explored at the fundamental level that could potentially lead to more sustainable and futuristic cements.

7.2 Further work

7.2.1 C-S-H: Modelling

(i) C-S-H in cements

So far we have been considering only synthetic C-S-H and most of the experimental constraints for the model are from the work on synthetic C-S-H. The outer C-S-H from the Portland cement hydration is not very different. From the NMR experiments, it is found to have less dimeric silicates compared to our C-S-H [14,56,154,168] and morphologically they are oriented foil-like structures [24,148,165] compared to synthetic C-S-H which are mostly foils. The Brick model can make any silicate chain structure as shown in Chapters 4, 5 and 6. The interlayer structuring, however, should not be any different except for the incorporation of other ions, which is more pronounced in blended cements. C-S-H is found to incorporate certain amounts of aluminum and alkali ions (potassium and sodium) to give C-K-N-A-S-H [27,177] in a realistic cement hydrate. In Portland cement, incorporation of these elements in C-S-H are also observed, but to a lesser extent [118]. In blended cements, a significant aluminium content [6] in the reactants results mainly in the

formation of C-A-S-H [178–181]. From the atomistic point of view, the incorporation of these other minor ions in C-S-H can be initially done by substituting silicates or calcium from their minimum energy positions (pairing and bridging sites).

A preliminary work on C-A-S-H is in progress. From ^{27}Al NMR there exists tetra, penta and hexa coordinated aluminum species incorporated in C-S-H [178,180,181]. So far, the position of these tetra coordinated is confirmed in C-S-H as being at the bridging site [182]. The hexa coordinated aluminum is assumed to exist as a different phase, the so-called "Third Aluminate Hydrate" (TAH) [178] in the interlayer or on the surface of C-S-H. The relative percentage of this hexa coordinated aluminum species increases with increasing Ca/Si ratio of the C-S-H. But there is no experimental evidence on the presence of such a phase. The penta coordinated is believed to exist in the interlayer and charge compensates the incorporation of a tetra coordinated aluminum in the silicate chain [180,183]. With the newly gained knowledge of the atomistic structure of C-S-H, these different aluminum species will be studied using both DFT calculations and MD simulations.

(ii) C-S-H : Surfaces and Edges

In addition to the incorporation of other elements in C-S-H, the most important work that needs to be taken on in the near future in C-S-H modeling studies is to create surfaces. The C-S-H phases have very high surface area and hence, most of the complex phenomena in cement hydration is probably significantly influenced by the interactions with the C-S-H surfaces. The presence of sulfates, zinc, poly carboxylate ether (PCE), gluconate and other organic or inorganic phases significantly affect the cement hydration possibly through its interaction with the growing C-S-H surfaces [184–186]. Hence, making realistic C-S-H surfaces and edges is an indispensable step towards further understanding of complex cement hydration. There exists some work on C-S-H surfaces where a defective surface is created by randomly incorporating defects on a single linear chain of silicates with the rest of the bulk structure belonging to the original tobermorite structure [187]. However such an approach will only work for the (001) surface of a defective tobermorite where you can cut at the interlayer. When the interlayer is perpendicular to the surface, that is for instance, the (010) plane, [93] then the interlayer species could influence the events at the interface.

The Brick model can make surfaces as shown in Chapter 4. We can precisely define the building units on the surface. However, there are many possible features on a single surface that one can make. One thing to do will be to swap a surface feature with one from the bulk and compare the energies. That is,

- if the surface has a $<S<$ unit and somewhere in the bulk there is a $<C<$ unit, then the energy of this surface slab configuration is E_{SC}

- Now another surface can be made with just one change, the $<S<$ unit on the surface is swapped with a $<C<$ unit in the bulk. The energy of this configuration E'_{SC} can be compared with E_{SC} to see which configuration is more favored or which chemical unit would like to be on the surface.

- This procedure can be used to compare all types of building blocks on different surfaces.

It will also be quite interesting to study edges with the presence of adsorbing ions. This could give insights into general adsorption of ions and nucleation and growth of C-S-H in the presence of different ions in solution.

7.2.2 C-S-H: Experiments suggested from the new modelling insights gained in this thesis

(i) Interlayer distance

One of the most used characteristics of C-S-H is its interlayer distance [17,20,128]. The interlayer distance is measured from the XRD pattern of a dried C-S-H (in almost all cases) [167]. The interlayer distance is found to decrease with increasing Ca/Si ratio of the synthetic C-S-H as measured with XRD. The highest Ca/Si ratio achieved for the synthetic C-S-H was ~1.5 and its interlayer distance is around 11.5 Å (or lower depending on the drying condition) [17,20,128] . The low angle 2θ peak around 6-9˚ is usually taken as the peak corresponding to the interlayer distance of C-S-H which will roughly correspond to the d_{001} planar distance of the tobermorite family [188]. In the in-situ XRD measurement of Alite (the main phase in Portland cement) hydration by Bergold et al. [189], it is difficult to see any low angle peak corresponding to C-S-H. So, is a distinctive peak corresponding to some repetitive distance in the order of ~11-12 Å an effect of drying?

With a collaborative work of EPFL and CSEM Neuchatel, we are looking at the XRD patterns with and without drying of high Ca/Si ratio C-S-H. This work aims to establish if interlayer distance is really a feature of C-S-H or is an effect of the drying, forcing the calcium silicate sheet structure to collapse and perhaps drive some water out of the interlayer. It is admissible that C-S-H will have an interlayer spacing but the question is whether it is a fixed distance as observed by the dried C-S-H experiments or can it vary depending on the interlayer water and calcium content, i.e. do all layers have to have

the same composition. The work is in progress and the preliminary results show no peaks at low angle for a non-dried wet sample.

(ii) Calcium position

Another practically challenging but extremely interesting question to answer is the exact locations and the environment of calcium ions in C-S-H. This could possibly confirm the results in chapter 6. Some of the techniques that can be used are ^{43}Ca NMR or EXAFS, which can be carried out on dried and non-dried samples.

Bibliography

[1] K.L. Scrivener, V.M. John, E.M. Gartner, Eco-efficient cements: {Potential}, economically viable solutions for a low-{CO}2, cement-based materials industry, Paris, 2016.

[2] H.F.W. Taylor, Cement chemistry, Thomas Telford, 1998. doi:10.1016/S0958-9465(98)00023-7.

[3] J.W. Bullard, H.M. Jennings, R.A. Livingston, A. Nonat, G.W. Scherer, J.S. Schweitzer, et al., Mechanisms of cement hydration, Cem. Concr. Res. 41 (2011) 1208–1223. doi:10.1016/j.cemconres.2010.09.011.

[4] K.L. Scrivener, A. Nonat, Hydration of cementitious materials, present and future, Cem. Concr. Res. 41 (2011) 651–665. doi:10.1016/j.cemconres.2011.03.026.

[5] P. Juilland, E. Gallucci, R. Flatt, K. Scrivener, Dissolution theory applied to the induction period in alite hydration, Cem. Concr. Res. 40 (2010) 831–844. doi:10.1016/j.cemconres.2010.01.012.

[6] B. Lothenbach, K. Scrivener, R.D. Hooton, Supplementary cementitious materials, Cem. Concr. Res. 41 (2011) 1244–1256. doi:10.1016/j.cemconres.2010.12.001.

[7] K.L. Scrivener, R.J. Kirkpatrick, Innovation in use and research on cementitious material, Cem. Concr. Res. 38 (2008) 128–136. doi:10.1016/j.cemconres.2007.09.025.

[8] V.G. Papadakis, S. Antiohos, S. Tsimas, Supplementary cementing materials in concrete. Part II: A fundamental estimation of the efficiency factor, Cem. Concr. Res. 32 (2002) 1533–1538. doi:10.1016/S0008-8846(02)00829-3.

[9] E. Gallucci, K. Scrivener, Crystallisation of calcium hydroxide in early age model and ordinary cementitious systems, Cem. Concr. Res. 37 (2007) 492–501. doi:10.1016/j.cemconres.2007.01.001.

[10] S. Galmarini, A. Aimable, N. Ruffray, P. Bowen, Changes in portlandite morphology with solvent composition: Atomistic simulations and experiment, Cem. Concr. Res. 41 (2011) 1330–1338. doi:10.1016/j.cemconres.2011.04.009.

[11] S. Galmarini, P. Bowen, Atomistic simulation of the adsorption of calcium and hydroxyl ions onto portlandite surfaces - Towards crystal growth mechanisms, Cem. Concr. Res. 81 (2016) 16–23. doi:10.1016/j.cemconres.2015.11.008.

[12] S. Galmarini, A. Kunhi Mohamed, P. Bowen, Atomistic Simulations of Silicate Species Interaction with Portlandite Surfaces, J. Phys. Chem. C. 120 (2016) acs.jpcc.6b07044. doi:10.1021/acs.jpcc.6b07044.

[13] S. Galmarini, A. Aimable, N. Ruffray, P. Bowen, Cement and Concrete Research Erratum to " Changes in portlandite morphology with solvent composition : Atomistic simulations and experiment " [Cement Concrete Res . 41 (2011) 1330 – 1338], Cem. Concr. Res. 61–62 (2014) 71. doi:10.1016/j.cemconres.2014.03.009.

[14] A.R. Brough, C.M. Dobson, I.G. Richardson, G.W. Groves, Application of Selective 29Si Isotopic Enrichment to Studies of the Structure of Calcium Silicate Hydrate (C-S-H) Gels, J. Am. Ceram. Soc. 77 (1994) 593–596. doi:10.1111/j.1151-2916.1994.tb07034.x.

[15] I.G. Richardson, G.W. Groves, Microstructure and microanalysis of hardened cement pastes involving ground granulated blast-furnace slag, J. Mater. Sci. 27 (1992) 6204–6212. doi:10.1007/BF01133772.

[16] X. Cong, R.J. Kirkpatrick, 29Si MAS NMR study of the structure of calcium silicate hydrate, Adv. Cem. Based Mater. 3 (1996) 144–156. doi:10.1016/S1065-7355(96)90046-2.

[17] G. Renaudin, J. Russias, F. Leroux, F. Frizon, C. Cau-dit-Coumes, Structural characterization of C-S-H and C-A-S-H samples-Part I: Long-range order investigated by Rietveld analyses, J. Solid State Chem. 182 (2009) 3312–3319. doi:10.1016/j.jssc.2009.09.026.

[18] H.F.W.W. Taylor, Proposed Structure for Calcium Silicate Hydrate Gel, J. Am. Ceram. Soc. 69 (1986) 464–467. doi:10.1111/j.1151-2916.1986.tb07446.x.

[19] R.F. Feldman, P.J. Sereda, A New Model for Hydrated Portland Cement and its Practical Implications, Eng. J. 53 (1970) 53–59.

[20] I.G. Richardson, Model structures for C-(A)-S-H(I), Acta Crystallogr. Sect. B Struct. Sci. Cryst. Eng. Mater. 70 (2014) 903–923. doi:10.1107/S2052520614021982.

[21] I.G.G. Richardson, Tobermorite/jennite- and tobermorite/calcium hydroxide-based models

for the structure of C-S-H: applicability to hardened pastes of tricalcium silicate, [beta]-dicalcium silicate, Portland cement, and blends of Portland cement with blast-furnace slag, met, Cem. Concr. Res. 34 (2004) 1733–1777. doi:10.1016/j.cemconres.2004.05.034.

[22] I.G. Richardson, G.W. Groves, Models for the composition and structure of calcium silicate hydrate (C-S-H) gel in hardened tricalcium silicate pastes, Cem. Concr. Res. 22 (1992) 1001–1010. doi:10.1016/0008-8846(92)90030-Y.

[23] A. Nonat, The structure and stoichiometry of C-S-H, Cem. Concr. Res. 34 (2004) 1521–1528. doi:10.1016/j.cemconres.2004.04.035.

[24] A. Bazzoni, Study of early hydration mechanisms of cement by means of electron microscopy, 2014.

[25] A. Grudemo, Variation with solid-phase concentration of composition, structure and strength of cement pastes at high age, Cem. Concr. Res. 14 (1984) 123–132. doi:10.1016/0008-8846(84)90088-7.

[26] L.B. Skinner, S.R. Chae, C.J. Benmore, H.R. Wenk, P.J.M. Monteiro, Nanostructure of Calcium Silicate Hydrates in Cements, Phys. Rev. Lett. 104 (2010) 195502. doi:10.1103/PhysRevLett.104.195502.

[27] I.G. Richardson, The calcium silicate hydrates, Cem. Concr. Res. 38 (2008) 137–158. doi:10.1016/j.cemconres.2007.11.005.

[28] A. YazdanYar, U. Aschauer, P. Bowen, Interaction of biologically relevant ions and organic molecules with titanium oxide (rutile) surfaces: A review on molecular dynamics studies, Colloids Surfaces B Biointerfaces. 161 (2018) 563–577. doi:10.1016/j.colsurfb.2017.11.004.

[29] H.D. Herce, A.E. Garcia, Molecular dynamics simulations suggest a mechanism for translocation of the HIV-1 TAT peptide across lipid membranes, Proc. Natl. Acad. Sci. 104 (2007) 20805–20810. doi:10.1073/pnas.0706574105.

[30] P. Faucon, J.M.M. Delaye, J. Virlet, J.F.F. Jacquinot, F. Adenot, Study of the structural properties of the C---S---H(I) {BY} molecular dynamics simulation, Cem. Concr. Res. 27 (1997) 1581–1590. doi:10.1016/S0008-8846(97)00161-0.

[31] R.K. Mishra, R.J. Flatt, H. Heinz, Force field for tricalcium silicate and insight into nanoscale

properties: Cleavage, initial hydration, and adsorption of organic molecules, J. Phys. Chem. C. 117 (2013) 10417–10432. doi:10.1021/jp312815g.

[32] R.K. Mishra, A.K. Mohamed, D. Geissbühler, H. Manzano, T. Jamil, R. Shahsavari, et al., cemff: A force field database for cementitious materials including validations, applications and opportunities, Cem. Concr. Res. 102 (2017) 68–89. doi:10.1016/j.cemconres.2017.09.003.

[33] Y.-W. Dong, M.-L. Liao, X.-L. Meng, G.N. Somero, Structural flexibility and protein adaptation to temperature: Molecular dynamics analysis of malate dehydrogenases of marine molluscs., Proc. Natl. Acad. Sci. U. S. A. 115 (2018) 1274–1279. doi:10.1073/pnas.1718910115.

[34] T. Diaz de la Rubia, G.H. Gilmer, Structural Transformations and Defect Production in Ion Implanted Silicon: A Molecular Dynamics Simulation Study, Phys. Rev. Lett. 74 (1995) 2507–2510. doi:10.1103/PhysRevLett.74.2507.

[35] M. Vijayakumar, S. Kerisit, Z. Yang, G.L. Graff, J. Liu, J. a Sears, et al., Combined 6,7 Li NMR and Molecular Dynamics Study of Li Diffusion in Li 2 TiO 3, J. Phys. Chem. C. 113 (2009) 20108–20116. doi:10.1021/jp9072125.

[36] M. Matsumoto, S. Saito, I. Ohmine, D. Mn, J. Am, R. Macroscopic, et al., Molecular dynamics simulation of the ice nucleation and growth process leading to water freezing, Nature. 416 (2002) 409–413. doi:10.1038/416409a.

[37] M. De Vivo, M. Masetti, G. Bottegoni, A. Cavalli, Role of Molecular Dynamics and Related Methods in Drug Discovery, J. Med. Chem. 59 (2016) 4035–4061. doi:10.1021/acs.jmedchem.5b01684.

[38] N. Marzari, Materials modelling: The frontiers and the challenges, Nat. Mater. 15 (2016) 381–382. doi:10.1038/nmat4613.

[39] N. Mounet, M. Gibertini, P. Schwaller, D. Campi, A. Merkys, A. Marrazzo, et al., Two-dimensional materials from high-throughput computational exfoliation of experimentally known compounds, Nat. Nanotechnol. 13 (2018) 246–252. doi:10.1038/s41565-017-0035-5.

[40] W. Zhang, A.R. Oganov, A.F. Goncharov, Q. Zhu, S.E. Boulfelfel, A.O. Lyakhov, et al., Unexpected stable stoichiometries of sodium chlorides, Science (80-.). 342 (2013) 1502–1505. doi:10.1126/science.1244989.

[41] E. Bonaccorsi, S. Merlino, H.F.W.F.W. Taylor, The crystal structure of jennite, Ca9Si6O18(OH)6·8H2O, Cem. Concr. Res. 34 (2004) 1481–1488. doi:10.1016/j.cemconres.2003.12.033.

[42] E. Bonaccorsi, S. Merlino, A.R. Kampf, The crystal structure of tobermorite 14 Å (plombierite), a C-S-H phase, J. Am. Ceram. Soc. 88 (2005) 505–512. doi:10.1111/j.1551-2916.2005.00116.x.

[43] S. Merlino, E. Bonaccorsi, T. Armbruster, The real structure of tobermorite 11Å: normal and anomalous forms, OD character and polytypic modifications, Eur. J. Mineral. 13 (2001) 577–590. doi:10.1127/0935-1221/2001/0013-0577.

[44] S.A. Hamid, The crystal structure of the 11A natural tobermorite, Zeitschrift Für Krist. 154 (1981) 189–198.

[45] R.J. Kirkpatrick, J.L. Yarger, P.F. McMillan, Y. Ping, X. Cong, Raman spectroscopy of C-S-H, tobermorite, and jennite, Adv. Cem. Based Mater. 5 (1997) 93–99. doi:10.1016/S1065-7355(97)00001-1.

[46] I.G. Richardson, G.W. Groves, Microstructure and microanalysis of hardened ordinary Portland cement pastes, J. Mater. Sci. 28 (1993) 265–277. doi:10.1007/BF00349061.

[47] S. Soyer-Uzun, S.R. Chae, C.J. Benmore, H.-R.R. Wenk, P.J.M. Monteiro, Compositional evolution of calcium silicate hydrate (C-S-H) structures by total X-ray scattering, J. Am. Ceram. Soc. 95 (2012) 793–798. doi:10.1111/j.1551-2916.2011.04989.x.

[48] C. Meral, C.J.J. Benmore, P.J.M.M. Monteiro, The study of disorder and nanocrystallinity in C–S–H, supplementary cementitious materials and geopolymers using pair distribution function analysis, Cem. Concr. Res. 41 (2011) 696–710. doi:10.1016/j.cemconres.2011.03.027.

[49] K. Mohan, H.F.W. Taylor, A trimethylsilylation study of tricalcium silicate pastes, Cem. Concr. Res. 12 (1982) 25–31. doi:10.1016/0008-8846(82)90095-3.

[50] J. Skibsted, C. Hall, Characterization of cement minerals, cements and their reaction products at the atomic and nano scale, Cem. Concr. Res. 38 (2008) 205–225. doi:10.1016/j.cemconres.2007.09.010.

[51] F. Brunet, P. Bertani, T. Charpentier, A. Nonat, J. Virlet, Application of 29 Si Homonuclear and 1 H− 29 Si Heteronuclear NMR Correlation to Structural Studies of Calcium Silicate Hydrates,

J. Phys. Chem. B. 108 (2004) 15494–15502. doi:10.1021/jp031174g.

[52] I. Klur, J.-F. Jacquinot, F. Brunet, T. Charpentier, J. Virlet, C. Schneider, et al., NMR Cross-Polarization when T, J. Phys. Chem. B. 104 (2000) 10162–10167. doi:10.1021/jp001342u.

[53] X. Cong, R.J. Kirkpatrick, 29Si and 17O NMR investigation of the structure of some crystalline calcium silicate hydrates, Adv. Cem. Based Mater. 3 (1996) 133–143. doi:10.1016/S1065-7355(96)90045-0.

[54] X. Cong, R.J. Kirkpatrick, 17O MAS NMR Investigation of the Structure of Calcium Silicate Hydrate Gel, J. Am. Ceram. Soc. 79 (1996) 1585–1592. doi:10.1111/j.1151-2916.1996.tb08768.x.

[55] J.J. Chen, J.J. Thomas, H.F.W.W. Taylor, H.M. Jennings, Solubility and structure of calcium silicate hydrate, Cem. Concr. Res. 34 (2004) 1499–1519. doi:10.1016/j.cemconres.2004.04.034.

[56] A.R. Brough, C.M. Dobson, I.G. Richardson, G.W. Groves, In situ solid-state NMR studies of Ca3SiO5: hydration at room temperature and at elevated temperatures using 29Si enrichment, J. Mater. Sci. 29 (1994) 3926–3940. doi:10.1007/BF00355951.

[57] N. Lequeux, A. Morau, S. Philippot, P. Boch, Extended X-ray Absorption Fine Structure Investigation of Calcium Silicate Hydrates, J. Am. Ceram. Soc. 82 (1999) 1299–1306.

[58] R. Rassem, H. Zanni-Théveneau, D. Heidemann, A.R. Grimmer, Proton high resolution solid state NMR study of C3S hydration, Cem. Concr. Res. 23 (1993) 169–176. doi:10.1016/0008-8846(93)90148-3.

[59] X. Cong, R. James Kirkpatrick, 17O and 29Si MAS NMR study of β–C2S hydration and the structure of calcium-silicate hydrates, Cem. Concr. Res. 23 (1993) 1065–1077. doi:10.1016/0008-8846(93)90166-7.

[60] P. Yu, R.J. Kirkpatrick, B. Poe, P.F. McMillan, X. Cong, Structure of Calcium Silicate Hydrate (C-S-H): Near-, Mid-, and Far-Infrared Spectroscopy, J. Am. Ceram. Soc. 82 (1999) 742–748. doi:10.1111/j.1151-2916.1999.tb01826.x.

[61] J.J. Thomas, J.J. Chen, H.M. Jennings, D.A. Neumann, Ca-OH bonding in the C-S-H gel phase of tricalcium silicate and white portland cement pastes measured by inelastic neutron

scattering, Chem. Mater. 15 (2003) 3813–3817. doi:10.1021/cm034227f.

[62] A.C.A. Muller, K.L. Scrivener, A.M. Gajewicz, P.J. McDonald, Densification of C-S-H measured by 1H NMR relaxometry, J. Phys. Chem. C. 117 (2013) 403–412. doi:10.1021/jp3102964.

[63] J. Skibsted, J. Hjorth, H.J. Jakobsen, Correlation between 29Si NMR chemical shifts and mean Si-O bond lengths for calcium silicates, Chem. Phys. Lett. 172 (1990) 279–283. doi:10.1016/0009-2614(90)85403-Y.

[64] K. Garbev, P. Stemmermann, L. Black, C. Breen, J. Yarwood, B. Gasharova, Structural features of C-S-H(I) and its carbonation in air-A Raman spectroscopic study. Part I: Fresh phases, J. Am. Ceram. Soc. 90 (2007) 900–907. doi:10.1111/j.1551-2916.2006.01428.x.

[65] I.L. Moudrakovski, R. Alizadeh, J.J. Beaudoin, Natural abundance high field (43)Ca solid state NMR in cement science., Phys. Chem. Chem. Phys. 12 (2010) 6961–9. doi:10.1039/c000353k.

[66] M.W. Grutzeck, A new model for the formation of calcium silicate hydrate (C-S-H), Mater. Res. Innov. 3 (1999) 160–170. doi:10.1007/s100190050143.

[67] G. Kovačević, B. Persson, L. Nicoleau, A. Nonat, V. Veryazov, Atomistic modeling of crystal structure of Ca1.67SiHx, Cem. Concr. Res. 67 (2015) 197–203. doi:10.1016/j.cemconres.2014.09.003.

[68] S. V. Churakov, Structural position of H2O molecules and hydrogen bonding in anomalous 11 ?? tobermorite, Am. Mineral. 94 (2009) 156–165. doi:10.2138/am.2009.2907.

[69] S. V. Churakov, Hydrogen bond connectivity in jennite from ab initio simulations, Cem. Concr. Res. 38 (2008) 1359–1364. doi:10.1016/j.cemconres.2008.08.004.

[70] S. V. Churakov, P. Mandaliev, Structure of the hydrogen bonds and silica defects in the tetrahedral double chain of xonotlite, Cem. Concr. Res. 38 (2008) 300–311. doi:10.1016/j.cemconres.2007.09.014.

[71] R. Shahsavari, M.J. Buehler, R.J.M. Pellenq, F.J. Ulm, First-principles study of elastic constants and interlayer interactions of complex hydrated oxides: Case study of tobermorite and jennite, J. Am. Ceram. Soc. 92 (2009) 2323–2330. doi:10.1111/j.1551-2916.2009.03199.x.

[72] J.-P. Korb, P.J.J. McDonald, L. Monteilhet, A.G.G. Kalinichev, R.J.J. Kirkpatrick, Comparison of

proton field-cycling relaxometry and molecular dynamics simulations for proton-water surface dynamics in cement-based materials, Cem. Concr. Res. 37 (2007) 348–350. doi:10.1016/j.cemconres.2006.02.009.

[73] A.G. Kalinichev, J. Wang, R.J. Kirkpatrick, Molecular dynamics modeling of the structure, dynamics and energetics of mineral–water interfaces: Application to cement materials, Cem. Concr. Res. 37 (2007) 337–347. doi:10.1016/j.cemconres.2006.07.004.

[74] A.G. Kalinichev, R.J. Kirkpatrick, Molecular Dynamics Modeling of Chloride Binding to the Surfaces of Calcium Hydroxide, Hydrated Calcium Aluminate, and Calcium Silicate Phases, Chem. Mater. 14 (2002) 3539–3549. doi:10.1021/cm0107070.

[75] H. Manzano, A. Ayuela, J.S. Dolado, On the formation of cementitious C-S-H nanoparticles, J. Comput. Mater. Des. 14 (2007) 45–51. doi:10.1007/s10820-006-9030-0.

[76] P.A. Bhat, N.C.C. Debnath, Theoretical and experimental study of structures and properties of cement paste: The nanostructural aspects of C–S–H, J. Phys. Chem. Solids. 72 (2011) 920–933. doi:10.1016/j.jpcs.2011.05.001.

[77] J.S. Dolado, M. Griebel, J. Hamaekers, A molecular dynamic study of cementitious calcium silicate hydrate (C-S-H) gels, J. Am. Ceram. Soc. 90 (2007) 3938–3942. doi:10.1111/j.1551-2916.2007.01984.x.

[78] J.S. Dolado, M. Griebel, J. Hamaekers, F. Heber, The nano-branched structure of cementitious calcium–silicate–hydrate gel, J. Mater. Chem. 21 (2011) 4445. doi:10.1039/c0jm04185h.

[79] R.J.-M.M. Pellenq, A. Kushima, R. Shahsavari, K.J. Van Vliet, M.J. Buehler, S. Yip, et al., A realistic molecular model of cement hydrates, Proc. Natl. Acad. Sci. 106 (2009) 16102–16107.

[80] P. Rejmak, J.S.J. Dolado, M.J. Stott, A. Ayuela, 29Si NMR in Cement: A Theoretical Study on Calcium Silicate Hydrates, J. Phys. Chem. 116 (2012) 9755–9761. doi:10.1021/jp302218j.

[81] C.C. Dharmawardhana, A. Misra, S. Aryal, P. Rulis, W.Y. Ching, Role of interatomic bonding in the mechanical anisotropy and interlayer cohesion of CSH crystals, Cem. Concr. Res. 52 (2013) 123–130. doi:10.1016/j.cemconres.2013.05.009.

[82] M.J. Abdolhosseini Qomi, K.J. Krakowiak, M. Bauchy, K.L. Stewart, R. Shahsavari, D. Jagannathan, et al., Combinatorial molecular optimization of cement hydrates., Nat.

Commun. 5 (2014) 4960. doi:10.1038/ncomms5960.

[83] A.C.T. Van Duin, A. Strachan, S. Stewman, Q. Zhang, X. Xu, W. a. Goddard, ReaxFFSiO reactive force field for silicon and silicon oxide systems, J. Phys. Chem. A. 107 (2003) 3803–3811. doi:10.1021/jp0276303.

[84] D. Hou, Z. Li, Molecular dynamics study of water and ions transport in nano-pore of layered structure: A case study of tobermorite, Microporous Mesoporous Mater. 195 (2014) 9–20. doi:10.1016/j.micromeso.2014.04.011.

[85] D. Hou, T. Zhao, H. Ma, Z. Li, Reactive Molecular Simulation on Water Confined in the Nanopores of the Calcium Silicate Hydrate Gel: Structure, Reactivity, and Mechanical Properties, J. Phys. Chem. C. 119 (2015) 1346–1358. doi:10.1021/jp509292q.

[86] D. Hou, Z. Li, T. Zhao, Reactive force field simulation on polymerization and hydrolytic reactions in calcium aluminate silicate hydrate (C–A–S–H) gel: structure, dynamics and mechanical properties, RSC Adv. 5 (2015) 448–461. doi:10.1039/C4RA10645H.

[87] D. Hou, T. Zhao, Z. Jin, H. Ma, Z. Li, Molecular Simulation of Calcium Silicate Composites: Structure, Dynamics, and Mechanical Properties, J. Am. Ceram. Soc. 98 (2015) 758–769. doi:10.1111/jace.13368.

[88] D. Hou, Z. Li, T. Zhao, P. Zhang, Water transport in the nano-pore of the calcium silicate phase: reactivity, structure and dynamics., Phys. Chem. Chem. Phys. 17 (2015) 1411–1423. doi:10.1039/c4cp04137b.

[89] M. Bauchy, H. Laubie, M.J. Abdolhosseini Qomi, C.G. Hoover, F.-J. Ulm, R.J.-M. Pellenq, Fracture toughness of calcium–silicate–hydrate from molecular dynamics simulations, J. Non. Cryst. Solids. 419 (2015) 58–64. doi:10.1016/j.jnoncrysol.2015.03.031.

[90] M. Bauchy, M. Javad, A. Qomi, C. Bichara, F. Ulm, R.J. Pellenq, Rigidity Transition in Materials : Hardness is Driven by Weak Atomic Constraints, 125502 (2015) 1–5. doi:10.1103/PhysRevLett.114.125502.

[91] R. Shahsavari, R.J.-M. Pellenq, F.-J. Ulm, Empirical force fields for complex hydrated calcio-silicate layered materials., Phys. Chem. Chem. Phys. 13 (2011) 1002–1011. doi:10.1039/c0cp00516a.

[92] H. Manzano, R.J.M. Pellenq, F.-J. Ulm, M.J. Buehler, A.C.T. van Duin, Hydration of Calcium Oxide Surface Predicted by Reactive Force Field Molecular Dynamics, Langmuir. 28 (2012) 4187–4197. doi:10.1021/la204338m.

[93] S.C. Galmarini, Atomistic simulation of cementitious materials, EPFL, 2013. doi:10.5075/epfl-thesis-5754.

[94] P.P. Ewald, Die Berechnung optischer und elektrostatischer Gitterpotentiale, Ann. Phys. 369 (1921) 253–287. doi:10.1002/andp.19213690304.

[95] G.W. Watson, E.T. Kelsey, N.H. de Leeuw, D.J. Harris, S.C. Parker, Atomistic simulation of dislocations, surfaces and interfaces in MgO, J. Chem. Soc. Faraday Trans. 92 (1996) 433. doi:10.1039/ft9969200433.

[96] W. Smith, T.R. Forester, DL_POLY_2.0: a general-purpose parallel molecular dynamics simulation package., J. Mol. Graph. 14 (1996) 136–41.

[97] W.G. Hoover, Canonical dynamics: Equilibrium phase-space distributions, Phys. Rev. A. 31 (1985) 1695–1697. doi:10.1103/PhysRevA.31.1695.

[98] S. Melchionna, G. Ciccotti, B.L. Holian, Hoover npt dynamics for systems varying in shape and size, Mol. Phys. 78 (1993) 533–544. doi:10.1080/00268979300100371.

[99] W. Hohenberg, P.; Kohn, Hohenberg, P.; Kohn, W., Phys. Rev. 136 (1964) B864–B871. doi:10.1103/PhysRev.136.B864.

[100] M. Born, R. Oppenheimer, Zur Quantentheorie der Molekeln, Ann. Phys. 389 (1927) 457–484. doi:10.1002/andp.19273892002.

[101] W. Kohn, L.J. Sham, Self-consistent equations including exchange and correlation effects, Phys. Rev. 140 (1965). doi:10.1103/PhysRev.140.A1133.

[102] J.P. Perdew, K. Burke, M. Ernzerhof, D. of Physics, N.O.L. 70118 J. Quantum Theory Group Tulane University, Generalized Gradient Approximation Made Simple, Phys. Rev. Lett. 77 (1996) 3865–3868. doi:10.1103/PhysRevLett.77.3865.

[103] D. Vanderbilt, Soft self-consistent pseudopotentials in a generalized eigenvalue formalism, Phys. Rev. B. 41 (1990) 7892–7895. doi:10.1103/PhysRevB.41.7892.

[104] J.D. Pack, H.J. Monkhorst, Special points for Brillouin-zone integrations, Phys. Rev. B. 16 (1977) 1748–1749. doi:10.1103/PhysRevB.16.1748.

[105] P. Giannozzi, S. Baroni, N. Bonini, M. Calandra, R. Car, C. Cavazzoni, et al., QUANTUM ESPRESSO: A modular and open-source software project for quantum simulations of materials, J. Phys. Condens. Matter. 21 (2009). doi:10.1088/0953-8984/21/39/395502.

[106] S. Galmarini, P. Bowen, Atomistic simulations to identify stable bulk defects in 14 A tobermorite - towards a realistic C-S-H model, In Prep. (2013).

[107] J.L.F. Abascal, C. Vega, A general purpose model for the condensed phases of water: TIP4P/2005, J. Chem. Phys. 123 (2005) 234505–234512. doi:10.1063/1.2121687.

[108] E. Bonaccorsi, S. Merlino, A.R. Kampf, The crystal structure of tobermorite 14 \AA (plombierite), a C-S-H phase, J. Am. Ceram. Soc. 88 (2005) 505–512. doi:10.1111/j.1551-2916.2005.00116.x.

[109] N.H.H. de Leeuw, S.C.C. Parker, C.R.A.R.A. Catlow, G.D.D. Price, Modelling the effect of water on the surface structure and stability of forsterite, Phys. Chem. Miner. 27 (2000) 332–341. doi:10.1007/s002690050262.

[110] C.L. Freeman, J.H. Harding, D.J. Cooke, J.A. Elliott, J.S. Lardge, D.M. Duffy, New Forcefields for Modeling Biomineralization Processes, J. Phys. Chem. C. 111 (2007) 11943–11951. doi:10.1021/jp071887p.

[111] P. Mark, L. Nilsson, Structure and dynamics of the TIP3P, SPC, and SPC/E water models at 298 K, J. Phys. Chem. A. 105 (2001) 9954–9960. doi:10.1021/jp003020w.

[112] W. Primak, H. Kaufman, R. Ward, X-Ray Diffraction Studies of Systems Involved in the Preparation of Alkaline Earth Sulfide and Selenide Phosphors1, J. Am. Chem. Soc. 70 (1948) 2043–2046. doi:10.1021/ja01186a018.

[113] H.E. Petch, The hydrogen positions in portlandite, Ca(OH)2, as indicated by the electron distribution, Acta Crystallogr. 14 (1961) 950–957. doi:10.1107/S0365110X61002771.

[114] L. Levien, C.T. Prewitt, D.J. Weidner, Structure and elastic properties of quartz at pressure, Am. Mineral. 65 (1980).

[115] MUMME W.G., CRYSTAL-STRUCTURE OF TRICALCIUM SILICATE FROM A PORTLAND-CEMENT CLINKER AND ITS APPLICATION TO QUANTITATIVE XRD ANALYSIS, Neues Jahrb. Fur Mineral. Monatshefte . (1995) 145–160.

[116] M.R. Andalibi, A. Kumar, B. Srinivasan, P. Bowen, K. Scrivener, C. Ludwig, et al., On the Mesoscale Mechanism of Synthetic Calcium-Silicate-Hydrate Precipitation: A Population Balance Modeling Approach, J. Mater. Chem. A. 6 (2017) 363–373. doi:10.1039/C7TA08784E.

[117] A. Kumar, Synthetic Calcium Silicate Hydrates, EPFL, 2017. doi:10.5075/epfl-thesis-7658.

[118] B. Lothenbach, A. Nonat, Calcium silicate hydrates: Solid and liquid phase composition, Cem. Concr. Res. (2015). doi:10.1016/j.cemconres.2015.03.019.

[119] C. Prati, M.G. Gandolfi, Calcium silicate bioactive cements: Biological perspectives and clinical applications, Dent. Mater. 31 (2015) 351–370. doi:10.1016/j.dental.2015.01.004.

[120] C.-C. Ho, C.-K. Wei, S.-Y. Lin, S.-J. Ding, Calcium silicate cements prepared by hydrothermal synthesis for bone repair, Ceram. Int. 42 (2016) 9183–9189. doi:10.1016/j.ceramint.2016.03.013.

[121] K. Okano, S. Miyamaru, A. Kitao, H. Takano, T. Aketo, M. Toda, et al., Amorphous calcium silicate hydrates and their possible mechanism for recovering phosphate from wastewater, Sep. Purif. Technol. 144 (2015) 63–69. doi:10.1016/j.seppur.2015.01.043.

[122] J. Zhao, Y.-J. Zhu, J. Wu, J.-Q. Zheng, X.-Y. Zhao, B.-Q. Lu, et al., Chitosan-coated mesoporous microspheres of calcium silicate hydrate: Environmentally friendly synthesis and application as a highly efficient adsorbent for heavy metal ions, J. Colloid Interface Sci. 418 (2014) 208–215. doi:10.1016/j.jcis.2013.12.016.

[123] L. Dezerald, J.J. Kohanoff, A.A. Correa, A. Caro, R.J.-M. Pellenq, F.J. Ulm, et al., Cement As a Waste Form for Nuclear Fission Products: The Case of 90Sr and Its Daughters, Environ. Sci. Technol. 49 (2015) 13676–13683. doi:10.1021/acs.est.5b02609.

[124] H.F.W. Taylor, Cement Chemistry, Thomas Telford, 1997.

[125] J.J. Chen, L. Sorelli, M. Vandamme, F.-J. Ulm, G. Chanvillard, A Coupled Nanoindentation/SEM-EDS Study on Low Water/Cement Ratio Portland Cement Paste: Evidence for C–S–H/Ca(OH)2 Nanocomposites, J. Am. Ceram. Soc. 93 (2010) 1484–1493.

doi:10.1111/j.1551-2916.2009.03599.x.

[126] K. Garbev, G. Beuchle, M. Bornefeld, L. Black, P. Stemmermann, Cell Dimensions and Composition of Nanocrystalline Calcium Silicate Hydrate Solid Solutions. Part 1: Synchrotron-Based X-Ray Diffraction, J. Am. Ceram. Soc. 91 (2008) 3005–3014. doi:10.1111/j.1551-2916.2008.02484.x.

[127] K. Garbev, M. Bornefeld, G. Beuchle, P. Stemmermann, Cell Dimensions and Composition of Nanocrystalline Calcium Silicate Hydrate Solid Solutions. Part 2: X-Ray and Thermogravimetry Study, J. Am. Ceram. Soc. 91 (2008) 3015–3023. doi:10.1111/j.1551-2916.2008.02601.x.

[128] S. Grangeon, F. Claret, Y. Linard, C. Chiaberge, X-ray diffraction: A powerful tool to probe and understand the structure of nanocrystalline calcium silicate hydrates, Acta Crystallogr. Sect. B Struct. Sci. Cryst. Eng. Mater. 69 (2013) 465–473. doi:10.1107/S2052519213021155.

[129] C.S. Walker, S. Sutou, C. Oda, M. Mihara, A. Honda, Calcium silicate hydrate (C-S-H) gel solubility data and a discrete solid phase model at 25 °C based on two binary non-ideal solid solutions, Cem. Concr. Res. 79 (2016) 1–30. doi:10.1016/j.cemconres.2015.07.006.

[130] S. Grangeon, A. Fernandez-Martinez, A. Baronnet, N. Marty, A. Poulain, E. Elkaïm, et al., Quantitative X-ray pair distribution function analysis of nanocrystalline calcium silicate hydrates: a contribution to the understanding of cement chemistry, J. Appl. Crystallogr. 50 (2017) 14–21. doi:10.1107/S1600576716017404.

[131] J. Hirljac, Z.-Q. Wu, J.F. Young, Silicate polymerization during the hydration of alite, Cem. Concr. Res. 13 (1983) 877–886. doi:10.1016/0008-8846(83)90089-3.

[132] L. Nicoleau, M.A. Bertolim, Analytical Model for the Alite (C3S) Dissolution Topography, J. Am. Ceram. Soc. 99 (2016) 773–786. doi:10.1111/jace.13647.

[133] P.W. Brown, J. Pommersheim, G. Frohnsdorff, A kinetic model for the hydration of tricalcium silicate, Cem. Concr. Res. 15 (1985) 35–41. doi:10.1016/0008-8846(85)90006-7.

[134] P.W. Brown, E. Franz, G. Frohnsdorff, H.F.W. Taylor, Analyses of the aqueous phase during early C3S hydration, Cem. Concr. Res. 14 (1984) 257–262. doi:10.1016/0008-8846(84)90112-1.

[135] H.M. Jennings, Aqueous Solubility Relationships for Two Types of Calcium Silicate Hydrate, J.

Am. Ceram. Soc. 69 (1986) 614–618. doi:10.1111/j.1151-2916.1986.tb04818.x.

[136] I. García Lodeiro, D.E. Macphee, A. Palomo, A. Fernández-Jiménez, Effect of alkalis on fresh C–S–H gels. FTIR analysis, Cem. Concr. Res. 39 (2009) 147–153. doi:10.1016/j.cemconres.2009.01.003.

[137] D.A. Hall, D.C. Maus, G.J. Gerfen, S.J. Inati, L.R. Becerra, F.W. Dahlquist, et al., Polarization-enhanced NMR spectroscopy of biomolecules in frozen solution, Science (80-.). 276 (1997) 930–932. doi:10.1126/science.276.5314.930.

[138] T. Maly, G.T. Debelouchina, V.S. Bajaj, K.-N. Hu, C.-G. Joo, M.L. Mak-Jurkauskas, et al., Dynamic nuclear polarization at high magnetic fields, J. Chem. Phys. 128 (2008) 052211. doi:10.1063/1.2833582.

[139] Q.Z. Ni, E. Daviso, T. V. Can, E. Markhasin, S.K. Jawla, T.M. Swager, et al., High frequency dynamic nuclear polarization, Acc. Chem. Res. 46 (2013) 1933–1941. doi:10.1021/ar300348n.

[140] R.P. Sangodkar, B.J. Smith, D. Gajan, A.J. Rossini, L.R. Roberts, G.P. Funkhouser, et al., Influences of Dilute Organic Adsorbates on the Hydration of Low-Surface-Area Silicates, J. Am. Chem. Soc. 137 (2015) 8096–8112. doi:10.1021/jacs.5b00622.

[141] D.A. Kulik, Improving the structural consistency of C-S-H solid solution thermodynamic models, Cem. Concr. Res. 41 (2011) 477–495. doi:10.1016/j.cemconres.2011.01.012.

[142] D.A. Kulik, T. Wagner, S. V. Dmytrieva, G. Kosakowski, F.F. Hingerl, K. V. Chudnenko, et al., GEM-Selektor geochemical modeling package: Revised algorithm and GEMS3K numerical kernel for coupled simulation codes, Comput. Geosci. 17 (2013) 1–24. doi:10.1007/s10596-012-9310-6.

[143] B. Lothenbach, F. Winnefeld, Thermodynamic modelling of the hydration of Portland cement, Cem. Concr. Res. 36 (2006) 209–226. doi:10.1016/j.cemconres.2005.03.001.

[144] M. Rosay, L. Tometich, S. Pawsey, R. Bader, R. Schauwecker, M. Blank, et al., Solid-state dynamic nuclear polarization at 263 GHz: spectrometer design and experimental results, Phys. Chem. Chem. Phys. 12 (2010) 5850–5860. doi:10.1039/C003685B.

[145] I.T. Todorov, W. Smith, K. Trachenko, M.T. Dove, DL_POLY_3: new dimensions in molecular dynamics simulations via massive parallelism, J. Mater. Chem. 16 (2006) 1911–1918.

doi:10.1039/B517931A.

[146] J.P. Perdew, K. Burke, M. Ernzerhof, D. of Physics, N.O.L. 70118 J. Quantum Theory Group Tulane University, Generalized Gradient Approximation Made Simple, Phys. Rev. Lett. 77 (1996) 3865–3868. doi:10.1103/PhysRevLett.77.3865.

[147] J.R. Yates, C.J. Pickard, F. Mauri, Calculation of NMR chemical shifts for extended systems using ultrasoft pseudopotentials, Phys. Rev. B. 76 (2007) 024401. doi:10.1103/PhysRevB.76.024401.

[148] L. Nicoleau, A. Nonat, D. Perrey, The di- and tricalcium silicate dissolutions, Cem. Concr. Res. 47 (2013) 14–30. doi:10.1016/j.cemconres.2013.01.017.

[149] I. g. Richardson, J. Skibsted, L. Black, R. j. Kirkpatrick, Characterisation of cement hydrate phases by TEM, NMR and Raman spectroscopy, Adv. Cem. Res. 22 (2010) 233–248. doi:10.1680/adcr.2010.22.4.233.

[150] F. Brunet, P. Bertani, T. Charpentier, A. Nonat, J. Virlet, Application of 29Si Homonuclear and 1H−29Si Heteronuclear NMR Correlation to Structural Studies of Calcium Silicate Hydrates, J. Phys. Chem. B. 108 (2004) 15494–15502. doi:10.1021/jp031174g.

[151] A. Rawal, B.J. Smith, G.L. Athens, C.L. Edwards, L. Roberts, V. Gupta, et al., Molecular Silicate and Aluminate Species in Anhydrous and Hydrated Cements, J. Am. Chem. Soc. 132 (2010) 7321–7337. doi:10.1021/ja908146m.

[152] R. Alizadeh, L. Raki, J.M. Makar, J.J. Beaudoin, I. Moudrakovski, Hydration of tricalcium silicate in the presence of synthetic calcium–silicate–hydrate, J. Mater. Chem. 19 (2009) 7937. doi:10.1039/b910216g.

[153] E.M. Foley, J.J. Kim, M.M. Reda Taha, Synthesis and nano-mechanical characterization of calcium-silicate-hydrate (C-S-H) made with 1.5 CaO/SiO2 mixture, Cem. Concr. Res. 42 (2012) 1225–1232. doi:10.1016/j.cemconres.2012.05.014.

[154] E. Pustovgar, R.P. Sangodkar, A.S. Andreev, M. Palacios, B.F. Chmelka, R.J. Flatt, et al., Understanding silicate hydration from quantitative analyses of hydrating tricalcium silicates, Nat. Commun. 7 (2016) 10952. doi:10.1038/ncomms10952.

[155] C. Sauvée, M. Rosay, G. Casano, F. Aussenac, R.T. Weber, O. Ouari, et al., Highly Efficient,

Water-Soluble Polarizing Agents for Dynamic Nuclear Polarization at High Frequency, Angew. Chemie Int. Ed. 52 (2013) 10858–10861. doi:10.1002/anie.201304657.

[156] A. Lesage, M. Lelli, D. Gajan, M.A. Caporini, V. Vitzthum, P. Miéville, et al., Surface Enhanced NMR Spectroscopy by Dynamic Nuclear Polarization, J. Am. Chem. Soc. 132 (2010) 15459–15461. doi:10.1021/ja104771z.

[157] A.J. Rossini, A. Zagdoun, M. Lelli, A. Lesage, C. Copéret, L. Emsley, Dynamic Nuclear Polarization Surface Enhanced NMR Spectroscopy, Acc. Chem. Res. 46 (2013) 1942–1951. doi:10.1021/ar300322x.

[158] L.R. Becerra, G.J. Gerfen, R.J. Temkin, D.J. Singel, R.G. Griffin, Dynamic nuclear polarization with a cyclotron resonance maser at 5 T, Phys. Rev. Lett. 71 (1993) 3561–3564. doi:10.1103/PhysRevLett.71.3561.

[159] J.J. Thomas, H.M. Jennings, A.J. Allen, Determination of the Neutron Scattering Contrast of Hydrated Portland Cement Paste using H2O/D2O Exchange, Adv. Cem. Based Mater. 7 (1998) 119–122. doi:10.1016/S1065-7355(97)00086-2.

[160] D. Gajan, M. Schwarzwälder, M.P. Conley, W.R. Grüning, A.J. Rossini, A. Zagdoun, et al., Solid-Phase Polarization Matrixes for Dynamic Nuclear Polarization from Homogeneously Distributed Radicals in Mesostructured Hybrid Silica Materials, J. Am. Chem. Soc. 135 (2013) 15459–15466. doi:10.1021/ja405822h.

[161] L.B. Alemany, D.M. Grant, R.J. Pugmire, T.D. Alger, K.W. Zilm, Cross polarization and magic angle sample spinning NMR spectra of model organic compounds. 2. Molecules of low or remote protonation, J. Am. Chem. Soc. 105 (1983) 2142–2147. doi:10.1021/ja00346a007.

[162] A. Lesage, M. Bardet, L. Emsley, Through-Bond Carbon−Carbon Connectivities in Disordered Solids by NMR, J. Am. Chem. Soc. 121 (1999) 10987–10993. doi:10.1021/ja992272b.

[163] D. Lee, G. Monin, N.T. Duong, I.Z. Lopez, M. Bardet, V. Mareau, et al., Untangling the Condensation Network of Organosiloxanes on Nanoparticles using 2D 29Si–29Si Solid-State NMR Enhanced by Dynamic Nuclear Polarization, J. Am. Chem. Soc. 136 (2014) 13781–13788. doi:10.1021/ja506688m.

[164] X. Xue, M. Kanzaki, Proton Distributions and Hydrogen Bonding in Crystalline and Glassy

Hydrous Silicates and Related Inorganic Materials: Insights from High-Resolution Solid-State Nuclear Magnetic Resonance Spectroscopy, J. Am. Ceram. Soc. 92 (2009) 2803–2830. doi:10.1111/j.1551-2916.2009.03468.x.

[165] I.G. Richardson, The nature of C-S-H in hardened cements, Cem. Concr. Res. 29 (1999) 1131–1147. doi:10.1016/S0008-8846(99)00168-4.

[166] S. Merlino, E. Bonaccorsi, T. Armbruster, The real structures of clinotobermorite and tobermorite 9 Å: OD character, polytypes, and structural relationships, Eur. J. Mineral. (2000) 411–429. doi:10.1127/0935-1221/2000/0012-0411.

[167] C. Roosz, S. Gaboreau, S. Grangeon, D. Prêt, V. Montouillout, N. Maubec, et al., Distribution of Water in Synthetic Calcium Silicate Hydrates, Langmuir. 32 (2016) 6794–6805. doi:10.1021/acs.langmuir.6b00878.

[168] A. Nonat, X. Lecoq, The Structure, Stoichiometry and Properties of C-S-H Prepared by C3S Hydration Under Controlled Condition, in: D.P. Colombet, P.H. Zanni, D.A.-R. Grimmer, P.P. Sozzani (Eds.), Nucl. Magn. Reson. Spectrosc. Cem. Mater., Springer Berlin Heidelberg, 1998: pp. 197–207.

[169] A.J. Allen, J.J. Thomas, H.M. Jennings, Composition and density of nanoscale calcium-silicate-hydrate in cement., Nat. Mater. 6 (2007) 311–316. doi:10.1038/nmat1871.

[170] A. Kumar, B.J. Walder, A. Kunhi Mohamed, A. Hofstetter, B. Srinivasan, A.J. Rossini, et al., The Atomic-Level Structure of Cementitious Calcium Silicate Hydrate, J. Phys. Chem. C. 121 (2017) 17188–17196. doi:10.1021/acs.jpcc.7b02439.

[171] X. Cong, R.J. Kirkpatrick, {29Si} {MAS} {NMR} study of the structure of calcium silicate hydrate, Adv. Cem. Based Mater. 3 (1996) 144–156. doi:10.1016/S1065-7355(96)90046-2.

[172] A. Kunhi Mohamed, S.C. Parker, P. Bowen, S. Galmarini, An atomistic building block description of C-S-H - Towards a realistic C-S-H model, Cem. Concr. Res. 107 (2018) 221–235. doi:10.1016/j.cemconres.2018.01.007.

[173] A.M. Gajewicz, E. Gartner, K. Kang, P.J. McDonald, V. Yermakou, A1H NMR relaxometry investigation of gel-pore drying shrinkage in cement pastes, Cem. Concr. Res. 86 (2016) 12–19. doi:10.1016/j.cemconres.2016.04.013.

[174] M. Wyrzykowski, P.J. McDonald, K.L. Scrivener, P. Lura, Water Redistribution within the Microstructure of Cementitious Materials due to Temperature Changes Studied with 1H NMR, J. Phys. Chem. C. 121 (2017) 27950–27962. doi:10.1021/acs.jpcc.7b08141.

[175] S. Grimme, Semiempirical {GGA}-type density functional constructed with a long-range dispersion correction, J. Comput. Chem. 27 (2006) 1787–1799.

[176] T.C. POWERS, Structure and Physical Properties of Hardened Portland Cement Paste, J. Am. Ceram. Soc. 41 (1958) 1–6. doi:10.1111/j.1151-2916.1958.tb13494.x.

[177] I.G. Richardson, G.W. Groves, The incorporation of minor and trace elements into calcium silicate hydrate (CSH) gel in hardened cement pastes, Cem. Concr. Res. 23 (1993) 131–138. doi:10.1016/0008-8846(93)90143-W.

[178] M.D. Andersen, H.J. Jakobsen, J. Skibsted, Incorporation of Aluminum in the Calcium Silicate Hydrate (C−S−H) of Hydrated Portland Cements: A High-Field 27 Al and 29 Si MAS NMR Investigation, Inorg. Chem. 42 (2003) 2280–2287. doi:10.1021/ic020607b.

[179] G.K. Sun, J.F. Young, R.J. Kirkpatrick, The role of Al in C-S-H: NMR, XRD, and compositional results for precipitated samples, Cem. Concr. Res. 36 (2006) 18–29. doi:10.1016/j.cemconres.2005.03.002.

[180] X. Pardal, F. Brunet, T. Charpentier, I. Pochard, A. Nonat, 27 Al and 29 Si Solid-State NMR Characterization of Calcium-Aluminosilicate-Hydrate, Inorg. Chem. 51 (2012) 1827–1836. doi:10.1021/ic202124x.

[181] E. L'Hôpital, B. Lothenbach, G. Le Saout, D. Kulik, K. Scrivener, Incorporation of aluminium in calcium-silicate-hydrates, Cem. Concr. Res. 75 (2015) 91–103. doi:10.1016/j.cemconres.2015.04.007.

[182] L. Pegado, C. Labbez, S. V. Churakov, Mechanism of aluminium incorporation into C–S–H from ab initio calculations, J. Mater. Chem. A. 2 (2014) 3477. doi:10.1039/c3ta14597b.

[183] Z. Dai, T.T. Tran, J. Skibsted, Aluminum incorporation in the C-S-H phase of white portland cement-metakaolin blends studied by 27 Al and 29 Si MAS NMR spectroscopy, J. Am. Ceram. Soc. 97 (2014) 2662–2671. doi:10.1111/jace.13006.

[184] B. Mota, T. Matschei, K. Scrivener, The influence of sodium salts and gypsum on alite

hydration, Cem. Concr. Res. 75 (2015) 53–65. doi:10.1016/j.cemconres.2015.04.015.

[185] A. Bazzoni, S. Ma, Q. Wang, X. Shen, M. Cantoni, K.L. Scrivener, The {Effect} of {Magnesium} and {Zinc} {Ions} on the {Hydration} {Kinetics} of {C}3S, J. Am. Ceram. Soc. 97 (2014) 3684–3693. doi:10.1111/jace.13156.

[186] R.J. Flatt, Y.F. Houst, A simplified view on chemical effects perturbing the action of superplasticizers, Cem. Concr. Res. 31 (2001) 1169–1176. doi:10.1016/S0008-8846(01)00534-8.

[187] I. Androniuk, C. Landesman, P. Henocq, A.G. Kalinichev, Adsorption of gluconate and uranyl on C-S-H phases: Combination of wet chemistry experiments and molecular dynamics simulations for the binary systems, Phys. Chem. Earth. 99 (2017) 194–203. doi:10.1016/j.pce.2017.05.005.

[188] A. Hartmann, D. Schulenberg, J. Buhl, Synthesis and Structural Characterization of CSH-Phases in the Range of C/S = 0.41 - 1.66 at Temperatures of the Tobermorite Xonotlite Crossover, J. Mater. Sci. Chem. Eng. 3 (2015) 39–55. doi:10.4236/msce.2015.311006.

[189] S.T. Bergold, F. Goetz-Neunhoeffer, J. Neubauer, Quantitative analysis of C–S–H in hydrating alite pastes by in-situ XRD, Cem. Concr. Res. 53 (2013) 119–126. doi:10.1016/j.cemconres.2013.06.001.

[190] E. Salager, G.M. Day, R.S. Stein, C.J. Pickard, B. Elena, L. Emsley, Powder Crystallography by Combined Crystal Structure Prediction and High-Resolution 1H Solid-State NMR Spectroscopy, J. Am. Chem. Soc. 132 (2010) 2564–2566. doi:10.1021/ja909449k.

Chapter VIII. Appendix

8.1 CementFFv1

Force field in DLPOLY FIELD file format

UNITS	eV					
MOLECULES	5					
HYDROXYL						
NUMMOL	48					
atoms	2					
	O	16	-1.4	0	0	0
	H	1.008	0.4			
bonds	1					
mors	1	2	7.0525	0.9429	3.1749	
finish						
CA	CORE					
NUMMOL	120					
atoms	1					
	CA	39.88	2	0	0	0
finish						
SI	CORE					
NUMMOL	144					
atoms	1					
	SI	28.09	4	0	0	0
finish						
OS	CORE					
NUMMOL	384					
atoms	1					
	OS	16	-2	0	0	0
finish						
TIP4P/2005	water					
NUMMOL	168					
atoms	4					
	OW	15.9996	0	0	0	0
	OM	0	-1.1128	0	0	0
	HW	1.0008	0.5564	0	0	0

	HW	1.0008	0.5564	0	0	0	
rigid	bodies	1					
	4	1	2	3	4		
FINISH							
vdw	25						
SI	OS	buck	1283.9073	0.3205	10.6616		
OS	OS	buck	22764	0.149	27.88		
OS	MG	buck	1428.5	0.2945	0		
SI	O	buck	983.556	0.3205	10.6616		
OS	O	buck	22764	0.149	13.94		
OS	OW	buck	22764	0.149	28.92		
MG	O	buck	941.5	0.2945	0		
O	O	buck	22764	0.149	6.97		
O	OW	nm	0.0013	9	6	4.63	
O	H	nm	0.0073	9	6	2.71	
OS	H	nm	0.0073	9	6	2.71	
OS	HW	buck	396.27	0.25	0		
H	OW	nm	0.0555555	9	6	1.81712	
OW	AL	buck	584.3	0.2991	0		
O	AL	buck	1022.3	0.2991	0		
OS	AL	buck	1460.3	0.2991	0		
SI	OW	buck	1283.556	0.3205	10.6616		
MG	OW	buck	454.5	0.2945	0		
OS	K	buck	65269.71	0.2134	0		
O	K	buck	45688.8	0.2134	0		
OW	K	buck	26107.9	0.2134	0		
O	CA	buck	2251.05	0.297	0		
CA	OS	buck	1090.4	0.3437	0		
CA	OW	buck	1186.6	0.297	0		
OW	OW	lj	0.0080314	3.1589			
tbp	5						
OS	SI	OS	shrm	15.4963	109.466667	1.6	1.6
O	SI	OS	shrm	15.4963	109.466667	1.6	1.6
O	SI	O	shrm	15.4963	109.466667	1.6	1.6
SI	OS	SI	shrm	15.4963	132	1.6	1.6
SI	O	H	shrm	15.4963	141.5	1.6	1.2
CLOSE							

8.2 CementFFv2

Force field in DLPOLY FIELD file format

UNITS	eV					
MOLECULES	5					
HYDROXYL						
NUMMOL	96					
atoms	2					
	Oh	16	-1.4	0	0	0
	H	1.008	0.4	0	0	0
bonds	1					
mors	1	2	7.0525	0.9429	3.1749	
finish						
CA	CORE					
NUMMOL	240					
atoms	1					
	Ca	39.88	2	0	0	0
finish						
SI	CORE					
NUMMOL	288					
atoms	1					
	Si	28.09	4	0	0	0
finish						
OS	CORE					
NUMMOL	768					
atoms	2					
	O	15.79	0.848	0	0	0
	O(S)	**0.2**	**-2.848**	**0**	**0**	**0**
shell	1	1				
	1	2	74.9204			
finish						
TIP4P/2005	water					
NUMMOL	336					
atoms	4					
	Ow	15.9996	0	0	0	0
	Om	0	-1.1128	0	0	0
	Hw	1.0008	0.5564	0	0	0
	Hw	1.0008	0.5564	0	0	0
rigid	bodies	1				
	4	1	2	3	4	
FINISH						
vdw	16					
Si	O(S)	buck	1283.9073	0.3205	10.6616	

O(S)	O(S)	buck	22764	0.149	27.88			
Si	Oh	buck	983.556	0.3205	10.6616			
O(S)	Oh	buck	22764	0.149	13.94			
O(S)	Ow	buck	22764	0.149	28.92			
Oh	Oh	buck	22764	0.149	6.97			
Oh	Ow	nm	0.0013	9	6	4.63		
Oh	H	nm	0.0073	9	6	2.71		
O(S)	H	nm	0.0073	9	6	2.71		
O(S)	**Hw**	**buck**	**512**	**0.25**	**0**			
H	**Ow**	**nm**	**0.0555555**	**9**	**6**	**2**		
Si	Ow	buck	1283.556	0.3205	10.6616			
Oh	Ca	buck	2251.05	0.297	0			
Ca	**O(S)**	**buck**	**2152.3566**	**0.309227**	**0.09944**			
Ca	**Ow**	**buck**	**1286.6**	**0.297**	**0**			
Ow	Ow	lj	0.0080314	3.1589				
tbp	4							
O	Si	O	shrm	15.4963	109.466667	1.7	1.7	3
Oh	Si	O	shrm	15.4963	109.466667	1.7	1.7	3
Oh	Si	Oh	shrm	15.4963	109.466667	1.7	1.7	3
Si	Oh	H	shrm	15.4963	141.5	1.7	1.2	2.6
CLOSE								

8.3 Supplementary information 1: An Atomistic Builiding Block Description of C-S-H – Towards a realistic C-S-H model

8.3.1 Introduction

This supplementary materials contains mainly additional graphics and schemas to further illustrate the building block model described in the main part of the article as well as some computational details and some additional results.

8.3.2 C-S-H Building Block Description

This section contains supplementary figures to further illustrate the building block model. In Figure S31 different tobermorite structures are compared by looking at their reduced unit cell from different angles. Four different structures are shown: 11 Å normal tobermorite [43] (<|S<C_5>|S><|S<$_5$>|S>), Hamids 11 Å tobermorite structure [44] (<S'<C_2>S'><'S'<$_2$>'S'>), 14 Å tobermorite [42] (<S'<C_7>S'>) and finally clinotobermorite [166] (<S|<C_2>|S>). The reduced unit cells for these structures can be found in separate files in the supplementary material. These can be used to construct C-S-H structures using different underlying models. Other model structures, such as a staggered-chain clinotobermorite with no interconnected chains (no |S groups), as considered by Richardson [20], can be used as well.

In Figure S32 and Figure S33 different types of disorder known to exist in 14 Å tobermorite, namely the positional disorder of the interlayer calcium and different stacking sequences and corresponding layer geometries [42] are illustrated.

Finally in Figure S34 different surface planes discussed in the paper are shown. The five surfaces ((100), (001), (010), (-201) and (0-11)) correspond to the following indices for the unit cell reported by Bonaccorsi et al. [42]: (1-10), (001), (012), (100) and (010). Furthermore the protonated silanol groups which make it easy to see that for some surfaces (e.g. the (100) or the (010)) the direction of the surface normal is important are highlighted. In fact, due to the low symmetry of tobermorite, for example the (100) and the (-100) surfaces are not equivalent.

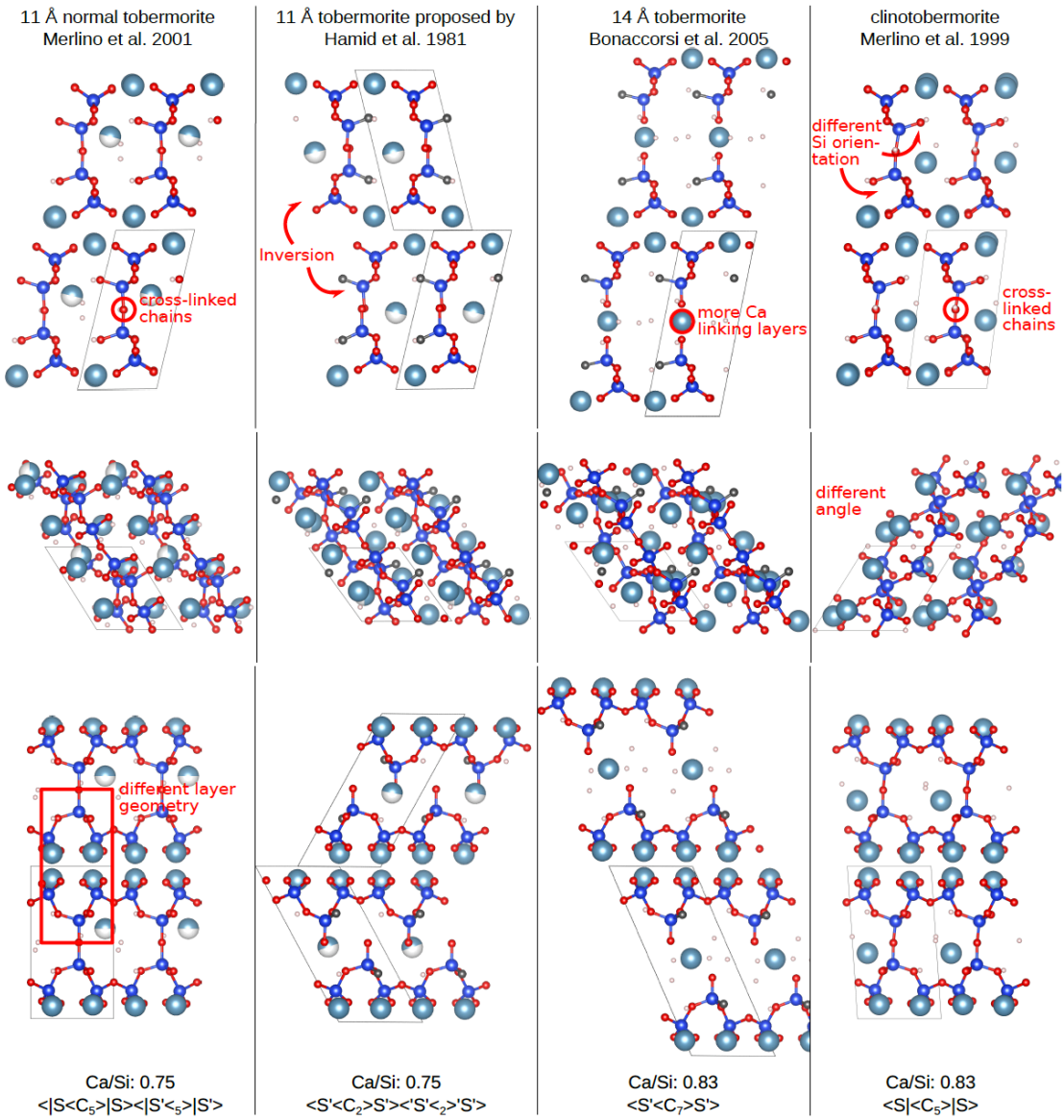

Figure S31: Geometrical comparison of different tobermorite structures reported in the literature and definition of the reduced cell used for structural characterisation. Si: blue. Ca: turquoise, O: red, H_2O: white, OH: black.

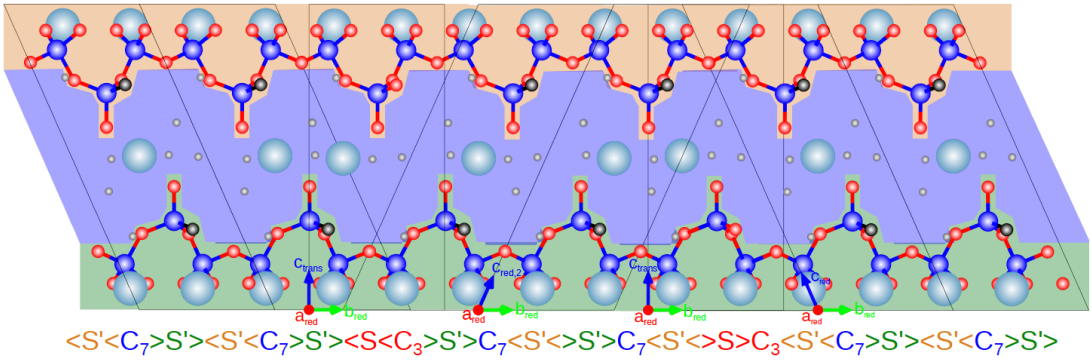

Figure S32: Layer structure with alternate $a_{red} = a'$, $b_{red} = b'$, $c_{red} = 0.5 \cdot (c' - a') - b'$ *and* $a_{red,2} = a'$, $b_{red,2} = b'$, $c_{red,2} = 0.5 \cdot (c' - a') + b'$ *unit cells and the corresponding defect units in between. Si: blue. Ca: turquoise, O: red,* H_2O*: white, OH: black.*

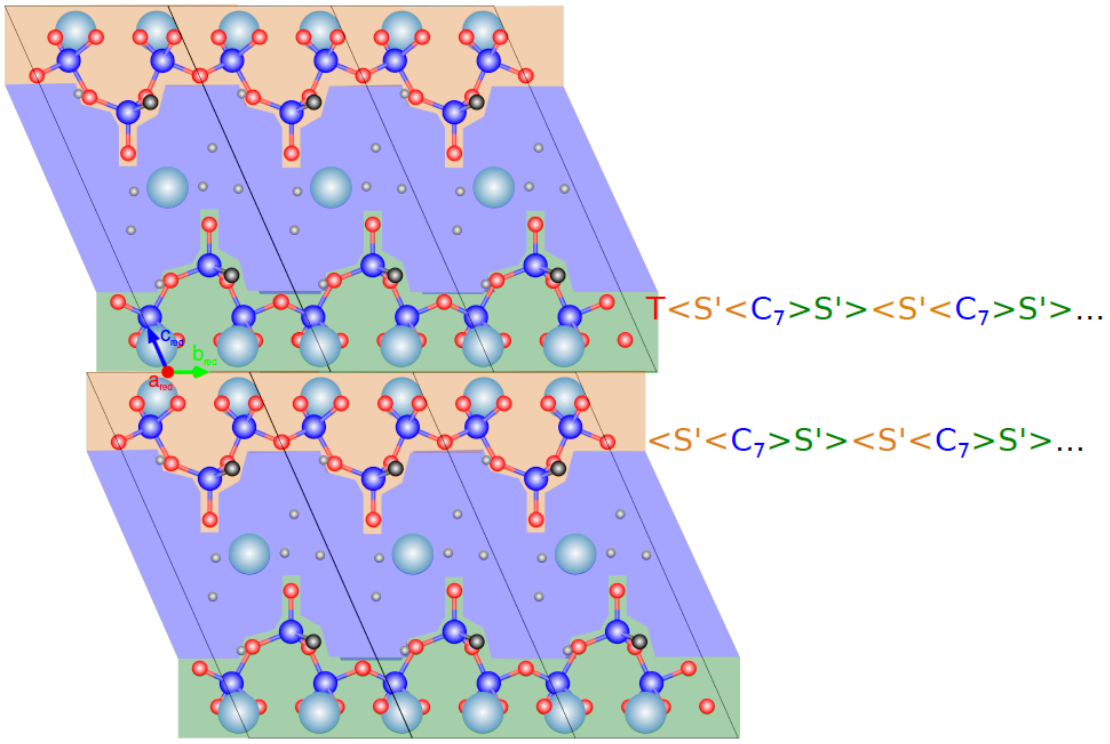

Figure S33: Different stacking in the calcium-silicate layer which has also been observed by the original structure characterization by Bonaccorsi et al. [42]. *T , as described in the article section 4.5.1, indicates that the origin of that layer is shifted by bred=2 . Si: blue. Ca: turquoise, O: red, H_2O: white, OH: black.*

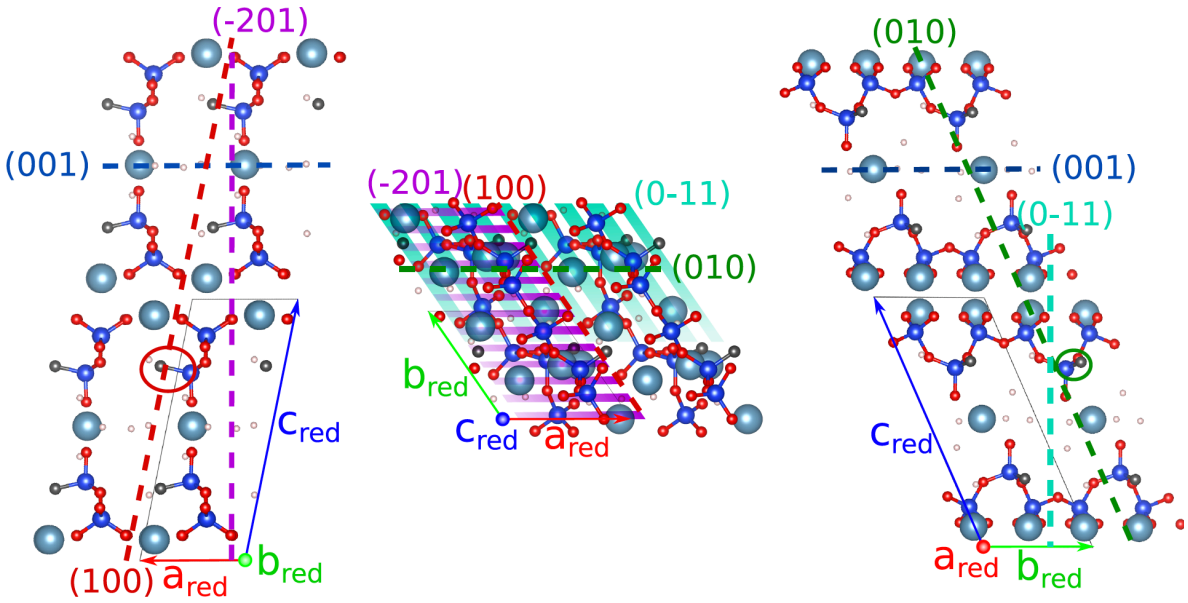

Figure S34: Different possible surfaces as discussed in the text: (100), (001), (010), (-201) and (0-11). For some surfaces the direction of the surface normal is important and e.g. the (100) and the (-100) are not equivalent. This can be seen from the direction of the protonated silanol groups highlighted by circles. Si: blue. Ca: turquoise, O: red, H_2O: white, OH: black.

8.3.3 Further Characteristics of Previous Models

In Figure S35 a larger view of the atomistic structure of the Model 1 sample 1 structure reported by Kovacevic et al. [67] can be found. In Figure S36 the charge distribution of the structure as calculated with the building block description is shown.

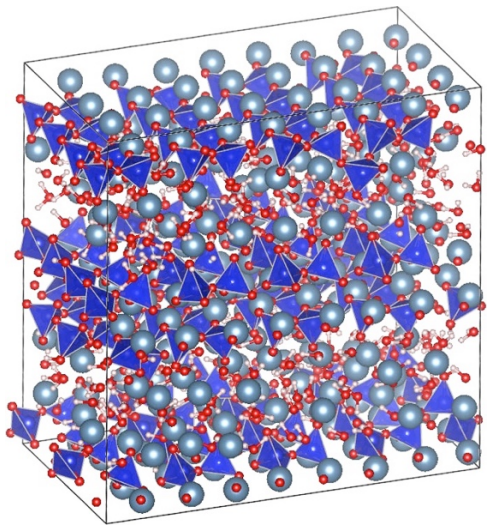

Figure S35: Atomistic structure of the Model 1 sample 1 structure reported by Kovacevic et al. [67] Si: blue. Ca: turquoise, O: red, H: white

+1	-1	-3	+1
+2	+1	-3	+2
+1	-2	-1	-2
+2	0	-1	+1

+1	-1	-1	+1
-1	+3	-1	-1
+2	+2	-2	0
0	+2	-1	-1

Figure S36: Charge distribution of the Model 1 sample 1 structure reported by Kovacevic et al. [67] as calculated according to the building block description as can be found in the main part of the paper.

8.3.4 III Full scale defective structure

In Figure S37 a larger view of the atomistic structure of the full scale Ca/Si = 1.67 structure discussed in the main text is shown.

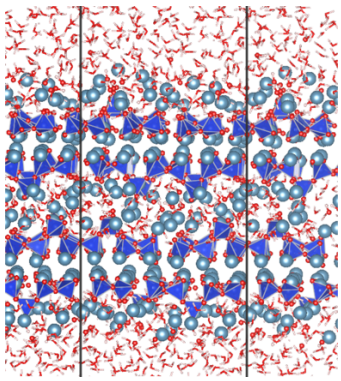

Figure S37: Atomistic view of the full scale Ca/Si = 1.67 structure discussed in the main text. Si: blue. Ca: turquoise, O: red, H: white.

8.3.5 V Calculated XRD-spectra

Calculated XRD spectra for structures minimised by DFT compared to classical MD minimised and experimental structure (Figure S38) and classical energy minimisation (Figure S39) respectively.

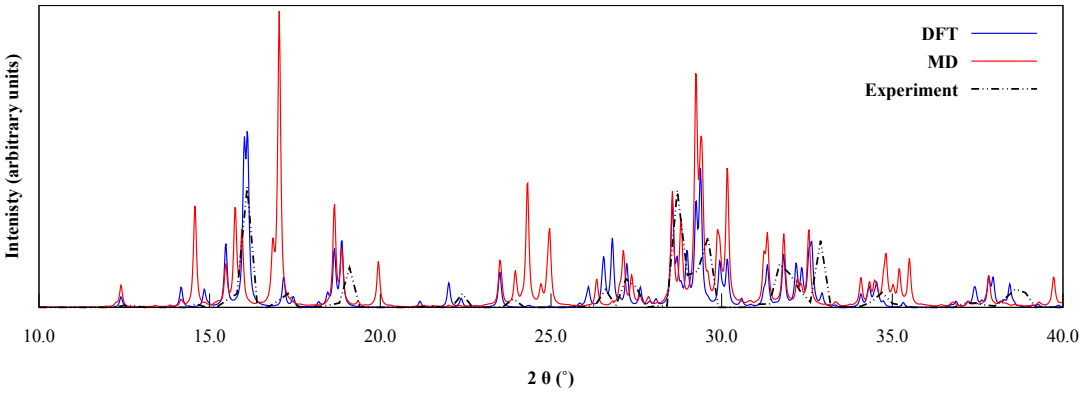

Figure S38: Simulated XRD patterns of the 14 Å tobermorite structure as experimentally reported [42] *(black), after DFT minimization (blue) and after molecular dynamics minimization of a bulk supercell (4x3x1 units) for 1.4 ns at 300 K in a NST ensemble (red).*

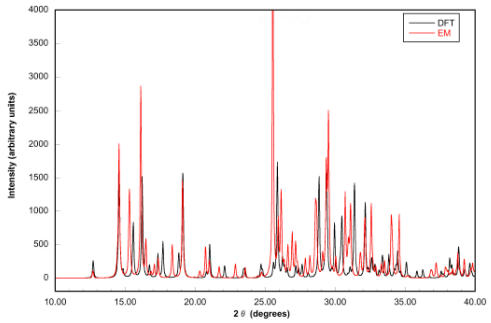

(a) <S<CC$_7$>S>

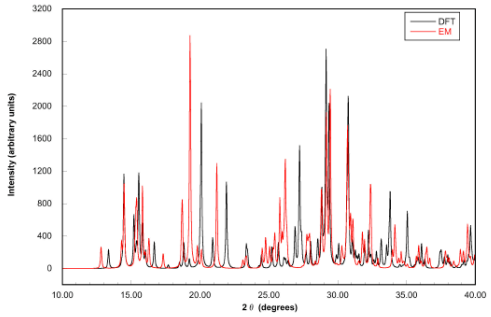

(b) <S<C°C°$_7$>' '>

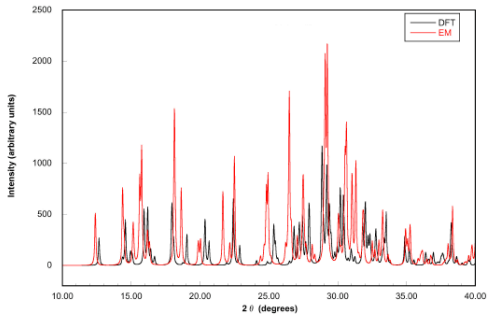

(c) <S<CC$_7$>°C°>

Figure S39: Simulated XRD patterns of different Ca/Si ratio tobermorite structure after DFT minimization (black) and after energy minimization at constant pressure (red).

8.4 Supplementary information 2 : The Atomic-Level Structure of Cementitious Calcium Silicate Hydrate

Here the only relevant sections of the supplementary material are shown for the sake of brevity (and environment). For the complete information, kindly visit **DOI:** 10.1021/acs.jpcc.7b02439

8.4.1 Structural model

It is known that C-S-H resembles a defective tobermorite.[16,165] To create a structure based on defective tobermorite that possesses high Ca:Si ratios, we build substructures of C-S-H according to the following procedure:

- Deprotonate silanol in the bridging tetrahedrons and replace it with a $CaOH^+$ ion in the interlayer.
- Remove a bridging silicate tetrahedron, performing charge compensation by adding two protons or a proton and a $CaOH^+$ ion or addition of a Ca^{2+} to coordinate the bridging site (Ca_B site in Figure S40).
- Add $Ca(OH)_2$ units in the interlayer space (Ca_I and Ca_A) to obtain higher Ca:Si ratios.

We study the effect of these different defect units (Figure S40A) on the ^1H chemical shifts. Reduced unit cells are constructed by connecting the defect units through an aqueous interlayer or an aqueous interlayer with a Ca_I and additional OH^- for charge balance (Figure S40B). In order to study medium range effects, we also consider different ways to combine the reduced unit cells, resulting in chain, dimer, and pentamer motifs (Figure S40C).

All the structures are first partially relaxed with energy minimization using METADISE[95] with a force field potential previously used for cementitious materials.[12] If the atomic bond distances, calcium coordination and local charge neutrality are satisfactory then they are relaxed using density function theory (DFT). For the former two criteria, we require specifically that Ca-O bonds are between 2.2 Å and 2.9 Å and that calcium coordination numbers are near six. The condition of local charge neutrality is implemented as systems with large distances between charged species consistently exhibit higher energies than systems for which this is not the case. Additional water molecules can be added to the interlayer to help satisfy these criteria. Depending on the initial atomic coordinates, especially those that specify the positioning of the interlayer water, the reduced unit cells may relax into different structures with the same defect classification.

These structures are again checked for the calcium coordination, lack of disruption of the main layer calcium-silicate backbone chain, and local charge neutrality. Once all the criteria are met, ^1H and ^{29}Si chemical shift calculations are performed on the candidates. The chemical shielding σ_{calc} was calculated using the generalized gradient approximation (GGA) functional PBE[146] within the Quantum Espresso code[105] and the GIPAW method.[147] For each calculation a plane-wave maximum cutoff energy of 80 Ry, and a Monkhorst-Pack grid of *k*-points[104] corresponding to 0.033 $Å^{-1}$ in reciprocal space was employed. These values were tested for convergence of calculated energy and chemical shielding.

The convergence criteria for force, energy and pressure for structural relaxation were set to 10^{-3} E_h/a_0, 10^{-4} E_h, and 500 bar respectively. The final pressure of each relaxed structure was less than 150 bar. For structures which contain Ca_I, the final pressure was usually below 50 bar. To ensure this 500 bar threshold was sufficient, we performed an additional DFT relaxation of the structure based upon the ACcaV2 motif, setting a cell pressure threshold of 0.01 bar. Because of this stricter convergence criteria, O – O distances throughout the structure change by 0.05 - 0.1 Å, resulting in a ^{1}H chemical shift RMSD of 0.59 ppm and a ^{29}Si chemical shift RMSD of 0.34 ppm relative to the structure calculated with the higher convergence threshold for pressure. The higher ^{1}H chemical shift RMSD corresponds to the fact that proton chemical shifts are more sensitive to changes in the hydrogen bonding network than ^{29}Si. In NMR crystallography, two systems are considered identical if the ^{1}H chemical shift RMSD is below 0.5 ppm.[190] We justify a slightly higher limit for the C-S-H considering that most of the protons of weakly bonded interlayer species have lower barriers to conformational rearrangement relative to crystals of small organic molecules. Indeed, there is a correlation between the largest ^{1}H chemical shift changes occur for species near 0 ppm, as shown in Figure S41. If the proton chemical shifts corresponding to these non-hydrogen bonded H_2O are excluded from the comparison, we calculate a ^{1}H chemical shift RMSD of 0.38 ppm, which is well below the cutoff of 0.5 ppm. Therefore, a stricter convergence criterion for the DFT relaxation does not affect our interpretation of the ^{1}H chemical shifts nor the conclusions drawn from them.

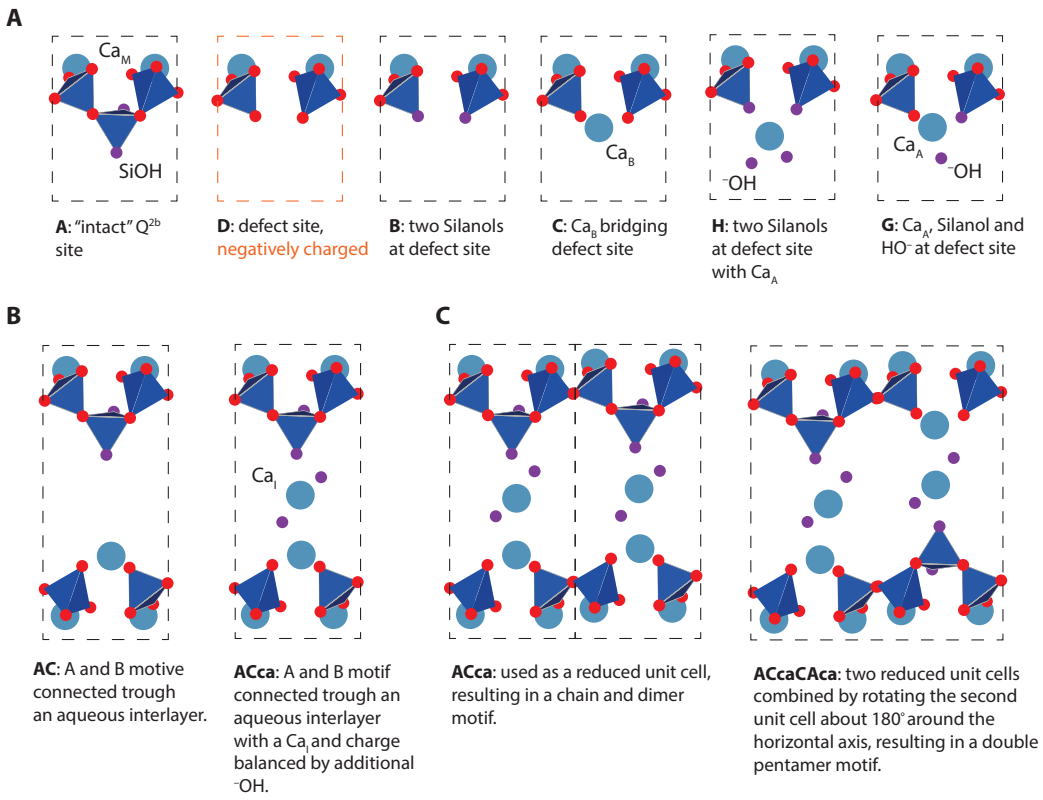

Figure S40 | Defect classification. (A) Simple defect units. (B) Simple defect units are combined with added interlayer water to form reduced unit cells. ^{1}H chemical shifts are calculated for structurally viable reduced unit cells. (C) Two possible ways of combining two reduced unit cells, showing how infinite chain, dimer, and

pentamer motifs can be generated. The water in the aqueous interlayer and the hydrogen atoms are not shown.

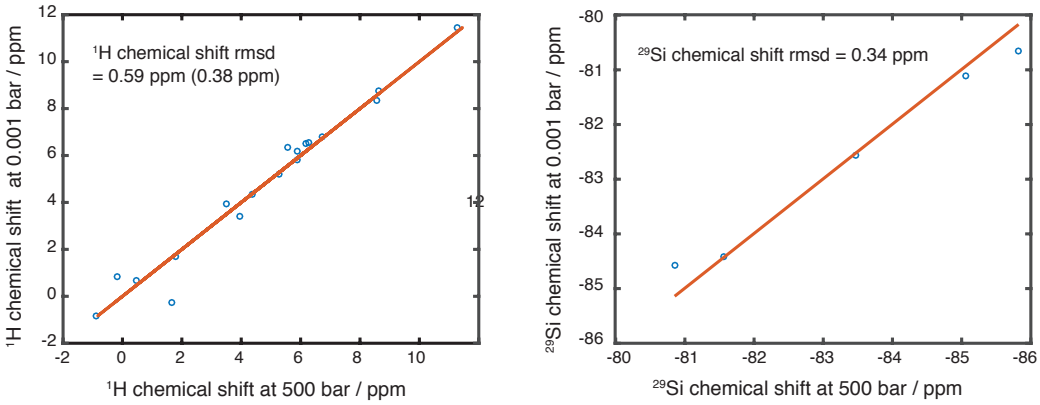

Figure S41 | Calculated chemical shift correlations between DFT structures of C-S-H based upon the ACcaV2 motif at 500 bar and 0.001 bar.

Using the constraints from 1D ^{29}Si NMR and INADEQUATE experiments, we have calculated the number of dimers and the mean repeat index of the distribution. These two values are then used to fit a chain distribution, which was determined using the following Monte Carlo procedure:

1. We define a cutoff of n = 10 for the repeat index (x_n = 0 for $n \geq 11$).
2. For $n \geq 2$, the mole fractions are generated by a random number that is uniformly distributed between 0 to its theoretical maximum value given by the contribution to the $Q^{(2p)}$-$Q^{(2p)}$ correlation for that Ca:Si ratio:

$$x_{n\geq 2} = r \text{ where } 0 \leq r \leq \frac{1-x_0}{n-1}$$

3. Pentamers constitute the remaining fraction.
4. A chain distribution is accepted only if the difference between mean repeat index ($\sum_n x_n n$) obtained from the distribution and that calculated from the NMR constraints is less than 0.0005.
5. This procedure is iterated and the average fractions are stored.
6. The iteration is continued until the average values of the distribution converge to a unique distribution.

The random chain distributions calculated for each Ca:Si ratio are shown in Figure S43. For constructing our representative C-S-H structures, the longest chain used is a tetradecamer (n = 4), as indicated in Figure S43C.

The reduced unit cells deemed likely structural elements are permuted and stacked in the directions of the crystal axes in order to build a three-dimensional crystal structure satisfying all of our

experimental NMR constraints. The proposed structures are shown in Figure S42 and their silicate species distributions are compared with the experimental values in Figure S43 (A and B).

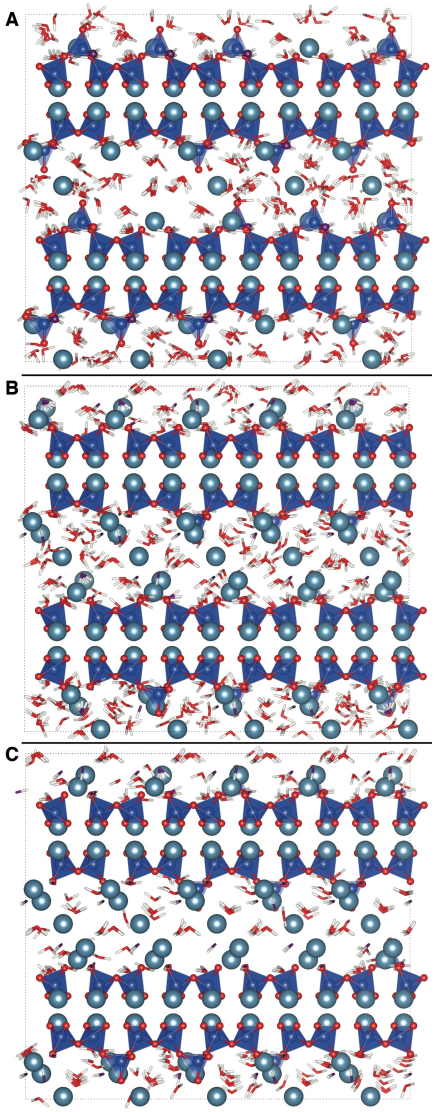

Figure S42 | Proposed structures satisfying the NMR constraints for Ca:Si = 1.25 (A), Ca:Si = 1.75 (B) and Ca:Si = 2.00 (C) viewed along the [100] direction. The relative positions of hydroxyls and water molecules have been relaxed with energy minimization at 0 K. Corresponding relaxed structures using MD are shown in Figure S44.

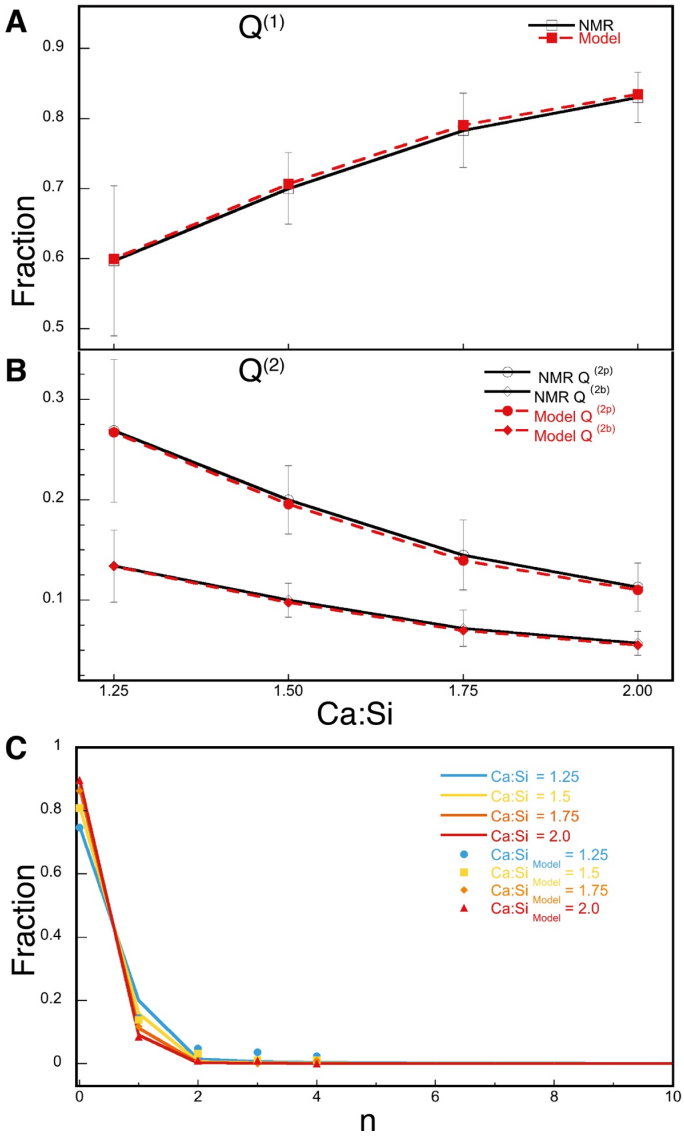

Figure S43 | Distribution of silicate species determined by NMR compared to those predicted by the random distribution model. (A) Comparison between $Q^{(1)}$ populations and (B) $Q^{(2)}$ populations. The experimental values are shown in unfilled markers connected by solid lines whereas the corresponding values in our proposed structures are shown in filled markers connected by dashed lines. (C) Distribution of silicate chains according to the random distribution model. The mole fractions (up to n = 4) used in our representative C-S-H structures are shown as markers.

8.4.2 Structural Relaxation

Initial structural relaxation was performed with classical molecular dynamics using force field potentials. The force field parameters used are known to describe well cementitious material systems.[12] Simulations were done using a constant pressure ensemble at 300 K and a time step of

0.7 fs using Velocity Verlet integration algorithms implemented in DLPOLY.[145] Ewald summation was used to take into account the long range forces above a cutoff distance of 8.5 Å. Snapshots after 2 ns of molecular dynamics simulation of each structure are shown in Figure S44 and are found to be structurally stable. Stoichiometry of the structures, bond distances and average calcium coordination numbers of bulk structures minimized after 2 ns are presented in Table S7. The bond distances from MD simulations are realistic. Histograms showing the distribution of coordination numbers for main phase calcium, interlayer calcium, and grand total of all calcium in these bulk C-S-H representations are shown in Figure S45. A systematic shift of the coordination number toward lower values is inevitable due to anharmonic vibrational motion of the atoms with respect to their proper equilibrium positions, an effect which is a function of the choice of force field used for the simulations. To estimate the magnitude of this shift for these systems, we carried out MD simulations on the known structure of 14 Å tobermorite for which 20% of the calcium are six coordinate and 80% are seven coordinate. The 2 ns MD snapshot of 14 Å tobermorite indicates roughly 30% fivefold coordination and 70% sixfold coordination. Therefore, we expect the results in Figure S45 to systematically underestimate a proper coordination number by nearly one.

We also find that in the Ca:Si = 1.75 structure 20% of Ca atoms are charge compensated by hydroxyl ions. Thomas et al.[61] calculated this value to be 23% in C-S-H with Ca:Si = 1.7 in hydrated cement samples and argued that such a bonding is possible only if a structural motif resembling jennite is present. Our results show that the jennite structural motif is not required to give this hydroxyl charge compensation – a highly defective tobermorite is sufficient. We have not considered any structures with a defective jennite motif, in which a missing dimer is replaced by two OH^- groups. Pentamers, octamers, undecamers and tetradecamers are the only non-dimers in our proposed structures limited by the box size considered. Generally, the interlayer separation distance shrinks up to 2 Å (down from 14 Å) upon structural relaxation for Ca:Si ≤ 1.5, affirming our choice of 14 Å tobermorite as a reasonable base structure. Clinotobermorite or other orthotobermorites can also be treated as the base structure satisfying the ^{29}Si and ^{1}H NMR constraints but without additional information describing the calcium environment in C-S-H it is difficult to evaluate which form of tobermorite would serve as the best base structure.

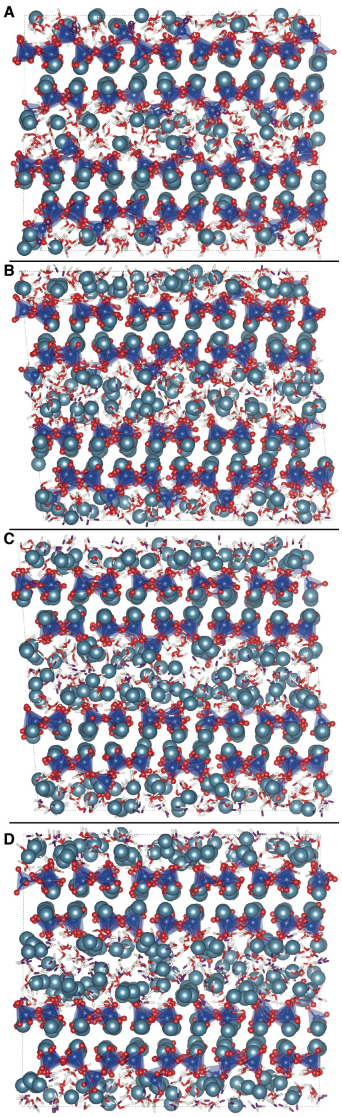

Figure S44 | Snapshots of bulk structures relaxed for 2 ns using classical MD simulations. The structures shown are (A) Ca:Si = 1.25, (B) Ca:Si = 1.5 , (C) Ca:Si = 1.75 and (D) Ca:Si = 2.0 respectively viewed along the [100] axes. All simulations produced structurally stable defective tobermorite features.

Ca:Si	Chemical formula	$Ca - OH/Ca$ [%]	$Ca - O$ [Å]	$Si - O$ [Å]	CN (Ca-O)
1.25	$Ca_{1.25}\,Si\,O_{3.2}\,(OH)_{0.1}(H_2O)_{1.82}$	0	2.3 ± 0.12	1.55 ± 0.08	5.9
1.50	$Ca_{1.5}\,Si\,O_{3.35}\,(OH)_{0.30}(H_2O)_{1.91}$	10	2.3 ± 0.12	1.55 ± 0.08	5.9
1.75	$Ca_{1.75}\,Si\,O_{3.39}\,(OH)_{0.71}(H_2O)_{1.72}$	20.1	2.3 ± 0.12	1.55 ± 0.08	5.8
2.00	$Ca_2\,Si\,O_{3.41}\,(OH)_{1.18}(H_2O)_{1.31}$	29.4	2.3 ± 0.12	1.55 ± 0.08	5.8

Table S7 | Structural characteristics of the representative C-S-H structures. These values are given for MD structures relaxed for 2 ns. These values show that the chemical and physical environment in the structures are

realistic. Ca-OH/Ca indicates the percentage of Ca atoms charge compensated by hydroxyl ions. The errors on the force field were estimated to be around 5% on distances[11]

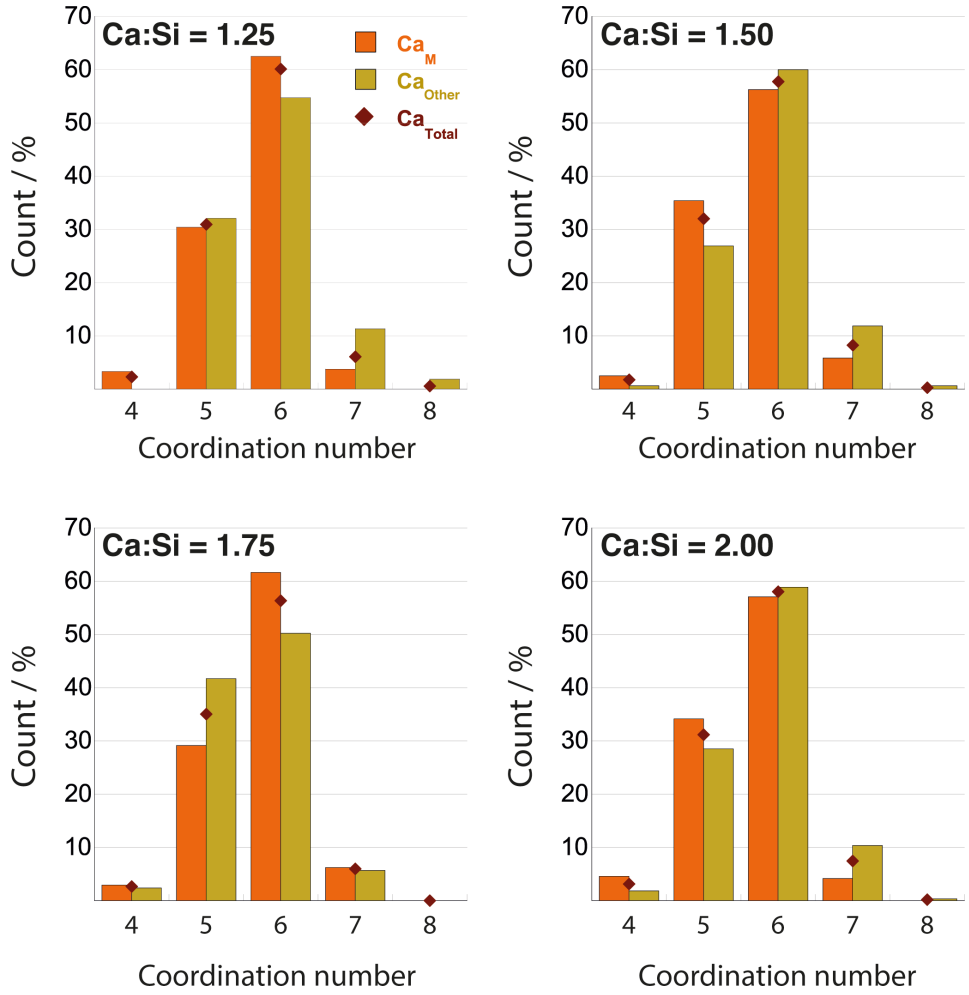

Figure S45 | Histograms showing populations of coordination numbers for each of the representative C-S-H structures. These values are given for MD structures relaxed for 2 ns. Orange and green bars indicate coordination of main phase and all other calcium, defined as Ca_M and Ca_{Other}. The black markers indicate the coordination over all calcium in the structure (Ca_{Total}). Owing to positional bias in the MD simulated structures, the populations are systematically shifted toward lower coordination number by nearly one.

8.4.3 Proton chemical shift calculations

The ^{1}H chemical shift calculations are performed on the set of reduced unit cells displayed in Figure S46. These reduced unit cells are selected to ensure a wide variety of different local defect environments, classified according to Figure S40A, are captured. We also probe the influence of Ca_I in the aqueous interlayer and perform a test of the influence of medium range interactions by studying the containing pentamers rather than infinitely long silicate chains and dimers, which are the only types of chains possible without juxtaposition of different reduced unit cells. Calculated proton chemical shift spectra for each of these structural candidates are shown in Figure S47. Structures that are not distinguishable on the basis of defect classification may have different arrangements of water molecules in the interlayer, representing viable structures with different local energy minima and indicated as different "versions" in Figure S47.

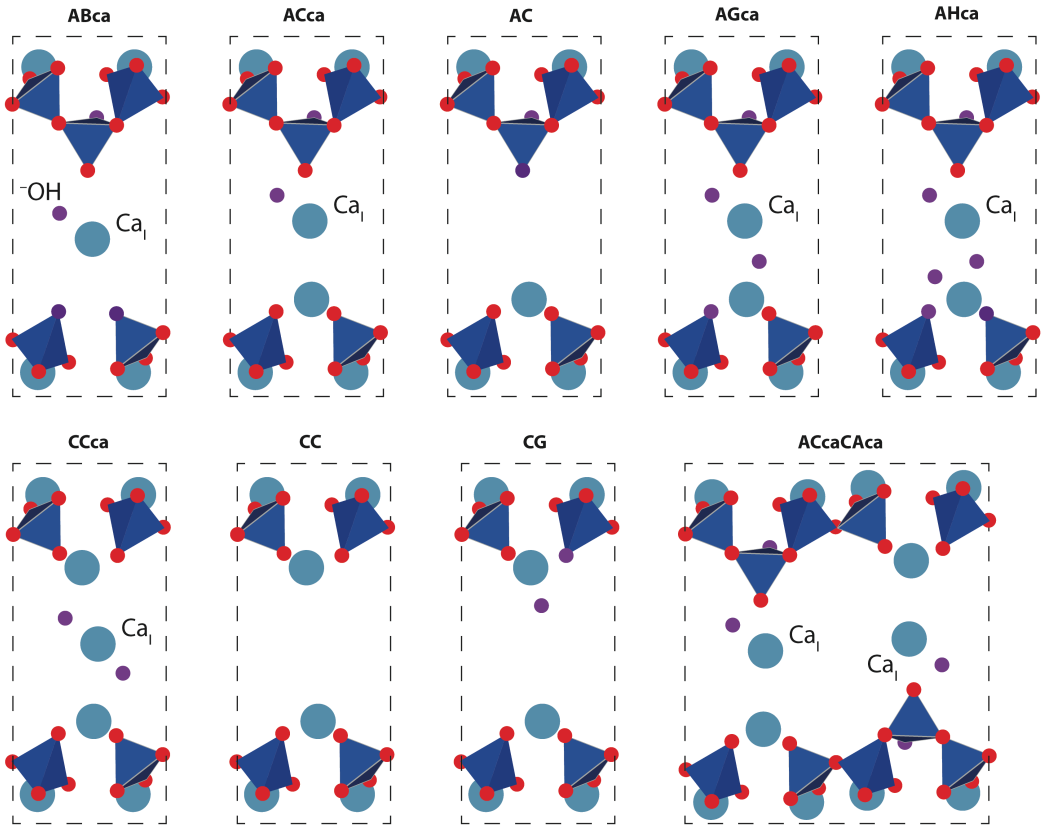

Figure S46 | Reduced unit cells used in ^{1}H and ^{29}Si chemical shift calculations. Interlayer water molecules are not shown.

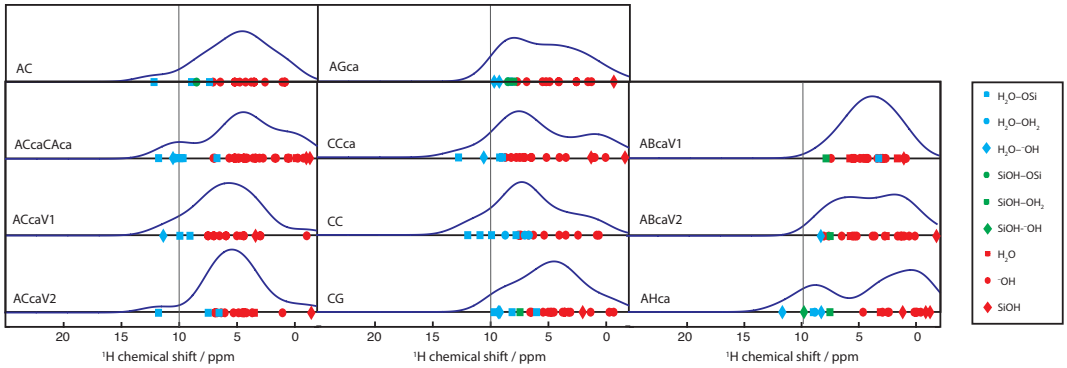

Figure S47 | Calculated spectra of ^{1}H GIPAW isotropic magnetic shifts for the investigated reduced unit cells of C-S-H. The line-shapes $\boldsymbol{S(\delta)}$ are extrapolated from the calculated chemical shifts $\boldsymbol{\delta_{calc}}$ as $\boldsymbol{S(\delta) = \frac{1}{\sqrt{2\,\pi R^2}}\, exp\left[-\frac{1}{2}\left(\frac{\delta-\delta_{calc}}{R}\right)^2\right]}$ with R = 1.5 ppm. In general, structures with Ca_B at the bridging site (types AC, CC, CG) better reproduce the characteristic tail in the ^{1}H line shape above 10 ppm. Structures that are identical according to our defect classification scheme but possess different arrangements of water molecules in the interlayer are distinguished by V1 or V2.

8.4.4 ^{29}Si chemical shift calculations

In addition to the ^{1}H chemical shift calculations, we also calculate ^{29}Si chemical shift parameters (Figure S48) for all structures used in Figure S47. The calculated ^{29}Si chemical shifts are compared to previous calculations[80] and to our experimental results. To the level of intrinsic accuracy of ^{29}Si chemical shift calculations, there is good agreement between the three datasets, allowing us to conclude that the C-S-H models proposed here are a good approximation of the studied systems.

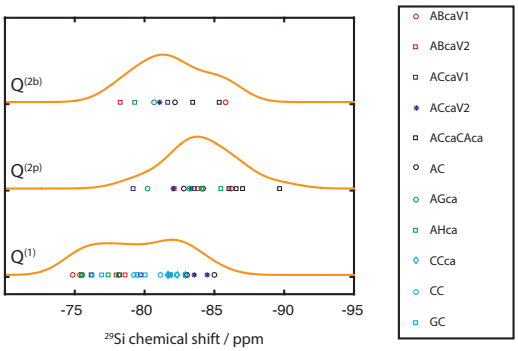

Figure S48 | Overlap of calculated ^{29}Si GIPAW isotropic magnetic shift spectra for each different Si site in the calculated structures shown in Figure S47. The line-shapes $\boldsymbol{S(\delta)}$ are extrapolated from the calculated chemical shifts $\boldsymbol{\delta_{calc}}$ as $\boldsymbol{S(\delta) = \frac{1}{\sqrt{2\,\pi R^2}}\, exp\left[-\frac{1}{2}\left(\frac{\delta-\delta_{calc}}{R}\right)^2\right]}$ with R = 1.5 ppm.

Chapter IX. Co-authored publications

THE JOURNAL OF PHYSICAL CHEMISTRY C

Article

pubs.acs.org/JPCC

Atomistic Simulations of Silicate Species Interaction with Portlandite Surfaces

Sandra Galmarini,*[,†] Aslam Kunhi Mohamed,[‡] and Paul Bowen[‡]

[†]Building Science and Technology, Eidgenössische Materialprüfungs- und Forschungsanstalt (EMPA), CH-8600 Dübendorf, Switzerland

[‡]Powder Technology Laboratory (LTP), Ecole Polytechnique Fédérale de Lausanne (EPFL), CH-1015 Lausanne, Switzerland

Supporting Information

ABSTRACT: Portlandite ($Ca(OH)_2$, CH) is the second most abundant hydrate formed in the reaction of Portland cement with water, making it an important component in the built environment. Formation of CH is closely linked to the growth of the main hydrate phase, calcium silicate hydrate (C−S−H), affecting the microstructure and properties of cement. Understanding the interplay between the growth of CH and C−S−H is the key to comprehend the hydration reaction kinetics. This interplay mainly happens via the interaction of the different species present in the pore solution with the hydrates formed. It has been speculated that silicate species poison the growth of portlandite. In this work, we give evidence and propose a mechanism toward this experimentally observed effect using atomistic simulations. We also study the stability of a Ca−Si complex ($CaSiO_2(OH)_2$) expected to exist in pore solution using metadynamics calculations. We find that the adsorption of this stable Ca−Si complex at the (0001) portlandite surface is energetically favorable, contrary to the previously observed adsorption of the CH growth species Ca2+ and OH−. Additionally, the adsorbed complex retains a certain mobility at the surface. Growth poisoning is thus likely to happen by preferential adsorption of Ca−Si complexes. The interplay of CH and C−S−H growth is likely to be enhanced by the easier polymerization of calcium−silicate species adsorbed at portlandite surfaces.

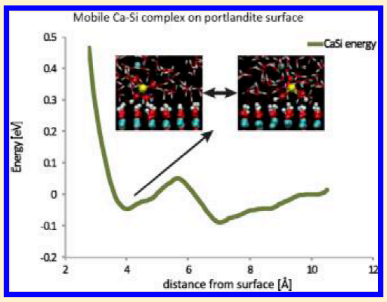

DOI: 10.1021/acs.jpcc.6b07044

J. Phys. Chem. C 2016, 120, 22407−22413

Cement and Concrete Research 102 (2017) 227–230

Contents lists available at ScienceDirect

Cement and Concrete Research

journal homepage: www.elsevier.com/locate/cemconres

Discussion

A discussion on the paper "Role of porosity on the stiffness and stability of (001) surface of the nanogranular C–S–H gel"

Hegoi Manzano[a,*], Aslam Kunhi Mohamed[b], Ratan K. Mishra[c], Paul Bowen[b]

[a] Condensed Matter Physics Department, University of the Basque Country, UPV/EHU, 48080 Bilbao, Spain
[b] Powder Technology Laboratory, EPFL Lausanne, CH-1015 Lausanne, Switzerland
[c] Department of Civil, Environmental and Geomantic Engineering, ETH Zurich, CH-8093 Zürich, Switzerland

ARTICLE INFO

Keywords:
C–S–H gel
Stiffness
Porosity
Surface energy
Molecular dynamics simulation

ABSTRACT

This paper is a discussion of a recent publication by Sekkal and coworkers, which investigated the elasticity, cohesion, and stability of the C-S-H (001) surface as a function of porosity using molecular dynamics simulations. In our discussion, we highlight some doubts about their model system for the C-S-H structure. We also comment on the defined stoichiometry, applied methodology and on various incongruous results and erroneous interpretations. We also draw attention to the lack of fundamental details provided by the authors and how it could be improved both conceptually and practically to allow readers to better understand the paper.

Cement and Concrete Research 102 (2017) 68–89

Contents lists available at ScienceDirect

Cement and Concrete Research

journal homepage: www.elsevier.com/locate/cemconres

cemff: A force field database for cementitious materials including validations, applications and opportunities

Ratan K. Mishra[a,*], Aslam Kunhi Mohamed[b], David Geissbühler[b], Hegoi Manzano[c], Tariq Jamil[d], Rouzbeh Shahsavari[e,*], Andrey G. Kalinichev[f,k], Sandra Galmarini[g], Lei Tao[e], Hendrik Heinz[d], Roland Pellenq[h], Adri C.T. van Duin[i], Stephen C. Parker[j], Robert J. Flatt[a], Paul Bowen[b,*]

[a] Department of Civil, Environmental and Geomatic Engineering, ETH Zurich, CH-8093 Zürich, Switzerland
[b] Powder Technology Laboratory (LTP), EPFL Lausanne, CH-1015 Lausanne, Switzerland
[c] Condensed Matter Physics Department, University of the Basque Country, UPV/EHU, 48080 Bilbao, Spain
[d] Department of Chemical and Biological Engineering, University of Colorado Boulder, Boulder, CO 80303-0596, USA
[e] Department of Civil and Environmental Engineering, Rice University, Houston, TX 77005, USA
[f] Laboratoire SUBATECH (UMR-6457), Institut Mines-Télécom Atlantique, F-44307 Nantes, France
[g] Building Science and Technology, Eidgenössische Materialprüfungs- und Forschungsanstalt (EMPA), CH-8600 Dübendorf, Switzerland
[h] Department of Civil and Environmental Engineering, Massachusetts Institute of Technology, 77 Massachusetts Av., Cambridge, 02139, MA, USA
[i] Department of Mechanical and Nuclear Engineering, The Pennsylvania State University, University Park, PA 16802, USA
[j] Department of Chemistry, University of Bath, Claverton Down, Bath BA2 7AY, United Kingdom
[k] International Laboratory for Supercomputer Atomistic Modelling and Multi-Scale Analysis, National Research University Higher School of Economics, Moscow, Russia

ARTICLE INFO

Keywords:
Cement force field database (***cemff***)
Force field (FF)
Parameterizations
Molecular simulation
Nanoscale mechanisms

ABSTRACT

This paper reviews atomistic force field parameterizations for molecular simulations of cementitious minerals, such as tricalcium silicate (C_3S), portlandite (CH), tobermorites (model C-S-H). Computational techniques applied to these materials include classical molecular simulations, density functional theory and energy minimization. Such simulations hold promise to capture the nanoscale mechanisms operating in cementitious materials and guide in performance optimization. Many force fields have been developed, such as Born–Mayer–Huggins, InterfaceFF (IFF), ClayFF, CSH-FF, CementFF, GULP, ReaxFF, and UFF. The benefits and limitations of these approaches are discussed and a database is introduced, accessible via a web-link (http://cemff.epfl.ch). The database provides information on the different force fields, energy expressions, and model validations using systematic comparisons of computed data with benchmarks from experiment and from ab-initio calculations. The ***cemff*** database aims at helping researchers to evaluate and choose suitable potentials for specific systems. New force fields can be added to the database.

http://dx.doi.org/10.1016/j.cemconres.2017.09.003

Chapter X. Curriculum vitae

Aslam Kunhi Mohamed

aslam.kunhimohamed@gmail.com

Born: 6th January 1988

Nationality: Indian

Education:

2014-18	PhD in Materials Science and Engineering, EPFL Switzerland
2011-13	Masters in Materials Science and Engineering, EPFL Switzerland
2006-10	Bachelors in Metallurgical and Materials Engineering, IITM India

Professional experience:

2013-14	Scientific Assistant at the Laboratory of Construction Materials, EPFL
2013	Six months internship in Sika Technology AG Zurich, Switzerland
2011-13	Research Assistant at the Laboratory of Construction Materials, EPFL
2009	Two months internship in HEG Ltd Bhopal, India

Distinctions:

2011-13	Research Assistant Scholarship at EPFL
2006	1st Rank/100,000+ applicants in Kerala state Engineering Entrance Examination
	532nd rank/600,000+ applicants in All India Engineering Entrance Examination
2004	Air India Scholastic Excellence Award

Journal publications:

1. Kunhi Mohamed, A., Parker, S. C., Bowen, P., and Galmarini, S. (2018). An atomistic building block description of C-S-H - Towards a realistic C-S-H model. *Cement and Concrete Research*, 107(May 2018):221–235

2. Kumar, A., Walder, B. J., Kunhi Mohamed, A., Hofstetter, A., Srinivasan, B., Rossini, A. J., Scrivener, K., Emsley, L., and Bowen, P. (2017). The Atomic-Level Structure of Cementitious Calcium Silicate Hydrate. *Journal of Physical Chemistry C*, 121(32):17188–17196

3. Mishra, R., Mohamed, A., Geissbuhler, D., Manzano, H., Jamil, T., Shahsavari, R., Kalinichev, A., Galmarini, S., Tao, L., Heinz, H., Pellenq, R., van Duin, A., Parker, S., Flatt, R., and Bowen, P. (2017). cemff: A force field database for cementitious materials including validations, applications and opportunities. *Cement and Concrete Research*, 102(September):68–89

4. Manzano, H., Kunhi Mohamed, A., Mishra, R. K., and Bowen, P. (2017). A discussion on the paper "Role of porosity on the stiffness and stability of (001) surface of the nanogranular C–S–H gel". *Cement and Concrete Research*, 102(November 2016):227–230

5. Galmarini, S., Kunhi Mohamed, A., and Bowen, P. (2016). Atomistic simulations of silicate species interaction with portlandite surfaces. *Journal of Physical Chemistry C*, 120(39):22407–22413

6. Raghukiran, N., Mohamed, A. K., and Kumar, R. (2014). Study of the influence of silicon phase morphology on the microstructural stress distribution in Al-Si alloys using object oriented finite element modeling. *Advanced Engineering Materials*, 16(1):112–121

7. Kumar, A., Srinivasan, B., Kunhi Mohamed, A., Lambert, D., Massonnet, G., Scrivener, K., and Bowen, P. (2018). A Controlled synthesis and characterization of homogeneous Calcium Silicate Hydrates phase with high Calcium to Silicate ratio. *Cement and Concrete Research*, (in review)

Conferences:

Paper Kunhi Mohamed A.; Galmarini S. C.; Bowen P.; Scrivener K. L. Atomistic Structure of C-S-H from Defec tive Tobermorite Structures: Variations of Defects and Features *ICCC 2015, Beijing* **2015**

Talk Kunhi Mohamed A.; Galmarini S. C.; Bowen P.; Scrivener K. L. Atomistic simulation of C-S-H: defects, stoichiometry and structures *Mechanism and Modelling of Waste Cement interactions, Murten CH* **2016**

Talk Kunhi Mohamed A.; Raghukiran N.; Devaraj S.; Kumar R, Microstructural effect on mechanical proper- ties of Aluminum Silicon alloys *NMD ATM, Bangalore,IN* **2010**

Poster Kunhi Mohamed A.; Galmarini S. C., Parker S.; Scrivener K. L., Bowen, P Atomistic structure of calcium silicate hydrate in cementitious systems *EUROMAT- Thessaloniki, Greece* **2017**

Invited Talks

U. Surrey MSC ETN ERICA kick-off meeting, Liphook UK, Feb 2018

UCL Modelling Surface and Defect Properties of Materials, London UK, Apr 2018

EMPA C-A-S-H II workshop, EMPA, Dubendorf Switzerland, Apr 2018

Languages:

Proficient	Malayalam, English
Beginner	French, German